Structure-Reactivity Relation, Optical Properties and Real-Time Study of Ultrafast Processes in Atomic Clusters

DISSERTATION

zur Erlangung des akademischen Grades
doctor rerum naturalium
(dr. rer. nat.)
im Fach Chemie

eingereicht an der
Mathematisch-Naturwissenschaftlichen Fakultät I
Humboldt-Universität zu Berlin

von
Herr Dipl.-Chem. MitricRoland
geboren am 14.01.1969 in Ravensburg

Präsident der Humboldt-Universität zu Berlin:
Prof. Dr. J. Mlynek

Dekan der Mathematisch-Naturwissenschaftlichen Fakultät I:
Prof. Dr. M. Linscheid

Gutachter:

1. Prof. Dr. Vlasta Bonacic-Koutecky
2. Prof. Dr. Joshua Jortner
3. Prof. Dr. Piercarlo Fantucci

eingereicht am: 2. Dezember 2003
Tag der mündlichen Prüfung: 19. Dezember 2003

Contents

1 Introduction **5**

2 Methodological **9**

2.1 Quantum mechanical description of molecular systems . . . 9
2.2 Born-Oppenheimer approximation . . . 11
2.3 Methods for the exploration of the potential energy surfaces . . . 13
  2.3.1 Geometry optimization methods . . . 13
  2.3.2 Characterization of stationary points and vibrational analysis . . . 15
  2.3.3 Transition state optimization and reaction pathways . . . 16
2.4 Electronic structure calculations . . . 17
  2.4.1 Hartree-Fock method . . . 17
  2.4.2 Configuration interaction method . . . 19
  2.4.3 Coupled cluster method . . . 21
  2.4.4 Density functional theory . . . 22
    2.4.4.1 The Kohn-Sham method . . . 23
    2.4.4.2 Local density methods . . . 26
    2.4.4.3 Gradient corrected methods . . . 26
    2.4.4.4 Hybrid functionals . . . 28
    2.4.4.5 The optimized effective potential method (OEP) . . . 29
    2.4.4.6 Computational aspects of the DFT methods . . . 29
    2.4.4.7 Analytic derivatives of the DFT energy . . . 31
    2.4.4.8 Performance . . . 33
  2.4.5 Ab initio methods for calculation of excited electronic states . . . 33
    2.4.5.1 Linear response methods . . . 33
    2.4.5.2 Equation-of-motion coupled cluster (EOM-CC) method . . . 37
  2.4.6 Basis sets . . . 39
  2.4.7 Effective core potentials (ECP) . . . 40

2.5 Theoretical approach to ultrafast spectroscopy . . . 42
  2.5.1 Wigner (phase-space) representation of quantum mechanics . . . 43
  2.5.2 The semiclassical Wigner method . . . 45
  2.5.3 Femtosecond pump-probe signals based on semiclassical multistate nuclear dynamics 46
  2.5.4 Ab initio adiabatic and nonadiabatic MD "on the fly" . . . 50
2.6 Laser control of ultrafast processes . . . 54
  2.6.1 Density matrix formalism of the optimal control theory . . . 56

3 Structural and electronic properties of pure gold and bimetallic silver-gold clusters: Reactivity aspects 58

3.1 Introduction . . . 58
3.2 Computational . . . 59
3.3 Neutral gold clusters Au_n (n=2-10) . . . 61
3.4 Bimetallic charged and neutral gold-silver trimers, tetramers and pentamers . . . 65
  3.4.1 $\mathrm{Ag}_m\mathrm{Au}_n^{0,+,-}$ (m+n=3) . . . 65
  3.4.2 $\mathrm{Ag}_m\mathrm{Au}_n^{0,+,-}$ (m+n=4) . . . 65
  3.4.3 $\mathrm{Ag}_m\mathrm{Au}_n^{0,+,-}$ (m+n=5) . . . 69
  3.4.4 Neutral bimetallic silver-gold $\mathrm{Ag}_n\mathrm{Au}_n$ (n=3,4,5,10) and $\mathrm{Ag}_{12}\mathrm{Au}_8$ clusters . . . 69
3.5 Electronic properties of bimetallic silver-gold clusters in context of their reactivity . . . 72
3.6 Reactivity of AgAu^- dimer towards CO and O_2 . . . 74
3.7 Conclusions . . . 75

4 Reactivity of gold and silver anions towards oxygen 76

4.1 Introduction . . . 76
4.2 Experimental methods . . . 77
4.3 Theoretical methods and accuracy . . . 78
4.4 Results . . . 79
  4.4.1 Hydrated gold cluster anions $\mathrm{Au}_n\mathrm{OH}^-$ . . . 79
  4.4.2 Adsorption of molecular oxygen on hydrated gold cluster anions $\mathrm{Au}_n\mathrm{OH}(\mathrm{O}_2)^-$ . . . 82
  4.4.3 Cooperative activation of molecular oxygen by anionic silver clusters . . . 86
  4.4.4 Reactivity of atomic gold anions toward oxygen and oxidation of CO . . . 88
4.5 Conclusions . . . 89

5 **Theoretical consideration of the reactions between vanadium-oxide cluster cations and ethylene** **91**

5.1 Introduction and motivation . . . 91

5.2 Experimental studies . . . 92

5.3 Computational methods . . . 92

5.4 Results and discussion . . . 93

5.4.1 Structures of $V_xO_y^+$ clusters . . . 93

5.4.2 Structures of $V_xO_y^+$-C_2H_4 complexes . . . 95

5.4.3 Reactions of $V_xO_y^+$ with ethylene . . . 97

5.4.3.1 $V_2O_4^+$+C_2H_4 . . . 97

5.4.3.2 $V_2O_6^+$+C_2H_4 . . . 99

5.4.3.3 $V_2O_5^+$+C_2H_4 . . . 100

5.4.3.4 $V_4O_{10}^+$+C_2H_4 . . . 107

5.4.4 IR-MPD spectroscopy of $V_xO_y^+$-C_2H_4 complexes . . . 108

5.5 Conclusions . . . 110

6 **Ab initio study of the absorption spectra of Ag_n (n=5-9) clusters** **112**

6.1 Introduction and motivation . . . 112

6.2 Computational . . . 113

6.3 Structures and absorption spectra for Ag_{5-9} clusters . . . 114

6.3.1 Structural properties . . . 114

6.3.2 Absorption spectra . . . 117

6.4 Comparison of absorption spectra with experimental findings . . . 120

6.4.1 Ag_5 and Ag_7 . . . 120

6.4.2 Ag_8 . . . 121

6.4.3 Ag_9 . . . 125

6.5 Conclusions . . . 127

7 **Theoretical investigation of the ultrafast NeNePo spectroscopy of coinage metal clusters** **129**

7.1 Motivation and introduction . . . 129

7.2 Wigner distribution approach for the simulation of NeNePo spectra . . . 131

7.2.1 Nuclear dynamics and NeNePo-ZEKE signals of Ag_2Au . . . 133

7.2.2 Nuclear dynamics and NeNePo-ZEKE signals of Ag_4 . . . 138

7.2.3 Nuclear dynamics and NeNePo-ZEKE signals of Au_4 . . . 144

7.3 Conclusions . . . 149

8 Kinetics and equilibrium of small metallic clusters: Ab initio confinement molecular dynamics study of Au_4 151

8.1 Introduction an motivation 151

8.2 The problem 152

8.3 Computational 153

8.4 Kinetics 154

8.5 Results and discussion 155

9 New strategy for optimal control of femtosecond pump-dump processes; Illustration on the isomerization in Na_3F_2 cluster 158

9.1 Introduction 158

9.2 Optimal control strategy 159

9.3 Nonstoichiometric Na_nF_{n-1} clusters 163

9.4 Optimal control of the isomerization of Na_3F_2 163

9.5 Summary and conclusion 168

10 Conclusions 170

11 Zusammenfassung 173

Chapter 1

Introduction

The study of atomic as well as of molecular clusters has become an established and recognized area due to the numerous important discoveries emerging from pronounced size dependent microscopic properties which clusters, either isolated in the gas phase or embedded in different media can exhibit [1, 2, 3, 4, 5]. The interest of the cluster science was first focused on scalable properties concerning a smooth transition from small particles to solids. In this respect clusters may be viewed as bridging systems between the atoms and the bulk. However, in the meantime it has become evident that the non-scalable properties in the nanosize regime which are a consequence of the quantum confinement can lead to the emergence of fully new phenomena and to the striking new unexpected properties of small clusters.

Experimentally, the study of mass selected clusters involved their electronic and optical properties as well as their reactivity towards organic and inorganic molecules [4]. Parallel to the experimental studies, the theory provided information on structural and electronic properties of gas phase clusters and the connection between energetics, structural and electronic properties as a function of the size has been established [1, 5]. Comparison between theoretical absorption spectra and the experimental ones recorded at low temperatures has furthermore allowed to identify the structures of metal clusters responsible for the observed properties [1]. Due to the advances in conceptual and technical aspects of the femtosecond pump-probe spectroscopy pioneered by Zewail [6, 7, 8] the ultrafast time-resolved studies of cluster dynamics became available in the last decade. These studies can provide insight into the nature and timescales of processes such as conformational changes and internal vibrational energy redistributions.

In this work three aspects will be addressed:

(A) Structural, electronic properties and reactivity of metal clusters

(B) Stationary optical properties of silver clusters

(C) Real time investigation and control of ultrafast processes in noble metal clusters and in nonstoichiometric sodium fluoride clusters

(A) An area in which the nonscalability of cluster properties plays an important role is the chemical reactivity and the catalytic activity of clusters. A particularly striking example are the small gold clusters showing unusually high catalytic activity even at low temperatures, in sharp contrast to the bulk gold surfaces which are inert [9, 10]. A model reaction in the studies of the catalytic activity of gold clusters is the low temperature oxidation of CO which requires the binding and the activation of molecular oxygen.

The binding energies for O_2 are well correlated with the electronic structure of the clusters and only those clusters with unpaired electrons and low electron affinities are able to activate molecular oxygen while those with high electron affinities and closed shell electronic structure are inert [11, 12]. In this work structural and electronic properties of pure gold and mixed silver-gold clusters have been studied in the framework of the density functional theory in order to provide the basis for the systematic study of the reactivity of coinage metal clusters. The mixed silver-gold clusters are particularly interesting since their electronic properties can be tuned by changing the composition. Due to the fact that the reactivity is strongly correlated with electronic properties such as ionization potentials and electron affinities, it is expected that this provides a way for tailoring the chemical reactivity of these systems.

An important question which still needs to be answered is the way in which the activation of molecular oxygen can be promoted and controlled. From the experimental studies it is well known that traces of moisture can play a very important role and can increase the reactivity of clusters [13, 14, 15]. In this work it is shown that the unreactive gold clusters can be activated for the binding of molecular oxygen by binding an electron acceptor group such as OH which changes the electronic structure of the clusters. At the same time the bare clusters which were reactive prior to the binding of OH become unreactive. Moreover a cooperative binding of molecular oxygen can be induced on anionic silver clusters leading to the new oxidized species. This provides the evidence that the reactivity of the clusters can be tuned by binding suitable groups as convincingly demonstrated in recent experiments [16, 17].

Another important area from the application point of view is the design of catalysts for the selective oxidation of hydrocarbons [18]. For this purpose transition metal oxides are widely used. However, the mechanisms which govern catalytic reactions are still not well understood and the elucidation of the structure-reactivity relationship at metal oxide surfaces plays a key role in understanding catalytic activity and selectivity. The study of gas phase clusters serves as a recognized approach to model the active sites on catalytic surfaces since the influence of factors such as size, composition, stoichiometry, charge and oxidation state can systematically be investigated in the studies of mass selected clusters [19, 20]. In this work, the reactions of cationic vanadium oxide clusters with ethylene have been studied. The experiments performed by Castleman and coworkers [21] have shown significant and highly cluster size specific reaction pathways which motivated the theoretical studies performed in this work. The theoretical results presented here together with experimental findings provide evidence for the selectivity of $V_xO_y^+$ clusters and allow to propose a general mechanism for the oxidation of ethylene .

(B) As already mentioned, the reduction of the size leading to the nanoscale regime gives rise to fully new and unexpected properties. This concerns in particular the optical properties and can potentially offer numerous possibilities for the applications. Recently, photoactivated fluorescence has been produced upon visible illumination of silver oxide films and it is attributed to the photochemically generated silver nanoclusters [22, 23]. The photoproduction of small Ag_n clusters might be utilized in optical storage. Moreover, due to the fact that the fluorescence is strongly size dependent this gives a potential for a parallel readout and can increase storage capacity due to the possibility of color mixing for different cluster sizes. In this work absorption patterns of small silver clusters have been determined using accurate quantum chemical methods based on the coupled cluster theory. Their comparison with the experimental absorption and fluorescence-excitation spectra allowed to assign the most stable structures of the Ag_n (n=5-9) clusters to the measured data and to give the theoretical interpretation of the observed absorption and emission properties of the small mass selected silver clusters.

(C) One experimental technique which is well suited for the exploration of the dynamics of the neutral mass selected clusters is the negative ion-to-neutral-to-positive ion (NeNePo) spectroscopy introduced by

Wöste, Berry and colleagues [24]. The idea of this method is to prepare mass selected anionic clusters which are then subjected to the photodetachment with an ultrashort pump-pulse. In this way a neutral cluster in the non-equilibrium geometry is prepared and its time evolution can be monitored by probing with a second ultrashort pulse which ionizes the system to the cationic state.

One of the aims of this work was to determine the conditions under which different processes can be observed in the NeNePo spectroscopy and to determine the general scope of the method. From a theoretical point of view, the understanding of the ultrashort dynamics of clusters requires a development and application of methods for multistate dynamics involving all degrees of freedom. In this work a combination of the ab-initio molecular dynamics "on the fly" carried out in the framework of the density-functional theory (DFT) with the semiclassical Wigner distribution method has been introduced. This allowed to establish a general approach for the accurate simulations of the NeNePo pump-probe spectra in systems of considerable complexity which are unaccessible to the treatment by the standard quantum dynamics methods. This formalism has been applied to the small coinage metal clusters and the typical situations which can arise have been illustrated on the examples of the mixed trimer (Ag_2Au) and pure tetramers (Ag_4 and Au_4). The theoretical simulations presented in this work also stimulated the experimental studies which fully confirmed the theoretical predictions. Ab initio MD simulations "on the fly" also offer a general framework for the exploration of the potential energy surfaces and can be employed for calculation of the equilibrium properties of clusters and the kinetics of cluster isomerization reactions. In this work, ab initio MD "on the fly" has been implemented in the framework of the confinement molecular dynamics introduced by Chekmarev [25]. The scope of the method has been illustrated on the example of Au_4 cluster and is complementary to the studies performed in the framework of the NeNePo spectroscopy.

Parallel to the advancement of the methods for the interrogation of the cluster dynamics in recent years the development of the pulse shaping techniques [26, 27, 28, 29] permitted also the design of femtosecond laser pulses which are able to guide the molecular dynamics to the desired target, such as a given fragmentation channel, a particular isomer or a desired reaction product. From the experimental side a closed loop learning control proposed by Judson and Rabitz [30] opened the possibility to apply the optimal control to more complex systems. Since the potential energy surfaces of multidimensional systems are complicated and mostly not available, the idea was to combine the femtosecond laser system with a computer-controlled pulse shaper to produce specific laser pulses which act on the system and induce photochemical processes. After detection of the reaction product the learning algorithm is used to modify the field based on information obtained from the experiment and in this way the yield of the desired product can be amplified and the undesired products can be suppressed. The drawback of such multi-parameter optimization schemes is that they often lead to very complicated pulse forms in which a relevant physical information is hidden. Since the tailored laser pulses select the pathways and excitation channels which optimally lead to the desired product, their analysis should allow to establish the mechanism of the process. Therefore, development of theoretical methods are needed which allow to design interpretable optimal laser pulses for complex systems such as clusters and to establish the connection between underlying dynamics and the pulse shapes. For this purpose ab initio adiabatic and non-adiabatic molecular dynamics "on the fly" is particularly suitable because it can be applied to relatively complex systems and moreover it can be implemented directly in the procedure for the optimal control. In this work a new strategy for optimal control with tailored pump-dump pulses which drive a system via an electronically excited state to a desired product in the ground state is developed. It is based on the concept of the intermediate target in the excited state which selects the appropriate Franck-Condon window at a given time delay between the two pulses mandatory for reaching optimally the desired product. The method is formulated in the Wigner representation and allows the implementation based on classical trajectories which can be propagated using ab initio MD “on the fly” which makes it suitable for the systems with considerable number of degrees of freedom. The scope of the strategy is shown by optimizing and analyzing the pump- and dump-pulses which drive the isomerization process in the Na_3F_2 cluster suppressing the passage through the conical intersection. The concept of the intermediate target has a general nature and can be extended to the control of photochemical isomerization in complex systems.

This thesis is organized as follows: In chapter 2 the theoretical methods used in the studies performed in this work are presented. This involves the electronic structure theory for the description of the ground and excited states as well as the semiclassical Wigner distribution approach for the simulation of the femtosecond pump-probe spectra and for the optimal control based on the ab initio MD “on the fly”.

In the part A structural, electronic properties as well as reactivity of atomic clusters is addressed. Chapter 3 is devoted to the structural and electronic properties of the pure gold and mixed silver-gold clusters. The systematic study of pure gold clusters in the range Au_n (n=2-10) and of mixed trimers, tetramers and pentamers has been performed. In addition, the electronic properties are discussed in the context of the reactivity. In Chapter 4 the reactions of the hydrated anionic gold clusters Au_nOH^- (n=2-5) and anionic silver clusters Ag_n^- (n=1,5) with molecular oxygen have been studied. Moreover the mechanism for the CO oxidation on $AuO^-_{1.2.3}$ has been investigated. Chapter 5 presents the study of structural properties of $V_xO_y^+$(x=2,4, y=2-6, 10) and their reactivity towards ethylene.

Part B of the thesis is devoted to the stationary optical properties of metal clusters. In Chapter 6 the stationary absorption spectra of Ag_n(n=5-9) clusters are reported and a structural assignment has been made in comparison with the available experimental spectra.

The subject of the part C is the real time dynamics and the control of femtosecond processes. In Chapter 7 the simulations of NeNePo spectra of small coinage metal clusters (Ag_2Au, Ag_4 and Au_4) are presented and the scope of the NeNePo technique is established. The studies of the cluster dynamics from Chapter 7 are complemented by the study of the kinetics of the Au_4 isomerization based on the confined molecular dynamics simulations in the framework of the ab initio molecular dynamics. Chapter 9 presents a new strategy for the optimal control of cluster dynamics formulated in the framework of the semiclassical Wigner distribution approach and illustrated on the example of the controlled isomerization of the Na_3F_2 cluster. Finally, conlusions are given in Chapter 10.

Chapter 2

Methodological

2.1 Quantum mechanical description of molecular systems

The understanding of the properties of matter on a microscopic scale can be achieved in the framework of quantum mechanics [31]. Within quantum mechanics the most complete description of the state of a physical system is given by a state vector which is an element of the complex linear Hilbert space. The notion of an abstract state vector has been introduced into the quantum mechanics by Dirac and has enabled to unify seemingly different representations of Heisenberg and Schrödinger in an mathematically elegant way. Consequently, throughout this work Dirac's notation representing the state of a physical system by a "ket" vector $|\Psi\rangle$ will be used. The physical observables are associated with linear hermitian operators which act on the state vectors, and the form of these operators is established by requiring them to satisfy certain commutation relations[1]. The time evolution of a state vector $|\Psi(t)\rangle$ is determined by the time dependent Schrödinger equation,

$$i\hbar\frac{\partial}{\partial t}|\psi\rangle = \hat{H}|\psi\rangle \tag{2.1}$$

where $\hat{H}$ is the Hamilton operator (Hamiltonian) corresponding to the total energy of the system. This operator can be obtained by replacing the classical observables in the classical Hamilton function [32] with corresponding quantum mechanical operators. For a N particle system the classical Hamilton function in the nonrelativistic limit and in the absence of external fields is the sum of kinetic and potential energy:

$$H = \sum_{i=1}^{N}\frac{|\mathbf{p}_i|^2}{2m_i} + V(\mathbf{r}_1, \mathbf{r}_2, ..., \mathbf{r}_N) \tag{2.2}$$

where $\mathbf{p}_i$ are classical momenta and $V(\mathbf{r}_1, \mathbf{r}_2, ..., \mathbf{r}_N)$ is the potential energy of the system.

Most commonly used representation of the quantum mechanics is the position representation. Since the eigenstates $|x\rangle$ of a position operator $\hat{x}$ form a complete set, any quantum state $|\Psi(t)\rangle$ can be expanded into position eigenstates. Using the completeness relation,

$$\mathbf{1} = \int_{-\infty}^{\infty} dx|x\rangle\langle x| \tag{2.3}$$

---

[1] Generally, in cartesian coordinate system it is required that the operators associated with the position and momenta of the particles satisfy:

$$[\hat{x}_i, \hat{x}_j] = \hat{0} \quad [\hat{p}_i, \hat{p}_j] = \hat{0} \quad [\hat{x}_i, \hat{p}_j] = i\hbar\delta_{ij}\hat{I}$$

These relations form the cornerstone of the quantum mechanics and are called by Dirac "fundamental quantum conditions".

this gives the representation of a state vector,

$$|\Psi(t)\rangle = \mathbf{1}|\Psi(t)\rangle = \int_{-\infty}^{\infty} dx|x\rangle\langle x|\Psi(t)\rangle. \tag{2.4}$$

The projection of a state vector $|\Psi(t)\rangle$ onto the position eigenvector $|x\rangle$ is called a wavefunction and is usually denoted by $\Psi(x,t)$,

$$\Psi(x,t) = \langle x|\Psi(t)\rangle \tag{2.5}$$

According to Born the square of this function corresponds to probability density for finding the particle at the position x. More generally the state vector can be expanded into the eigenstates of any hermitian operator associated with some observable A giving various different representations of quantum mechanics. Possible results of a measurement of the observable A are always eigenvalues of the associated quantum mechanical operator, and probabilities for different results are given by squares of the expansion coefficients of the state vector $|\Psi(t)\rangle$ into the eigenstates of the operator $\hat{A}$. This summarizes the basic principle of quantum mechanics with the accent on the independence on the particular representation. Later in this work so called Wigner (or phase space) representation [33, 34] will be described and used since it is very convenient for development of semiclassical approximations and gives a very appealing picture of the abstract quantum states. Introducing quantum mechanical operators associated with coordinates and momenta using the prescription $\mathbf{r} \rightarrow \mathbf{r}\cdot$ and $\mathbf{p} \rightarrow \frac{\hbar}{i}\nabla$ the time dependent Schrödinger equation in nonrelativistic limit and in the absence of external fields for a N-particle system becomes,

$$i\hbar\frac{\partial\Psi(\mathbf{r}_1,\mathbf{r}_2,...,\mathbf{r}_N,t)}{\partial t} = \sum_{i=1}^{N} -\frac{\hbar^2}{2m_i}\nabla^2\Psi(\mathbf{r}_1,\mathbf{r}_2,\cdots,\mathbf{r}_N,t) + V(\mathbf{r}_1,\mathbf{r}_2,\cdots,\mathbf{r}_N)\Psi(\mathbf{r}_1,\mathbf{r}_2,\cdots,\mathbf{r}_N,t). \tag{2.6}$$

If the Hamiltonian does not contain explicit time dependence, the separation of time and space variables can be performed by substituting $\Psi(\mathbf{r}_1,\mathbf{r}_2,\cdots,\mathbf{r}_N,t) = \psi(\mathbf{r}_1,\mathbf{r}_2,...,\mathbf{r}_N)e^{-\frac{iEt}{\hbar}}$ which leads to the time independent Schrödinger equation

$$\sum_{i=1}^{N} -\frac{\hbar^2}{2m_i}\nabla^2\psi(\mathbf{r}_1,\mathbf{r}_2,\cdots,\mathbf{r}_N) + V(\mathbf{r}_1,\mathbf{r}_2,\cdots,\mathbf{r}_N)\psi(\mathbf{r}_1,\mathbf{r}_2,\cdots,\mathbf{r}_N) = E\psi(\mathbf{r}_1,\mathbf{r}_2,...,\mathbf{r}_N). \tag{2.7}$$

Solutions of this equation determine physically measurable energies of the system and the time dependence in the state with definite energy E is carried out by a phase factor $e^{-\frac{iEt}{\hbar}}$. Such states are called stationary states since the mean values of any physical observable in such a state are time independent. However due to the linearity of the Schrödinger equation any superposition of stationary states is also a solution with the particular characteristics that the average values of the observables become functions of time. Therefore it can be said that the dynamics in the framework of quantum mechanics emerges from the interference of stationary sates. For a molecular system composed of some number of atomic nuclei and electrons and taking into account only the Coulomb interaction and in the absence of external fields the Hamiltonian has the form

$$\hat{H} = \sum_{A}^{nucl.} -\frac{\hbar^2}{2m_A}\nabla_A^2 + \sum_{i}^{el.} -\frac{\hbar^2}{2m_e}\nabla_i^2 + \sum_{A<B}^{nucl.} \frac{Z_A Z_B e^2}{4\pi\epsilon_0 r_{AB}} - \sum_{i}^{el.}\sum_{A}^{nucl.} \frac{Z_A e^2}{4\pi\epsilon_0 r_{iA}} + \sum_{i<j} \frac{e^2}{4\pi\epsilon_0 r_{ij}} \tag{2.8}$$

or written in a more compact form

$$\hat{H} = \hat{T}_n + \hat{T}_e + \hat{V}_{nn} + \hat{V}_{ne} + \hat{V}_{ee} \tag{2.9}$$

where the terms $\hat{T}_n$, $\hat{T}_e$, $\hat{V}_{nn}$, $\hat{V}_{ne}$, $\hat{V}_{ee}$ indicate the nuclear kinetic energy, electronic kinetic energy, nuclear-nuclear repulsion energy, electron-nuclear attraction energy and electron-electron repulsion energy. The solution of the time independent Schrödinger equation (2.7) for a molecular system with a Hamiltonian (2.8) represents a central task of quantum chemistry and in the next sections methods used for solving this problem will be described.

It should be also pointed out that the state vector $|\psi\rangle$ gives the most complete possible description of the state of the system, but there are situations such as for example ensembles of interacting systems to which no state vector can be associated. In order to treat these situations the formalism of quantum mechanics can be extended by introducing the density operator $\hat{\rho}$ [35] defined by

$$\hat{\rho} = \sum_i P_i |\psi_i\rangle\langle\psi_i| \tag{2.10}$$

where P_i represents the probability that the system is found in the state $|\psi_i\rangle$. The time evolution of the density operator is determined by the Liouville-von Neumann equation

$$i\hbar\frac{\partial\hat{\rho}}{\partial t} = [\hat{H}, \hat{\rho}]. \tag{2.11}$$

2.2 Born-Oppenheimer approximation

Molecular systems consist of atomic nuclei and electrons whose masses are very different and therefore it is expected that the time scales of their motion are very different. On a time scale of electronic motion the nuclei are almost stationary. On the other hand, on a time scale of the nuclear motion the electrons move so fast that their motion can be effectively replaced by a kind of averaged potential. This intuitive picture offers a starting point for introducing the Born-Oppenheimer approximation [36]. Since the masses of the atomic nuclei are much larger than the masses of the electrons, in the solution of the molecular Schrödinger equation (2.7) one can take initially $m_A \to \infty$. In this way the nuclear kinetic energy in the molecular Hamiltonian vanishes and nuclear coordinates become fixed parameters. For this fixed nuclear configuration the Schrödinger equation becomes

$$\hat{H}_{el}(\mathbf{R})\psi_{el}(\mathbf{r};\mathbf{R}) = E(\mathbf{R})\psi_{el}(\mathbf{r};\mathbf{R}) \tag{2.12}$$

where $\hat{H}_{el}(\mathbf{R})$ is the electronic Hamiltonian

$$\hat{H}_{el}(\mathbf{R}) = \hat{T}_e + \hat{V}_{nn} + \hat{V}_{ne} + \hat{V}_{ee} \tag{2.13}$$

and $\mathbf{R}$ and $\mathbf{r}$ denote the set of nuclear and electronic coordinates, respectively. Solution of this electronic Schrödinger equation gives a set of energies ($E_i(\mathbf{R})$ and wavefunctions $\psi_{el,i}(\mathbf{r})$ which are both parametrically dependent on the nuclear configuration. Now, as the eigenfunctions of an Hermitian operator the electronic wave functions build a complete set and therefore the true eigenfunction of the molecular Hamiltonian for finite masses can always be expanded into the electronic wavefunctions with expansion coefficients being only functions of nuclear coordinates

$$\psi(\mathbf{r},\mathbf{R}) = \sum_i \phi_{nucl,i}(\mathbf{R})\psi_{el,i}(\mathbf{r};\mathbf{R}). \tag{2.14}$$

Inserting this ansatz into the time independent Schrödinger equation one obtains a coupled set of equations which determine the nuclear wavefunctions $\phi_{nucl,i}(\mathbf{R})$:

$$[\hat{T}_n + E_i(\mathbf{R})]\phi_{nucl,i}(\mathbf{R}) - \sum_j \hat{B}_{ij}\phi_{nucl,j}(\mathbf{R}) = E\phi_{nucl,i}(\mathbf{R}) \quad i,j = 1,\cdots \tag{2.15}$$

where $\hat{B}_{ij}$ are the operators responsible for the coupling between electronic and nuclear degrees of freedom

$$\hat{B}_{ij} = \sum_A^{nucl.} \frac{\hbar^2}{2m_A}\Big[2\langle\psi_{el,i}(\mathbf{r};\mathbf{R})|\nabla_{R_A}|\psi_{el,j}(\mathbf{r};\mathbf{R})\rangle\nabla_{R_A} + \langle\psi_{el,i}(\mathbf{r};\mathbf{R})|\nabla^2_{R_A}|\psi_{el,j}(\mathbf{r};\mathbf{R})\rangle\Big] \tag{2.16}$$

Neglecting the coupling between different electronic states yields the adiabatic approximation in which the total molecular wavefunction (2.14) reduces to a single term $\psi(\mathbf{r},\mathbf{R}) = \phi_{nucl,i}(\mathbf{R})\psi_{el,i}(\mathbf{r};\mathbf{R})$. The nuclear wavefunction $\phi_{nucl,i}(\mathbf{R})$ is obtained as the solution of the equation

$$[\hat{T}_n + E_i(\mathbf{R}) - \hat{B}_{ii}]\phi_{nucl,i}(\mathbf{R}) = E\phi_{nucl,i}(\mathbf{R}). \tag{2.17}$$

It is interesting to note that introducing the vector filed $\mathbf{A}_R$ defined as

$$\mathbf{A}_R = i\hbar\sum_A^{nucl.}\langle\psi_{el,i}(\mathbf{r};\mathbf{R})|\nabla_{R_A}|\psi_{el,i}(\mathbf{r};\mathbf{R})\rangle \tag{2.18}$$

the equation for the nuclear wavefunction can be written in the form analogous to a form of the Schrödinger equation for a system of particles in the presence of the magnetic field derivable from the vector potential $\mathbf{A}$, namely

$$\sum_A^{nucl.}\Big[-\frac{\hbar^2}{2m_A}\Big(\nabla_{R_A} + \frac{1}{i\hbar}\mathbf{A}_R\Big)^2 + U^{(i)}(\mathbf{R})\Big]\phi_{nucl,i}(\mathbf{R}) = E\phi_{nucl,i}(\mathbf{R}) \tag{2.19}$$

where $U_i(\mathbf{R})$ is the effective adiabatic potential

$$U_i(\mathbf{R}) = E_i(\mathbf{R}) + \sum_A^{nucl.}\frac{\hbar^2}{2m_A}\langle\nabla_{R_A}\psi_{el,i}(\mathbf{r};\mathbf{R})|\nabla_{R_A}\psi_{el,i}(\mathbf{r};\mathbf{R})\rangle - \sum_A^{nucl.}\frac{1}{2m_A}|\mathbf{A}_R|^2 + V_{nn}(\mathbf{R}) \tag{2.20}$$

consisting of electronic energy, nuclear-nuclear repulsion energy and additional two correction terms. If the electronic state $E_i(\mathbf{R})$ is non-degenerate for all nuclear configurations then the vector function $\mathbf{A}_R$ vanishes [2]. More generally if $\nabla\times\mathbf{A}_R = 0$ then a gauge transformation

$$\begin{aligned}
\phi_{nucl,i}(\mathbf{R}) &\rightarrow exp\Big(-\frac{i}{\hbar}\int_{\mathbf{R}_0}^{\mathbf{R}}\mathbf{A}_R d\mathbf{R}\Big)\phi_{nucl,i}(\mathbf{R}) && (2.21)\\
\psi_{el,i}(\mathbf{r};\mathbf{R}) &\rightarrow exp\Big(\frac{i}{\hbar}\int_{\mathbf{R}_0}^{\mathbf{R}}\mathbf{A}_R d\mathbf{R}\Big)\psi_{el,i}(\mathbf{r};\mathbf{R}) && (2.22)\\
\mathbf{A}_R &\rightarrow \mathbf{0} && (2.23)
\end{aligned}$$

---

[2] From the difference $\mathbf{A}_R - \mathbf{A}_R^* = i\hbar\sum_A^{nucl.}\Big[\langle\psi_{el,i}(\mathbf{r};\mathbf{R})|\nabla_{R_A}|\psi_{el,i}(\mathbf{r};\mathbf{R})\rangle + \langle\nabla_{R_A}\psi_{el,i}(\mathbf{r};\mathbf{R})|\psi_{el,i}(\mathbf{r};\mathbf{R})\rangle\Big] = i\hbar\sum_A^{nucl.}\nabla_{R_A}\langle\psi_{el,i}(\mathbf{r};\mathbf{R})|\psi_{el,i}(\mathbf{r};\mathbf{R})\rangle$, and if the electronic wavefunction is normalizable it follows that the function $\mathbf{A}_R$ is always real. If additionally, the electronic state is non-degenerate for all nuclear configurations than the electronic wavefunction can be chosen real from which it follows that $\mathbf{A}_R$ necessarily vanishes in that case.

produces no change in the total wavefunction but reduces the nuclear Schrödinger equation to a simpler form eliminating $\mathbf{A}_R$,

$$\sum_{A}^{nucl.}\Big[-\frac{\hbar^2}{2m_A}\nabla^2_{R_A}+U_i(\mathbf{R})\Big]\phi_{nucl,i}(\mathbf{R})=E\phi_{nucl,i}(\mathbf{R}) \tag{2.24}$$

which is the usual form of the nuclear Schrödinger equation in the Born-Oppenheimer (BO) approximation [36]. It should be pointed out that the nuclear potential (2.20) contains, in addition to electronic energy $E_i(\mathbf{R})$, a small correction term dependent on the inverse masses of the nuclei which, however, is usually neglected. This leads to the usual picture of nuclei moving in the potential $E_i(\mathbf{R})$ determined by the solution of the electronic Schrödinger equation

$$\sum_{A}^{nucl.}\Big[-\frac{\hbar^2}{2m_A}\nabla^2_{R_A}+E_i(\mathbf{R})\Big]\phi_{nucl,i}(\mathbf{R})=E\phi_{nucl,i}(\mathbf{R}). \tag{2.25}$$

If the BO approximation is applied to more complex molecules condition that $\nabla\times\mathbf{A}_R=0$ might be violated for isolated nuclear configurations where the electronic state becomes degenerate. The phase integral involved in the gauge transformation

$$\Phi=\oint\mathbf{A}_R d\mathbf{R} \tag{2.26}$$

which is called Berry's geometric phase [37][3] can in this case aquire finite values for different closed paths in the parameter space leading to distinct spectral features which have been also obtained experimentally [39].

The functions $E_i(\mathbf{R})$ which arise in the framework of the BO approximation and which plays a role of a potential in the Schrödinger equation for nuclear wavefunction is called potential energy surface (PES) and has a central role in the theoretical treatment of structural and dynamical properties of molecular systems. Moreover, most of the notions from chemistry like molecular structure, isomers, transition states and reaction pathways are based on the BO approximation and have their exact definitions in terms of the potential energy surface. The treatment of the molecular systems within the BO approximation is also closely connected with the ability to find accurate solutions of the electronic Schrödinger equation (2.12) which is a main subject of quantum chemistry.

2.3 Methods for the exploration of the potential energy surfaces

2.3.1 Geometry optimization methods

From a chemical point of view the most interesting points of the PES are stationary points in which the gradient of the energy with respect to the nuclear coordinates vanishes since between them one finds stable structures (local minima) and transition states (first order saddle points). Therefore, one of the most important tasks of quantum chemistry is to find and to characterize the stationary points. For this purpose methods for minimization of a function of several variables are used [40]. Although it is possible to perform the optimization using energy as the only available information[4] in quantum chemistry the gradient based minimization methods are preferred [41, 42] due to efficiency reasons. However, the

---

[3] Berry's phase has actually been taken into account in a natural way in 1963 by Herzberg and Longuet-Higgins [38] while treating the problem of coupled systems with degeneracy while studying polyatomic molecules

[4] Using for example the downhill simplex method or the Fletcher-Powell algorithm [40].

necessary condition is that the analytic energy gradients can be efficiently calculated [43]. In addition some optimization methods are based on the use of second derivative information (Hessian matrix)[5]. Conceptually, the simplest gradient based optimization method is the *steepest descent* method in which the coordinates are changed in the direction of the negative gradient vector as long as energy can be lowered, then a new gradient vector is calculated and the procedure is repeated iteratively until the desired accuracy is achieved. This method is guaranteed to lead to a local minimum but it suffers from a very slow convergence in the vicinity of the minimum. However, it can be used to start the optimization procedure and after the region of the minimum is reached the optimization can be continued using a more sophisticated approach. Another deficiency of the steepest descent is that the directions of the two subsequent minimizations are necessarily orthogonal to each other meaning that each new step partially spoils the previous result and leads to the oscillations around a smooth downhill path leading to the minimum. This drawback is solved by another class of gradient based methods called *conjugated gradient methods* in which the search for a local minimum is not performed directly in the gradient direction but in a direction which is a combination of the previous gradient direction which guarantees that the displacement remains orthogonal to all previous minimization directions. There are different ways how this can be achieved and the most commonly used variants are known under names of Fletcher-Reeves, Polak-Ribiere and Hestenes-Stiefel [40]. Finally the last class of local minimization methods use in addition to the energy gradient also the Hessian matrix. Namely, expanding the energy function about the current configuration $\mathbf{R}_n$ in a Taylor series up to the second order gives the energy which is a quadratic function of the displacement from the equilibrium:

$$E(\mathbf{R}) = E(\mathbf{R}_n) + \mathbf{g}^T(\mathbf{R} - \mathbf{R}_n) + \frac{1}{2}(\mathbf{R} - \mathbf{R}_n)^T\mathbf{H}(\mathbf{R} - \mathbf{R}_n) \tag{2.27}$$

and its minimum can be determined by requiring that the gradient vanishes leading to the following equation for the displacement

$$\mathbf{R} - \mathbf{R}_n = -\mathbf{H}^{-1}\mathbf{g}. \tag{2.28}$$

For a function which is quadratic in coordinates this procedure would lead to a minimum in one step while for the function which contains terms beyond second order this formula may be used iteratively to reach the stationary point. The method is called Newton-Raphson method [41] and has the advantage that the convergence is quadratic near the stationary point. The drawback is that the calculation of the Hessian matrix using ab initio quantum chemical methods is computationally very demanding. Another problem of the Newton-Raphson method is connected with step control. Namely, in the region where one Hessian eigenvalue becomes very small the change in coordinates can according to Equation (2.28) become very large leading to the escape from the region of the stationary point. This problem can be solved by introducing shifting parameters which shift the Hessian eigenvalues and prevent in this way that the step size becomes too large. Most commonly used methods for geometry optimization in quantum chemistry are so called Hessian updating schemes also known as pseudo Newton-Raphson methods. The explicit calculation of the Hessian matrix in each step is avoided and the gradient information is used to estimate and update Hessian. The methods of this kind are known under the names of Davidson-Fletcher-Powell (DFP) [44] and Broyden-Fletcher-Goldfarb-Shanno (BFGS) [45] methods and are commonly used for the geometry optimizations in quantum chemical programs. The efficiency of the geometry optimizations is significantly influenced by the choice of nuclear coordinates in which the energy is expressed. The "best"

---

[5] The Hessian matrix with the elements H_{ij} is defined as a matrix of second derivatives of the energy with respect to nuclear coordinates $H_{ij} = \frac{\partial^2}{\partial R_i \partial R_j}$.

possible coordinates should have a minimal coupling between each other and the energy function should be as close to a quadratic function as possible. Coordinates which usually show good convergence behavior are the natural internal coordinates introduced by Pulay [46].

It should be pointed out that all methods described above are local minimization methods meaning that they usually locate the nearest local minimum. The location of the global minimum is a considerably more difficult and there are many approaches devised for this goal. Most commonly used are:

- Simulated annealing [47],
- Stochastic and Monte Carlo methods [48],
- Molecular dynamics combined with quenching along the classical trajectory [48],
- Genetic algorithms [49] and
- Diffusion methods [50].

By increasing the size of the system global optimization becomes an increasingly complicated task and neither of these methods is guaranteed to work always in a general case.

2.3.2 Characterization of stationary points and vibrational analysis

Once the stationary point on the PES is found its character can be determined by the calculation of the eigenvalues of the Hessian matrix. In the stationary point R_0 the energy gradient vanishes and for small displacements the energy from Equation (2.27) becomes approximately a quadratic function:

$$E(\mathbf{R}) = E(\mathbf{R}_n) + \frac{1}{2}(\mathbf{R} - \mathbf{R}_n)^T \mathbf{H}(\mathbf{R} - \mathbf{R}_n) + \textit{higher orders}. \tag{2.29}$$

Since the Hessian matrix is a real symmetric matrix its diagonalization leads to real eigenvalues[6]. If all nonzero eigenvalues are positive, small displacements from the stationary point lead to the increase in energy for all directions indicating a minimum on the PES. Except of the minima, of particular interest in the study of chemical reactivity are transition states which are characterized by exactly one negative eigenvalue of the Hessian (first order saddle points) [41]. Stationary points with more negative eigenvalues are of little chemical importance since their existence implies that it is possible to find lower energy pathways connecting the minima. Eigenvalues of the Hessian matrix are also directly related to the harmonic vibrational frequencies of the small oscillations about the stationary point [51]. Namely, in mass weighted coordinates[7] the Lagrange function [32] for the classical motion of the nuclei can be written as,

$$L = \frac{1}{2}\dot{\mathbf{q}}^T\dot{\mathbf{q}} - \frac{1}{2}\mathbf{q}^T\mathbf{H}\mathbf{q} \tag{2.31}$$

where $\mathbf{q}$ is the column vector composed of $3N$ mass weighted coordinates, the superscript T denotes the transposition of a vector (converting it from a column to a row vector) and $\mathbf{H}$ is the Hessian matrix in mass weighted coordinated. Inserting this function in the Lagrange equations of motion $\frac{d}{dt}\left(\frac{\partial L}{\partial \dot{q}_i}\right) - \frac{\partial L}{\partial q_i} =$

---

[6] From the invariance of the energy with respect to overall translation and rotation it follows that for nonlinear molecule six eigenvalues are zero (for linear five). It is important to note that this is valid only for the stationary point on the PES. For any other point on the PES the three eigenvalues corresponding to translations are also always zero but the ones corresponding to rotations are not necessarily zero leading to coupling between rotation and vibrations

[7] For a system with N atoms mass weighted coordinates are defined as,

$$q_1 = \sqrt{m_1}\Delta x_1, q_2 = \sqrt{m_1}\Delta y_1, q_3 = \sqrt{m_1}\Delta z_1, q_4 = \sqrt{m_2}\Delta x_2, ... \tag{2.30}$$

where Δx_1 is the cartesian displacement of the first atom from the equilibrium position etc.

0 for $i = 1, 3N$ leads to the following set of equations for the classical oscillations of the nuclei around the equilibrium position:

$$\ddot{\mathbf{q}} = \mathbf{H}\mathbf{q}. \tag{2.32}$$

As already mentioned **H** can be diagonalized by a similarity transformation with an orthogonal matrix **L** consisting of eigenvectors of **H** giving rise to a diagonal matrix Λ with the eigenvalues of **H** as elements

$$\Lambda = \mathbf{L}^T\mathbf{H}\mathbf{L}. \tag{2.33}$$

Inverting this expression and inserting it into the Equation (2.32) a system of classical equations of motion for a system of uncoupled harmonic oscillators is obtained

$$\ddot{\mathbf{Q}} = \Lambda\mathbf{Q} \tag{2.34}$$

where **Q** is the set of normal coordinates obtained by linear transformation of the mass weighted coordinates with the eigenvector matrix **L**. General solution of this set of equations is the superposition of harmonic oscillations with frequencies $\omega_i = \sqrt{\lambda_i} \quad i = 1, 3N$ which are called harmonic frequencies. In the quantum mechanical treatment of the molecular vibrations the classical harmonic vibrational frequencies determine the separation between energy levels and are usually a good approximation for the observed bands in infrared spectra of molecules and clusters.

2.3.3 Transition state optimization and reaction pathways

While the location of the local minima is a relatively easy task which can be accomplished using methods described in Section 2.3.1, location of transition state structures is much more difficult and there is no general method which is guaranteed to work in all cases. The methods which are currently used for this purpose can be divided into:

- Methods interpolating between two minima and
- Local methods.

The methods from the first class assume that the structures of the reactants and the products are known and try to interpolate the transition state structure between these two known structures. Among those most widely used are the *linear synchronous transit* (LST) [52] , *quadratic synchronous transit* (QST) [53] and *synchronous transit-guided quasi newton* (STQN) [54] methods. The estimates of the transition structure are in these methods obtained by linear or quadratic interpolation between the reactant and the product structures. After the TS region is located a quasi-Newton-Raphson optimization is performed. Other methods which should be mentioned are the *self penalty walk method* [55], the *saddle algorithm* [56],and the *chain method* [57]. Among methods using local information most commonly used is the Newton-Raphson method [40]. Once, the TS region is located this method converges to the TS very rapidly. However, this means that the search should be started in the region where the Hessian has exactly one negative eigenvalue requiring a fairly good guess for the TS structure. Since interpolation methods require many function and gradient evaluations and have often poor convergence characteristics, pseudo Newton-Rapshon methods are preferred algorithms used in combination with ab initio quantum chemical methods.

After the transition state is located it needs to be proven that it connects the desired minima. A good indication for that can be gained from the analysis of the normal mode corresponding to the negative

Hessian eigenvalue. However, strictly speaking this can be proven by calculation of the minimum energy pathway from the TS to the connecting minima. If this is done in mass weighted coordinates the minimum energy pathway is also called intrinsic reaction coordinate (IRC) [58] and is defined as a path tangential to the gradient vector. It can be obtained by solution of the differential equation:

$$\frac{d\mathbf{q}}{ds} = -\frac{\mathbf{g}}{|\mathbf{g}|} \tag{2.35}$$

where $\mathbf{q}$ is the vector of mass weighted coordinates, s is the path length and $\mathbf{g}$ is the energy gradient vector. This equation is solved by numerical integration[8] starting from a geometry slightly distorted from the TS in the direction of normal mode with negative Hessian eigenvalue. There is also a method developed by Gonzales and Schlegel [59] which avoids direct solving of the differential Equation (2.35) and instead of that employs a series of successive constrained optimizations starting from the TS.

2.4 Electronic structure calculations

2.4.1 Hartree-Fock method

The Hartree-Fock (HF) method [60, 61] is conceptually the simplest approach for the solution of the electronic Schrödinger equation (2.12) and also presents a basis for more accurate methods. The idea of the method is to separate the many-electron Hamiltonian into a sum of one-electron Hamiltonians in which the electron-electron interaction is treated in an averaged way. In the case of N independent electrons and taking into account the Pauli principle the HF wavefunction can be described by a single Slater determinant,

$$\psi_{HF}(\mathbf{x}_1, \mathbf{x}_2, \cdots, \mathbf{x}_N) = \frac{1}{\sqrt{N!}} \begin{vmatrix} \chi_i(\mathbf{x}_1) & \chi_j(\mathbf{x}_1) & \cdots & \chi_k(\mathbf{x}_1) \\ \chi_i(\mathbf{x}_2) & \chi_j(\mathbf{x}_2) & \cdots & \chi_k(\mathbf{x}_2) \\ \cdots & \cdots & \cdots & \cdots \\ \chi_i(\mathbf{x}_N) & \chi_j(\mathbf{x}_N) & \cdots & \chi_k(\mathbf{x}_N) \end{vmatrix} \tag{2.36}$$

where N electrons occupy N spin orbitals $\chi_i, \chi_j, \cdots, \chi_k$. A spin orbital χ_i is constructed as a product of a spatial function φ_i and a spin dependent function σ which can take only two values corresponding to the two possible spin states of the electron (usually denoted as α and β states)

$$\chi_i(\mathbf{x}_1) = \varphi_i(\mathbf{r}_i)\sigma. \tag{2.37}$$

The pairs of electrons with α and β spin can be either described by the same spatial orbital leading to the so called restricted Hartree-Fock procedure (RHF), or each electron can occupy his own spatial orbital giving rise to the unrestricted HF procedure (UHF). According to the variational principle, the best wavefunction of the form (2.36) is obtained by minimizing the expectation value of the electronic energy $E_{HF} = \langle\psi_{HF}|\hat{H}_{el}|\psi_{HF}\rangle$ which leads to a set of coupled integro-differential equations whose solutions are the optimal spin orbitals,

$$\hat{h}(1)\chi_i(1) + \sum_{j\neq i} \Big[\int d\mathbf{x}_2 \frac{|\chi_j(2)|^2}{r_{12}} \Big] \chi_i(1) - \sum_{j\neq i} \Big[\int d\mathbf{x}_2 \frac{\chi_j^*(2)\chi_i(2)}{r_{12}} \Big] \chi_j(1) = \epsilon_i \chi_i(1) \tag{2.38}$$

---

[8] by using for example the simple Euler method or various Runge-Kutta methods.

where[9]

$$\hat{h}(1) = -\frac{1}{2}\nabla^2 - \sum_A \frac{Z_A}{r_{1A}} \tag{2.39}$$

represents the kinetic energy of the electron plus the potential energy of interaction with all nuclei. In the Hartree-Fock equation (2.38) the exact electron-electron repulsion is replaced by an averaged potential consisting of two terms. The first one is the classical Coulomb potential formed by all other electrons and the second term is the so called exchange term whose presence is a consequence of the antisymmetric character of the electronic wavefunction. Introducing the coulomb and exchange operators $\hat{J}(1)$ and $\hat{K}(1)$ which are defined by their actions on the spin orbitals as

$$\hat{J}(1)\chi_i(1) = \sum_{j\neq i}\Big[\int d\mathbf{x}_2 \frac{|\chi_j(2)|^2}{r_{12}}\Big]\chi_i(1) \tag{2.40}$$

$$\hat{K}(1)\chi_i(1) = \sum_{j\neq i}\Big[\int d\mathbf{x}_2 \frac{\chi_j^*(2)\chi_i(2)}{r_{12}}\Big]\chi_j(1) \tag{2.41}$$

one can introduce the Fock operator $\hat{F}$

$$\hat{F} = \hat{h}(1) + \hat{J}(1) - \hat{K}(1). \tag{2.42}$$

The Hartree-Fock equation (2.38) can then be written in a more compact pseudo-eigenvalue form

$$\hat{F}(1)\chi_i(1) = \epsilon_i\chi_i(1) \tag{2.43}$$

However, since the Fock operator is dependent on all occupied spin-orbitals through the coulomb and exchange terms this is really a nonlinear equation and it requires an iterative solution procedure. In order to transform it into a form which allows efficient numerical solution a set of basis functions $g_k(\mathbf{r}), k = 1, M$ is introduced and the spatial part of the spin orbitals φ_i is expanded according to

$$\varphi_i = \sum_{k=1}^{M} c_{ki} g_k. \tag{2.44}$$

Introducing this expansion into the Equation (2.43) and performing integration over the spin variables assuming the restricted form of the spin orbitals leads to the following matrix eigenvalue equation (Roothan-Hall equation),

$$\mathbf{Fc} = \mathbf{Sc}\epsilon \tag{2.45}$$

where $\mathbf{F}$ is the Fock matrix with the elements

$$F_{ij} = H_{ij}^{core} + \sum_{k}^{N/2}\sum_{lm} P_{lm}[\langle ij|lm\rangle - \langle il|mj\rangle] \tag{2.46}$$

$\mathbf{S}$ is the overlap matrix and ϵ is the diagonal matrix of the orbital energies. In the expression for the Fock matrix elements, H_{ij}^{core} is the core Hamiltonian matrix element consisting of the kinetic energy and

---

[9] In this section atomic units are used with ($\hbar = 1$, $m_e = 1$ and $e^2/4\pi\epsilon_0 = 1$).

nuclear attraction integrals (one electron integrals)

$$\begin{aligned} H_{ij}^{core} &= T_{ij} + V_{ij}^{nucl.} && (2.47) \\ &= \int d\mathbf{r}_1 g_i^*(1)[-\frac{1}{2}\nabla^2 g_j(1)] + \int d\mathbf{r}_1 g_i^*(1)\Big[-\sum_A \frac{Z_A}{r_{1A}}\Big] g_j(1) && (2.48) \end{aligned}$$

$\langle ij|kl\rangle$ are the electron-electron repulsion integrals (two electron integrals) and P_{lm} is the density matrix element defined as

$$P_{lm} = 2\sum_k^{N/2} c_{lk}c_{mk}^*. \tag{2.49}$$

The iterative procedure for the solution of the Roothaan-Hall equations starts with some initial guess for the density matrix[10]. Then the necessary integrals over basis functions are calculated and the Fock matrix is formed and diagonalized giving new orbital energies and new density matrix. This procedure is continued until a convergence (self-consistence) is achieved. The success of this iterative procedure is very dependent on the quality of the initial guess and there are number of techniques for improving the convergence behavior. The simplest one is the *damping method* in which a current density matrix $\mathbf{P}_{n+1}$ is replaced by a weighted average $\mathbf{P}_{n+1} = \alpha\mathbf{P}_n + (1-\alpha)\mathbf{P}_{n+1}$ leading to the damping of the oscillations which are often a reason for bad convergence. Another method is the *level shifting* method [62] in which the energies of the unoccupied orbitals are shifted allowing to reduce the mixing with occupied orbitals which can also be a reason for oscillations. This procedure guarantees a convergence, but if large shifting parameters are used the convergence rate becomes very low. The *direct inversion of iterative subspace* procedure by Pulay [63] is an extrapolation procedure in which the information on all previous density matrices is used to construct the guess which will minimize the error in the next iteration. It shows a quadratic convergence if the solution is approached sufficiently. In addition to all these methods it is also possible to minimize directly the energy [64] using for example Newton-Raphson technique, however this is computationally a very demanding task.

2.4.2 Configuration interaction method

As described in the previous section the HF wavefunction represents the best possible description of a N electron system based on a single Slater determinant. Any attempt to improve this solution systematically and to take into account the electron correlation will therefore have to be based on a multi-determinant wavefunction. Namely, as a result of performing the HF calculation with a finite basis set consisting of M basis functions, a set of 2M spin orbitals is obtained. In the HF wavefunction of a N-electron system only N orbitals with the lowest energies are occupied and 2M-N remain unoccupied (virtual orbitals). This gives the possibility to construct many Slater determinants by distributing N electrons among 2M spin orbitals. Using a HF wavefunction as a reference all other determinants can be described by the number of electrons which have been promoted from occupied to virtual orbitals. A single excited determinant ψ_i^p is obtained by promoting one electron from an occupied orbital χ_i into the unoccupied orbital χ_p,

$$\psi_i^p = |\chi_1, \chi_2, \cdots, \chi_p, \chi_k, \chi_N|. \tag{2.50}$$

A doubly excited determinant χ_{ij}^{pq} is in an analogous way obtained by promoting two electrons from the occupied orbitals χ_i and χ_j into the virtual orbitals χ_p and χ_q and the higher excited determinants are

---

[10] Initial guess can be obtained by diagonalization of the core Hamiltonian, by summing up the atomic densities or by performing an Extended Hückel (EHT) or similar semiempirical calculations.

defined in the analogous way.

$$\psi_{ij}^{pq} = |\chi_1, \chi_2, \cdots, \chi_p, \chi_q, \chi_k, \chi_N| \tag{2.51}$$

A better approximation for a N-electron wavefunction can then be obtained by writing the electronic wavefunction ψ_{el} as a linear combination of all possible Slater determinants

$$\psi_{CI} = C_0\psi_{HF} + \sum_{i,p} C_i^p \psi_i^p + \sum_{\substack{i<j \\ p<q}} C_{ij}^{pq} \psi_{ij}^{pq} + \cdots \tag{2.52}$$

which is called the *configuration interaction* method [60]. If the basis set is infinite this method is exact and for a finite basis set it gives the best possible energy. The total number of determinants which can be formed by distributing N electrons over 2M spin orbitals is of the order $\binom{2M}{N}$ which is even for moderately large basis sets a very large number. This makes so called full-CI[11] calculations unpracticable and truncation of the expansion (2.52) is necessary in order to extend the applicability of the method. The difference between the HF energy and the full-CI energy in the limit of the complete basis set is called correlation energy. The expansion coefficients in the wavefunction (2.52) are determined by minimizing the expectation value of the energy $E_{CI} = \langle\psi_{CI}|\hat{H}_{el}|\psi_{CI}\rangle$ which leads to a set of linear equations for the coefficients **C** written in a matrix notation as

$$\mathbf{HC} = \mathbf{EC}. \tag{2.53}$$

The energy of the ground states as well as of the excited state can be obtained by diagonalizing the matrix **H**. Since the electronic Hamiltonian consists only of one-electron and two-electron operators all matrix elements in the CI matrix between two determinants which differ by more than two spatial molecular orbitals will be zero. Moreover, according to the Brillouin theorem all matrix elements between the HF wavefunction and singly excited determinants are also zero. Also, since the molecular Hamiltonian does not contain spin all matrix elements between determinants with different total spin are zero. In the first approximation, this allows to restrict the expansion to the second order including only single and doubly excited determinants leading to the CISD procedure.[12] The matrix elements between the determinants differing by one or two molecular orbitals can be calculated according to the Slater-Condon rules [60]. Due to the very large size of the CI matrix standard diagonalization methods cannot be used. Instead of that iterative methods are used which can extract one or a few desired eigenvalues and eigenvectors. The most commonly used algorithm is the Davidson algorithm [65].

A major deficiency of all truncated CI methods is that they are not size-extensive [60]. By this is meant that the energy of k noninteracting systems is not a $k-$multiple of the energy of a single such system. The size-extensivity together with the property to correctly describe the dissociation problem is called size-consistency. The extreme consequence of the lack of size-extensivity is that the correlation energy of infinite systems in truncated CI methods is always zero. The size-extensivity becomes particularly important for calculation of properties involving variable number of electrons (e. g. ionization process).

---

[11] A method taking into account all possible excited determinants

[12] Although single excited determinants do not directly couple with the ground state they couple with doubly excited determinants and affect in this way indirectly the energies.

2.4.3 Coupled cluster method

The coupled cluster (CC) method [66, 67, 68] is based on the exponential wave function ansatz

$$|\psi_{CC}\rangle = e^{\hat{T}}|\psi_0\rangle \tag{2.54}$$

$$exp(\hat{T}) = I + \hat{T} + \frac{1}{2!}\hat{T}^2 + \frac{1}{3!}\hat{T}^3 + \cdots \tag{2.55}$$

where ψ_0 is the HF reference wavefunction and $\hat{T}$ is the cluster operator defined as

$$\hat{T} = \hat{T}_1 + \hat{T}_2 + \hat{T}_3 + \cdots + \hat{T}_N. \tag{2.56}$$

The operators $\hat{T}_i, (i = 1, \cdots, N)$ generate successively all single, double etc. excitations. For example the effect of $\hat{T}_1$ and $\hat{T}_2$ on the HF reference function is given by

$$\hat{T}_1|\psi_0\rangle = \sum_i^{occ.}\sum_p^{vir.} t_i^p|\psi_i^p\rangle \tag{2.57}$$

$$\hat{T}_2|\psi_0\rangle = \sum_{i<j}^{occ.}\sum_{p<q}^{vir.} t_{ij}^{pq}|\psi_{ij}^{pq}\rangle \tag{2.58}$$

Inserting the exponential ansatz (2.55) into the Schrödinger equation, multiplying from left with ψ_0^* and integrating leads to the expression for the energy which includes only amplitudes for the single and double excitations

$$E_{CC} = E_0 + \sum_i^{occ.}\sum_p^{vir.} t_i^p\langle\psi_0|H|\psi_i^p\rangle + \sum_{i<j}^{occ.}\sum_{p<q}^{vir.} t_{ij}^{pq}\langle\psi_0|H|\psi_{ij}^{pq}\rangle \tag{2.59}$$

$$= E_0 + \sum_{i<j}^{occ.}\sum_{p<q}^{vir.}(t_{ij}^{pq} + t_i^p t_j^q - t_i^q t_j^p)(\langle\chi_i\chi_j|\chi_p\chi_q\rangle - \langle\chi_i\chi_j|\chi_q\chi_p\rangle). \tag{2.60}$$

Taking into account all excitations in the cluster operator $\hat{T}$ leads to a procedure which is equivalent to the full-CI method. Taking into account only $\hat{T}_1$ and $\hat{T}_2$ gives the CCSD method. In this case the exponential operator has the form

$$e^{\hat{T}_1+\hat{T}_2} = \hat{I} + \hat{T}_1 + (\hat{T}_2 + \frac{1}{2}\hat{T}_1^2) + (\hat{T}_2\hat{T}_1 + \frac{1}{6}\hat{T}_1^3) + (\frac{1}{2}\hat{T}_2^2 + \frac{1}{2}\hat{T}_2\hat{T}_1^2 + \frac{1}{24}\hat{T}_1^4) + \cdots. \tag{2.61}$$

Hence, it follows that truncation of the cluster operator at the doubly excited configurations leads to the wavefunction which contains all single and double excitations, but in addition to that also all "disconnected"[13] triple and quadruple excitations and many other disconnected excitations up to the infinite order. The inclusion of additional higher order excitations up to the infinite order make the CC method size consistent. The equation for the amplitudes of single and double excitations can be obtained by inserting the exponential ansatz (2.55) into the Schrödinger equation, multiplying from the left with all singly excited ψ_m^r and doubly excited determinants ψ_{mn}^{rs}, respectively, and integrating. This leads to the

---

[13] Connected triple and quadruple excitations correspond to the operators $\hat{T}_3$, $\hat{T}_4$ and $\hat{T}_3\hat{T}_1$ and their contributions are presumably small.

set of coupled nonlinear equations for the amplitudes

$$
\begin{aligned}
&\langle\psi_m^r|\hat{H}|\psi_0\rangle + \sum_{i}^{occ.}\sum_{p}^{vir.} t_i^p \langle\psi_m^r|\hat{H}|\psi_i^p\rangle \\
&\quad + \sum_{i<j}^{occ.}\sum_{p<q}^{vir.}(t_{ij}^{pq} + t_i^p t_j^q - t_i^q t_j^p)\langle\psi_m^r|H|\psi_{ij}^{pq}\rangle + \\
&\quad \sum_{i<j<k}^{occ.}\ \sum_{p<q<u}^{vir.a}(t_{ij}^{pq} + \cdots + t_i^p t_j^q t_k^u + \cdots)\langle\psi_m^r|\hat{H}|\psi_{ijk}^{pqu}\rangle = E_{CCSD} t_m^r
\end{aligned}
\tag{2.62}
$$

$$
\begin{aligned}
&\langle\psi_{mn}^{rs}|\hat{H}|\psi_0\rangle + \sum_{i}^{occ.}\sum_{p}^{vir.} t_i^p \langle\psi_{mn}^{rs}|\hat{H}|\psi_i^p\rangle + \\
&\quad \sum_{i<j}^{occ.}\sum_{p<q}^{vir.}(t_{ij}^{pq} + t_i^p t_j^q - t_i^q t_j^p)\langle\psi_{mn}^{rs}|\hat{H}|\psi_{ij}^{pq}\rangle + \sum_{i<j<k}^{occ.}\ \sum_{p<q<u}^{vir.}(t_{ij}^{pq} + \cdots + t_i^p t_j^q t_k^u + \cdots)\langle\psi_{mn}^{rs}|\hat{H}|\psi_{ijk}^{pqu}\rangle \\
&\quad + \sum_{i<j<k<l}^{occ.}\ \sum_{p<q<u<v}^{vir.}(t_{ij}^{pq} t_{kl}^{uv} + \cdots + t_{ij}^{pq} t_k^u t_l^v + \cdots + t_i^p t_j^q t_k^u t_l^v + \cdots)\langle\psi_{mn}^{rs}|\hat{H}|\psi_{ijkl}^{pquv}\rangle \\
&\quad = E_{CCSD}(t_{mn}^{rs} + t_m^r t_n^s - t_m^s t_n^r).
\end{aligned}
\tag{2.63}
$$

These equations contain again matrix elements which can be expressed in terms of the MO integrals according to the Slater-Condon rules and are nonlinear in the amplitudes which requires an iterative solution procedure. Formally the CCSD method scales with M^6 in the limit of a large basis set. Analytic energy gradients have also been formulated in the framework of the CC methods [69, 70] and have been used in this work for performing geometry optimizations.

2.4.4 Density functional theory

Density functional (DFT) methods [71] represent an alternative and very efficient approach for the calculation of molecular properties which does not require the knowledge of the wavefunction. The roots of the DFT methods can be traced to the early days of quantum mechanics when Thomas and Fermi [72] used statistical mechanics to express the energy of an atom as a functional of the electron density. Important contributions to the early density functional theory were made also by Dirac [73] and Slater [74], who introduced first local exchange functional, and von Weizsäcker [75] who has improved Thomas-Fermi kinetic energy functional by adding terms dependent on the gradient of the electron density. However, a sound theoretical basis for theory was given in the early sixties by Hohenberg and Kohn [76] and a computational approach has been developed by Kohn and Sham [77] which removed the deficiencies of the early approaches and allowed to perform more accurate calculations on molecular systems. DFT is formally based on two theorems proven first by Hohenberg and Kohn.

As already mentioned the Hamilton operator for a system composed of N electrons and M nuclei in the Born-Oppenheimer approximation is given by

$$\hat{H} = \hat{T}_e + \hat{V}_{ne} + \hat{V}_{ee} + \hat{V}_{nn}. \tag{2.64}$$

This operator is composed of the kinetic energy operator for the electrons, the nuclear-electron attraction operator, the electron-electron repulsion operator and a constant term corresponding to the nuclear-

nuclear repulsion. Now, fixing an external potential $\hat{V}_{ne}$ determines uniquely the wavefunction, and the electron density can then easily be obtained by performing integration[14] meaning that the electron density $\rho(\mathbf{r}_1)$ is a functional of the external potential $\hat{V}_{ne}$. The *first Hohenberg-Kohn theorem* [76] states that converse is also true. Namely, for a nondegenerate ground state[15] the external potential and therefore the energy and all other properties are unique functionals of the electron density $\rho(\mathbf{r}_1)$. Thus, for a given external potential the total energy can then be written as

$$E[\rho(\mathbf{r})] = \int V_{ne}\rho(\mathbf{r})d\mathbf{r} + F[\rho(\mathbf{r})] \tag{2.65}$$

where $F[\rho(\mathbf{r})]$ is an universal functional which is independent on the external potential and which has the same form for all N-electron systems. This functional can further be partitioned into the kinetic energy and electron-electron repulsion functionals,

$$F[\rho(\mathbf{r})] = T[\rho(\mathbf{r})] + V_{ee}[\rho(\mathbf{r}]. \tag{2.66}$$

The electron-electron term can further be partitioned into the classical Coulomb interaction term and non-classical terms which include exchange interaction and electronic correlation.

$$V_{ee}[\rho] = J[\rho] + \text{nonclassical terms.} \tag{2.67}$$

$$J[\rho] = \frac{1}{2}\int\int \frac{\rho(\mathbf{r}_1)\rho(\mathbf{r}_2)}{r_{12}} d\mathbf{r}_1 d\mathbf{r}_2 \tag{2.68}$$

The *second Hohenberg-Kohn theorem* [76] has the form of the variational principle and states that for any trial density $\tilde{\rho}$ such that $\tilde{\rho} \geq 0$ and $\int \tilde{\rho} d\mathbf{r} = N$

$$E[\tilde{\rho}] \geq E_0 \tag{2.69}$$

where E_0 is the exact energy. This means that the exact ground state density can then be obtained from the stationary principle

$$\delta\{E[\rho] - \epsilon[\int \rho(\mathbf{r})d\mathbf{r} - N]\} = 0 \tag{2.70}$$

as solution of the corresponding Euler-Lagrange equation,

$$\frac{\delta E[\rho]}{\delta \rho} = V_{ne} + \frac{\delta F[\rho]}{\delta \rho}. \tag{2.71}$$

It should be noted that if the exact universal functional $F[\rho]$ is known, Equation (2.71) is an exact equation for the ground state density.

2.4.4.1 The Kohn-Sham method

Since the early work of Thomas and Fermi there were many attempts to construct explicit formulas for various energy contributions in the universal density functional $F[\rho]$. The simplest one is obtained by

---

[14] For an N-electron system the electron density is obtained by $\rho(\mathbf{r}_1) = N\int\cdots\int d\sigma_1 d\mathbf{x}_2 d\mathbf{x}_3 \cdots d\mathbf{x}_N |\psi(\mathbf{x}_1, \mathbf{x}_2, \cdots, \mathbf{x}_N)|^2$ where the integration is performed over the spin coordinates of the electron 1 and the position and spin coordinates of all other electrons.

[15] This constraint can be actually relaxed and the Hohenberg-Kohn theorem can be proven more generally by using the Levy's constrained search method.

considering a homogenous electron gas. It can be shown that the kinetic energy functional has in this case the form,

$$T[\rho] = C_F \int \rho(\mathbf{r})^{5/3} d\mathbf{r} \tag{2.72}$$

with $C_F = \frac{3}{10}(3\pi^2)^{2/3}$ and for the exchange energy the Dirac-Slater functional

$$K[\rho] = C_S \int \rho(\mathbf{r})^{4/3} d\mathbf{r} \tag{2.73}$$

with the constant $C_S = \frac{3}{4}(\frac{3}{\pi})^{1/3}$ can be derived. This allows the construction of the explicit density functionals and the optimal ground state electron density can be obtained by numerical solution of the Euler-Lagrange equation (2.71). It is possible to improve these expressions to some extent by including the higher order gradient dependent terms which take into account the inhomogeneity of the electron density. But nevertheless, it has been shown that all these explicit models cannot even qualitatively describe molecular systems[16]. The main reason for the failure of the explicit models is a very poor description of the kinetic energy which represents the largest contribution to the total energy.

A way out has been proposed by Kohn and Sham [77] who introduced the reference non-interacting system allowing to calculate the kinetic energy contribution $T_S[\rho]$ explicitly. In this way a very large part of the kinetic energy can be calculated exactly. The remaining part of the functional $F[\rho]$ *defines* the exchange and correlation functional

$$E_{xc}[\rho] = F[\rho] - T_S[\rho] - J[\rho]. \tag{2.74}$$

This functional contains the residual kinetic energy $(T[\rho] - T_S[\rho])$ and the non-classical electron-electron repulsion energy which includes the exchange energy, the self-interaction and the electronic correlation. For a non-interaction system the kinetic energy can be calculated exactly by introducing a set of one-electron orbitals ϕ_i, which are obtained as solutions of the effective one-electron Schrödinger equation called Kohn-Sham equation

$$[-\frac{1}{2}\nabla^2 + V_{eff}(\mathbf{r})]\phi_i = \epsilon_i \phi_i. \tag{2.75}$$

The total electronic density is obtained from the one-electron orbitals as

$$\rho[\mathbf{r}] = \sum_{i=1}^{N} \sum_{\sigma} |\phi_i^\sigma|^2. \tag{2.76}$$

Performing the variation of the energy functional $E[\rho]$ with additional constraints, that the electron density is positive everywhere and that it integrates to the total number of electrons, the following expression for the effective potential V_{eff} is obtained

$$V_{eff}(r) = \frac{1}{2} \int \frac{\rho(\mathbf{r}')}{|\mathbf{r} - \mathbf{r}'|} d\mathbf{r}' + V_{ne}(\mathbf{r}) + V_{xc}(\mathbf{r}) \tag{2.77}$$

where V_{xc} is the exchange-correlation potential obtained as functional derivative of the exchange-correlation energy with respect to the electron density. Once the Kohn-Sham orbitals are determined, the exact ki-

---

[16] For example in the framework of the Thomas Fermi model no molecular system is stable with respect to dissociation as proven by Teller [78].

netic energy for the non-interacting reference system can be calculate according to

$$T_S = \sum_{i=1}^{N} \langle\phi_i| - \frac{1}{2}\nabla^2 |\phi_i\rangle \tag{2.78}$$

It should be pointed out that the above formalism can be generalized to the spin-polarized formalism [71] where the separate electron densities for the α and β electrons are introduced so that their sum is the total electron density

$$\rho(\mathbf{r}) = \rho(\mathbf{r})^{\alpha} + \rho(\mathbf{r})^{\beta}. \tag{2.79}$$

The densities can then be decomposed into the unrestricted Kohn-Sham orbitals as

$$\rho(\mathbf{r})^{\alpha} = \sum_{i}^{N_\alpha} |\phi_i^{\alpha}|^2 \tag{2.80}$$

$$\rho(\mathbf{r})^{\beta} = \sum_{i}^{N_\beta} |\phi_i^{\beta}|^2. \tag{2.81}$$

Introducing separate densities for α and β electrons requires also generalization of the energy functional which is in the framework of the spin polarized formalism given by

$$E[\rho^{\alpha}, \rho^{\beta}] = \sum_{i,\sigma} \langle\phi_i^{\sigma}| - \frac{1}{2}\nabla^2 |\phi_i^{\sigma}\rangle + J[\rho^{\alpha}, \rho^{\beta}] + \int d\mathbf{r} V_{ne}(\mathbf{r})[\rho^{\alpha}(\mathbf{r}) + \rho^{\beta}(\mathbf{r})] + E_{xc}[\rho^{\alpha}, \rho^{\beta}]. \tag{2.82}$$

After performing variation of this functional the corresponding unrestricted Kohn-Sham equations are obtained as

$$[-\frac{1}{2}\nabla^2 + V_{eff}^{\alpha}(\mathbf{r})]\phi_i^{\alpha} = \epsilon_i^{\alpha}\phi_i^{\alpha} \tag{2.83}$$

$$[-\frac{1}{2}\nabla^2 + V_{eff}^{\beta}(\mathbf{r})]\phi_i^{\beta} = \epsilon_i^{\beta}\phi_i^{\beta} \tag{2.84}$$

with spin dependent effective potentials

$$V_{eff}^{\alpha} = V_{ne}(\mathbf{r}) + \int \frac{\rho^{\alpha}(\mathbf{r}') + \rho^{\beta}(\mathbf{r}')}{|\mathbf{r}' - \mathbf{r}|} d\mathbf{r}' + \frac{\delta E_{xc}[\rho^{\alpha}, \rho^{\beta}]}{\delta\rho^{\alpha}(\mathbf{r})} \tag{2.85}$$

$$V_{eff}^{\beta} = V_{ne}(\mathbf{r}) + \int \frac{\rho^{\alpha}(\mathbf{r}') + \rho^{\beta}(\mathbf{r}')}{|\mathbf{r}' - \mathbf{r}|} d\mathbf{r}' + \frac{\delta E_{xc}[\rho^{\alpha}, \rho^{\beta}]}{\delta\rho^{\beta}(\mathbf{r})}. \tag{2.86}$$

Although it is expected that in the absence of a magnetic field the spin-polarized Kohn-Sham theory reduces to the spin-unpolarized one, this is strictly true only in the case when the exact exchange-correlation functional is used. However, since we are forced to use only approximate functionals a spin-polarized functional offers a better description of the real system. This is particularly the case for open shell systems.

The Kohn-Sham equations have the same structure as Hartree-Fock equations (or Pople-Nesbet equations [79] in the unrestricted case) and can be solved using the self-consistent procedure. However, using the Kohn-Sham method the *exact* ground state energy can in principle be obtained at the same computational demand as in the HF method provided the exact exchange-correlation functional is known. The challenge of the modern density functional theory lies therefore in the development of accurate exchange-correlation functionals.

2.4.4.2 Local density methods

The basic assumption of the local density methods is that the electron density can *locally* be treated as a uniform electron gas. For the exchange energy Dirac's expression [73] is used which has in the spin polarized case the following form

$$E_x^{LSDA}[\rho_\alpha,\rho_\beta] = -\frac{3}{2}(\frac{3}{4\pi})^{1/3}\int[\rho_\alpha^{4/3}(\mathbf{r}) + \rho_\beta^{4/3}(\mathbf{r})]d\mathbf{r}. \tag{2.87}$$

The general form of the local spin density approximation for the correlation functional is

$$E_c^{LSDA}[\rho_\alpha,\rho_\beta] = \int \rho(\mathbf{r})\epsilon_c(\rho_\alpha(\mathbf{r}),\rho_\beta(\mathbf{r}))d\mathbf{r} \tag{2.88}$$

where $\epsilon_c(\rho_\alpha(\mathbf{r}),\rho_\beta(\mathbf{r}))$ is the correlation energy per electron in a homogenous electron gas. This has been calculated exactly by Ceperley and Alder using the Green's functions quantum Monte Carlo method [80]. Vosko, Wilk and Nusair (VWN) interpolated these Monte-Carlo results using Pade's approximation and have obtained the following analytic correlation functional

$$\epsilon_c(r_s) \quad = A\{ln(\tfrac{x^2}{X(x)}) + \tfrac{2b}{Q}tan^{-1}(\tfrac{Q}{2x+b}) - \tfrac{bx_0}{X(x_0)}[ln(\tfrac{(x-x_0)^2}{X(x)}) + \quad 2(\frac{b+2x_0}{Q})tan^{-1}(\frac{Q}{2x+b})]\} \tag{2.89}$$

$$X(x) = x^2 + bx + c \tag{2.90}$$

$$Q = (4c - b^2)^{1/2} \tag{2.91}$$

where x_0, b, and c are constants [81]. The r_s is the Wigner-Seitz radius which is related to the electron density by

$$r_s = \left(\frac{3}{4\pi\rho}\right)^{1/3}. \tag{2.92}$$

The LSDA method gives a fairly good description of equilibrium structures but generally has a tendency to overbind the systems. The main reason for this is the error in exchange energy which is systematically to low by about ten percent. The source of this error is the self interaction energy, whose presence becomes obvious if one considers an one electron system in which exact exchange energy should be zero. The LSDA exchange energy has also wrong asymptotic behavior. Namely, in the case of the finite system the exchange energy functional should asymptotically behave as

$$E_x = -\frac{1}{2}\int\frac{\rho}{r}d\mathbf{r} \quad \text{as r} \rightarrow \infty \tag{2.93}$$

which is not satisfied for the LSDA functional [82]. Also, the correlation energy is usually overestimated high by a factor of roughly two leading to the poor quality of the results obtained at the LSDA level of theory.

2.4.4.3 Gradient corrected methods

A way to go beyond the local density approximation is to include terms in the exchange-correlation functional which are dependent on the gradient of the electron density. In the limit of slowly varying densities the exchange-correlation energy has a gradient expansion [76] given by

$$E_{xc}^{GEA}[\rho] = E_{xc}^{LSDA} + \sum_{\sigma\sigma'} \int B_{xc}^{\sigma\sigma'}(\rho_\alpha(\mathbf{r}), \rho_\beta(\mathbf{r}))\nabla\rho_\alpha \cdot \nabla\rho_\beta d\mathbf{r} + \cdots . \tag{2.94}$$

However, this extension does not lead to an improvement of the LSDA results, in fact, in practice results are often even worse. The reason for this lies in the wrong asymptotic behavior of the gradient expansion approximation (GEA). Namely, the exchange functional can be written in terms of the exchange-hole function $\rho_x(\mathbf{r}_1, \mathbf{r}_2)$ as

$$E_x[\rho] = \frac{1}{2}\int\int \frac{\rho(\mathbf{r}_1)\rho_x(\mathbf{r}_1, \mathbf{r}_2)}{|\mathbf{r}_1 - \mathbf{r}_2|} d\mathbf{r}_1 d\mathbf{r}_2 \tag{2.95}$$

where $\rho_x(\mathbf{r}_1, \mathbf{r}_2)$ is defined in terms of the first order density matrix $\rho_1(\mathbf{r}_1, \mathbf{r}_2)$as

$$\rho_x(\mathbf{r}_1, \mathbf{r}_2) = -\frac{1}{2}\frac{|\rho_1(\mathbf{r}_1, \mathbf{r}_2)|^2}{\rho(\mathbf{r}_1)}. \tag{2.96}$$

From the definition of the exchange-hole function it can be shown that it has the following properties (known also as the sum rules)

$$\rho_x(\mathbf{r}_1, \mathbf{r}_1) = -\rho(\mathbf{r}_1) \tag{2.97}$$

$$\int \rho_x(\mathbf{r}_1, \mathbf{r}_2) d\mathbf{r}_2 = -1 \tag{2.98}$$

$$\rho_x(\mathbf{r}_1, \mathbf{r}_2) \leq 0. \tag{2.99}$$

The LSDA approximation satisfies the exact conditions (2.97-2.99). However, the GEA expansion violates the conditions (2.98) and (2.99) which explains its failure to provide accurate corrections beyond the LSDA.

Another approximation which also uses second order gradient expansion but which manages the difficulties with GEA is known as generalized gradient approximation (GGA). The exchange energy within this approximation is given by

$$E_x^{GGA} = E_x^{LSDA} - \sum_{\sigma\sigma'} \int F(\chi_\sigma)\rho_\sigma^{4/3}(\mathbf{r}) d\mathbf{r}. \tag{2.100}$$

The argument of the function F, is the reduced density gradient for the spin σ

$$\chi_\sigma(\mathbf{r}) = \frac{|\nabla\rho_\sigma(\mathbf{r})|}{\rho_\sigma^{4/3}(\mathbf{r})}. \tag{2.101}$$

In order to obtain the expression for the function F Perdew used the second order GEA expansion with a cutoff radius which allowed to impose conditions (2.98) and (2.99) [83]. This led to the widely used Perdew-Wang functional (PW86) [84] with the function F of the form

$$F^{PW86} = \{1 + 1.296\Big(\frac{\chi_\sigma}{(24\pi^2)^{1/3}}\Big)^2 + 14\Big(\frac{\chi_\sigma}{(24\pi^2)^{1/3}}\Big)^4 + 0.2\Big(\frac{\chi_\sigma}{(24\pi^2)^{1/3}}\Big)^6\}^{1/15}. \tag{2.102}$$

Another commonly used exchange functional is the Becke's B88 functional [85]. It has been obtained by imposing correct r^{-1} asymptotic behavior which leads to the function F with the form

$$F^{B88} = \frac{\beta\chi_\sigma^2}{1 + 6\beta\chi_\sigma sinh^{-1}(\chi_\sigma)} \tag{2.103}$$

containing one parameter β which has been obtained by fitting the exact exchange energies of the noble gas atoms. The overall performance of the two above mentioned exchange functionals in combination with various correlation functionals is very similar. One of the most popular correlation functionals is the Lee-Yang-Parr (LYP) [86] correlation functional

$$\begin{aligned} E_c^{LYP} &= -a\int d\mathbf{r}\frac{\gamma(\mathbf{r})}{1+d\rho^{-1/3}(\mathbf{r})}\{\rho(\mathbf{r}) + 2b\rho^{-5/3}(\mathbf{r})[2^{2/3}C_F(\rho_\alpha^{8/3}(\mathbf{r}) + \rho_\beta^{8/3}(\mathbf{r})) \\ & -\rho(\mathbf{r})t_W + \frac{1}{9}(\rho_\alpha(\mathbf{r})t_W^\alpha + \rho_\beta(\mathbf{r})t_W^\beta) + \frac{1}{18}(\rho_\alpha(\mathbf{r})\nabla^2\rho_\alpha(\mathbf{r}) + \\ & \rho_\beta(\mathbf{r})\nabla^2\rho_\beta(\mathbf{r}))]e^{-c\rho^{-1/3}}\} \end{aligned} \tag{2.104}$$

where

$$\gamma(\mathbf{r}) = 2[1 - \frac{\rho_\alpha^2(\mathbf{r}) + \rho_\beta^2(\mathbf{r})}{\rho^2(\mathbf{r})}]. \tag{2.105}$$

and t_W is the von Weizsäcker local kinetic energy density

$$t_W(\mathbf{r}) = \frac{1}{8}\Big[\frac{|\nabla\rho(\mathbf{r})|^2}{\rho(\mathbf{r})} - \nabla^2\rho(\mathbf{r})\Big]. \tag{2.106}$$

This correlation functional has been obtained by expanding the Cole-Salvetti's expression for the correlation energy [87], which was originally formulated in terms of electron density and the Laplacian of the Hartree-Fock second order density matrix, in terms of electron density and the local kinetic energy density. Generally, inclusion of the gradient corrected terms improves significantly accuracy for binding energies with respect to the overbinding tendency of LSDA.

2.4.4.4 Hybrid functionals

Since, in the framework of the Kohn-Sham formalism the exchange energy can be in principle calculated exactly using

$$E_x^{exact} = -\frac{1}{2}\sum_{\sigma=\alpha,\beta}\sum_{j,k=1}^{N}\int\int\frac{\phi_{j\sigma}^*(\mathbf{r}_1)\phi_{k\sigma}^*(\mathbf{r}_2)\phi_{k\sigma}(\mathbf{r}_1)\phi_{j\sigma}(\mathbf{r}_2)}{|\mathbf{r}_1 - \mathbf{r}_2|}d\mathbf{r}_1 d\mathbf{r}_2 \tag{2.107}$$

an obvious way to construct a density functional would be to add a correlation contribution to this expression. However, it has been shown that this combination does not lead to a viable approach for the calculation of molecular properties. The reason for this is that the local correlation methods (LSDA and GGA) do not have proper long range character which would allow to compensate the longe range exchange hole. Another approach, based on adiabatic connection formula [88], has been introduced by Becke [89]. Namely, if one introduces the coupling strength parameter λ into the universal functional (2.66) which switches the electron-electron interaction

$$F[\rho(\mathbf{r})] = T[\rho(\mathbf{r})] + \lambda V_{ee}[\rho(\mathbf{r})] \tag{2.108}$$

it can be shown that the exact exchange-correlation energy can be calculated from the adiabatic connection formula

$$E_{xc} = \int_0^1 \langle \psi_\lambda | V_{xc}(\lambda) | \psi_\lambda \rangle d\lambda. \tag{2.109}$$

The exact dependence of the exchange-correlation potential $V_{xc}(\lambda)$ on the coupling strength parameter is not known but in the $\lambda = 0$ limit there is no electron-electron interaction and the only part which contributes to the exchange-correlation energy is the exchange energy which can be calculated exactly by (2.107). A possible approach to include exact exchange based on the adiabatic connection formula is to define a hybrid functional as first proposed by Becke [89],

$$E_{xc} = aE_x^{LSDA} + (1-a)E_x^{exact} + b\Delta E_x^{B88} + E_c^{VWN} + c\Delta E_c^{GGA}. \tag{2.110}$$

This functional contains three semiempirical parameters whose role is to correct the LSDA or GGA near the $\lambda = 0$ limit and their values are obtained by fitting to the experimental data. Various hybrid functionals can differ by the correlation functional used. The most commonly used correlation functionals are the LYP [86] functional and the PW91 [90] functional which lead to the B3LYP and B3PW91 hybrid methods. The inclusion of the exact exchange in this way has been shown to lead to the significant improvement over the GGA results particularly by reducing further the overbinding tendency which is particularly strong for all local DFT methods.

2.4.4.5 The optimized effective potential method (OEP)

Another approach to include the exact exchange follows the same line as the original approach proposed by Kohn and Sham for calculation of the kinetic energy contribution. In this approach, in addition to the exact calculation of the kinetic energy T_s the exchange energy is calculated using Equation (2.107) and the energy functional becomes then

$$E[\rho] = -\frac{1}{2}\sum_{i,\sigma}\int \phi_i^{\sigma *}\nabla^2\phi_i^\sigma d\mathbf{r}_1 - \frac{1}{2}\sum_\sigma\sum_{j,k=1}^N\int\int\frac{\phi_j^{\sigma *}(\mathbf{r}_1)\phi_k^{\sigma *}(\mathbf{r}_2)\phi_k^\sigma(\mathbf{r}_1)\phi_j^\sigma(\mathbf{r}_2)}{|\mathbf{r}_1-\mathbf{r}_2|}d\mathbf{r}_1 d\mathbf{r}_2 + J[\rho] + V_{ne}[\rho] + E_c[\rho]. \tag{2.111}$$

It should be pointed out that now the only approximation comes from the correlation functional. Performing the variation of this functional with respect to the Kohn-Sham orbitals under orthogonality constraint again leads to the equations with the same structure like the Kohn-Sham Equations (2.75). However the optimized effective potential (OEP) [91, 92, 93] V_{eff} (cf. Equation (2.77)) is now a solution of a rather complicated integral equation which has to be solved numerically. Computational effort involved in solution of these equations is very high compared to the GGA functionals which limits the applicability of the method only to small molecules. However, this approach gives better total energies and properties than any other type of functionals and in contrast to the hybrid functionals, the OEP based exchange potentials are local.

2.4.4.6 Computational aspects of the DFT methods

Kohn-Sham equations can be transformed into the matrix form analogous to the Roothaan-Hall equations (cf. Equation (2.45))of the Hartree-Fock theory by expanding the Kohn-Sham orbitals into the finite set of basis functions. This leads to the following matrix equation

$$\mathbf{H}_{KS}\mathbf{C} = \mathbf{S}\mathbf{C}\epsilon \tag{2.112}$$

where $\mathbf{H}_{KS}$is a matrix operator analogous to the Fock operator with the matrix elements:

$$H_{ij}^{KS} = \int d\mathbf{r}_1 g_i(\mathbf{r}_1) \left\{ -\frac{1}{2}\nabla_1^2 - \sum_{A=1}^{M} \frac{Z_A}{r_{1A}} + \int \frac{\rho(\mathbf{r}_2)}{r_{12}} d\mathbf{r}_2 + V_{xc}(\mathbf{r}_1) \right\} g_j(\mathbf{r}_1) \tag{2.113}$$

where $g_i(\mathbf{r}_1)$ are the basis functions. While the first three terms in this matrix element can be evaluated analytically the last term has in general a complicated dependence on the integration variables and requires numerical evaluation. For this purpose electron density is represented on a discrete grid [94, 95] and the integral is evaluated approximately as

$$\int d\mathbf{r}_1 g_i(\mathbf{r}_1) V_{xc}(\mathbf{r}_1) g_j(\mathbf{r}_1) \cong \sum_{k=1}^{N_{grid}} g_i(\mathbf{r}_k) V_{xc}(\mathbf{r}_k) g_j(\mathbf{r}_k) W_k \tag{2.114}$$

where W_K are the weights of the grid points. A careful choice of the integration grid influences significantly the quality of the results obtained from the DFT calculations. The computational cost involved in the evaluation of the exchange-correlation integrals increases cubically with the system size due to the linear increase of the number of grid points and quadratic dependence on the number of basis functions. The Coulomb term can be evaluated using basis set expansion as in the HF method which leads to formal M^4 dependence on the size of the basis set. However, in the framework of the DFT method this scaling can be reduced to M^3 by using the density fitting method [96, 97]. In this approach electron density is represented in terms of an auxiliary atom-centered basis set

$$\rho(\mathbf{r}) = \sum_k c_k a_k(\mathbf{r}). \tag{2.115}$$

The Coulomb term in the KS matrix element (2.113) becomes then

$$J = \int d\mathbf{r}_1 g_i(\mathbf{r}_1) \int d\mathbf{r}_2 \frac{\rho(\mathbf{r}_2)}{r_{12}} g_j(\mathbf{r}_1) = \sum_k \int\int d\mathbf{r}_1 d\mathbf{r}_2 \frac{g_i(\mathbf{r}_1) g_j(\mathbf{r}_1) a_k(\mathbf{r}_2)}{r_{12}} \tag{2.116}$$

The coefficients c_k are obtained by the least square minimization of the deviation from the true electron density which can be shown to be mathematically equivalent to the replacement of the true two-electron integrals by the approximate expression

$$\langle g_i g_j | g_k g_l \rangle \cong \sum_{kl} \langle g_i g_j | a_k \rangle \langle a_k | a_l \rangle^{-1} \langle a_l | g_k g_l \rangle. \tag{2.117}$$

This approximation looks formally like an insertion of the identity, expressed in terms of the auxiliary basis set, into the two-electron integrals which is the reason why a shorthand notation RI-J is used for this procedure. In this work an extensive use of this approximation has been made, in particular because it allows very efficient molecular dynamics simulations in which energy gradients are calculated in each step. Alternatively, the second approach which also reduces the scaling to M^3 is based on the Poisson equation. Namely, the electrostatic potential generated by the electron density ρ

$$V(\mathbf{r}_1) = \int \frac{\rho(\mathbf{r}_2)}{r_{12}} d\mathbf{r}_2 \tag{2.118}$$

can be directly obtained by the numerical solution of the Poisson equation

$$\nabla^2 V(\mathbf{r}_1) = -4\pi\rho(\mathbf{r}_1). \tag{2.119}$$

For this purpose there is a number of efficient techniques in which the potential is represented on a grid and either fast Fourier transform (FFT) or multigrid methods are used. Once the potential is obtained the Coulomb term can be calculated again with an effort scaling with M^3 according to

$$J = \int d\mathbf{r}_1 g_i(\mathbf{r}_1) \int d\mathbf{r}_2 \frac{\rho(\mathbf{r}_2)}{r_{12}} g_j(\mathbf{r}_1) = \int d\mathbf{r}_1 g_i(\mathbf{r}_1) V_{el}(\mathbf{r}_1) g_j(\mathbf{r}_1) \cong \sum_{k=1}^{N_{grid}} g_i(\mathbf{r}_k) V_{el}(\mathbf{r}_k) g_j(\mathbf{r}_k). \tag{2.120}$$

It should be noted that both of these approaches can be used only when the exact HF exchange is not present in the density functional since the exact exchange functional is non-local and does not allow simplification of this form which restricts the application of these methods to the non-hybrid functionals.

The scaling of the DFT methods can be furthermore reduced all way down to the linear scaling [98] by using the fast multipole methods (FMM) enabling to extend the applicability of the DFT methods to very large systems. Most of the density functional programs which are currently in use are based on the basis set approach which was described above, but there is also an alternative possibility of direct solution of the KS equations on a grid without involving the basis set representation. Currently there are various real space multigrid approaches emerging which are especially suitable for the implementation on the massively parallel computer architectures and which eventually might also lead to the linear scaling with the systems size.

2.4.4.7 Analytic derivatives of the DFT energy

The analytic first derivatives of the molecular total energy [43] with respect to nuclear displacements are one of the most useful quantities which ab initio quantum chemical methods can provide. They facilitate location of stationary points (cf. Section 2.3.1) and allow to perform molecular dynamics simulations. In this section the calculation of the analytic first derivatives in the framework of the DFT methods [99, 100, 101] will be shortly presented since they have been mostly used in this work to perform the geometry optimizations and MD simulations.

Within the Kohn-Sham DFT formalism, the total electronic energy can be expressed as:

$$E_{DFT} = \sum_{\mu\nu} P_{\mu\nu} H_{\mu\nu} + \frac{1}{2} \sum_{\mu\nu\lambda\sigma} P_{\mu\nu} P_{\lambda\sigma} (\mu\nu|\lambda\sigma) + E_{xc}(P^\alpha, P^\beta) \tag{2.121}$$

Here the $P_{\mu\nu}$ represents the one-electron total density matrix which is in spin-unrestricted formalism given by:

$$\begin{aligned} P &= P_\alpha + P_\beta && (2.122)\\ P^{\alpha}_{\mu\nu} &= \sum_i^{N_\alpha} c^{*\alpha}_{\mu i} c^{\alpha}_{\nu i}, && (2.123)\\ P^{\beta}_{\mu\nu} &= \sum_i^{N_\beta} c^{*\beta}_{\mu i} c^{\beta}_{\nu i}. && (2.124)\end{aligned}$$

where $c_{\mu i}$ are the Kohn-Sham orbital expansion coefficients. The first term in Equation (2.121) gives the total one-electron energy and $H_{\mu\nu}$ is the matrix element of the one-electron Hamiltonian (cf. Equation (2.48)), the second term represents the Coulomb interaction of the electrons and the final term is the exchange-correlation energy which is a functional of he individual spin densities. As already discussed, the exchange-correlation functional generally involves the spin-densities and their derivatives and can be generally written as:

$$E_{xc} = \int f(\rho_\alpha, \rho_\beta, \gamma_{\alpha\alpha}, \gamma_{\alpha\beta}, \gamma_{\beta\beta}) d\mathbf{r} \tag{2.125}$$

where the spin densities are defined by

$$\rho_\alpha = \sum_{\mu\nu} P^{\alpha}_{\mu\nu} \phi^*_\mu \phi_\nu \quad \rho_\beta = \sum_{\mu\nu} P^{\beta}_{\mu\nu} \phi^*_\mu \phi_\nu \tag{2.126}$$

and the γ's are the density gradient invariants:

$$\begin{aligned} \gamma_{\alpha\alpha} &= \nabla\rho_\alpha \cdot \nabla\rho_\alpha, \quad \gamma_{\alpha\beta} = \nabla\rho_\alpha \cdot \nabla\rho_\beta \\ \gamma_{\beta\beta} &= \nabla\rho_\beta \cdot \nabla\rho_\beta && (2.127)\end{aligned}$$

The gradient of the energy can be calculated by differentiating the expression (2.121) with respect to the displacement of the nucleus A yielding

$$\nabla_A E_{DFT} = \sum_{\mu\nu} P_{\mu\nu} \nabla_A H_{\mu\nu} + \frac{1}{2} \sum_{\mu\nu\lambda\sigma} P_{\mu\nu} P_{\lambda\sigma} \nabla_A (\mu\nu|\lambda\sigma) + \nabla_A E_{XC}(P^\alpha, P^\beta) - \sum_{\mu\nu} W_{\mu\nu} \nabla_A S_{\mu\nu} \tag{2.128}$$

where $W_{\mu\nu}$ are the matrix elements of the energy-weighted density matrix

$$W_{\mu\nu} = \sum_i^{N_\alpha} \epsilon^\alpha_i c^\alpha_{\mu i} c^\alpha_{\nu i} + \sum_i^{N_\beta} \epsilon^\beta_i c^\beta_{\mu i} c^\beta_{\nu i}. \tag{2.129}$$

The calculation of the energy gradients involves the derivatives of the one- and two electron integrals as well as the derivative of the exchange-correlation potential which requires the use of the numerical integration. The evaluation of the energy gradients employing numerical quadratures is somewhat complicated by the fact that the quadrature weights depend on the nuclear configuration and hence have a nonzero gradient with respect to nuclear displacement [100]. In this work the analytic energy gradients in the framework of the DFT method have been employed to perform the geometry optimizations as well as ab initio MD simulations.

2.4.4.8 Performance

The proper choice of the exchange-correlation functional plays a crucial role for the quality of the results obtained from the DFT. The simplest LSDA method gives generally good geometries and vibrational frequencies, but due to its wrong asymptotic behavior it greatly overbinds the systems. All gradient corrected functionals (GGA) perform significantly better and allow to calculate much more accurate thermochemical data but still show the overbinding tendency . Elaborate comparisons in the literature [102] have shown that the GGA functionals give results comparable or better than MP2 at the computational cost which is similar to the HF approach. Even better performance is found for the hybrid class of functionals whose accuracy approaches much more elaborate G2 models [103]. One deficiency of the DFT methods is that the weak van der Waals type interactions are very poorly represented [104]. This is illustrated by the fact that while the LSDA method gives small attractive interactions between the rare gas atoms, all gradient corrected methods predict purely repulsive interactions. On the other hand interactions dominated by the electrostatic contributions like hydrogen bonding are well described in the framework of the DFT.

2.4.5 Ab initio methods for calculation of excited electronic states

2.4.5.1 Linear response methods

A straightforward method for the calculation of excited state energies and wavefunctions is based on the configuration interaction (CI) procedure which has been described previously. Within this approach, the excited states are obtained by diagonalization of the CI matrix in the same way like the ground state energy and wavefunction. In order to achieve proper accuracy of the CI method large CI spaces have to be considered and also a careful choice of the involved configurations has to be made. This makes the application of CI methods computationally rather demanding.

Another alternative are the linear response methods based on time dependent perturbation theory [105]. Generally the perturbation is of the form

$$\hat{V}(t) = \hat{B}F(t) \tag{2.130}$$

where $F(t)$ is a function of time and $\hat{B}$ is some operator. For example in the case of the interaction with the electromagnetic field $F(t)$ is simply a time dependent electric field and $\hat{B}$ is the dipole moment operator. The problem which is subject of the response theory is how the expectation value of some observable represented by an operator $\hat{A}$ evolves with time. Let us assume that the system is at $t = -\infty$ in its ground state $|0\rangle$ and that the perturbation is switched on gradually from zero at $t = -\infty$. The total time dependent Hamiltonian is now $\hat{H} = \hat{H}_0 + \hat{V}(t)$, where $\hat{H}_0$ is the unperturbed system Hamiltonian. We wish to solve the full time dependent Schrödinger equation for the time evolution of the system state

$$i\hbar\frac{\partial}{\partial t}|\psi(t)\rangle = [H_0 + \hat{V}(t)]|\psi(t)\rangle. \tag{2.131}$$

If we now go over to the interaction (Dirac's) representation by writing the time dependent wavefunction $|\psi(t)\rangle$ in the form

$$|\psi(t)\rangle = e^{-\frac{iH_0t}{\hbar}}|\psi_I(t)\rangle, \tag{2.132}$$

the following differential equation is obtained for the time evolution of the wavefunction $|\psi_I(t)\rangle$ in the interaction representation:

$$i\hbar\frac{\partial}{\partial t}|\psi_I(t)\rangle = \tilde{V}_I|\psi_I(t)\rangle \tag{2.133}$$

where $\tilde{V}_I$ is the interaction representation of the perturbation operator

$$\tilde{V}_I(t) = e^{\frac{i\hat{H}_0 t}{\hbar}t}V(t)e^{\frac{-i\hat{H}_0 t}{\hbar}t}. \tag{2.134}$$

This differential equation can be transformed to the equivalent integral equation

$$|\psi_I(t)\rangle = |\psi_I(t=-\infty)\rangle - \frac{i}{\hbar}\int_{-\infty}^{t} dt'\tilde{V}_I(t')|\psi_I(t^{'})\rangle. \tag{2.135}$$

This equation can now be linearized by assuming that the perturbation is small, which allows to iterate only once and to replace the wavefunction $|\psi_I(t')\rangle$ under the integral sign by $|\psi_I(t=-\infty)\rangle = |0\rangle$

$$|\psi_I(t)\rangle = |0\rangle - \frac{i}{\hbar}\int_{-\infty}^{t} dt'\tilde{V}_I(t')|0\rangle. \tag{2.136}$$

With this approximate wavefunction the response of the observable A can be calculated

$$\langle A(t)\rangle = \langle\psi_I(t)|\tilde{A}(t)|\psi_I(t)\rangle = \langle 0|\tilde{A}|0\rangle + \frac{i}{\hbar}\int_{-\infty}^{t}\langle 0|[\tilde{B}_I(t'),\tilde{A}_I(t)]|0\rangle E(t')dt'. \tag{2.137}$$

By introducing the theta function $\Theta(t-t')$ under the integral sign the upper limit of integration can be extended to $+\infty$ and the change of the expectation value of A can be written as

$$\Delta A(t) = \int_{-\infty}^{+\infty} R(t,t')E(t')dt' \tag{2.138}$$

where $R(t,t')$is the linear response function defined as

$$R(t,t') = \langle\langle\tilde{B}_I(t');\tilde{A}_I(t)\rangle\rangle = \frac{i}{\hbar}\Theta(t-t')\langle 0|[\tilde{B}_I(t'),\tilde{A}_I(t)]|0\rangle. \tag{2.139}$$

The linear response function can be Fourier transformed to the frequency domain in which after inserting the complete set of eigenstates of the unperturbed Hamiltonian it has the form

$$R(\omega) = \sum_{i\neq 0}\Big[\frac{\langle 0|\hat{B}|i\rangle\langle i|\hat{A}|0\rangle}{\omega-\omega_{i0}+i\eta} - \frac{\langle 0|\hat{A}|i\rangle\langle i|\hat{B}|0\rangle}{\omega+\omega_{i0}-i\eta}\Big] \tag{2.140}$$

where η is a small number which insures the convergence of the integrals involved in the Fourier transform for $\omega = \omega_{i0}$. In the spectral representation the physical meaning of the response function becomes obvious. Its poles correspond to the excitation energies of the system and the residues correspond to the intensities of the transitions. It should be pointed out that the operators $\hat{A}$ and $\hat{B}$ can also be number non-conserving operators corresponding to the removal or addition of electrons, in which case the minus sign in the response function should be replaced by the plus sign and the poles correspond to the electron affinities and ionization potentials. Response methods represent therefore a very general approach for the calculation of the dynamical response of the system to various kinds of perturbations. In this work they have primarily been used to calculate the optical properties of clusters. Although the direct evaluation of the response function according to the expression (2.140) suggests to require the knowledge of all excited states in order to perform the sum over all states it is possible to evaluate response functions in a indirect way. This is also the main power of the response techniques. Namely, the time development of the response function is determined by the Ehrenfest equation of motion

$$i\hbar\frac{d\langle\langle\hat{B}(t);\hat{A}(t')\rangle\rangle}{dt}=\delta(t-t')\langle 0|[\hat{B}(t);\hat{A}(t')]|0\rangle+\langle\langle[\hat{B}(t),\hat{H}];A(t')\rangle\rangle \tag{2.141}$$

which transformed in the frequency domain becomes

$$\omega\langle\langle\hat{B};\hat{A}\rangle\rangle=\langle 0|[\hat{B},\hat{A}]|0\rangle+\langle\langle\hat{B};[\hat{H},\hat{A}]\rangle\rangle. \tag{2.142}$$

Now, this expression can be applied iteratively to yield

$$\langle\langle\hat{B};\hat{A}\rangle\rangle=\frac{1}{\omega}\langle 0|[\hat{B},\hat{A}]|0\rangle+\frac{1}{\omega^2}\langle 0|[\hat{B},[\hat{H},\hat{A}]]|0\rangle+\frac{1}{\omega^3}\langle 0|[\hat{B},[\hat{H},[\hat{H},\hat{A}]]]|0\rangle\cdots \tag{2.143}$$

By introducing Hamilton superoperators which act on operators in operator space and whose action is defined as

$$\begin{aligned}\mathbf{I}\hat{A}&=\hat{A}\\ \mathbf{H}\hat{A}&=[\hat{H},\hat{A}]\\ \mathbf{H}^2\hat{A}&=[\hat{H},[\hat{H},A]]\end{aligned} \tag{2.144}$$

the above expression for the linear response function in the propagator space can be written compactly as

$$\langle\langle\hat{B};\hat{A}\rangle\rangle=\langle 0|[\hat{B},(\omega\mathbf{I}-\mathbf{H})^{-1}\hat{A}]|0\rangle. \tag{2.145}$$

Introducing the scalar product (metric) in the operator space defined as

$$(\hat{B}|\hat{A})=\langle 0|[\hat{B}^\dagger,\hat{A}]|0\rangle \tag{2.146}$$

and inserting a “resolution of identity” in the superoperator space representing a complete set of excitation and deexcitation operators the linear response function becomes

$$\langle\langle\hat{B};\hat{A}\rangle\rangle=(\hat{B}|\hat{h})(\hat{h}|\omega\mathbf{I}-\mathbf{H}|\hat{h})^{-1}(\hat{h}|\hat{A}) \tag{2.147}$$

where $\hat{h}$ is, in the case of number conserving polarization operator which is relevant in the treatment of the optical properties, a set of operators:

$$\hat{h}=\hat{h}_2,\hat{h}_4,\hat{h}_6,\cdots \tag{2.148}$$

with $\hat{h}_2$ being an operator which generates all single excitations and de-excitations, $\hat{h}_4$ all double excitations and de-excitations etc. This formalism allows now to develop various approximations for the linear response functions by restricting the excitation level (similar as in the CI method). A reference function from which the excitations are considered may be taken either as HF or as multi-configurational HF (MCSCF) wavefunction. The simplest approximation can be obtained by taking the HF wavefunction as a reference and including only single excitations and de-excitations which leads to the so called random phase approximation (RPA) [106]. In order to get a working set of equations in the framework of the RPA method the $\hat{h}_2$ set of operators can be furthermore split into an excitation and de-excitation part $\hat{h}_2 = \hat{e}, \hat{d}$ which allows to write the linear response function as

$$\langle\langle \hat{B}; \hat{A} \rangle\rangle = [(\hat{B}|\hat{e}), (\hat{B}|\hat{d})] \begin{bmatrix} \omega\mathbf{I} - \mathbf{A} & -\mathbf{B} \\ -\mathbf{B} & -\omega\mathbf{I} - \mathbf{A} \end{bmatrix}^{-1} \begin{bmatrix} (\hat{e}|\hat{A}) \\ (\hat{d}|\hat{A}) \end{bmatrix}. \tag{2.149}$$

The matrix $\mathbf{A}$ involves elements between the singly excited configurations and the matrix $\mathbf{B}$ involves the matrix elements between the doubly excited configurations and the reference state. The corresponding matrix elements can be expressed in terms of the orbital energies and two electron integrals and they can easily be calculated after the SCF procedure has been performed. The matrix elements are given by

$$A_{ij}^{ab} = \langle \psi_i^a | \hat{H} | \psi_j^b \rangle - E_0 \delta_{ij} \delta_{ab}$$

$$B_{ij}^{ab} = -\langle \psi_0 | \hat{H} | \psi_{ij}^{ab} \rangle \tag{2.150}$$

and can further be expressed in terms of one and two electron integrals by using Slater-Condon rules. The inverse of the matrix in Equation (2.149) is normally not calculated directly due to the large dimensions involved, but instead iterative techniques similar to the direct methods for diagonalization of the large CI matrices are used. First an intermediate vector $\mathbf{X}$ is introduced as

$$\begin{bmatrix} \omega\mathbf{I} - \mathbf{A} & -\mathbf{B} \\ -\mathbf{B} & -\omega\mathbf{I} - \mathbf{A} \end{bmatrix}^{-1} \begin{bmatrix} (\hat{e}|\hat{A}) \\ (\hat{d}|\hat{A}) \end{bmatrix} = \mathbf{X} \tag{2.151}$$

which can be obtained by iterative solution of the following set of equations

$$\begin{bmatrix} \omega\mathbf{I} - \mathbf{A} & -\mathbf{B} \\ -\mathbf{B} & -\omega\mathbf{I} - \mathbf{A} \end{bmatrix} \mathbf{X} = \begin{bmatrix} (\hat{e}|\hat{A}) \\ (\hat{d}|\hat{A}) \end{bmatrix}. \tag{2.152}$$

If the right hand side of Equation (2.152) is set to zero, the poles of the linear response function corresponding to the excitation energies can be determined.

In principle there are two ways to go beyond the simple RPA approximation.One may improve the reference function by using the MCSCF wavefunction instead of the HF wavefunction and one may also include higher order excitation operators. Since the RPA method includes single excitations and some double excitations it typically gives very good results for excited states which are dominant by singly excited configurations, however due to the contribution of the double excitations the results are better than the simplest CI procedure which includes only single excitations. The quality of the absorption spectra calculated by the RPA method is somewhere in between the CIS and CISD procedures. In order to achieve better accuracy linear response methods based on coupled cluster reference wavefunctions have been developed in the framework of the equation of motion (EOM) methods.

2.4.5.2 Equation-of-motion coupled cluster (EOM-CC) method

The equation-of-motion coupled cluster method (EOM-CC) offers a natural extension of the ground state coupled cluster theory that permits a reliable treatment of the excited electronic states [107, 108]. This method is conceptually a single reference method and provides the same unambiguous treatment of excited states as CC method does for the ground state, since the only choices are the atomic basis set and the excitation level of the operators. In the EOM-CC approach to excited electronic states the final wave function is parameterized as

$$|\psi_{ex}\rangle = \hat{\mathcal{R}}|\psi_g\rangle \tag{2.153}$$

where the subscripts ex and g refer to the excited and the ground electronic states and $\hat{R}$ is a linear excitation operator which in a second quantization formalism has the form

$$\begin{aligned} \hat{R} &= \hat{R}_0 + \hat{R}_1 + \hat{R}_2 + \hat{R}_3 + \cdots && (2.154) \\ \hat{R}_n &= \frac{1}{n!^2}\sum r_{ijk...}^{abc...} a^\dagger i b^\dagger j c^\dagger k \cdots . && (2.155) \end{aligned}$$

In the above expression $i, j, k, ...$ represent the orbitals that are occupied in the Slater determinant reference function, while $a, b, c, ...$ represent the unoccupied orbitals. In the EOM-CC approach the ground state wave function is given by the coupled-cluster approximation (cf. Section 2.4.3)

$$|\psi_g\rangle = e^{\hat{T}}|\psi_0\rangle \tag{2.156}$$

where $|\psi_0\rangle$ is a single Slater determinant, usually chosen to be the SCF solution. Insertion of Equations (2.153) and (2.156) into the Schrödinger equation yields

$$\hat{H}\hat{R}e^{\hat{T}}|\psi_0\rangle = E\hat{R}e^{\hat{T}}|\psi_0\rangle \tag{2.157}$$

and since both $\hat{R}$ and $\hat{T}$ commute due to the fact that both are excitation operators Equation (2.157) can be transformed into the eigenvalue form

$$e^{-\hat{T}}\hat{H}e^{\hat{T}}\hat{R}|\psi_0\rangle = E\hat{R}|\psi_0\rangle \tag{2.158}$$

or by introducing the similarity transformed Hamiltonian $\bar{H} = e^{-\hat{T}}He^{\hat{T}}$

$$\bar{H}\hat{R}|\psi_0\rangle = E\hat{R}|\psi_0\rangle. \tag{2.159}$$

So far, the EOM-CC procedure is still formally exact and equivalent to the Full-CI procedure. However, in practical calculations the $\hat{T}$ and $\hat{R}$ operators are truncated usually at double level of excitation leading to the EOM-CCSD approximation. It should be emphasized that the EOM-CCSD approximation provide an exact treatment of the two-electron systems. Due to the nonlinearity of the transformation, the similarity transformed Hamiltonian $\bar{H}$ includes higher excitations than double allowing to obtain results superior to those obtained in the same determinantal subspace (corresponding to the CISD method) although the $\hat{T}$ and $\hat{R}$ operators are truncated at the double level of excitation. The effective Hamiltonian $\bar{H}$ can be expressed in the spin-orbital basis as

$$\bar{H} = \sum_{pq} F_{pq} p^\dagger q + \frac{1}{4} \sum_{pqrs} W_{pqrs} p^\dagger q^\dagger s r + \cdots \tag{2.160}$$

The one- and two-body amplitudes F_{pq} and W_{pqsr} can be expressed in terms of the Fock matrix elements, the two-electron integrals and the coupled cluster amplitudes t_i^p and t_{ij}^{pq} (cf. Section 2.4.3). Formal expressions for these matrix elements are given in Ref. [109]. In the matrix representation the effective Hamiltonian assumes the form

$$\bar{H} = \begin{pmatrix} E_{CC} & \cdots & \cdots \\ 0 & \ddots & \cdots \\ 0 & \vdots & \ddots \end{pmatrix} \tag{2.161}$$

where the zero entries follow from the condition that the $\hat{T}$ amplitudes obey the coupled cluster equations (cf. Section 2.4.3). Diagonalization of this Hamiltonian gives the energies of the excited electronic states. It can also be seen that the usual ground CCSD solution is obtained as a special case for which $\hat{R} = \hat{R}_0 = \hat{I}$. Due to the nonunitarity of the coupled cluster operator $e^{\hat{T}}$ the operator $\bar{H}$ is not Hermitian and as a result each eigenvalue of $\bar{H}$ is associated with two eigenvectors that correspond to distinct bra and ket states

$$\langle\tilde{\psi}| = \langle\psi_0|\hat{L}e^{-\hat{T}} \tag{2.162}$$

$$|\psi\rangle = e^{\hat{T}}\hat{R}|\psi_0\rangle \tag{2.163}$$

where $\hat{L}$ represents the left eigenvector of $\bar{H}$. Due to the non-Hermitian nature of the EOM-CC approach, transition moments are not well defined. However, since the intensity of the optical transitions is determined by the square of the transition moments it can be calculated unambiguously using the “left” and the “right” transition moments. The oscillator strength of an optical transition in dipole approximation is given by

$$f_e = \frac{2}{3} T_e D \tag{2.164}$$

where T_e is the transition energy and D is the dipole strength which can be calculated according to

$$D = \langle\tilde{\psi}_g|\hat{\mu}|\psi_x\rangle\langle\tilde{\psi}_x|\hat{\mu}|\psi_g\rangle. \tag{2.165}$$

Computationally, the EOM-CCSD calculations can be carried out after the ground state coupled cluster solution is obtained. For this purpose the one- and two-particle matrix elements involved in Equation (2.160) are constructed and written to a disk in an ordered list. After the $\bar{H}$ matrix elements have been constructed the eigenvalues can be found. For this purpose an iterative Davidson algorithm is usually used [65].

As a measure of the quality of the EOM-CCSD excitation energy the approximate excitation level (AEL) is used. The AEL is defined by the equation

$$AEL = \frac{1}{2} \sum_p |\rho_{pp}^{ex} - \rho_{pp}^{g}| \tag{2.166}$$

and measures the number of electrons that are excited from the CCSD ground state. For EOM-CCSD, results obtained for transitions to states having an AEL significantly larger than one should be regarded with reservation since the parameterization of the excited state wave function cannot accurately describe states with significant contribution of double excitations. This is due to the double excitation component of $\hat{R}$ which allows to expand the wave function beyond the singly excited determinants. However, within the EOM-CCSD method no such flexibility is available for describing doubly excited states since for this purpose triple excitation operators are needed [109].

The computational demands of the EOM-CCSD method are considerable, since each excited state requires about 60 % of the ground state CCSD calculation, primarily to extract iteratively eigenvalues and vectors from a matrix of rank equal to all single and double excitations. In order to reduce the computational demand the similarity transformed equation-of-motion coupled-cluster method (STEOM-CC) has been introduced [110]. The idea of the approach is to perform the similarity transformation of the second quantized Hamiltonian $\bar{H}$ which reduces the coupling between singly excited determinants and more highly excited ones. As a consequence, excitation energies can be obtained to a good approximation by diagonalizing the transformed Hamiltonian in the space of single excitations only, reducing thereby significantly the computational demand.

2.4.6 Basis sets

Essentially all quantum chemical methods, with exception of those in which the wavefunction is represented on a three dimensional real space grid and whose applications are up to date limited only to very small systems, use finite sets of basis functions to expand the wavefunction (LCAO approximation). This allows to reformulate the problem of the solution of the Schrödinger equation into the matrix form and to use linear algebra techniques for its solution. The accuracy of the results obtained by quantum chemical calculations is therefore crucially dependent on the quality of the basis sets used. An ideal basis function should resemble atomic orbitals as close as possible and should allow efficient evaluation of the involved integrals. The first requirement is fairly well satisfied with the Slater type orbitals (STO) of the form

$$s_{A,\zeta,n,l,m} = N_{\zeta,n,l,m} Y_{l,m}(\theta,\phi) r_A^{n-1} exp(-\zeta r_A^2) \tag{2.167}$$

where n, l, m are the quantum numbers $Y_{l,m}$ is the spherical harmonic function and r_A represents the distance of the nucleus A. Due to their exponential form which corresponds to the asymptotic behavior of the atomic orbitals and the cusp (discontinuous derivative) at the nucleus, the STO functions ensure rapid convergence of the LCAO expansion. However, the calculation of the three- and four-center two-electron integrals cannot be performed analytically with the STO functions restricting their application to very small systems. The most commonly used basis functions in quantum chemistry are the gaussian type atomic orbitals (GTOs) introduced by Boys [111] which can be written either in the cartesian or polar forms as

$$\begin{aligned} g_{A,\zeta,n,l,m}(\mathbf{r}) &= N_{\zeta,l,m,n} x_A^l y_A^m z_A^n exp(-\zeta r_A^2) && (2.168)\\ g_{A,\zeta,n,l,m}(\mathbf{r}) &= N_{\zeta,l,m,n} Y_{l,m}(\theta,\phi) r^{(2n-2-l)} exp(-\zeta r_A^2) && (2.169) \end{aligned}$$

and are centered at the atomic nuclei of the system of interest. Here, $\mathbf{r}_A$ represents the cartesian coordinates with respect to the nucleus A and $N_{\zeta,l,m,n}$ is the normalization constant. The sum $l+m+n$ determines the type of orbital (for example $l+m+n=0$ is an s-orbital, $l+m+n=1$ a p-orbital etc.). Due to the fact that the gaussian basis functions have a r^2 dependence in the exponential they do not have the correct exponential asymptotic behavior and do not satisfy the cusp condition at the nucleus. Therefore, generally more GTOs than STOs are needed to achieve the same level of accuracy. To alleviate this problem to some extent several GTOs are often grouped together forming a contracted gaussian functions. Each contracted gaussian is taken to be a fixed linear combination of the original or primitive gaussians centered at the same atomic nucleus:

$$g_i(\mathbf{r}) = \sum_j C_{ij} g_j(\mathbf{r}) \tag{2.170}$$

with the contraction coefficients C_{ij} which remain fixed during the calculations reducing therefore the number of parameters to be optimized. The central advantage of GTOs relies on the fact that the two-electron integrals on three or four different atomic centers can be reduced to integrals over two different centers leading to the efficient procedure for the evaluation of the molecular integrals [112]. Explicit formulas for the one- and two-electron integrals over GTOs have been derived by Taketa [113], but currently a more efficient approach based on the Rys polynomials [114] is commonly used.

As mentioned in previous sections the computational cost of the quantum chemical calculations is critically dependent on the number of basis functions. The smallest possible basis sets are obtained by assigning only one set of functions for each atomic shell occupied in the atomic ground state. This would correspond to a single s-function for hydrogen and helium, two s-functions and one set of p-functions for the first row of the periodic table and so on. These basis sets are called minimum basis sets. A significant improvement over the minimal basis sets is obtained by doubling the number of basis functions, producing double zeta (DZ) type of basis sets. The doubling of the basis functions provides a much better description since it allows to describe different kinds of bonding situations simultaneously, such as σ and π bonding since both, the tighter functions (with larger ζ exponents) and the more ones functions (smaller ζ exponents), are present and can separately participate either in σ or π bonding. Since the core orbitals usually do not have a significant influence on the chemical bonding and therefore are independent of the chemical environment, a variation of the DZ basis sets in which only the number of valence orbitals is doubled can be introduced leading to the split valence basis sets introduced by Pople [115, 116, 117]. Further step in the hierarchy of basis sets are triple zeta basis sets (TZ) in which the number of basis functions is tripled with respect to the minimum basis.

When bonds are formed in molecules atomic orbitals become polarized by the adjacent atoms. This distortion can be taken into account by introducing additional basis functions with higher values of angular momentum. For a single determinant wavefunction the first set of polarization functions with the next higher value of angular momentum is sufficient to account for the polarization effects produced by the molecular environment. However, if higher correlated methods are used, the higher angular momentum functions become essential. Additionally, in order to provide an accurate description of anionic species or excited electronic states addition of diffuse basis functions (with smaller ζ exponents) which are able to describe the electron densities at larger distances from the atomic centers is usually necessary. The exponents of the added diffuse functions are optimized to yield atomic excitation energies, ionization potentials and electron affinities which are in agreement with the experimental data.

2.4.7 Effective core potentials (ECP)

The quantum chemical calculations involving heavier elements become increasingly demanding due to the increasing number of electrons. On the other hand, most of the chemical properties of atoms and molecules are determined by the interactions of the valence electrons. This has led to the development of approximate ab initio quantum chemical methods in which only valence electrons are treated explicitly and the core electrons are handled by means of the effective core potentials (ECP) [118]. In addition to reduction of the computational demand by reducing the number of electrons, the ECP approach allows also to include approximately the relativistic effects which become increasingly important in heavier elements [119]. In general, due to the relativistic increase in mass the core s-orbitals contract and in order to preserve the orthogonality of the s-orbitals the distribution of the valence s-electrons must also contract. On the other hand, p-orbitals and in particular d-orbitals tend to expand due to the better shielding of the nuclear charge by the contracted core. Since in this work only the relativistic ECP have been used in the following only the method for their derivation will be described.

The objective of the ECP approach is to replace the potentials in the molecular Hamiltonian (2.9) by new potentials which are dependent only upon the coordinates of the valence electrons, but at the same time take into account the influence of the inert core electrons. For this purpose as a starting point the atomic Fock operator

$$\hat{F} = -\frac{\nabla_r^2}{2} - \frac{Z}{r} + \frac{l(l+1)}{2r^2} + \sum_{j=1}^{N}(\hat{J}_i - \hat{K}_i) \tag{2.171}$$

can be taken. If now the orbitals are divided into N_{core} core orbitals and N_{val} valence orbitals, the Fock operator (2.171) can be written as

$$\hat{F} = -\frac{\nabla_r^2}{2} - \frac{Z}{r} + \frac{l(l+1)}{2r^2} + \hat{V}_{core} + \hat{V}_{val} \tag{2.172}$$

where

$$\hat{V}_{core} = \sum_{a}^{N_{core}} (\hat{J}_a - \hat{K}_a) \tag{2.173}$$

and

$$\hat{V}_{val} = \sum_{i}^{N_{val}} (\hat{J}_i - \hat{K}_i). \tag{2.174}$$

The central idea of the ECP approach is to replace the non-local operator from Equation (2.173) by the local one electron effective core potential $\hat{V}_{ECP}$. At the same time the nuclear charge Z is replaced by the effective charge $Z_{eff} = Z - N_{core}$. For the construction of the the RECPs several approaches have been proposed [120]. Generally, the first step in the derivation of the RECP is a numerical all-electron Dirac-Hartree-Fock (DHF) [119] calculation on an atomic generator state ${}^{2S+1}M^{q+}$. As generator state a chemically relevant oxidation state of the involved element is chosen. In this way the set of orbital energies $\varepsilon_{n,l,j}$ and numerical orbitals $\phi_{n,l,j}$ is obtained. As a starting point for the construction of the RECP the nodeless pseudo-orbitals are then derived from the valence orbitals $\phi_{n,l,j}$. For this purpose a shape consistent procedure [121] is commonly used. This method requires that the pseudo-orbital $\chi_i^{l,j}$ exactly matches the original valence orbital $\phi_{n,l,j}$ for $r \geq r_m$ where r_m is the radius at which $\phi_{n.l,j}$ has its outermost maximum. Within the core region the pseudo-orbital $\chi_i^{l,j}$ is represented by

$$\chi_i^{l,j} = \sum_{m=0}^{4} c_m r^{m+l+2} \quad r < r_m \tag{2.175}$$

and the coefficients c_m are obtained by the requirement that $\chi_i^{l,j}$ matches the original orbital and its derivatives at $r = r_m$. The RECP corresponding to the pseudo-orbital $\chi_i^{l,j}$ is obtained by inverting the eigenvalue equation for $\chi_i^{l,j}$:

$$\Big[-\frac{\nabla_r^2}{2} - \frac{Z_{eff}}{r} + \frac{l(l+1)}{2r^2} + \hat{V}_{val} + \hat{V}_{l,j}^{eff}\Big]\chi_i^{l,j} = \epsilon_i^{l,j}\chi_i^{l,j}. \tag{2.176}$$

The DHF eigenstates $\chi_i^{l,j}$ are eigenstates of the total angular momentum $\hat{j} = \hat{l} + \hat{s}$ and the resultant RECPs are no longer uniquely defined for a particular l value. However, since the RECPs are usually used in the framework of the nonrelativistic quantum chemistry where the one-electron wavefunctions are eigenfunctions of $\hat{l}$ and $\hat{s}$ rather than of $\hat{j}$ so called l-averaged RECPs (ARECP) are derived by statistical averaging over all of the appropriate j-dependent RECPs which are associated with a given l value:

$$\hat{V}_l^{ARECP}(r) = \frac{l\hat{V}_{l,j-\frac{1}{2}}^{RECP}(r) + (l+1)\hat{V}_{l,j+\frac{1}{2}}^{RECP}(r)}{2l+1}. \tag{2.177}$$

The total ARECP taking into account all possible l-values is then given by

$$\hat{V}^{ARECP}(r) = \sum_l \hat{V}_l^{ARECP}(r) \sum_{m=-l}^{l} |lm\rangle\langle lm|. \tag{2.178}$$

At this point the numerical ARECP can be used together with a large gaussian basis set for the valence orbitals to derive analytical valence pseudo-orbitals. This can be accomplished by solving the HF equations for atomic orbitals expressed as linear combination of gaussian functions. Also the analytical form of the ARECP can be obtained by fitting the numerical potential with

$$r^2 V_l^{ARECP}(r) = \sum_k A_{l,k} r^{n_{l,k}} e^{-\zeta_{l,k} r^2}. \tag{2.179}$$

It is important to emphasize that the ECP approximation cannot a priori describe atomic properties in which the number of electrons is changed (ionization energies and electron affinities) due to the change in intrashell correlation accompanying the change in the number of electrons. Also the electronic excitations are also often affected by the intrashell correlation. If accurate description of these properties is needed for a particular problem of interest, it is possible to optimize the coefficients and exponents in Equation (2.179) as well as the GTO basis by including available experimental values.

2.5 Theoretical approach to ultrafast spectroscopy

Femtosecond spectroscopy became a powerful technique for probing the real time intramolecular dynamics in molecules and clusters [8]. The technique is based on the preparation of the coherent superposition of the molecular eigenstates by an ultrashort laser pulse and probing its subsequent time evolution by a second time-delayed ultrashort laser pulse. In this way a molecular dynamics on a femtosecond time scale can be observed and the processes such as configurational rearrangements, bond breaking and intramolecular vibrational energy redistributions (IVR) can be studied.

Generally, the simulations of the laser induced ultrafast processes involve the interaction of the molecular system having multiple electronic states with laser fields. The Hamiltonian of a molecular system represented in terms of adiabatic electronic states which are coupled to an electromagnetic field $\varepsilon(t)$ by a dipole interaction can be written as

$$\hat{H} = \hat{H}_{mol} + \hat{H}_{int} = \sum_a |a\rangle \hat{h}_a(\mathbf{Q}) \langle a| - \varepsilon(t) (\sum_{a,b} |a\rangle \hat{\mu}_{ab}(\mathbf{Q}) \langle b| + h.c.) \tag{2.180}$$

with the vibrational Hamiltonian $\hat{h}_a(\mathbf{Q})$ of the adiabatic electronic state a, the collection of the vibrational coordinates $\mathbf{Q}$ and the transition dipole matrix elements $\hat{\mu}_{ab}(\mathbf{Q})$. The dynamics of the system described by this Hamiltonian is governed by the time dependent Schrödinger equation (2.1) or, more generally, by the Liouville-von Neumann equation (2.11) for the time evolution of the density matrix. The grid based numerical methods for the solution of the time dependent Schrödinger equation represent powerful tools for studying and understanding dynamics of diatomic, triatomic and tetratomic systems provided that accurate precalculated potential energy surfaces are available. However, due to the fact that the computational demand of the full quantum mechanical propagation methods scales essentially as M^N where M is the number of grid points and N is the dimension of the problem, the applicability of these methods is limited to systems with few degrees of freedom. Particularly attractive for the treatment of more complex systems are semiclassical methods which make use of classical trajectories with quantal initial conditions. The quantum mechanical Liouville-von Neumann equation offers an appropriate starting point for establishing semiclassical approaches. This can be achieved in the Wigner's phase space representation of quantum mechanics which allows the transition to the classical limit in which the nuclear dynamics on a single electronic surface is described by the classical Liouville equation of nonequilibrium statistical mechanics. This approach is characterized by the conceptual simplicity of classical mechanics and by the ability to describe approximately quantum phenomena and the optical transitions by means of the averaged ensemble over the classical trajectories. Moreover the introduction of quantum corrections can be made in a systematic manner. The method requires less computational effort than full quantum mechanical calculations, it provides physical insight in ultrafast processes and it is applicable to complex systems. Moreover, it can be combined directly with quantum chemistry methods for electronic structure calculations to carry out the multi-state dynamics at different levels of accuracy including precalculated energy surfaces as well as the ab initio MD ”on the fly”. In the following Section 2.5.1, the Wigner space representation of quantum mechanics will be presented providing the formal framework in which semiclassical approaches can be developed and systematically improved. Then, in Section 2.5.2 the semiclassical propagation method based on the classical limit of the Liouville-von Neumann equation will be outlined. In Section 2.5.3 the method for the simulation of the pump-probe spectra based on the Wigner representation of the density matrix will be described. Finally, methods for the ab initio MD “on the fly” involving the ground and excited states adiabatic and nonadiabatic MD will be presented in Section 2.5.4.

2.5.1 Wigner (phase-space) representation of quantum mechanics

As first pointed out by Born [122], quantum mechanics is a statistical theory and cannot predict the outcome of a single measurement. In this respect it is possible to draw a close parallel between the quantum mechanics of a single particle and the classical statistical mechanics of an ensemble of particles. In the framework of the classical statistical mechanics, a well suited formalism for description of the behavior of an statistical ensemble is formulated in terms of the phase space which consists of the position and momentum coordinates for all particles and a central quantity for description of the ensemble is the phase space distribution function. Its time evolution is governed by the Liouville equation. Quantum mechanics, on the other hand, describes the systems in terms of an abstract state vector $|\psi\rangle$ or a density operator $\hat{\rho}$ and the question arises if it is possible to use these quantities to construct a phase space distribution function whose properties would resemble as close as possible to the properties of the classical distribution functions. On the other hand, such a representation is useful because it provides an insight into the properties of the quantum state in terms of the classical concepts, but it also enables to establish a smooth connection between quantum and classical mechanics and opens a possibility to develop semiclassical approaches. It has been first introduced by Wigner [33, 123] by defining the phase space distribution function $P(\mathbf{q},\mathbf{p})$ for a state described by the density operator $\hat{\rho}$ by:

$$P(\mathbf{q},\mathbf{p}) = \frac{1}{(2\pi\hbar)^N}\int d\mathbf{s}\langle\mathbf{q}+\frac{\mathbf{s}}{2}|\hat{\rho}|\mathbf{q}-\frac{\mathbf{s}}{2}\rangle e^{-\frac{i}{\hbar}\mathbf{ps}}. \tag{2.181}$$

As it can easily be shown that if one integrates the Wigner function $P(\mathbf{q},\mathbf{p})$ over the momentum variables $\mathbf{p}$ or the position variables $\mathbf{q}$ the probability distribution of position or momentum, respectively, is obtained

$$\int d\mathbf{p}P(\mathbf{q},\mathbf{p}) = \langle\mathbf{q}|\hat{\rho}|\mathbf{q}\rangle \tag{2.182}$$

$$\int d\mathbf{q}P(\mathbf{q},\mathbf{p}) = \langle\mathbf{p}|\hat{\rho}|\mathbf{p}\rangle. \tag{2.183}$$

An important property of the Wigner distribution function, however, is that it can take on negative values which prevents its interpretation as a true phase space probability distribution function. In fact, the quantum mechanical concept of the interference of probability amplitudes is exactly reflected in the negative parts of the Wigner function. Nevertheless, the Wigner function provides an exact phase space representation of quantum mechanics [17] and allows to calculate quantum mechanical expectation values using concepts of classical statistical mechanics. Specifically, the Wigner equivalent of a quantum operator $\hat{A}$ is defined by

$$A_w(\mathbf{q},\mathbf{p}) = \frac{1}{(2\pi\hbar)^N}\int d\mathbf{s}\langle\mathbf{q}+\frac{\mathbf{s}}{2}|\hat{A}|\mathbf{q}-\frac{\mathbf{s}}{2}\rangle e^{-\frac{i}{\hbar}\mathbf{ps}}. \tag{2.184}$$

With this definition the quantum mechanical expectation values can now be calculated by performing phase space integration in an analogous way as in the classical statistical mechanics giving

$$\langle\hat{A}\rangle = \int\int d\mathbf{q}d\mathbf{p}A_w(\mathbf{q},\mathbf{p})P(\mathbf{q},\mathbf{p}) \tag{2.185}$$

for the expectation value of the operator $\hat{A}$.

The equation for the time evolution of the Wigner distribution function $P(\mathbf{q},\mathbf{p},t)$ can be obtained by transforming the quantum Liouville-von Neumann equation for the time evolution of the density matrix $i\hbar\dot{\hat{\rho}} = [\hat{H},\hat{\rho}]$ into the Wigner representation giving

---

[17] It should be pointed out that the phase space representation provided by the Wigner function is not unique. In fact, there is an infinite amount of possible phase space distribution functions which achieve the same goal, but Wigner function is unique in the sense that it has simple properties.

$$\begin{aligned}\frac{\partial P(\mathbf{q},\mathbf{p},t)}{\partial t} &= \frac{2}{\hbar}H_W sin\left[\frac{\hbar}{2}(\frac{\overleftarrow{\partial}}{\partial \mathbf{q}}\frac{\overrightarrow{\partial}}{\partial \mathbf{p}}-\frac{\overleftarrow{\partial}}{\partial \mathbf{p}}\frac{\overrightarrow{\partial}}{\partial \mathbf{q}})\right]P(\mathbf{q},\mathbf{p},t)\\ &= \sum_{i=1}^{N}\left(\frac{\partial H}{\partial q_i}\frac{\partial P}{\partial p_i}-\frac{\partial H}{\partial p_i}\frac{\partial P}{\partial q_i}\right)-\frac{\hbar^2}{24}\sum_{i=1}^{N}\frac{\partial^3 V}{\partial^3 q_i}\frac{\partial P}{\partial^3 p_i}-\frac{\hbar^2}{1920}\sum_{i=1}^{N}\frac{\partial^5 V}{\partial^5 q_i}\frac{\partial^5 P}{\partial^5 p_i}+\ldots \quad (2.186)\end{aligned}$$

where the arrows indicate the direction of the operation of the derivatives. N is the number of the degrees of freedom and V is the potential energy of the system. The first two terms on the right hand side are just the classical Liouville equation for the time evolution of the phase space density while the following terms which are multiplied by $\hbar$ give "non-local" quantum corrections.

2.5.2 The semiclassical Wigner method

The semiclassical Wigner method [123] can be introduced by taking the limit $\hbar \rightarrow 0$ in the exact Equation (2.186) leading to the classical Liouville equation

$$\frac{\partial P(\mathbf{q},\mathbf{p},t)}{\partial t}=\sum_{i=1}^{N}\left(\frac{\partial H}{\partial q_i}\frac{\partial P}{\partial p_i}-\frac{\partial H}{\partial p_i}\frac{\partial P}{\partial q_i}\right). \quad (2.187)$$

Then, if the initial distribution $P(\mathbf{q}_0,\mathbf{p}_0,t=0)$ corresponding to the Wigner transform of the initial quantum state is given, the solution of Equation (2.186) can be obtained by propagating a swarm of classical trajectories according to the Hamilton's equations of motion

$$\dot{\mathbf{q}}=\frac{\partial H}{\partial \mathbf{p}}, \quad \dot{\mathbf{p}}=\frac{\partial H}{\partial \mathbf{q}} \quad (2.188)$$

with each trajectory weighted corresponding to the value of the Wigner function in the phase space point at initial time. It should be pointed out that this propagation method is exact for the harmonic systems where all derivatives higher than the second vanish in the exact Equation (2.186). In the framework of this method all quantum effects are contained in the initial distribution $P(\mathbf{q}_0,\mathbf{p}_0,t=0)$. For the generation of the initial conditions needed for the simulations of the dynamics of molecules and clusters a thermal initial ensemble specified by the Wigner distribution function of a canonical ensemble

$$P(\mathbf{q}_0,\mathbf{p}_0)=\frac{1}{(\pi\hbar)^N}\prod_{i=1}^{N}tanh\Big(\frac{\hbar\omega_i}{2k_BT}\Big)\times exp\Big[-\frac{2}{\hbar\omega_i}(p_{0,i}^2+\omega_i^2q_{0,i}^2)tanh\Big(\frac{\hbar\omega_i}{2k_BT}\Big)\Big] \quad (2.189)$$

where N is the number of vibrational degrees of freedom, ω_i are the frequencies of the normal modes and T is the temperature, can be used. The semiclassical Wigner method for the time propagation is particularly suitable for studying the nuclear dynamics of the systems with considerable number of degrees of freedom for which the quantum mechanical treatment of the dynamics becomes prohibitive and the precalculation of the potential energy surfaces is not possible. For this purpose ab initio MD with forces calculated "on the fly" can be employed. As has been demonstrated, the combination of accurate quantum mechanical initial conditions and classical propagation gives rise to the classical densities that are in very close agreement with their quantum mechanical analogues [124]. In quantum mechanics a wavepacket evolving under a time-independent Hamiltonian $\hat{H}$ can be expanded in a coherent superposition of the eigenstates:

$$\psi(\mathbf{q},t)=\sum_n c_n\psi_n(\mathbf{q})e^{-iE_nt/\hbar} \tag{2.190}$$

which gives rise to the interference phenomena reflected in the time dependence and the shape of the wavepacket. This principle of superposition holds because of the linearity of the time-dependent Schrödinger equation. In full analogy, however, the classical Liouville equation for the time evolution of the classical density $P(\mathbf{q},\mathbf{p})$ can be written as

$$i\frac{\partial P}{\partial t}=i\left(\frac{\partial H}{\partial q}\frac{\partial P}{\partial p}-\frac{\partial H}{\partial p}\frac{\partial P}{\partial q}\right)\equiv\hat{L}P. \tag{2.191}$$

Since the classical Liouville operator $\hat{L}$ is Hermitian, it has a spectrum of real eigenvalues (λ_n) and corresponding orthogonal eigenfunctions $P_n(\mathbf{q},\mathbf{p})$ and the classical evolving density can be expanded in a coherent superposition of these eigenfunctions:

$$P(\mathbf{q},\mathbf{p},t)=\sum c_nP_n(\mathbf{q},\mathbf{p})e^{-i\lambda_nt} \tag{2.192}$$

in full analogy with (2.190). Thus, classical dynamics of nonstationary ensembles results from a coherent superposition of oscillatory eigenfunctions just as in the quantum mechanical case. However, the important difference is that the classical operator $\hat{L}$ can have continuous eigenvalues for bound systems for which $\hat{H}$ has a discrete spectrum of eigenvalues. This leads for example to the absence of the important effect of recurrences in the classically evolving densities. Moreover, the typical quantum effects such as tunneling are not adequately described in the classical limit.

In order to include the nonlocality of quantum mechanics and to extend the approach, the "entangled trajectory method" has recently been proposed [125] allowing to treat tunneling. In this method the next higher term proportional to $\hbar^2$ in the Equation (2.186) is kept leading to the time evolution in which the trajectories are not independent anymore. However, the implementation of this approach in terms of the ab-initio MD on the fly is still computationally very demanding since it requires the calculation of the third derivatives of the potential energy.

2.5.3 Femtosecond pump-probe signals based on semiclassical multistate nuclear dynamics

For the formulation of the semiclassical approach for the simulation of femtosecond spectra it is convenient to use Wigner representation of the quantum mechanics [124, 126]. The dynamics of the system in the interaction with the electromagnetic field described by the Hamiltonian from Equation (2.180) is in the Wigner representation characterized by Wigner distribution functions $P_{ab}(\mathbf{q},\mathbf{p},t)$ which are defined as the Wigner transform of the vibrational density matrix elements $\rho_{ab}(\mathbf{Q},\mathbf{Q}',t)=\langle a|\langle\mathbf{Q}|\hat{\rho}|\mathbf{Q}'\rangle|b\rangle$. As already mentioned, the equation of motion for the Wigner distribution can be obtained by transforming the quantum mechanical Liouville-von Neumann equation for the density operator, which for the vibronic density matrix takes the following form:

$$i\hbar\frac{\partial\hat{\rho}_{ab}}{\partial t}=\hat{h}_a\hat{\rho}_{ab}-\hat{\rho}_{ab}\hat{h}_b-\varepsilon(t)\sum_c(\hat{\mu}_{ac}\hat{\rho}_{cb}-\hat{\rho}_{ac}\hat{\mu}_{cb}). \tag{2.193}$$

The intramolecular dynamics is determined by the vibrational Hamiltonians $\hat{h}_a$ and $\hat{h}_b$ and is described by the first two terms on the right hand side of Equation (2.193). The simulation of the pump-probe signals requires the explicit consideration of the coupling to the external electromagnetic field which is described by the last term on the right hand side of Equation (2.193). By performing the transformation to the Wigner representation Equation (2.193) becomes:

$$\begin{aligned} i\hbar\frac{\partial P_{ab}(\mathbf{q},\mathbf{p},t)}{\partial t} &= h_a(\mathbf{q},\mathbf{p})exp\left(\frac{\hbar}{2i}(\frac{\overleftarrow{\partial}}{\partial\mathbf{q}}\frac{\overrightarrow{\partial}}{\partial\mathbf{p}}-\frac{\overleftarrow{\partial}}{\partial\mathbf{p}}\frac{\overrightarrow{\partial}}{\partial\mathbf{q}})\right)P_{ab}(\mathbf{q},\mathbf{p},t)- \\ & P_{ab}(\mathbf{q},\mathbf{p},t)exp\left(\frac{\hbar}{2i}(\frac{\overleftarrow{\partial}}{\partial\mathbf{q}}\frac{\overrightarrow{\partial}}{\partial\mathbf{p}}-\frac{\overleftarrow{\partial}}{\partial\mathbf{p}}\frac{\overrightarrow{\partial}}{\partial\mathbf{q}})\right)h_b(\mathbf{q},\mathbf{p})+ \\ & \varepsilon(t)\sum_c^{a\neq c}(\mu_{ac}P_{cb}(\mathbf{q},\mathbf{p},t)-P_{ac}(\mathbf{q},\mathbf{p},t)\mu_{cb}). \end{aligned} \tag{2.194}$$

The description of the optical excitation processes in a system with multiple electronic states is in the framework of the Wigner representation described by Equation (2.194). The "classical limit" of this equation can be obtained by performing the $\hbar$-expansion of the exponentials in Equation (2.194) and restricting to the lowest order. Moreover, a further simplification of the equation above can be obtained by assuming that the electromagnetic fields are weak enough to use the perturbation theory. In this case, the Wigner distribution can be expanded in a perturbation series written as $P_{ab}=\sum_i P_{ab}^{(i)}$ where the subscript i indicates the order in the field. With these assumptions the classical limit for the non-diagonal elements $(a\neq b)$ becomes:

$$\begin{aligned} i\hbar\frac{\partial P_{ab}^{(i)}(\mathbf{q},\mathbf{p},t)}{\partial t} &= (h_a(\mathbf{q},\mathbf{p})-h_b(\mathbf{q},\mathbf{p}))P_{ab}^{(i)}(\mathbf{q},\mathbf{p},t)+ \\ & \varepsilon(t)\sum_c^{a\neq c}(\mu_{ac}P_{cb}^{(i-1)}(\mathbf{q},\mathbf{p},t)-P_{ac}^{(i-1)}(\mathbf{q},\mathbf{p},t)\mu_{cb}), \quad a\neq b, \end{aligned} \tag{2.195}$$

and for the diagonal elements $(a=b)$ representing occupation densities

$$\begin{aligned} i\hbar\frac{\partial P_{aa}^{(i)}(\mathbf{q},\mathbf{p},t)}{\partial t} &= \frac{\hbar}{i}[\frac{\partial h_a(\mathbf{q},\mathbf{p})}{\partial\mathbf{q}}\frac{\partial P_{aa}^{(i)}(\mathbf{q},\mathbf{p})}{\partial\mathbf{p}}-\frac{\partial h_a(\mathbf{q},\mathbf{p})}{\partial\mathbf{p}}\frac{\partial P_{aa}^{(i)}(\mathbf{q},\mathbf{p})}{\partial\mathbf{q}}]+ \\ & \varepsilon(t)\sum_c^{a\neq c}(\mu_{ac}P_{ca}^{(i-1)}(\mathbf{q},\mathbf{p},t)-P_{ac}^{(i-1)}(\mathbf{q},\mathbf{p},t)\mu_{ca}). \end{aligned} \tag{2.196}$$

Assuming the initial conditions $P_{ab}^{(0)}(\mathbf{q},\mathbf{p},t=0)=P_{ab}^{(0)}(\mathbf{q},\mathbf{p})$ for the Wigner distributions and $\mathbf{q}_a(t=0;\mathbf{q}_{a0})=\mathbf{q}_{a0}$ and $\mathbf{p}_a(t=0;\mathbf{p}_{a0})=\mathbf{p}_{a0}$ for coordinates and momenta, respectively, the Equations (2.195) and (2.196) can be iteratively solved to yield

$$\begin{aligned}
P^{(i)}_{ab}(\Gamma,t) &= \frac{1}{i\hbar}\int_0^t dt_1 exp\Big[-\frac{i}{\hbar}V_{ab}(\Gamma)(t-t_1)\Big]\varepsilon(t_1)\times \\
&\sum_c^{a\neq c}\Big[\mu_{ac}P^{(i-1)}_{cb}(\Gamma,t_1)-P^{(i-1)}_{ac}(\Gamma,t_1)\mu_{cb}\Big],\quad a\neq b \qquad (2.197) \\
P^{(i)}_{aa}(\Gamma,t) &= \frac{1}{i\hbar}\int\int d\Gamma_{ao}\int_0^t dt_2\delta(\Gamma-\Gamma_a(t-t_2;\Gamma_{a0}))\varepsilon(t_2)\times \\
&\sum_d^{d\neq a}\Big[\mu_{ad}P^{(i-1)}_{da}(\Gamma_{a0},t_2)-P^{(i-1)}_{ad}(\Gamma_{a0},t_2)\mu_{da}\Big] \qquad (2.198)
\end{aligned}$$

with the abbreviations $\Gamma = \mathbf{q},\mathbf{p}$ and the definition $\delta(\Gamma-\Gamma_a(t-t_2;\Gamma_{a0})) \equiv \delta(\mathbf{q}-\mathbf{q}_a(t-t_2;\mathbf{q}_{a0}))\delta(\mathbf{p}-\mathbf{p}_a(t-t_2;\mathbf{p}_{a0}))$. The energy gap between the electronic states a and b is given by he quantity $V_{ab}(\Gamma) = h_a(\Gamma) - h_b(\Gamma)$. Finally, by inserting Equation (2.197) into (2.198) the final expression for the occupation densities P_{aa} of the electronic state a reads:

$$\begin{aligned}
P^{(i)}_{aa}(\Gamma,t) &= \frac{1}{\hbar^2}Re\int d\Gamma_{a0}\int_0^t dt_2\int_0^{t_2} dt_1\delta(\Gamma-\Gamma_a(t-t_2;\Gamma_{a0}))\varepsilon(t_2)\varepsilon(t_1)\times \\
&\sum_{c,d}\mu_{ad}(\mu_{dc}P^{(i-2)}_{ca}(\Gamma_{a0},t_1)-P^{(i-2)}_{dc}(\Gamma_{a0},t_1)\mu_{ca})\times \\
&exp\Big[-\frac{i}{\hbar}V_{da}(\Gamma_{a0})(t_2-t_1)\Big]. \qquad (2.199)
\end{aligned}$$

In order to simulate the pump-probe signals a further specification of the pulse by a Gaussian envelope $\varepsilon(t) = exp[-\frac{t^2}{2\sigma^2}]cos(\omega t)$ centered around the laser frequency ω can be introduced in Equation (2.199). Assuming that the laser pulses have short duration σ the product of the laser pulses can be approximated by

$$\begin{aligned}
\varepsilon(t_1)\varepsilon(t_2) &= exp\Big(-\frac{t_1^2}{2\sigma^2}\Big)exp\Big(-\frac{t_2^2}{2\sigma^2}\Big)cos(\omega t_1)cos(\omega t_2) \\
&= exp\Big(-\frac{(t_1-t_2)^2}{4\sigma^2}\Big)exp(-\frac{(t_1+t_2)^2}{4\sigma^2}\Big)cos(\omega t_1)cos(\omega t_2) \\
&\approx exp\Big(-\frac{t_2^2}{\sigma^2}\Big)exp(-\frac{(t_1-t_2)^2}{4\sigma^2}\Big)cos(\omega t_1)cos(\omega t_2) \\
&\equiv I(t_2)exp\Big(-\frac{(t_1-t_2)^2}{4\sigma^2}\Big)cos(\omega t_1)cos(\omega t_2). \qquad (2.200)
\end{aligned}$$

Using the variable substitution

$$\begin{aligned}
\tau_1 &= t-t_2 \\
\tau_\alpha &= t_2-t_1 \qquad (2.201)
\end{aligned}$$

in Equation (2.200) and the rotating wave approximation (RWA), the density distribution of Equation (2.199) takes the following form:

$$\begin{aligned} P^{(i)}_{aa}(\Gamma,t) &= \frac{1}{\hbar^2}\int d\Gamma_{a0}\int_0^t d\tau_1\int_0^{t-\tau_1} d\tau_\alpha\delta(\Gamma-\Gamma_a(\tau_1;\Gamma_{a0}))I(t-\tau_1)\times \\ &\sum_{c,d}\mu_{ad}\left(\mu_{dc}P^{(i-2)}_{ca}(\Gamma_{a0},t-\tau_1-\tau_\alpha)-P^{(i-2)}_{dc}(\Gamma_{a0},t-\tau_1-\tau_\alpha)\mu_{ca}\right)\times \\ &exp[-\frac{i}{\hbar}(\hbar\omega-V_{da}(\Gamma_{a0}))\tau_\alpha]exp[-\frac{\tau_\alpha^2}{4\sigma^2}]. \end{aligned} \tag{2.202}$$

For short pulse durations σ the Gaussian $exp[-\frac{\tau_\alpha^2}{4\sigma^2}]$ in Equation (2.202) is strongly localized, thus the upper integration limit $t-\tau_1$ of the integration variable τ_α can be set up to infinity. This allows the analytic integration over τ_α yielding the Gaussian spectral distribution determined by the pulse duration σ:

$$\begin{aligned} P^{(i)}_{aa}(\Gamma,t) &= \frac{1}{\hbar^2}\int d\Gamma_{a0}\int_0^t d\tau_1\delta(\Gamma-\Gamma_a(\tau_1;\Gamma_{a0})I(t-\tau_1)\times \\ &\sum_{c,d}\mu_{ad}\left(\mu_{dc}P^{(i-2)}_{ca}(\Gamma_{a0},t-\tau_1)-P^{(i-2)}_{dc}(\Gamma_{a0},t-\tau_1)\mu_{ca}\right)\times \\ &exp\Big[-\sigma^2\frac{(\hbar\omega-V_{da}(\Gamma_{a0}))^2}{\hbar^2}\Big]. \end{aligned} \tag{2.203}$$

In the special case of the pump-probe process involving only three electronic states, the state 1 in which the system is prepared, the state 2 to which the pump pulse excites the system and the final state 3 to which the system is transferred by the probe-pulse and assuming that both interactions with the fields are of first order allow to apply Equation (2.203) only twice (i=2) leading to the following expression for the occupation $P^{(2)}_{22}(t)$ of the probe state 2:

$$\begin{aligned} P^{(2)}_{22}(t) &= \int d\mathbf{q}d\mathbf{p}P^{(2)}_{22}(\mathbf{q},\mathbf{p},t) \\ &\sim \int d\mathbf{q}_0 d\mathbf{p}_0\int_0^t d\tau_2\int_0^{t-\tau_2} d\tau_1 exp\left[-\sigma_{pr}^2\frac{[\hbar\omega_{pr}-V_{21}(\mathbf{q}_1(\tau_1;\mathbf{q}_0,\mathbf{p}_0))]^2}{\hbar^2}\right]\times \\ &exp\left[-\sigma_{pu}^2\frac{[\hbar\omega_{pu}-V_{10}(\mathbf{q}_0,\mathbf{p}_0)]^2}{\hbar^2}\right] I_{pu}(t-\tau_1-\tau_2)I_{pr}(t-\tau_2-t_d)P_{00}(\mathbf{q}_0,\mathbf{p}_0), \end{aligned} \tag{2.204}$$

where dipole matrix elements have been assumed to be constant. The indices pu and pr label the corresponding parameters of the pump- and the probe-field, respectively, and t_d denotes the time delay. Since the integration over the pump-probe correlation function involving gaussian functions can be calculated explicitly the final expression for the pump-probe signal at the time delay t_d defined as a total population of the final state 2 reads:

$$\begin{aligned} S[t_d] &\sim \int\int d\mathbf{q}_0 d\mathbf{p}_0\int_0^\infty d\tau_1 exp\left\{-\frac{(\tau_1-t_d)^2}{\sigma_{pu}^2+\sigma_{pr}^2}\right\}\times \\ &exp\left\{-\frac{\sigma_{pr}^2}{\hbar^2}[E_{pr}-V_{21}(\mathbf{q}_1(\tau_1;\mathbf{q}_0,\mathbf{p}_0))]^2\right\}\times \\ &exp\left\{-\frac{\sigma_{pu}^2}{\hbar^2}[E_{pu}-V_{10}(\mathbf{q}_0)]^2\right\}P_{00}(\mathbf{q}_0,\mathbf{p}_0). \end{aligned} \tag{2.205}$$

The expression (2.205) can be implemented in the following way. First an ensemble of initial conditions reflecting the initial phase space density $P_0(\mathbf{q}_0, \mathbf{p}_0)$ is generated. Then, using these initial conditions, classical trajectories are propagated in the state populated by the pump pulse and each trajectory is weighted by the pump-pulse "filter" function:

$$exp\left\{-\frac{\sigma_{pu}^2}{\hbar^2}[E_{pu} - V_{10}(\mathbf{q}_0)]^2\right\}. \tag{2.206}$$

For each integration time τ_1 the average of the probe pulse window function

$$exp\left\{-\frac{\sigma_{pr}^2}{\hbar^2}[E_{pr} - V_{21}(\mathbf{q}_1(\tau_1; \mathbf{q}_0, \mathbf{p}_0))]^2\right\} \tag{2.207}$$

is calculated over the whole propagated ensemble and finally the pump-probe signal is obtained by convolution with the pump-cross corelation function

$$exp\left\{-\frac{(\tau_1 - t_d)^2}{\sigma_{pu}^2 + \sigma_{pr}^2}\right\} \tag{2.208}$$

which determines the temporal resolution of the signal. The formalism presented above represents a general theoretical framework for the simulations of pump-probe and pump-dump spectra and it has been used in this work for the simulations of the NeNePo spectra in combination with the ab-initio MD "on the fly" based on the density functional theory. The details of the implementation in the context of NeNePo spectroscopy are given in Section 7.2.

2.5.4 Ab initio adiabatic and nonadiabatic MD "on the fly"

Classical molecular dynamics (MD) simulations allow to study the real dynamics of the system by solving the classical Newton's equations of motion

$$m\frac{d^2\mathbf{r}_i}{dt^2} = -\nabla_i V \tag{2.209}$$

where V is the potential energy of the system and $\mathbf{r}_i$ is a vector that contains the cartesian coordinates of the i-th particle. In molecular dynamics, the most commonly used algorithm for the numerical solution of Equation (2.209) is the Verlet algorithm [127] in which the position and velocity of the nucleus i at time step $t_n = n\Delta t$ are obtained recurrently according to:

$$\begin{aligned}\mathbf{r}_i^{(n+1)} &= \mathbf{r}_i^{(n)} + \Delta t\mathbf{v}_i^{(n)} + \frac{1}{2}\Delta t^2\frac{\mathbf{F}_i}{m_i} && (2.210)\\ \mathbf{v}_i^{(n+1)} &= \mathbf{v}_i + \frac{1}{2}\Delta t[\frac{\mathbf{F}_i^{(n)} + \mathbf{F}_i^{(n+1)}}{m_i}]. && (2.211)\end{aligned}$$

The advantage of the Verlet algorithm over the traditional integration methods for the differential equation such as the Runge-Kutta method is that the Verlet algorithm is time-reversible which leads to an improved energy conservation. Moreover, it needs only one evaluation of forces per time step which leads to the significant computational savings. The time step Δt for the numerical integration is determined by the rate of the fastest process in the system and for simulations in molecules and clusters it has the value

$\sim$ 1fs. In standard MD simulations the total energy of the system defined as the sum of the kinetic and potential energy

$$E_{tot} = \frac{1}{2}\sum_{i=1}^{N} m_i \mathbf{v}_i^2 + V(\mathbf{r}_1, \mathbf{r}_2, ...) \tag{2.212}$$

is conserved.The temperature of the system can be defined by the mean kinetic energy according to the relation

$$\langle E_{kin}\rangle = \frac{f}{2}k_B T \tag{2.213}$$

where the f is the number of degrees of freedom. Alternatively, simulations in which the temperature is constant can also be performed by modifying the velocities in each time step. As indicated in Equation (2.213), if the temperature at a given moment is different from the desired temperature, all velocities may be scaled by a factor of $(T_{desired}/T_{actual})^2$ to achieve the desired temperature. A more sophisticated method to perform constant temperature simulations is to couple the system to a "heat bath" which gradually adds or removes the energy from the system [128]. The major computational effort in classical simulations is the calculation of the forces acting on all particles in each time step. For this purpose in principle any type of energy function such as force field, semi-empirical or ab initio electronic structure methods can be used. The dynamics simulations can be performed either by precalculating the global potential energy surface and fitting it to a convenient analytical form or directly by calculating the forces in each step of an MD simulation ("on the fly"). There are in principle two ways to perform the ab initio MD simulations "on the fly". The first one involves the determination of the completely converged wavefunction at each time step, while in the second, one the wavefunction and the nuclei evolve simultaneously (Car-Parrinello MD [129]). The ab initio MD simulations are useful for studying the real time investigations particularly involving ultrafast processes and chemical reactivity where they can provide an insight into the reaction mechanisms. While the conventional quantum chemical studies of the chemical reactivity mainly concentrate on studying previously defined reaction pathways with static calculations, the MD simulations may be employed to find and study a new complex reaction pathways as shown in chapter 5.

In this work only the simulations "on the fly" in connection with ab initio electronic structure methods described in Section 2.4 have been used. Specifically, in order to study the ultrafast processes involving the adiabatic ground state dynamics DFT methods have been employed. The MD "on the fly" in excited states based on correlated methods is in spite of substantial advances recently achieved still computationally very demanding. Therefore, simplifications are desirable provided that the results remain accurate. For example the adiabatic and nonadiabatic dynamics involving excited and ground based on the "frozen ionic bond" approximation was developed in the Bonačić-Koutecký group [130, 131, 132]. This simplified approach method yields accurate description of the systems such as nonstoichiometric sodium fluoride clusters $\mathrm{Na}_n\mathrm{F}_{n-1}$ [130] in which one electron moves in the effective field of the remaining (n-1) valence electrons which are involved in the ionic bonding and are separated by a large energy gap from the single excess electron. The ground state of the system can in this case be described at the restricted open-shell Hartree-Fock (ROHF) level of theory, yielding canonical MOs ϕ_i. The excited electronic states are obtained as eigenstates of an effective one excess electron Hamiltonian containing Coulomb and exchange operators with the core defined as

$$\hat{h}' = \hat{h} + \sum_{c<o}[2\hat{J}_c(1) - \hat{K}_c(1)] \tag{2.214}$$

where the sum extends over all doubly occupied orbitals c. The wavefunctions ψ_i of the individual states of the one-excess electron are then obtained as eigenfunctions of $\hat{h}'$ and can be expressed as

$$\psi_i = \sum_{j=0}^{M} D_{ji}\phi_j \quad (i = o, \cdots, M) \tag{2.215}$$

where o labels the open shell single occupied HOMO and $\mathbf{D}$ is an unitary matrix which diagonalizes $\mathbf{h}'$

$$\mathbf{h}'\mathbf{D} = \mathbf{DE}, \quad \mathbf{E} \equiv diag(\epsilon_i). \tag{2.216}$$

The eigenvalues ϵ_i are the energies of the one-excess electron and their differences correspond to transition energies. Therefore the total energy of an excited state has the following form:

$$E_i = E_{SCF} + \epsilon_i - \epsilon_o, \tag{2.217}$$

where ϵ_o is the ground state energy of the one-excess electron. Note that in spite that the energy difference $\epsilon_i - \epsilon_o$ might resemble a use of simple Koopmans theorem, the energy levels of the excess electron ϵ_i are (with the exception of ϵ_o) not equal to the SCF MO energy levels. They correspond to the excited states of the one-excess electron, which feels the constant field of the remaining electrons, being "frozen" in the ground state. The eigenvectors D_{ji} are used to obtain the transition density matrix $\gamma_{h,l}(j,k)$ between h-th and l-th states

$$\gamma_{h,l}(j,k) = D^*_{jh} D_{kl} \tag{2.218}$$

from which transition moments and subsequently the oscillator strengths can be computed. The total computational cost for the calculation of the absorption spectrum involving the transition energies and oscillator strengths amounts for the ROHF calculation, the single closed-shell iteration and a few matrix multiplications needed for the calculation of transition moments. For the calculation of the gradient of the total energy given by Equation (2.217), in addition to the gradient of the ROHF SCF energy, the derivatives of the excess electron energies $\nabla_{\mathbf{R}}\epsilon_i$ are needed. Using the definition of the orbital energies ϵ_i

$$\begin{aligned} \epsilon_i &= \langle\psi_i|\hat{h}'|\psi_i\rangle \\ &= \sum_{j,k} (D^\dagger)_{ij} h'_{jk} D_{kl} \end{aligned} \tag{2.219}$$

one obtains:

$$\begin{aligned} \nabla_{\mathbf{R}}\epsilon_i &= \sum_{jk} \Big[(\nabla_{\mathbf{R}} D^\dagger)_{ij} h'_{jk} D_{ki} + (D^\dagger)_{ij} h'_{jk} \nabla_{\mathbf{R}} D_{ki} + (D^\dagger)_{ij} (\nabla_{\mathbf{R}} h'_{jk}) D_{ki}\Big] \\ & \sum_{j} \epsilon_i \Big[(\nabla_{\mathbf{R}} D^\dagger)_{ij} D_{ji} + (D^\dagger)_{ij} \nabla_{\mathbf{R}} D_{ji}\Big] + \sum_{jk} (D^\dagger)_{ij} (\nabla_{\mathbf{R}} h'_{jk}) D_{ki}. \end{aligned} \tag{2.220}$$

Since the term in brackets corresponds to a derivative of the normalization condition

$$\sum_{jk} (D^\dagger)_{ij} D_{jk} = \delta_{ik} \tag{2.221}$$

the expression (2.220) reduces to:

$$\nabla_{\mathbf{R}}\epsilon_i = \sum_{jk}(D^{\dagger})_{ij}(\nabla_{\mathbf{R}}h'_{jk})D_{ki} \tag{2.222}$$

which requires the calculation of derivatives of the effective one-excess electron Hamiltonian $\nabla_{\mathbf{R}}h'_{jk}$. They are identical to the derivatives of the closed shell Fock matrix $\mathbf{F}$ obtained from the cation $\mathrm{Na}_n\mathrm{F}_n^+$ with the converged orbitals of the neutral system $\mathrm{Na}_n\mathrm{F}_{n-1}$. The gradient

$$\nabla_{\mathbf{R}}h'_{ij} = \nabla_{\mathbf{R}}h_{ij} + \sum_c[2\nabla_{\mathbf{R}}(ij|cc) - \nabla_{\mathbf{R}}(ic|cj)] \tag{2.223}$$

with one-electron and two-electron integrals in the MO basis is therefore reduced to

$$\begin{aligned}
\nabla_{\mathbf{R}}h'_{ij} &= h'^{\mathbf{R}}_{ij} + \sum_k(U^{\mathbf{R}}_{ki}h'_{kj} + U^{\mathbf{R}}_{kj}h'_{ik}) + \sum_k\sum_l U^{\mathbf{R}}_{kl}A_{ij,kl} && (2.224)\\
h'^{\mathbf{R}}_{ij} &= h^{\mathbf{R}}_{ij} + \sum_k[2(ij|kk)^{\mathbf{R}} - (ik|jk)^{\mathbf{R}}] && (2.225)\\
A_{ij,kl} &= 4(ij|kl) - (ik|jl) - (il|jk). && (2.226)
\end{aligned}$$

In the above equations the summations over k, l indices run from 1 to M, while i, j indices are confined to $o, \cdots M$. The quantities $U^{\mathbf{R}}_{kl}$ in Equation (2.224) describe the influence of geometry changes on the SCF eigenvectors $C_{\alpha i}$ which are defined as

$$\nabla_{\mathbf{R}}C_{\alpha i} = \sum_{j=1}^{M} C_{\alpha i}U^{\mathbf{R}}_{ji} \tag{2.227}$$

and are obtained as solutions of the extended general restricted open shell coupled perturbed Hartree-Fock equations (CPHF) [133] which are part of program packages for computation of analytic second derivatives of the ROHF energy. Notice that the "extended" CPHF equations are needed in order to obtain the $U^{\mathbf{R}}_{ki}$ quantities where the k, i indices may correspond both to occupied and to virtual orbitals, which are not necessary for analytic second derivatives of the ROHF energy. The appropriate computational procedure is described in references [134] and [135]. The quantities $h^{\mathbf{R}}_{ij}$, $(ij|kk)^{\mathbf{R}}$, $(ik|jk)^{\mathbf{R}}$ in Equation (2.225) represent derivatives of one- and two-electron integrals in the AO basis, transformed into the MO basis (not including derivatives of the SCF eigenvectors)

$$\begin{aligned}
h^{\mathbf{R}}_{ij} &= \sum_{\mu\nu}^{AO} C_{\mu i}C_{\nu j}\nabla_{\mathbf{R}}h_{\mu\nu} && (2.228)\\
(ij|kl)^{\mathbf{R}} &= \sum_{\mu\nu\rho\sigma}^{AO} C_{\mu i}C_{\nu j}C_{\rho k}C_{\sigma l}\nabla_{\mathbf{R}}(\mu\nu|\rho\sigma). && (2.229)
\end{aligned}$$

To summarize, the derivative of the effective one-excess electron Hamiltonian can be built just like the derivatives of the Fock matrix in the CPHF for a closed shell system (of the cation), but using the SCF eigenvectors $C_{\alpha j}$ and the $U^{\mathbf{R}}_{ji}$ coefficients obtained from a ROHF or extended CPHF calculation of the open shell neutral system. Once the analytic energy gradient of the one-excess energy is known, the velocity Verlet time propagation algorithm can be employed in order to solve equations of motions and to compute the classical trajectories of the nuclei in the adiabatic electronic excited state. The calculation of excited state energies and of gradients in the framework of the "frozen ionic bond" approximation is from a computational point of view considerably less demanding than in the framework of other approaches such as RPA or CI. Therefore, this approach allows to carry out adiabatic molecular dynamics in the excited states, calculating the forces "on the fly".

Moreover, the fast computation of the non-adiabatic couplings "on the fly" based on the analytic formulation similar to the one outlined here for the adiabatic MD given in [132] allows to carry out non-adiabatic MD. In this work Tully's stochastic fewest-switches procedure [136] which requires a simultaneous solving of the time-dependent Schrödinger equation for the one excess electron and classical equations of motion for the nuclei. The time dependent wavefunction $\Psi(\mathbf{r}, \mathbf{R}, t)$ which describes the electronic state at the time t can be expanded in terms of the adiabatic electronic basis functions ψ_j of the Hamiltonian with complex-valued time dependent coefficients

$$\Psi(\mathbf{r}, \mathbf{R}, t) = \sum_{j=0}^{M} c_j(t)\psi_j(\mathbf{r}; \mathbf{R}). \tag{2.230}$$

Substitution of this equation into the time-dependent Schrödinger Equation (2.1), multiplication by ψ_k^* from the left, and integration over the electronic coordinates $\mathbf{r}$ yields a set of linear differential equations of the first order for the expansion coefficients $c_j(t)$:

$$i\hbar\dot{c}_k(t) = \sum_j \left[\epsilon_j\delta_{kj} - i\dot{\mathbf{R}}(t)\cdot\langle\psi_k|\nabla_{\mathbf{R}}|\psi_j\rangle\right]c_j(t) \tag{2.231}$$

where the ϵ_j are the eigenvalues of the Hamiltonian and $\langle\psi_k|\nabla_{\mathbf{R}}|\psi_j\rangle$ are the nonadiabatic couplings. The system of Equations (2.231) has to be solved simultaneously with the classical equations of motion for the nuclei

$$M\ddot{\mathbf{R}} = -\nabla_{\mathbf{R}}E_m(\mathbf{R}) \tag{2.232}$$

where the force is the negative gradient of the potential energy of the "current" m-th adiabatic state. The hopping probabilities g_{ij} between the electronic states are determined by

$$g_{ij} = 2\frac{\Delta t}{c_i c_i^*}[Im(c_i^* c_j \epsilon_i \delta_{ij}) - Re(c_i^* c_j \dot{\mathbf{R}}\langle\psi_i|\nabla_{\mathbf{R}}|\psi_j\rangle)] \tag{2.233}$$

and the hopping can occur randomly. This procedure has been designed to satisfy the statistical distribution of state populations at each time according to the quantum probabilities $|c_i(t)|^2$ using minimal number of "hops". The nonadiabatic coupling matrix elements can be computed analytically in the framework of the "frozen ionic bond" approximation and allow to perform the simulations of the nonadiabatic processes in systems such as nonstoichiometric $\mathrm{Na}_n\mathrm{F}_{n-1}$ clusters for which this approximation is adequate yielding accurate results.

2.6 Laser control of ultrafast processes

One of the central goals of chemistry is to provide a way for the selective control of chemical reactions. The methods for the control can be divided into the "passive" and the "active" ones [137]. The "passive" methods of control emerged from the centuries of chemical experience combined with the laws of thermodynamics and statistical mechanics. They are essentially macroscopic and are based on the amplification of the yield of the desired product either by adjusting the equilibria between reactants in a way that those leading to the desired product are favored or by adjusting the rates of chemical reactions leading to the different products. This way of control is termed passive since no external fields are used to manipulate the reactant molecules, the evolution of the ensemble of molecules is incoherent and there is no control of the evolution on a microscopic molecular level. The idea of the active control is to use external fields whose intensity, phase and spectral content can vary with time to influence the reactant molecules and steer the dynamics on a microscopic level towards the desired outcome. This approach for the active control has particularly been stimulated in recent years by the advances in the laser technology.

Originally, several different proposals to achieve selectivity in chemical reactions using quantum interference effects have been proposed. Tannor and Rice [138, 139] introduced the pump-dump control scheme which is based on the use of time delay between two laser pulses to influence the evolution of the system. Basically, the first light pulse excites the system from the ground to the excited electronic states and creates a wavepacket which evolves on the excited state. At a convenient time delay when the systems reaches the configuration corresponding to the desired product a second light pulse is applied which transfers the system to the final state leading to the desired products. This control scheme relies on the fact that the potential energy surfaces corresponding to the different electronic states can have very different shapes and as a consequence the pathways which are energetically unaccessible in one state may be well accessible in some other electronic state.

Another control scheme based on quantum interference has been proposed by Brumer and Shapiro [140, 141]. This scheme exploits the interference between two possible pathways leading to the target products to induce the control. Two different light fields can be used to excite the system via those pathways and control is obtained by varying the relative phase of the two fields. Both Tannor-Rice and Brumer-Shapiro schemes in their original versions use simple unoptimized pulse sequences to achieve the control. However, the control problem can be formulated more generally in the framework of the optimal control theory [142, 143]. In this approach an optimal laser field is calculated by maximizing the yield of the desired product using variational approach with the restriction that the evolution of the system under influence of the light field must satisfy the time-dependent Schrödinger equation. In addition, a variety of other constraints such as restriction of the total energy of the field may be included in the procedure. A breakthrough in the experimental realization of the optimal control relies on the proposal by Rabitz and Judson [30] to use the experimental apparatus as an analog computer that solves the Schrödinger equation exactly, in real time, and optimizes the light field using a learning procedure. Essentially, the pulse sequence is optimized in a closed loop iterative procedure guided by the "fitness" information about the yield of the desired product which is obtained as an output from the measuring device. The disadvantage of this method is that it does not reveal the mechanism which is responsible for the optimal control and for the shapes of the optimal light fields which can assume very complicated and at the first sight unintuitive shapes.

Since the tailored laser pulses have the role to select pathways on the parts of the potential energy surfaces which optimally lead to the desired product, their analysis should allow to detect the mechanism of the optimal control and can also provide information about important parts of the PES. Therefore, the development of theoretical methods is needed which allow to design interpretable optimal laser pulses for complex systems such as clusters by establishing the connection between the underlying dynamics and the optimal pulse shapes. In the following section a mathematical formalism of the optimal control theory based on the density matrix approach [144, 145] will be presented. In this work this approach has been used in the framework of Wigner representation (Chapter 9) to develop a new strategy for the optimal pump-dump control in complex systems based on a semiclassical approach.

2.6.1 Density matrix formalism of the optimal control theory

The goal of the optimal control theory is to design the electromagnetic field which drives the time evolution of the molecular system in a way which maximizes the expectation value of some operator target $\hat{A}$ at a specified time t_f. The target operator $\hat{A}$ corresponds to the desired goal and can for example have the form of the projection operator to a desired product channel. In the framework of the density matrix formalism the expectation value of the operator $\hat{A}$ at the specified time delay t_d defines the yield of the control process and is given by

$$\langle A(t_f)\rangle = Tr[\hat{A}\hat{\rho}(t_f)] \tag{2.234}$$

where $\hat{\rho}(t_f)$ is the density operator at the time t_f. The time evolution of the density operator is determined by the Liouville-von Neumann equation

$$i\hbar\frac{\partial\hat{\rho}}{\partial t} = [\hat{H},\hat{\rho}]. \tag{2.235}$$

The time-dependent Hamiltonian for a system coupled to an electromagnetic field via dipole interaction has the form

$$\hat{H}(t) = \hat{H}_0 - \mu\cdot\varepsilon(t) \tag{2.236}$$

where $\hat{H}_0$ is the time-independent molecular Hamiltonian. The Liouville-von Neumann equation (2.235) can formally be solved by introducing the time propagator $\mathcal{G}(t,t_0)$ giving

$$\hat{\rho}(t) = \mathcal{G}(t,t_0)\hat{\rho}(t_0). \tag{2.237}$$

The expectation value $\langle A(t_f)\rangle$ is optimized subject to the constraints which act on the system and prevent that trivial or nonphysical solutions are found. For example, if the only constraint is that the total energy of the optimal field is finite then the functional to be optimized has the form

$$J(t_f) = \langle A(t_f)\rangle - \frac{\lambda}{2}\int_{t_0}^{t_f}\varepsilon(t)^2 dt \tag{2.238}$$

where λ is the Lagrange multiplier that limits the total energy of the field. The constraint that the equation of motion (2.235) is obeyed is automatically included in the functional (2.238) via the time propagator $\mathcal{G}(t,t_0)$. The optimal control field $\varepsilon(t)$ is obtained by performing the variation of the functional (2.238) and setting to zero

$$\delta J(t_f) = \delta\langle A(t_f)\rangle - \lambda\int_{t_0}^{t_f} dt\varepsilon(t)\delta\varepsilon(t) = 0. \tag{2.239}$$

The variation in the field and the resulting change in the system Hamiltonian induce a change in the density matrix which is to the first order in $\delta\varepsilon(t)$ given by

$$\delta\hat{\rho}(t) = \frac{i}{\hbar}\int_{t_0}^{t_f} dt\mathcal{G}(t,t_0)[\hat{\mu}\hat{\rho}(t) - \hat{\rho}(t)\hat{\mu}]\delta\varepsilon(t). \tag{2.240}$$

Then by substitution of (2.240) in (2.239) the equation for the optimal control field

$$K(t; t_f) = \lambda \varepsilon(t) \tag{2.241}$$

is obtained where the $K(t, t_f)$ stands for the control kernel,

$$K(t, t_f) = \frac{i}{\hbar} Tr \left\{ \hat{A}(t; t_f)[\hat{\mu}\hat{\rho}(t) - \hat{\rho}\hat{\mu}] \right\}. \tag{2.242}$$

In Equation (2.242) the density operator $\hat{\rho}(t)$ is propagated forward in time while the target operator $\hat{A}(t; t_f) = \hat{A}\mathcal{G}(t, t_0)$ is propagated backward in time from t_f to t under the influence of the field. Physically, the control kernel $K(t; t_f)$ defines the response of the system to a small functional variation in the field and since it depends implicitly on the field Equation (2.241) for the optimal field it needs to be solved iteratively. However, in the weak field limit perturbation theory can be used to calculate the control kernel. To the first order in the field $K(t, t_f)$ is given by

$$K^{(1)}(t, t_f) = \int_{t_0}^{t_f} dt' M(t', t) \tag{2.243}$$

where

$$M(t, t') = (\frac{i}{\hbar})^2 Tr \hat{A} \mathcal{G}_0(t_f - t)[\hat{\mu}\hat{\rho}(t) - \hat{\rho}(t)\hat{\mu}] \times \mathcal{G}_0(t - t')[\hat{\mu}\hat{\rho}(t') - \hat{\rho}(t)\hat{\mu}']\hat{\rho}(t_0) \quad t \geq t'. \tag{2.244}$$

It should be noted that in the evaluation of the response function (2.244) only the field free propagator $\mathcal{G}_0$ is involved.

The optimal field is obtained as the solution of the Fredholm-type integral equation:

$$\int_0^{t_f} dt' M(t, t') \varepsilon(t') = \lambda \varepsilon(t). \tag{2.245}$$

The eigenvectors of this equation are the optimal fields and the eigenvalues give the corresponding yields. The globally optimal field is associated with the largest eigenvalue.

Chapter 3

Structural and electronic properties of pure gold and bimetallic silver-gold clusters: Reactivity aspects

3.1 Introduction

The recent discovery of unusual catalytic activity of small supported gold clusters [9] in contrast to the inert bulk material has led to increased interest in structural and electronic properties of small gold clusters as function of their size. Also the study of combustion of CO on size selected small monodispersed gold clusters supported on magnesia allowed to identify Au_8 cluster as the smallest catalytically active species [10]. The reactivity of mass selected anionic gold clusters with molecular oxygen has been investigated showing that the anionic gold clusters with even number of atoms having low values of electron affinities react with molecular oxygen in contrast to those with odd number of atoms, thus exhibiting the even-odd oscillatory behavior as a function of the cluster size [11]. The connection between electron affinity and activation of molecular oxygen by gold clusters at low temperature has also been established based on the simple frontier orbital model [12].

The experimental values of electron affinities, vertical detachment energies and ionization potentials of pure gold clusters as function of their size are known from early investigations [146, 147, 148]. Structural properties of small anionic and neutral Au_n (n=3-8) clusters have been investigated theoretically [149, 150, 151, 152, 153]. In the case of cationic and anionic clusters, the structures have been determined in the framework of density functional method and used for structural assignment in ion mobility measurements [154, 155]. There are similarities for small clusters (n=3, 4), but also significant differences between the structures of charged gold and silver clusters larger than tetramers [154, 156, 157, 158]. The general tendency is that the gold clusters assume two-dimensional structures for much larger cluster sizes than the silver clusters due to the pronounced relativistic effects which lead to the participation of the d-electrons in the bonding. Since the calculated values of vertical detachment energies, electron affinities and collision cross sections are strongly structure dependent, the energy sequence of the isomers remains still an important issue and can strongly depend on the theoretical method applied. The experimental conditions, in particular the temperature may also significantly influence the measured properties. Therefore, an accurate determination of structural properties of pure gold clusters is important in order to address aspects of their reactivity. In fact, the theoretical treatment of the gold clusters is much more demanding than of silver clusters, since in the former case d electrons are expected to participate in the bonding and in the latter case they are localized in the core of the Ag atoms and do not play a key role for structural properties [159, 160].

In contrast to the pure gold and silver clusters, considerably less information is available about structural and electronic properties of bimetallic silver-gold clusters. Exception is an experimental work on photodetachment of Ag_mAu_n ($m+n \leq 4$) clusters [161], earlier theoretical work on mixed trimers [162] and our recent work presented here [163, 164, 165] which motivated recent experiments on cationic mixed clusters [166]. Several topics will be addressed. The role of the hetero-polar bonding versus homonuclear metallic bonding in small bimetallic clusters will be clarified, since the former can promote charge transfer from the Ag to the Au atoms due to the electronegativity difference between silver and gold. This opens the possibility to tune the properties of the bimetallic cluster in such a way to increase their catalytic potential. It is known that metal oxide support which is responsible for the charge transfer plays a key role for generating the catalytic activity of supported Au catalysts. In this context, it is of particular interest to find the structural patterns promoting charge transfer in bimetallic clusters. For this purpose it is necessary to search for the given size and the composition of clusters which can give rise to negatively charged gold species embedded in the environment of silver atoms. In other words the investigation of "ionic" versus "metallic" properties with charge transfer in bimetallic clusters is important for gaining an understanding about their possible role as reactive centers. In this regard it is also useful to compare the structural and electronic properties of bimetallic gold-silver clusters with those of gold and silver one-component systems.

3.2 Computational

The aim of this work is to investigate structural properties of bimetallic Ag_mAu_n clusters as a function of the size and composition for $3 \leq (m + n) \leq 20$ and to compare them with the properties of pure Ag_m and Au_n clusters. For this purpose the gradient corrected density functional method with relativistic effective core potentials taking into account either one valence electron per atom (1e-RECP) developed in the Bonačić-Koutecký group [163] or 19 valence electrons per Au and Ag atom (19e-RECP) has been employed.

The comparison of the ground state properties of homo- and hetero-nuclear neutral and charged dimers obtained employing 1e-RECP BLYP method with available experimental data shows that the calculated bond distances are in very satisfactory agreement with experimental values (cf. Table 3.1). Ionization potentials (IP), electron affinities (EA), vertical detachment energies (VDE) and dissociation energies deviate mostly by ~0.2 eV from the measured ones except for the IP of Au_2 for which this deviation is slightly larger (cf. Table 3.1). In order to determine the influence of d-electrons on bonding properties in Au clusters and in bimetallic clusters 19e-RECP from the Stuttgart group [174] with the [9s7p5d1f]/[7s5p3d1f] AO basis set for Au atom and the [8s7p5d1f]/[6s5p3d1f] AO basis set for Ag atom in the framework of DFT with the S-VWN [81] and Becke-Perdew parameterization (BP-86) [85, 175] has been employed. As shown in the previous work the combination of 1e-RECP with configuration interaction method allows an adequate description of the ground state properties of pure Ag clusters and compares well with the results obtained with 11e-RECP coupled cluster method [157, 158, 159, 160, 176]. The reason for this is that the d-electrons are localized in the atomic cores and do not participate directly in bonding. This has recently been confirmed experimentally for the cationic Ag clusters by using the ion mobility technique

Table 3.1: Ground state properties of the atoms and dimers obtained with the 1e-RECP BLYP and the 19e-RECP BP96(in square brackets) methods.

	r_e (Å)	r_e(exp.) (Å)	ω_e cm^{-1}	ω_e(exp.) cm^{-1}	D_e (eV)	D_e(exp.) (eV)	IP (eV)	IP(exp.) (eV)	VDE (eV)	VDE(exp.) (eV)
Au							9.25 [9.73]	9.23^a	2.27 [2.44]	2.31^a
Ag							7.58 [8.22]	7.58^a	1.23 [1.54]	1.30^a
Au_2	2.473 [2.526]	2.4719^b	180.0 [172.0]	190.9^b	2.52 [2.28]	2.29^b	$9.85 [9.50]^f$	9.20^e		
Au_2^+	2.674 [2.622]		116.0 [147.0]		1.92 [2.43]					
Au_2^-	2.625 [2.640]	2.582^b	123.0 [134.5]	149.0^b	1.92 [2.01]	1.92^b			2.12 [2.08]	2.01^b
Ag_2	2.543 [2.567]	2.5303^c	197.0 [188.4]	192.4^b	1.83 [1.74]	1.65^c	$7.83 [8.18]^f$	7.6557^b		
Ag_2^+	2.776 [2.728]		124.0 [132.4]		1.57 [1.78]					
Ag_2^-	2.684 [2.702]	2.600^c	139.0 [134.3]	145.0^b	1.40 [1.46]	1.37^c			0.92 [1.31]	1.06^b
AgAu	2.493 [2.552]	2.496^d	198.0 [183.0]		2.00 [2.10]	2.10^d	$8.85 [8.92]^f$			
$AgAu^+$	2.706 [2.700]		123.0 [139.0]		1.10 [1.40]					
$AgAu^-$	2.623 [2.681]		138.0 [135.0]		1.30 [1.30]				1.27 [1.72]	1.43^g

[a] Atomic energies are E_{Au}=-0.340041, E_{Ag}=-0.27851, E_{Au^-}=-0.42346, E_{Ag^-}=-0.32585 and E_{Au^+}=0.0, E_{Ag^+}=0.0 a.u. ;experimental values from Ref. [167]. The core-core repulsion has been corrected according to (CC(r_{ij})=1/r_{ij}+D$exp(-ar_{ij})$). Constants D and a obtained for 1e-RECP's from the fitting procedure are:
D_{Ag-Ag} = 1619.887392, a_{Ag-Ag} = 2.496301, D_{Au-Au} = 1911.131090, a_{Au-Au} = 2.465901, D_{Au-Ag} = 1765.509532, a_{Au-Ag} = 2.481101
[b] Ref. [168]. [c] Ref. [169, 170, 171]. [d] Ref. [172]. [e] Ref. [173].

[156] as well as theoretically for the neutral clusters [177]. The bond distances, frequencies and dissociation energies for homo-nuclear and hetero-nuclear neutral and charged dimers obtained with 1e-RECP BLYP and 19e-RECP BP86 approaches are given in Table 3.1 and compared with available experimental data [167, 170, 171, 178, 179]. The bond distance obtained from 1e-RECP BLYP are in better agreement with experimental data than those of the 19e-RECP BP86 procedure. The latter gives rise to distances slightly larger than the experimental ones which might influence computed structural properties, in particularly of very small systems. Dissociation energies (D_e) for silver and mixed dimers obtained from both treatments are in satisfactory agreement with the available experimental data. D_e for Au_2 calculated with 19e-RECP BP86 is in better agreement with the experimental value. Concerning the accuracy of IP values, considerable deviations from the experimental results are found for Au_2 at 1e-RECP BLYP level and for Au and Ag atom as well as for Ag_2 at the 19e-RECP BP86 level of calculations. The VDE values from 1e-RECP BLYP are in good agreement with experimental data, while 19e-RECP BP86 values are in general larger than experimental ones. Since the s-d excitation for Au and Ag atom is 1.74 eV and 3.97 eV, respectively, it is not surprising that inclusion of d electrons is important for the pure Au clusters while the 1e-RECP BLYP provides reliable results for Ag clusters. Therefore, for the neutral gold clusters 19e-RECP BP86 calculations have been carried out.

The accuracy of the electron correlation treatment at the DFT level of theory for Au clusters in the framework of 19e-RECP is difficult to judge. It seems that the DFT procedure gives rise to a relatively small s-d energy gap which might lead to overestimated hybridization effects. The only computationally convenient alternative to the DFT treatment of 19 electrons per atom is offered by the Møller-Plesset method (MP2) which is known to be less adequate for delocalized than for directional bonding. Both methods have been used with 19e-RECP for determination of structures of the cationic Ag_m^+ clusters [156]. The MP2 method gave rise to the 3D-structure of Ag_7^+ (pentagonal bipyramid) and DFT to the 2D planar structure although the energy difference between both structures is very small. The 3D-structure is in better agreement with ion mobility measurements [156]. In general MP2 and DFT yield similar results for cationic Ag clusters for which the correlation of d-electrons is not very important. In contrast, cationic gold clusters are predicted by DFT to be planar for larger sizes (e.g. Au_7^+) in agreement with ion mobility measurements [154], while MP2 predicts a 3D-structure for Au_7^+ similar to that of Ag_7^+. This indicates that MP2 might underestimate the contribution of the d-electrons to bonding in the Au_7^+ cluster. In fact, based on combined experimental and theoretical work [154, 156] the conclusion has been drawn that the number of bonds in stable structures of cationic silver clusters is larger than in those of cationic gold clusters for sizes $5 \leq n \leq 11$. Therefore, the DFT description might be more realistic for Au clusters than that offered by MP2 approach. Several comparisons between DFT and MP2 results for neutral Au and for Ag clusters have been performed and they showed that the two methods disagree mainly for gold systems. This discrepancy is particularly large, for example in the case of Au_8 for which the DFT energy difference between the most stable planar structure and the 3D-T_d form is ~ 0.5 eV, while MP2 yields T_d structure by ~ 0.81 eV lower than the planar one. Since MP2 has tendency to produce similar structures for gold and silver clusters, it seems that the correlation effects for d -electrons in the case of Au clusters are not sufficiently taken into account. Based on these findings the DFT method is used throughout the work.

In order to check the accuracy of the 1e-RECP BLYP procedure for the determination of structural properties of bimetallic clusters a comparison with the 19e-RECP BP86 approach for smaller clusters $3 \leq (m + n) \leq 8$ has been carried out. As it will be shown the structural properties of bimetallic clusters are in general well described by the 1e-RECP BLYP procedure, in particularly neutral species, since the s-d hybridization is considerably smaller than in the pure Au clusters. There are some exceptions which will be addressed below. All geometries have been fully optimized and vibrational analysis has been carried out for the majority of structures in order to determine the local minima on the energy surfaces.

3.3 Neutral gold clusters Au_n (n=2-10)

Due to their closed d-shells the coinage metal clusters can be considered as the bridge between alkali metal clusters in which only s-electrons are contributing to the bonding and the clusters of transition metals where the bonding is strongly influenced by d-electrons. In this respect gold clusters are particularly interesting due to the pronounced relativistic effects which lower the energy of the 6s orbital and therefore make the energy gap between s- and d-orbitals much smaller. It can therefore be expected that the influence of the d-electrons on the structural properties of gold clusters is much larger than in the case of silver clusters. An important question which arises in this context is at which size the gold clusters start to assume 3D structures?

Therefore, in this work the structural properties of the neutral gold clusters in the range from two to ten gold atoms have been studied using BP86 density functional method [85, 175] and the 19e-RECP. The obtained structures are shown in Figures 3.1 and 3.2. In contrast to the pure silver clusters which assume three dimensional structures at the size of seven the lowest energy structures of Au_n up to n=10 are planar at the DFT level of theory and they are not directly related to sections of the bulk phase. The calculated binding energies per atom are presented in Figure 3.3. In order to be sure that the global minima have been identified a large number of structures has been investigated and in addition molecular dynamics simulations have been performed starting from the most stable structure found. The binding energies per atom increase with the cluster size exhibiting pronounced even-odd alternation which indicates a larger stability of clusters with the even number of electrons than of those with odd number of electrons. In all cases the stable structures are well separated in energy from higher lying isomers with exception of

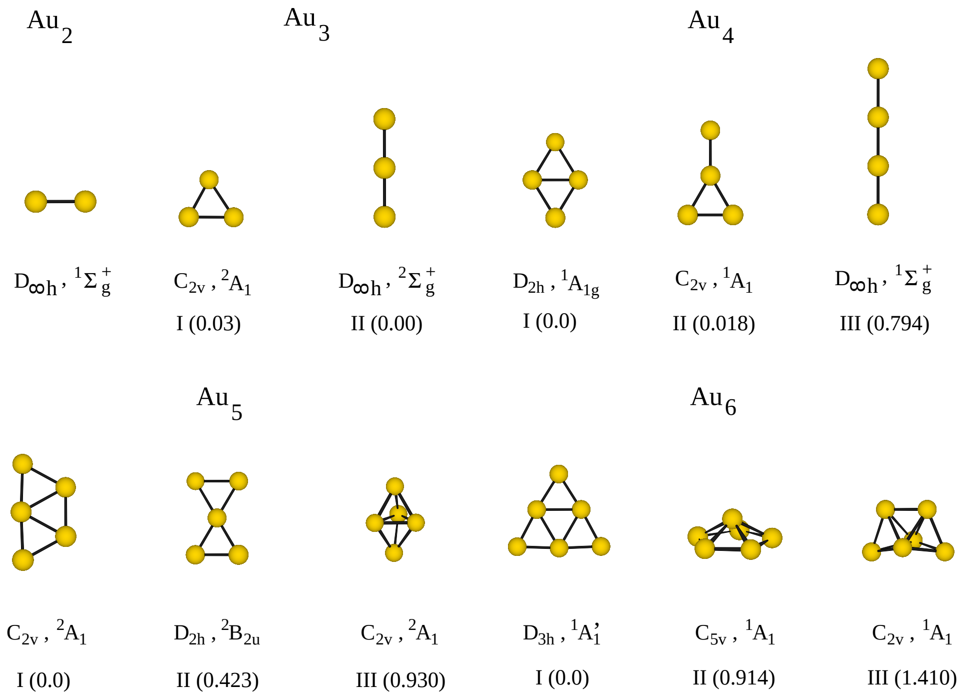

Figure 3.1: Structures of neutral gold clusters Au_n (n=2-6) optimized at the 19e-RECP/BP86 level of theory with labels of the symmetry group and of the ground electronic states. The energy difference (in eV) with respect to the lowest energy structure are given in brackets.

Au_3, Au_4 and Au_7 (cf. Figures 3.1 and 3.2). For the trimer the linear and isosceles triangular geometries are almost degenerate, for the tetramer the rhombic and T-form are very close in energy and for the heptamer two planar geometries with different patterns are competing in stability. It should be pointed out that the energy ordering of close lying isomers can depend on the details of the theoretical treatment [180]. This has been illustrated by a study carried out on structures of Au_3 employing different methods. The isosceles triangular geometry is the most stable structure at the level of the coupled cluster theory including single, double and triple excitations CCSD(T) with the two states, the $^2A_1$ and $^2B_2$ close in energy, arising from Jahn Teller effect. The linear form is slightly higher in energy. In this work the DFT study using the 1e-RECP gives rise to very similar results, but the energy of the linear form is slightly lower when the 19e-RECP is used.

At this point it is useful to address the role of d-electrons in the bonding in Au clusters. The rhombic and T-form of the tetramer are closer in energy, if the d-electrons are accounted for with 19e-RECP, but the former remains the most stable structure as in the 1e-RECP treatment. In contrast, 19e-RECP predicts planar structures of the heptamer to be considerably lower in energy (by 0.9 eV) than the 3D-structures, while the 1e-RECP gives rise to the 3D pentagonal bipyramid as the most stable form. Discrepancies between the two approaches in predicting the transition from 2D- to 3D-structures indicate that the inclusion of d-electrons in the treatment is important for the ground state properties of the pure Au clusters with nuclearity larger than six. This finding is also supported by investigations carried out on the cationic and anionic Au clusters using the same 19e-RECP BP86 treatment as in this work. Therefore a comparison of the results obtained for the neutral Au clusters can be made with those of Ref. [155] on cationic and anionic species where also experimental assignment of the structures is available. Cationic Au clusters larger than heptamer have 3D-forms related to the sections of the bulk phase in contrast to the anionic gold clusters which remain two-dimensional until the size of n=13 which indicates a substantial influence of charge on the structural properties. The lowest energy structures of Au_n (n=4 - 7) can

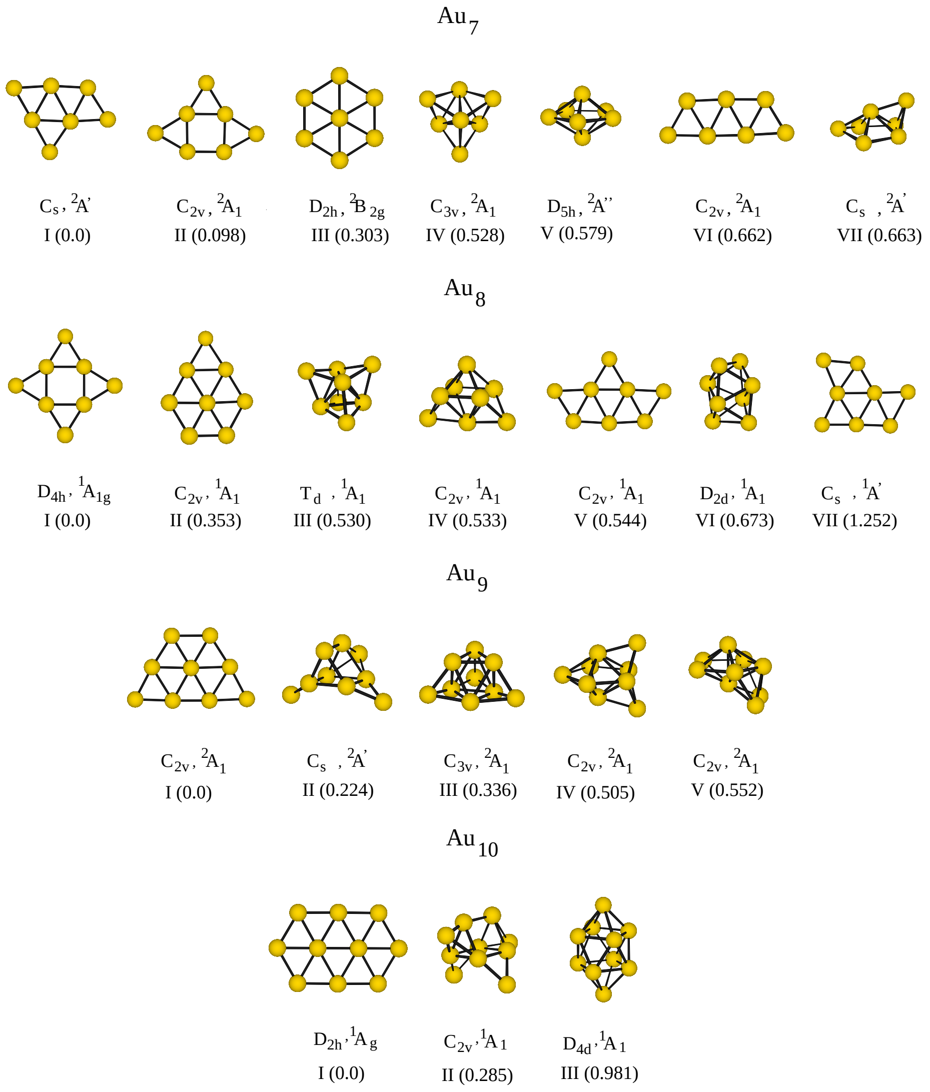

Figure 3.2: Structures of neutral gold clusters Au_n (n=7-10) optimized at the 19e-RECP/BP86 level of theory with labels of the symmetry group and of the ground electronic state. The energy difference (in eV) with respect to the lowest energy structure are given in brackets.

be derived by adding a single atom to the lowest energy structure of Au_{n-1} cluster, thus forming an additional triangular subunit. This pattern changes for the most stable structure of Au_8 in which the square subunit is capped by four atoms on each side. The structural motive changes again for Au_9 and Au_{10}. In the former case the single atom assumes a central position and therefore is highly coordinated and in the latter case two centered highly coordinated atoms are present (cf. Figure 3.2). For the lowest energy structures presented also the vertical ionization potentials (IP) have been calculated. In Figure 3.4 comparison with experimental IP's [173] is given showing a very good general agreement. Calculated IP's are systematically higher than the experimental values by $\sim 0.3 - 0.5$ eV[1] but follow the experimental trend very closely. Only exception is the Au_9 cluster for which the theoretical value is lower than the experimental one. The overall trend in IP gives further support for the structural assignment presented here.

What is the reason for the 2D-forms of Au_n clusters?

The s-d energy separation in Au atom is relatively small and as a consequence the d-electrons might

---

[1] As mentioned in section 2.4.7 this is due to the inability of the ECP approximation to take into account the inner shell relaxation which takes place upon ionization.

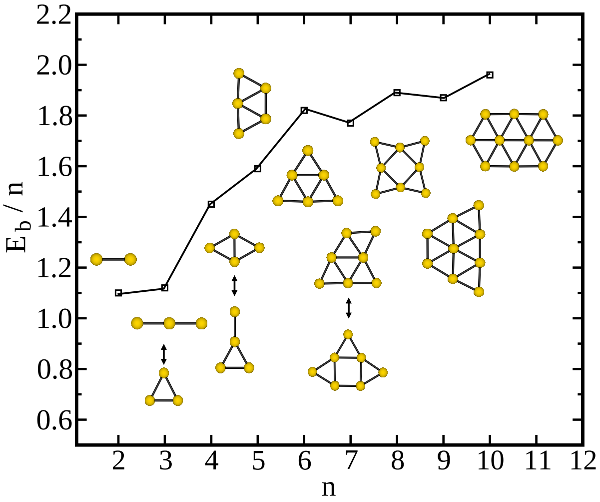

Figure 3.3: Binding energies per atom for neutral gold clusters $E_b/n = [E(Au_n) - nE(Au)]/n$ as function of the cluster size n calculated for the most stable structures on Figures 3.1 and 3.2. For isomers with energy difference smaller than 0.1 eV both structures are shown.

participate in bonding. However degree of their participation seems to be dependent upon structural properties. The analysis of DFT density of states (DOS) in terms of s-, p- and d-contributions has been carried out. Two different characteristic features have been identified for the 2D- and 3D-structures, for example in the case of Au_8. The DOS corresponding to the HOMO of the planar structure is dominated by d-contributions and the energy gap with respect to other DOS with mixed s- and d-character is very small. In contrast, DOS obtained for the T_d structure corresponding to the HOMO has larger s- than d-contributions and is strongly separated from lower energy DOS which are dominated by d-contributions. The analysis above indicates that the higher stability of the planar structure of Au_8 is due to larger contributions of d-electrons to the bonding than in the case of the T_d-3D structure. This explains qualitatively also why the neutral silver clusters which are characterized by s-type bonding assume 3D structures already for larger sizes than hexamer.

As already pointed out structural properties of Au clusters are very dependent on the particular method adopted for the description of electron correlation effects. According to ion mobility measurements [155] on cationic Au clusters it is to expect that also larger neutral Au clusters than hexamers assume planar structures as obtained from the DFT theory. Whether the neutral gold clusters are still planar until n = 10 or not remains to be verified. Notice, that the energy difference between 2D and 3D structures is smaller for Au_9 and Au_{10} clusters ($\Delta E \approx 0.2$ eV) than for Au_7 and Au_8 ($\Delta E \approx 0.5$ eV) at the DFT level of calculations. Since DFT tends to favor planar structures of Au clusters, the error of ~ 0.2 eV can not be presently excluded.

The above findings are particularly important for the study of the structural and electronic properties of bimetallic clusters. The key role of the polar hetero bonds and a charge transfer to the gold atoms is of crucial importance for structural properties of these systems as it will be shown in the following sections.

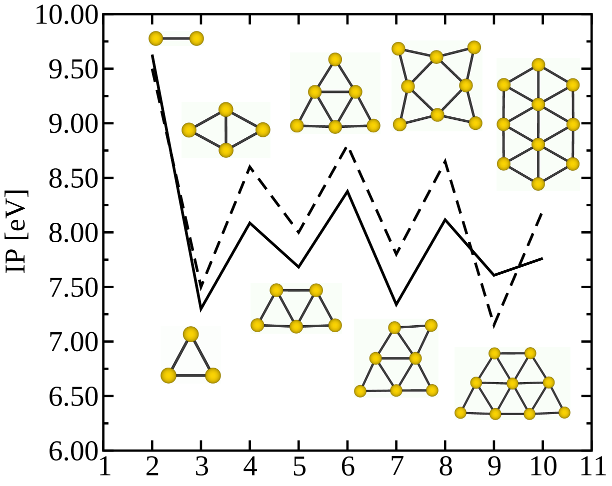

Figure 3.4: Calculated (full line) and experimental (dashed line, Ref. [173]) vertical ionization potentials and the most stable structures for Au_n(2-10).

3.4 Bimetallic charged and neutral gold-silver trimers, tetramers and pentamers

Due to the larger electronegativity of the Au atom the charge transfer occurs in bimetallic silver-gold systems leading to pronounced ionic character of the bonding. Consequently, in these systems Au atoms prefer positions which allow the largest charge transfer from silver to gold. In this work a detailed investigation of structural and ground state electronic properties of small bimetallic clusters has been carried out with the aim to establish the role of heteronuclear versus homonuclear bonding and to determine how their electronic properties can be tuned in order to influence their reactivity towards small inorganic molecules such as O_2, CO, NO, H_2O etc.

3.4.1 $Ag_mAu_n^{0,+,-}$ (m+n=3)

The structures of charged and neutral bimetallic trimers are summarized in Figure 3.5. In the anionic state both Ag_2Au^- and $AgAu_2^-$ are linear with gold atoms in peripheral positions. The linear structure is the most convenient one because it minimizes the repulsion of the excess electron localized at the ends of the chain. The energy ordering is the same in both RECP's. For neutral Ag_2Au the linear form with two hetero bonds is close in energy with the isosceles triangular structure in both RECP's although their energy ordering changes; the linear structure is more stable in 1e-RECP and the triangular one in 19e-RECP. In contrast, the neutral $AgAu_2$ assumes obtuse triangular form in both treatments. Cationic trimers Ag_2Au^+ and $AgAu_2^+$ have obtuse and isosceles triangular geometries with a positive charge localized at the silver atoms. The vertical ionization potentials and vertical detachment energies obtained from both 1e-RECP and 19e-RECP differ by 0.2-0.5 eV (cf. Table 3.2) and are in good agreement with available experimental data [161].

3.4.2 $Ag_mAu_n^{0,+,-}$ (m+n=4)

Structural and electronic ground state properties of bimetallic tetramers are presented in Figure 3.6. The tetramers represent an ideal system in which the transition from "metallic" system doped by the one Au-

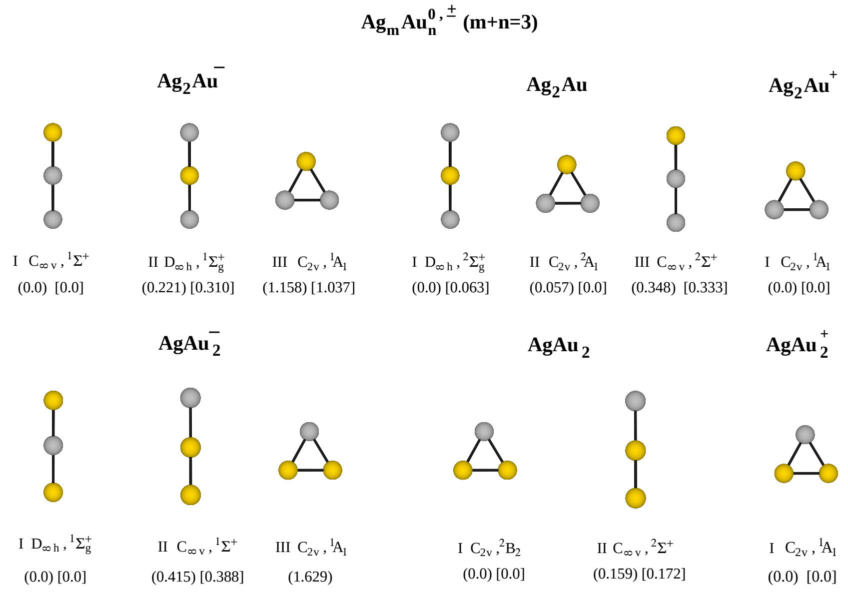

Figure 3.5: Structures of charged and neutral bimetallic trimers $Ag_mAu_n{}^{0,+,-}$(m+n=3) optimized at the 1e-RECP and 19e-RECP level of theory. The energy difference (in eV) with respect to the most stable structure obtained from the former and latter approach are given in the round and square brackets, respectively. I-III denote energy sequence of the isomers according to 1e-RECP results. Labels of the symmetry group and of the ground electronic state are also given.

Table 3.2: Vertical ionization potentials (IP_v) and vertical detachment energies (VDE) for Ag_mAu_n (m+n=2,3,4,5), Ag_nAu_n (n=3,4,5,10) and $Ag_{12}Au_8$ clusters obtained with 1e-RECP BLYP and 19e-RECP BP86 (in square brackets) methods.

Ag_mAu_n	IP_v (eV)	VDE (eV)	VDE(exp.)^a (eV)
AgAu	9.01 [8.95]	1.27 [1.72]	1.43
Ag_2Au	6.94 [6.71]	2.78 [3.09]	2.97
$AgAu_2$	6.73 [7.17]	3.47 [3.68]	3.86
Ag_3Au	7.14 [7.41]	1.56 [1.97]	1.66
Ag_2Au_2	7.87 [8.00]	1.62 [2.01]	1.62
$AgAu_3{}^b$(I) [II]	7.97 [8.02]	2.00 [2.17]	
$AgAu_3{}^b$(II) [I]		2.79 [3.02]	3.00
$AgAu_3{}^b$(III) [III]		3.13 [3.49]	
$AgAu_3{}^b$(IV) [IV]		2.72 [3.17]	
Ag_4Au	6.45 [6.76]	2.18 [2.47]	
Ag_3Au_2	6.71 [6.97]	2.44 [2.70]	
Ag_2Au_3	7.20 [7.37]	2.76 [3.02]	
Ag_1Au_4	7.41 [7.54]	2.98 [3.17]	
Ag_3Au_3	8.68 [8.49]	1.76 [2.13]	
Ag_4Au_4	8.44		
Ag_5Au_5	6.70		
$Ag_{10}Au_{10}$	6.37		
$Ag_{12}Au_8$	6.31		

[a] Experimental results from Ref. [161].
(I-IV), [I-IV] label isomers according to the energy sequence obtained with 1e-RECP and 19e-RECP, respectively.

atom to the ”ionic” AgAu-AgAu versus segregated Ag_2-Au_2 system back to the ”metallic” species doped by the one Ag-atom can be followed. All calculations have been performed using both 1e-RECP and 19e-RECP. This offered a good opportunity to check the reliability of the 1e-RECP approach which can be used to study much larger clusters, against the results obtained with 19e-RECP.

Bimetallic neutral and charged tetramers tend to assume rhombic structures with a number of hetero bonds determined by their composition. The gold atoms prefer exposed positions while the silver atoms form a maximum number of Ag-Ag bonds. Such topologies are convenient for a charge transfer from Ag to Au atoms and seem to be independent from the details of theoretical treatment.

In the stable structures of the anionic Ag_3Au^- and the neutral Ag_3Au clusters the Au atom is located at the long diagonal of the rhombus being doubly coordinated to Ag atoms in both RECP treatments. The energy ordering of the higher lying isomers of Ag_3Au^- (the linear and T-form) is more influenced by the details of the method. In contrast, for the neutral Ag_3Au the most stable structure is considerably lower in energy than all other isomeric forms, independent from the treatment (cf. Figure 3.6). In the case of the cationic Ag_3Au^+ tetramer, the 19e-RECP gives rise to two structures with almost equal energies in which the Au-atom is located at the long and the short diagonal of the rhombus, respectively. They contain the Ag_3^+ subunits with different geometries in which the positive charge is mainly located. The 1e-RECP inverses energy sequence of these two isomers (cf. Figure 3.6).

The stable structures of the anionic $Ag_2Au_2^-$ and the neutral Ag_2Au_2 tetramers assume rhombic forms with two Au atoms located at the long diagonal, thus favoring short distance Ag-Au and Ag-Ag bonds. This situation is convenient for charge transfer from Ag to Au atoms and simultaneously allows to minimize the repulsion of charges located at Au atoms. The global minimum of Ag_2Au_2 is well separated in energy from all other isomers, independent from the treatment. In contrast, in the case of the anionic $Ag_2Au_2^-$ cluster the 19e-RECP gives rise to small energy differences between the stable rhombic structure and other isomeric forms. Similarly, for the $Ag_2Au_2^+$ cluster, four isomers close in energy have been found. The structure with homonuclear bonding (Ag_2^+)-(Au_2) is in competition with the hetero bonded one due to the lack of one electron and the energy sequence is influenced by the treatment.

Finally, the structures of tetramers with a single Ag atom are characterized by a high coordination of Ag. For the neutral $AgAu_3$ and cationic $AgAu_3^+$ clusters the Ag atom is located at the short diagonal. In the case of the anion $AgAu_3^-$ the rhombic structure with the Ag atom at the short diagonal has almost the same energy as the T-form with the Ag atom in the central position at the 1e-RECP level of calculations. The 19e-RECP gives preference to the T-form with respect to the rhombic form. However, in both structures the Ag-atom is three-coordinated. It seems that the energy ordering of the isomers for the neutral species is less dependent on the theoretical treatment employed than for the charged systems.

The calculated IP’s and VDE’s are given in Table 3.2. The values of VDE’s for the stable rhombic structures of Ag_3Au^- and $Ag_2Au_2^-$ obtained from 1e-RECP are in excellent agreement with the experimental data [161], while the VDE’s obtained from the 19e-RECP are higher than the measured ones. In the case of $AgAu_3^-$ the VDE value for the T-form is considerably closer to the experimental finding [161] than the one for the rhombic structure, thus the 19e-RECP gives rise to an excellent agreement with experimental data [161].

In conclusion, the determination of structural properties of the neutral bimetallic tetramers is not dependent on the inclusion of d-electrons, but for the charged tetramers the influence of d-electrons on energy sequence of isomers might take place. However the general trend concerning structural properties of bimetallic tetramers remains the same in both treatments. The Au atoms prefer hetero bonding than

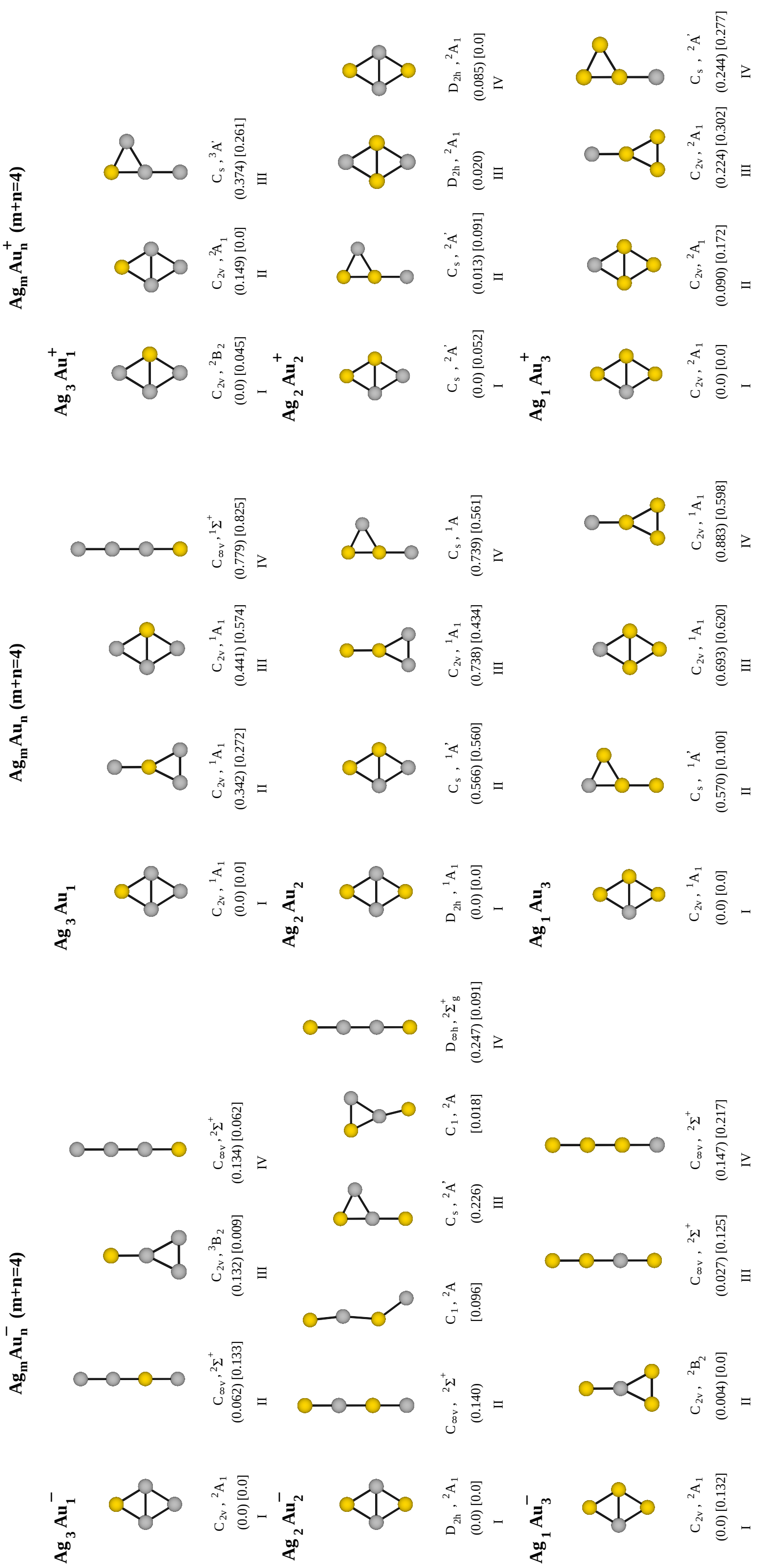

Figure 3.6: Structures of charged and neutral bimetallic tetramers $Ag_mAu_n{}^{0,+,-}$(m+n=4) optimized at the 1e-RECP and 19e-RECP level of theory. The energy difference with respect to the most stable structure obtained from the former and the latter approach are given in the round and square brackets, respectively. I-IV denote energy sequence of the isomers according to 1e-RECP BLYP results. Labels of the symmetry group and of the ground electronic states are also given.

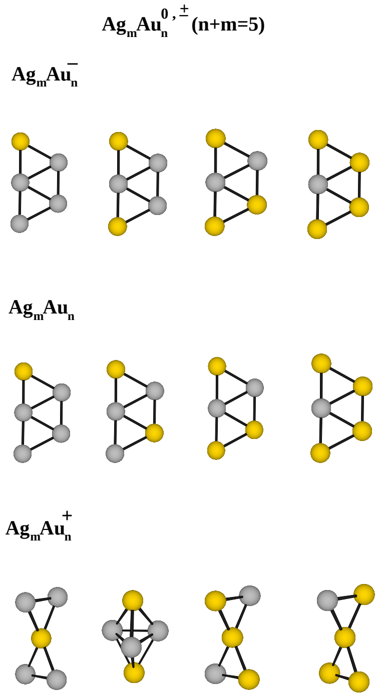

Figure 3.7: The most stable structures of charged and neutral bimetallic pentamers $\mathrm{Ag}_m\mathrm{Au}_n^{0,+,-}$ obtained from 1e-RECP BLYP method.

the homo-nuclear bonding and tend to take peripheral positions in order to withdraw charge from Ag atoms which are therefore higher coordinated.

3.4.3 $\mathbf{Ag}_m\mathbf{Au}_n^{0,+,-}$ (m+n=5)

Stable structures of anionic and neutral bimetallic pentamers assume planar trapezoidal structures with triangular subunits, in contrast to the cationic stable structures which prefer 3D-forms as shown in Figure 3.7. Due to a very large number of possible structures only the most stable structures are shown. The calculations using the 19e-RECP have been carried out only for the cases for which the energies of the stable structures are very close to those of the other isomers. Both treatments give rise to the equivalent stable structures as shown in Figure 3.7.

In all anionic and neutral stable trapezoidal structures of pentamers one Ag atom remains four-coordinated, independent from the composition. In fact the common structural properties of anionic and neutral pentamers concerning positions of hetero atoms are present with exception of $\mathrm{Ag}_3\mathrm{Au}_2^-$ and $\mathrm{Ag}_3\mathrm{Au}_2$ as can be depicted from Figure 3.7. Even in this case Au atoms prefer hetero bonding, which means that no segregation between the silver and the gold subunits occurs for the compositions (3+2) and (2+3).

The stable structures of cationic bimetallic pentamers tend to deviate from planarity. The lowest energy structures of $\mathrm{Ag}_4\mathrm{Au}^+$, $\mathrm{Ag}_2\mathrm{Au}_3^+$ and AgAu_4^+ assume double triangular forms sharing the Au atom. In the case of $\mathrm{Ag}_3\mathrm{Au}_2^+$ the trigonal bipyramid with peripheral positions of Au atoms competes in energy with the double triangular form.

3.4.4 Neutral bimetallic silver-gold $\mathbf{Ag}_n\mathbf{Au}_n$ (n=3,4,5,10) and $\mathbf{Ag}_{12}\mathbf{Au}_8$ clusters

In this section the study of the bimetallic clusters with equal number of silver and gold clusters is presented. The aim is to find out the preference for charge transfer in different structural patterns which include a maximal number of hetero bonds and segregation or embedding of two components and to determine the ionic character of the structures. The other aspect of this investigation is connected with the transition from 2D to 3D structures which occurs for one-component systems at different cluster sizes. For the neutral clusters Ag_7 assumes the 3D pentagonal bipyramid form and gold clusters are planar up to ten atoms as shown in Section 3.3. In addition to systems with equal number of silver and gold atoms the investigation of the $Ag_{12}Au_8$ cluster serves as a model for studying embedding of Au_8 in the surrounding of silver atoms in connection with the possible reactivity of bimetallic species.

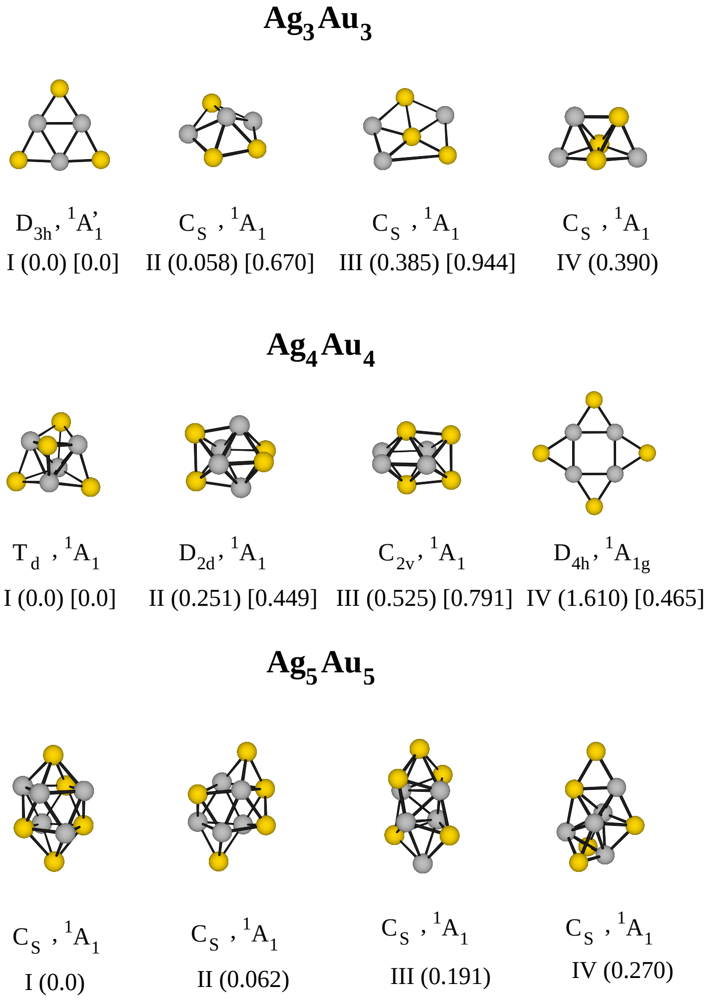

Figure 3.8: Structures of neutral bimetallic Ag_3Au_3, Ag_4Au_4 and Ag_5Au_5 clusters optimized at 1e-RECP and 19e-RECP level of theory. The energy differences with respect to the most stable structure (in eV) obtained from the the former and latter approach are given in round and square brackets, respectively. I-IV denote the energy sequence of isomers according to 1e-RECP BLYP results. Labels of the symmetry group and the ground electronic states are also given.

The results for Ag_3Au_3 and Ag_4Au_4 and Ag_5Au_5 are presented on Figure 3.8. Ag_3Au_3 and Ag_4Au_4 systems have been calculated using the 1e-RECP and 19e-RECP approaches while Ag_5Au_5 has been calculated only at the 1e-RECP level due to the size and large number of possible isomers. The most stable structure of the Ag_3Au_3 is the planar triangular form with negatively charged Au atoms located at the peripheral position independent from the treatment. The pentagonal pyramid and tetrahedral type of structures with different locations of hetero atoms have been investigated systematically at the 1e-RECP level. Several 3D-structures optimized with 19e-RECP are shown in Figure 3.8, but all of them have also substantially higher energies than the planar Ag_3Au_3. In contrast, the Ag_4Au_4 assumes 3D tetrahedral type of structure with negatively charged Au atoms located at the outside tetrahedron capping the inner silver tetrahedron and forming hetero bonds. Again systematic investigation of different 3D and 2D structures has been carried out with the 1e-RECP and energy ordering of several structures was checked against 19e-RECP results as shown in Figure 3.8. All of them lie energetically above the bimetallic T_d structure. The pure Ag_8 assumes also the T_d structure in contrast to the planar form of Au_8. In other words the hetero bonding influences substantially the structural properties of the gold octamer. Since the s-d separation in bimetallic systems is substantially larger than in the pure Au clusters, as evidenced by analysis based on DFT density of states (DOS), the structural properties of Ag_4Au_4 are closer to the ones obtained for Ag_8. Moreover the "ionic" nature of Ag_3Au_3 and Ag_4Au_4 is evidenced by large values of ionization potentials given in Table 3.2 .

After the transition to 3D-structures has been determined, 1e-RECP for larger systems which are computationally more demanding has been employed. Since the stable structure of Ag_4Au_4 is closer related to the structure of the silver than of the gold octamer the optimization of Ag_{10} and Ag_{20} has first been carried out and the corresponding structures were used as starting point for consideration of the bimetallic structures. A systematic investigation of Ag_5Au_5 has been carried out by placing Au atoms at different positions searching for the segregation between two components versus other patterns, e.g. such as achieving the largest charge transfer to the Au atoms. The latter proved to be more successful. The lowest energy structure found for Ag_5Au_5 is a deformed bicapped antiprism with a chain of Au atoms at the peripheral positions attracting the negative charge as shown in Figure 3.8. Other structures with segregation pattern or with larger number of hetero bonds have substantially higher energies. Correspondingly, the value of IP_v for Ag_5Au_5 is considerably lower than the one obtained for the T_d structure of Ag_4Au_4 with the maximum number of hetero bonds (cf. Figure 3.8).

For the bimetallic $Ag_{10}Au_{10}$ cluster structures with lowest energies contain Au atoms distributed in the icosahedral subunit of the deformed C_3 structure as shown in Figure 3.9. The three structures labeled by I, II and III are close in energy and they differ only in differently placed Au atom(s) within icosahedral subunit. The structure labeled by IV contains one Au atom outside the icosahedra and has by 0.2 eV higher energy with respect to the structure I. The lowest energy structure exhibits the largest charge transfer from the silver- to the gold-atoms. All Au atoms except of the central one have a negative charge while Ag atoms are positively charged. The Au_{10} subunit with one central atom is embedded in the surrounding of Ag atoms.

This pattern remains valid for the lowest energy structure found for $Ag_{12}Au_8$ as shown in Figure 3.9. In this case the Au_8 assumes the pentagonal bipyramidal structure capped by one atom and is also a part of an icosahedral subunit. All Au surface atoms are negatively charged. This Au_8 subunit embedded in Ag_{12} represents a good candidate for the reactive center, since three exposed Au atoms labeled by 1, 2 and 3 in Figure 3.9 have convenient positions to react with molecules. In fact such three-atomic facet of Au_8 have also been found in the model calculations of gold clusters supported on magnesia and used for the reactivity study with O_2 and CO molecules [10]. Notice that the structure II in Figure 3.9, which does not contain Au_3- facet has by ~ 0.13 eV higher energy than the structure I. In the structure III, which has even higher energy, one Au atom lies outside the icosahedral subunit. This indicates that the lowest energy structure I of $Ag_{12}Au_8$ represents an interesting model for studying the reactivity of bimetallic clusters.

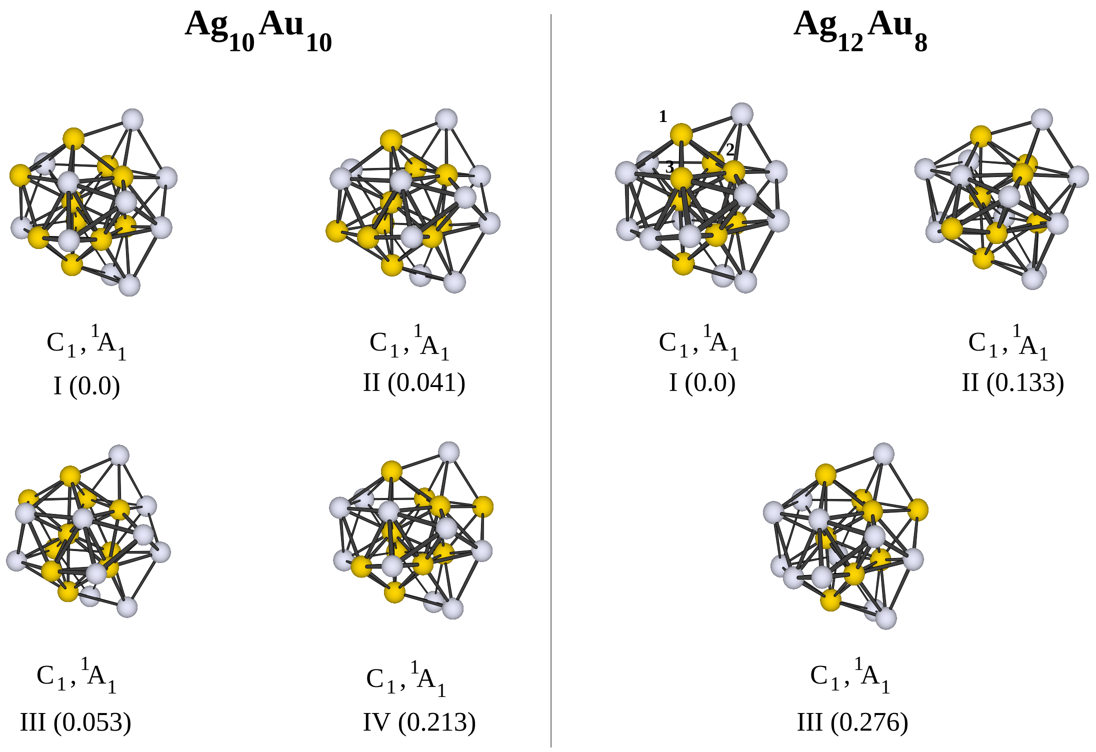

$Ag_{10}Au_{10}$

$C_1, {}^1A_1$
I (0.0)

$C_1, {}^1A_1$
II (0.041)

$C_1, {}^1A_1$
III (0.053)

$C_1, {}^1A_1$
IV (0.213)

$Ag_{12}Au_8$

$C_1, {}^1A_1$
I (0.0)

$C_1, {}^1A_1$
II (0.133)

$C_1, {}^1A_1$
III (0.276)

Figure 3.9: Optimized structures of $Ag_{10}Au_{10}$ and $Ag_{12}Au_8$ clusters at 1e-RECP level of theory with relative energy differences in brackets.

3.5 Electronic properties of bimetallic silver-gold clusters in context of their reactivity

Since the reactivity of metallic clusters with small molecules such as CO and O_2 is correlated with the IP and VDE values [11, 12] the influence of doping of pure gold clusters with Ag atoms on the VDE and IP values has been studied. This is particularly important in the case of binding of O_2 which according to the frontier orbital model occurs through electron transfer from the cluster into the empty π^*orbital of molecular oxygen. Therefore, it can be expected that the clusters with lower VDE values bind and activate stronger molecular oxygen. As can be seen from Figure 3.10 by varying the composition of clusters the VDE's and IP's can be tuned in a broad range, allowing to tune their capability to bind cooperatively CO and O_2 species.

The VDE values plotted in Figure 3.10 decrease with increasing number of Ag atoms and agree well with experimental data [161]. Anionic tetramers with odd number of electrons have lowest VDE values. A particular, almost anomalous decrease occurs for $Ag_2Au_2^-$ species with "ionic" character due to maximum number of hetero bonds and large transfer from Ag to Au atoms. Since it is experimentally known that clusters with low VDE's bind strongly molecular oxygen it can be concluded that this will be the case for $Ag_2Au_2^-$, $AuAg_2^-$, and Ag_4^-. The IP values shown in Figure 3.10 decrease with increasing number of Ag atoms as well. The largest values for IP have been calculated again for tetramers and in particular for Au_4, Au_3Ag and Au_2Ag_2 clusters. Bonding of CO molecule on transition metals is due to cooperative effects of σ-donation and $\pi-$back donation. Since s-electrons dominate bonding in bimetallic tetramers and in Au_4 with high IP values it is to expect that CO will act as σ donor and therefore bind stronger to these species. Therefore, proper combination of low VDE and high IP values may induce cooperative binding of O_2 and CO.

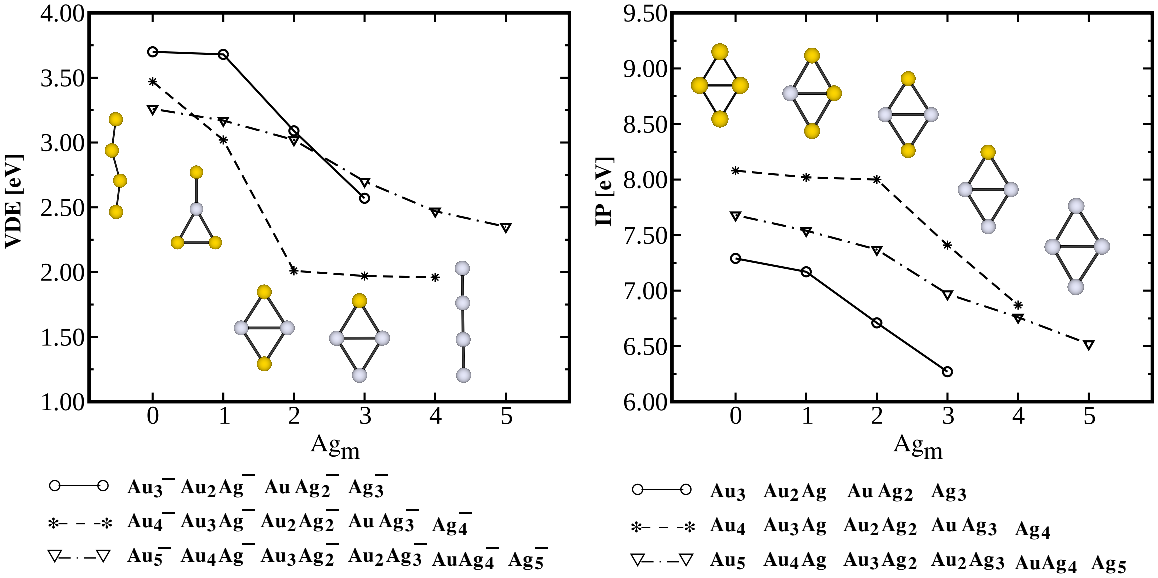

Figure 3.10: Calculated VDE and IP values for Au_nAu_m(n+m=3,4,5) varying the number of Ag atoms m.

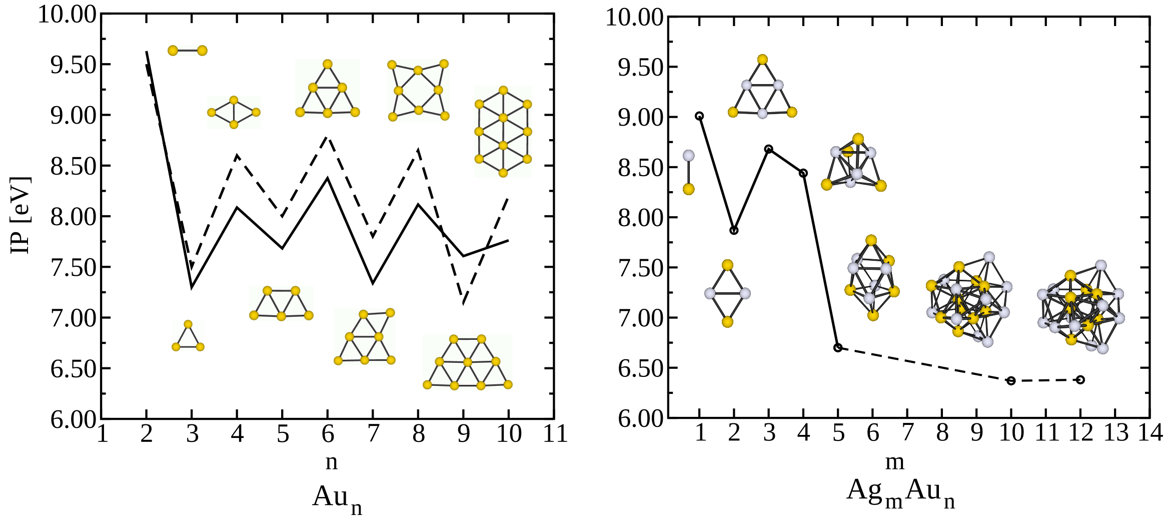

Figure 3.11: (Left side) Calculated (full line) and experimental (dashed line, Ref. [173]) vertical ionization potentials and the most stable structures for Au_n(2-10). (Right side) Vertical ionization potentials and structures for Ag_mAu_m(m=1-5).

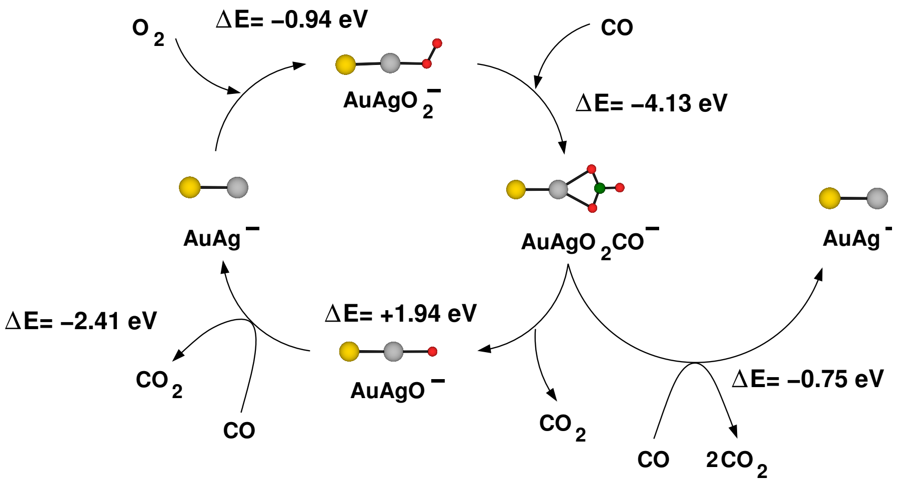

Figure 3.12: Catalytic cycle for the oxidation of CO on $AgAu^-$ dimer.

Values of IP's for the clusters with equal numbers of silver and gold atoms and comparison with those calculated for the pure clusters are shown in Figure 3.11. The IP's for Ag_3Au_3 and Ag_4Au_4 assume higher values than for Au_6 and Au_8 in contrast to what is expected, indicating pronounced ionic character of the bonding in these systems, since the Ag-component by itself should significantly decrease the IP values. Another interesting feature which can be inferred from Figure 3.11 is the transition from the "ionic" structures characterized by a large gap between the occupied and unoccupied orbitals to the "metallic" structures with a low gap and low ionization potentials. This transition occurs for Ag_5Au_5 and low ionization potentials remain also for $Ag_{10}Au_{10}$ and $Ag_{12}Au_8$ in which partly negatively charged gold subunits are embedded in the Ag surrounding.

3.6 Reactivity of $AgAu^-$ dimer towards CO and O_2

Bimetallic anionic dimer was chosen as a model system in order to study the catalytic oxidation of CO and to investigate the role of the charge transfer on the catalytic activity of silver-gold clusters. It is expected that the charge transfer can promote catalytic activity and, as shown in the previous section, varying the composition of the clusters may offer the possibility to influence their reactivity more easily than in the case of pure clusters. As presented in Figure 3.12 binding of molecular oxygen is exothermic by -0.94 eV. The corresponding complex has silver atom bound to an oxygen atom of the superoxide unit. The binding of the molecular oxygen to the gold atom leads to the complex which is by 0.61 eV less stable. Since oxygen withdraws very strongly the charge from metal atoms, binding to gold is energetically unfavorable because gold tends to keep negative charge due to its larger electronegativity. This feature might change for larger systems with adequate composition of hetero atoms. In the next step the complex $AuAgO_2^-$ can react with one CO molecule giving rise to the very stable complex with a carbonate-like unit bound to one silver atom. Once the complex is formed there are two possible pathways to close the catalytic cycle. In the first one the complex reacts with one CO molecule generating two CO_2 molecules and restoring the $AgAu^-$ dimer which therefore acts as a catalyst. This bimolecular reaction is exothermic by -0.75 eV. The second possible pathway is a unimolecular dissociation which is endothermic by 1.94 eV and gives rise to one CO_2 molecule and to highly reactive $AgAuO^-$ species . The latter reacts then with one CO molecule giving CO_2 in an exothermic process of -2.41 eV, allowing to close the catalytic cycle.

3.7 Conclusions

The theoretical study of structural and electronic properties of pure gold clusters in the range from two to ten atoms has revealed that these clusters assume 2D structures due to the s-d hybridization which favors more directional bonding and which is caused by the lowering of the s-d energy gap due to pronounced relativistic effects. The structure assignment proposed in this work is supported by the measured vertical ionization potentials. For bimetallic silver gold clusters the charge transfer from silver to gold plays a significant role for structural properties and the degree of s-d hybridization lies between the low one for Ag and the large one for Au. General pattern in small bimetallic clusters $3 \leq n+m \leq 5$ is that Ag atoms prefer to form more bonds than Au atoms and Au atoms prefer positions which maximize the charge transfer. Also, formation of hetero bonds is more favorable than of homo bonds as shown for Ag_mAu_n(n=2,3,4) giving rise to “ionic” species with high ionization potentials. Generally, structural properties of bimetallic clusters are more related to the structures of pure Ag- than of pure Au-clusters. In the case of larger bimetallic clusters such as $Ag_{12}Au_8$ and $Ag_{10}Au_{10}$ there are small negatively charged subunits present which might serve as reactive centers similarly to gold clusters supported on metal oxides. The theoretical predictions for the structures of mixed cationic clusters as well as the role of the charge transfer have been recently fully confirmed experimentally by Kappes and coworkers [166]. The reactivity aspect of bimetallic clusters has been illustrated on the example of the catalytic oxidation of CO with O_2 on $AgAu^-$ dimer. In summary, it has been shown that bimetallic silver-gold clusters have own interesting properties which can be important for reactivity studies.

Chapter 4

Reactivity of gold and silver anions towards oxygen

4.1 Introduction

The discovery that gold clusters prepared on oxide supports show a pronounced size- and support-dependent low temperature catalytic activity [9] and the fact that supported silver particles play an important role in industrial ethylene oxidation processes involving molecular oxygen [181] has led to increased number of cluster studies. Their aim was to determine how the reactivity of gas-phase clusters towards reactant gases such as O_2 and CO depend on the size, structure and electronic properties. The experimental studies of the reactivity of anionic gold and silver clusters with O_2 [11, 182, 183, 184] have found that the O_2 molecule binds only to the anionic clusters with even number of atoms while the clusters with odd number of atoms are inactive towards O_2 adsorption. Moreover, for clusters with even number of atoms no multiple adsorption of molecular oxygen has been observed. The reactivity correlates well with the measured electron affinities [185] and can be understood using a simple frontier orbital model. According to this model, the O_2 molecule may be considered as one electron acceptor and the binding of molecular oxygen occurs via the electron transfer from the cluster to the π^* MO of O_2. Therefore, for those clusters with an unpaired electron in their HOMO (even number of atoms and low electron affinities) a strong binding with O_2 occurs and for those with a closed shell electronic structure (odd number of atoms and high electron affinities) no binding occurs.

The studies of supported gold catalysts have revealed that traces of moisture are essential in order for the optimal activity of the catalysts to be achieved [13, 14, 15]. The possible explanation for this finding is that water assists in the dissociation of molecular oxygen. However, it is also possible that water's role is to maintain the appropriate termination of the oxide support. Up to date the role of the gold cluster versus the role of the support in the catalysis is still unclear. In order to investigate these different contributions to the catalytic activity a separate understanding of the activity of selected gas-phase gold clusters towards molecules of interest (O_2, CO etc.) in the presence of water is the first step to be achieved. A full oxidation cycle under low reactant coverage conditions has been observed experimentally on gold cluster anions as small as Au_6^- in fast-flow reactor experiments [186]. However, the question of the role of moisture in enhancing the CO oxidation activity of the supported gold clusters has yet to be addressed in gas-phase studies. The presence of H_2O derived adsorbates could significantly alter the O_2 adsorption activity and mechanism. Therefore in this work the adsorption of O_2 on hydrated gold clusters has been studied [16]. In this case the experiments show that the most abundant species have the composition Au_nOH^- and the strong electron withdrawing OH group causes the reactivity of anionic gold clusters to be inverted making gold clusters with odd number of atoms reactive toward binding of molecular oxygen.

Due to the fact that silver has lower electronegativity than gold the binding of the weaker electron acceptor groups than OH can activate them for the adsorption of molecular oxygen. Specifically, in this work it has been shown theoretically and confirmed experimentally that the binding of one oxygen molecule on anionic silver clusters may induce cooperative binding of the second oxygen molecule [17]. Another important issue concerns the molecular versus dissociative adsorption of O_2. It is known that adsorption of O_2 on Pt-group metals leads to the dissociation and that metal bound oxygen atoms are responsible for the activity in the oxidation of CO [187]. Recent experimental studies using photoelectron spectroscopy indicate that the oxygen is bound molecularly to all anionic gold clusters except anionic gold monomer Au^- [188]. In spite of many recent valuable experimental and theoretical contributions, the question remains, whether molecular or dissociated oxygen provides the mechanism for the oxidation of CO. In this work, a joint theoretical and experimental effort [189] will be briefly presented whose aim was to study the binding of oxygen to the atomic gold anion and the oxidation of CO on the on AuO^-.

4.2 Experimental methods

In order to study experimentally the reactivity of hydrated gold clusters near-atmospheric pressure flow reactor technique has been used [16]. It should be pointed out that the experiments have been carried out using heavy water (D_2O) in order to be able to distinguish complexes with water from hydroxylated clusters. Charged gold clusters are formed and equilibrated by laser vaporization of a rotating and translating gold rod in a high-pressure helium/D_2O stream, produced using a pulsed valve with a stagnation pressure of approximately 3.5 bar. In addition, the helium gas is bubbled through D_2O and is saturated with water vapor. The clusters are then exposed to a gas pulse from a secondary pulse valve containing a dilute reactant gas and expanded into vacuum. For detection of the reaction products a time-of-flight mass spectrometer with perpendicular pulsed extraction fields has been used. In order to control the temperature of the experiment a cooling sleeve (and heater) are added to the reactor so that the reaction temperature can be adjusted in the range from 220 K to 330 K.

In the experimental investigation of the reactivity of anionic silver clusters with O_2 a guided ion beam apparatus has been employed [190]. Mass selected silver cluster anions are allowed to react with molecular oxygen in a radio frequency (rf)-octopole ion trap. The trap is filled with about 1 Pa of helium buffer gas and a small partial pressure of oxygen. The temperature control inside the ion trap (20-300 K) is achieved via a closed cycle helium cryostat attached to the trap enclosure. The storage time of the ions defines the reaction time t_R after which all product ions are extracted and mass analyzed with a quadrupole mass spectrometer. The recorded product ion concentrations as a function of t_R allow to determine the rate constants and fit the reaction mechanism.

The reactions between AuO^- and CO have been studied experimentally using a fast flow mass spectrometer coupled to a laser vaporization source [191, 192]. Gold clusters were formed in a laser vaporization source by passing a continuous flow of oxygen seeded in helium over the metal plasma. This experimental setup enables the facile dissociation of oxygen molecules and the formation of clusters with dissociated oxygen which are not accessible in experiments involving the interaction of thermalized gold cluster anions with O_2 due to high barriers for the dissociation. The formed clusters exit the source region into the flow tube where the CO is introduced in varying amounts downstream at a reactant gas inlet. Once formed, most of the reaction products and the helium buffer gas are pumped away by a high volume roots pump. Those species that are not pumped off are sampled and focused by a set of electrostatic lenses into the quadrupole mass spectrometer where they are analyzed.

4.3 Theoretical methods and accuracy

Several theoretical studies dealing with the adsorption of molecular O_2 on anionic gold clusters based on density functional theory have been presented recently [193, 194, 195, 196]. These studies generally reproduce the trends of the reactivity with odd-N clusters showing much lower binding energies than even N-clusters due to a stable closed shell electronic structure. However, compared to the experimental dissociation-binding energy estimates, the theoretical binding energies for O_2 to the even-N clusters are systematically higher in the literature and significant ($\sim$ 0.5 eV) binding energies are even seen on the odd-N clusters [195, 196] which, however, have not been observed experimentally. In this work, DFT method with Becke's hybrid three-parameter nonlocal exchange functional combined with the Lee-Yang-Parr gradient corrected functional [85, 86, 89] has been used. For gold and silver 19e-RECP from Stuttgart group with the [9s7p5d1f/7s5p3d1f] and [8s7p6d1f/6s5p3d1f] AO basis set for gold and silver atoms, respectively, have been employed [174]. For oxygen and hydrogen atoms the 6-311G(d,p) triple-ζ split valence basis set has been used [197, 198].

To check the accuracy of the method calculated binding energies for small anionic gold clusters toward molecular oxygen have been compared with experimental data obtained from collision-induced dissociation (CID) studies of Lee and Ervin [199]. In the case of $Au_2O_2^-$ complex, the calculated binding energy of 1.06 eV is in excellent agreement with the CID dissociation threshold of 1.01±0.14 eV. For $Au_4O_2^-$ a dissociation threshold of 0.74 eV, which includes also the barrier, is in acceptable agreement with the CID result of 0.91±0.14 eV, while the calculated binding energy has the value of 0.64 eV. The latter value is also in agreement with the experimentally estimated binding energy of 0.5 eV for $Au_4O_2^-$. For species with even number of electrons such as $Au_3O_2^-$ and $Au_5O_2^-$ the binding energies of 0.015 eV and -0.06 eV have been calculated consistent with the fact that those species have not been seen in experiments [11, 182, 183, 184]. The tests performed show that proper treatment of the exchange part of the density functional combined with an accurate basis set is crucial for realistic description of the bonding between gold and oxygen. All non-hybrid density functionals tested show a tendency to give systematically too large binding energies (about 0.3 eV) while the hybrid functionals which include exact exchange give rise to binding energies whose accuracy is at comparable level as the much more demanding coupled cluster method. The structures presented in this work have been fully optimized using gradient-based minimization methods, and the character of the stationary points has been checked by performing harmonic vibrational analysis. The electron transfer from the clusters to the oxygen has been analyzed using natural bonding orbitals (NBO) analysis [200]. The reaction mechanism of the CO oxidation on AuO^- has been studied by performing ab-initio MD using forces calculated with the B3LYP method. This enabled to study the reaction mechanism in greater detail and to obtain basic information on the time scales of the processes involved as well as the energy dependence of the studied reaction channels.

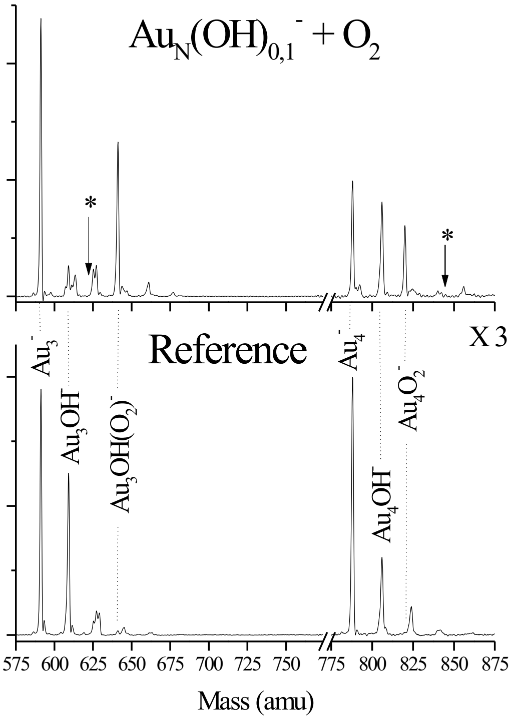

Figure 4.1: (Bottom) Mass spectrum of negatively charged gold clusters, Au_n^- and various hydrates of the form $Au_n(OH)_{0,1,2}(H_2O)_{0,1,2}^-$ generated by adding H_2O into the buffer gas of the cluster source and the secondary gas pulse is temporally offset from the main cluster pulse corresponding to the situation where no reactant gas (O_2) has been added. (Top) Mass spectrum obtained when the secondary gas pulse containing ~20% O_2:He is temporally overlapped with the main pulse. In addition to the depletion of the Au_4^- peak and Au_3OH^-, peaks appear at 32 amu higher mass, corresponding to the O_2 adsorption.

4.4 Results

4.4.1 Hydrated gold cluster anions Au_nOH^-

In the experiments performed with the aim to determine the influence of water on the adsorption activity of anionic gold clusters towards molecular oxygen the Au_nOH^- species have been observed as dominant products. In addition, with much weaker intensity hydrates of the form $Au_nOH^-(H_2O)_{1,2}$ have also been detected. The typical mass spectra obtained for Au_3^- and Au_4^- are shown in Figure 4.1. The structural and electronic properties of the Au_nOH^- clusters have been systematically investigated using methods described in Section 4.3. The optimized structures are shown in Figure 4.2 and properties are summarized in Table 4.1.

In all cases, the OH group is bound at a peripheral position analogously as previously found for bonding of the O_2 molecule on small anionic gold clusters [194]. However, the binding energies for the OH group are considerably higher than for O_2 due to the higher electron affinity of the OH group. The binding energies for complexes with the OH group and with molecular oxygen exhibit even-odd oscillations, with much higher absolute values for the former ones as shown in Figure 4.3.

As a consequence, in contrast to the O_2 complexes the anionic OH^- complexes with an odd number of Au atoms become also stable and have been detected experimentally. Of course, the complexes with even number of gold atoms are particularly stable. In the case of Au_2OH^- species, the binding energy

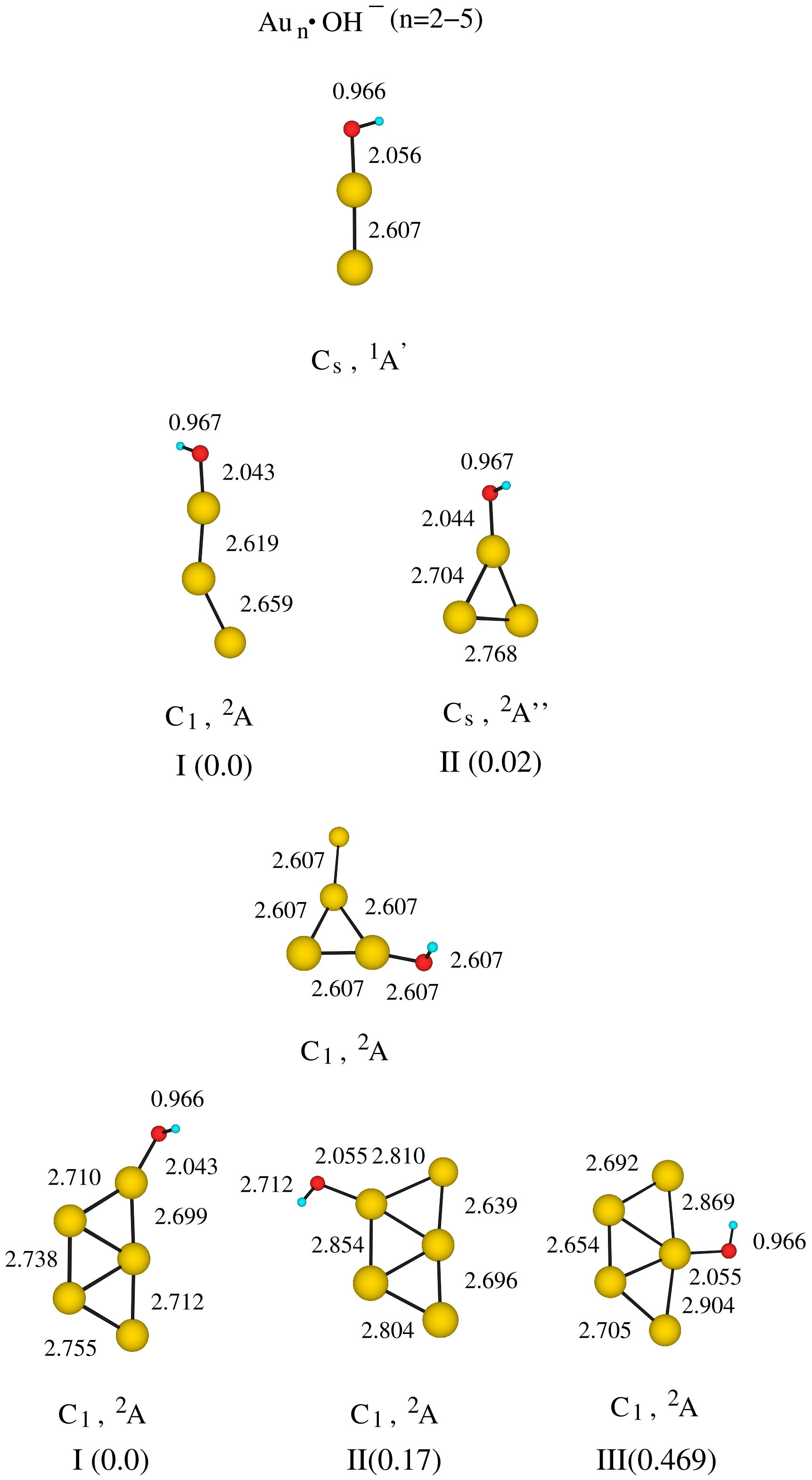

Figure 4.2: Optimized structures of the Au_nOH^- complexes (n=2-5). For the Au_5 system, ΔE values (in eV) for different isomers are given in parentheses. Oxygen and hydrogen atoms are labeled by large red and small blue circles, respectively. Isomers corresponding to the local minima whose relative energies are less than 1 eV with respect to the most stable structure are shown.

Table 4.1: Ground state energies and properties of optimized Au_nOH^-(n=2-5) clusters obtained with the B3LYP method.

Au_nOH^- n=2-5	Symm.(State)	Energy a.u	ΔE^a eV	E_b^b eV	NBO Charge Au_n	OH
Au_2OH^-	C_s ($^1A'$)	-347.514326		3.16	-0.35	-0.65
$Au_3OH^-(I)$	C_1 (^2A)	-483.314557		1.84	-0.63	-0.37
$Au_3OH^-(II)$	C_s (^2A”)	-483.313657	-0.02			
Au_4OH^-	C_1 (^1A)	-619.158765		3.00	-0.38	-0.62
Au_5OH^-(I)	C_1 (^1A)	-754.961885		2.30	-0.65	-0.35
Au_5OH^-(II)	C_1 (^1A)	-754.955443	-0.17			
Au_5OH^-(III)	C_1 (^1A)	-754.944645	-0.47			
$Au_2O_2^-$	C_1 (^2A)	-422.054480		1.06		
$Au_3O_2^-$	C_1 (^3A)	-557.869781		0.015		
$Au_4O_2^-$	C_1 (^2A)	-693.694330		0.64		
$Au_5O_2^-$	C_{2v} ($^3A_2$)	-829.497109		-0.06		

^{a}Energy difference with respect to the most stable structure. ^{b}Binding energy for the Au_nOH^- complexes is defined by E_b=E(Au_nOH^-)-E(Au_n^-)-E(OH), and for the $Au_nO_2^-$ complexes as E_b=E($Au_nO_2^-$)-E(Au_n^-)-E(O_2)

is -3.16 eV and a significant amount of electron transfer from the gold subunit to the OH group takes place, as can be seen from calculated natural charges (NBO) in Table 4.1. In this case the total charge on the cluster subunit is only -0.35e while the OH group carries -0.65e of charge. In contrast, the binding energy for the O_2 molecule to the Au_2^- dimer is significantly lower, with a value of 1.06 eV. Since the Au_3^- cluster has an even number of electrons, it is expected that the binding towards O_2 and OH group will be much weaker. While the complex with O_2 is not bound, the Au_3OH^- species is very stable, with the binding energy of 1.84 eV. The structures with the two lowest isomers with almost degenerate energies are shown in Figure 4.2. In the lowest energy isomer, the OH group is bound at the peripheral atom of the almost linear structure, while in the second isomer the OH group is bound to the triangular gold subunit. Weaker bonding in Au_3OH^- is also reflected in a significantly smaller amount of electron transfer to the OH group than in the case of Au_2OH^-. In fact, the charges on the two subunits are almost exactly inverted in comparison to the Au_2OH^- with -0.63e on the Au_3 subunit and -0.37e on the OH group. In the stable structure of the Au_4OH^- complex, the gold subunit assumes the T-form and the OH group is bound to a gold atom that is part of the triangular subunit. The binding energy of 3.16 eV is close to that of Au_2OH^- and the negative charge is again mainly localized at the OH group (-0.62e). At the same time, the binding energy towards O_2 is considerably lower (0.64 eV) due to a lower electron affinity than in the case of OH. The most stable structure of Au_5OH^- has a planar trapezoidal Au_5 subunit with the OH group placed at the peripheral position, which is most convenient to withdraw the charge from the two coordinated Au atoms. In other higher energy isomers shown in Figure 4.2 the OH group is attached to the three- and four- coordinated gold atom with less negative charge, respectively. The binding energy of Au_5OH^- is larger than in the case of Au_3OH^- and the charge transfer is again considerably reduced with respect to the complexes with an even number of gold atoms. The complex with molecular oxygen $Au_5O_2^-$ is not bound (-0.06 eV). The comparison of the binding energies for Au_nOH^- and $Au_n(O_2)^-$ complexes is shown in Figure 4.3.

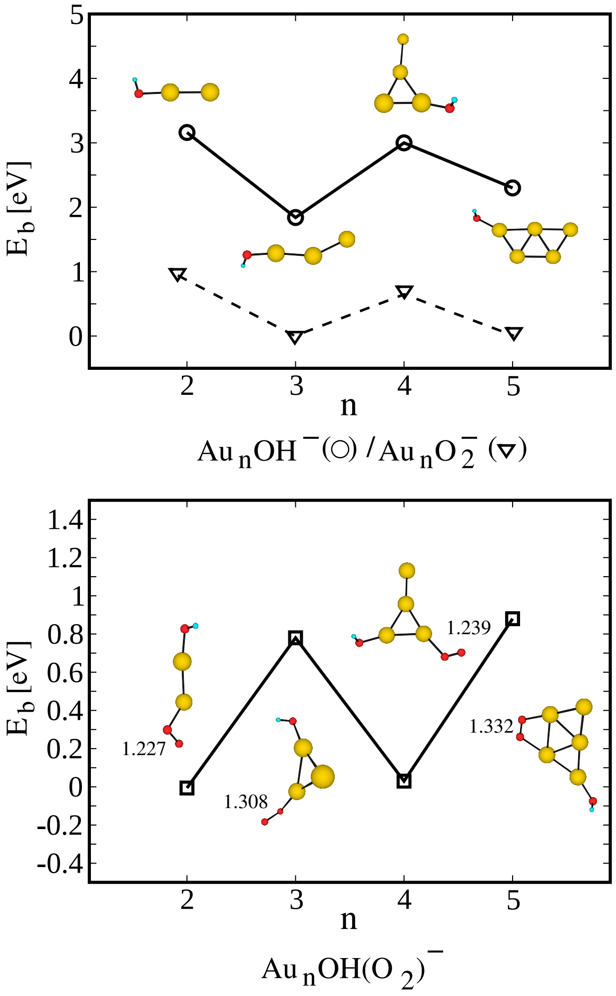

Figure 4.3: (Top) Binding energies of O_2 (triangles) and OH (circles) on Au_n^- clusters (n=2-5). (Bottom) O_2 adsorption energies on Au_nOH^- clusters.

4.4.2 Adsorption of molecular oxygen on hydrated gold cluster anions $Au_nOH(O_2)^-$

The adsorption of molecular oxygen on the Au_nOH^- clusters has been studied experimentally by introducing a secondary gas pulse containing dilute O_2: He and overlapping with the main cluster pulse. As can be seen from the experimental mass spectra in Figure 4.1 introducing O_2 results in depletion of several peaks in the mass spectrum as well as the growth of new peaks at 32 amu higher mass. For the even-n clusters, O_2 addition proceeds as expected, with the adsorption of a single molecule on the bare clusters as in

$$Au^-_{n(even)} + O_2 \rightarrow Au_{n(even)}O_2^- . \tag{4.1}$$

For the odd-n clusters, rather surprising results occur. Due to the fact that only weak binding is calculated for $Au_{n(odd)}O_2^-$ it is not surprising that no complexes of this type are observed experimentally. However, for odd-n Au_nOH^- clusters rather surprising results showing adsorption of a single O_2 molecule according to

$$Au_{n(odd)}OH^- + O_2 \rightarrow Au_nOH(O_2)^- \tag{4.2}$$

have been observed. In contrast for $Au_{n(even)}OH^-$ no O_2 adsorption activity is detected. This can be

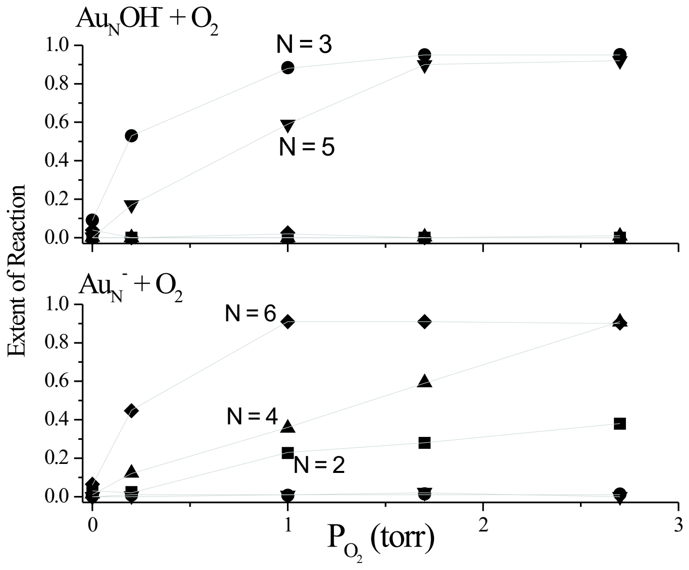

Figure 4.4: Cluster size dependence of the extent of reaction as a function of the partial pressure of O_2 in the reactor.

clearly seen in Figure 4.1 where after addition of molecular oxygen the peak corresponding to Au_3OH^- disappears and a new peak corresponding to $Au_3OH(O_2)^-$ arises. In contrast for Au_4OH^- no depletion of the Au_4OH^- peak after addition of molecular oxygen is observed. The size dependent adsorption activity of different cluster species can be quantitatively described by calculating the extent of reaction according to

$$\frac{[Au_nO_2^-]}{[Au_nO_2^-]+[Au_n^-]} \tag{4.3}$$

for bare clusters or by

$$\frac{[Au_nOH(O_2)^-]}{[Au_nOH(O_2)^-]+[Au_nOH^-]} \tag{4.4}$$

for the hydrated clusters.

The experimental extents of reaction [16] for different O_2 pressures are plotted in Figure 4.4.

This figure readily indicates the even-odd activity of the Au_nOH^-+O_2 reaction system. It is also interesting to note that the activity of Au_3OH^-at lower O_2 partial pressures even exceeds the activity of the Au_6^- cluster which is the most active bare gold cluster. This is an important finding which shows that the binding of the OH group can significantly increase the activity which may be particularly important for the catalytic CO oxidation. In order to investigate the reactivity of Au_nOH^- complexes toward O_2, structures of the $Au_nOH(O_2)^-$ complexes and their stabilities have been determined (cf. Figure 4.5 and Table 4.2).

It should be pointed out that only results for molecular oxygen adsorption are shown although in the case of Au_4OH^- and Au_5OH^- structures with dissociated oxygen are almost degenerate. However, due to an extremely large barrier for dissociation of molecular oxygen (∼O_2) (about 2 eV and higher) dissociation

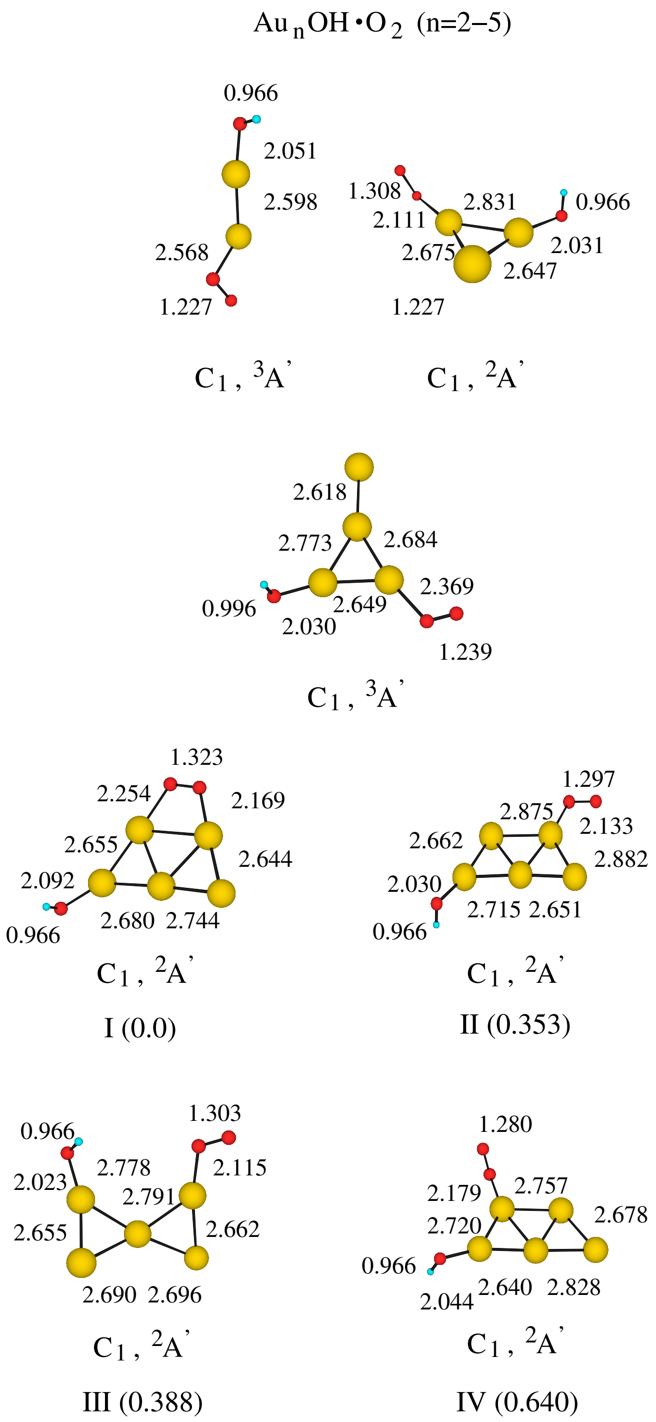

Figure 4.5: Optimized structures of $Au_nOH(O_2)^-$ complexes (n=2-5). For the Au_5 system, ΔE values (in eV) for different isomers are given in parentheses. Oxygen and hydrogen atoms are labeled by large red and small blue circles, respectively. Isomers corresponding to the local minima whose relative energies are less than 1 eV with respect to the most stable structure are shown.

Table 4.2: Ground state energies and properties of optimized $Au_nOH(O_2)^-$(n=2-5) clusters obtained from the B3LYP method.

$Au_nOH(O_2)^-$	Symm.(State)	Energy	ΔE	E_b	NBO Charge		
n=2-5		a.u	eV	eV	Au_n	OH	O_2
$Au_2OH(O_2)^-$	C_1 (^3A)	-497.883874		-0.006	-0.195	-0.638	-0.167
$Au_3OH(O_2)^-(I)$	C_1 (^2A)	-633.713091		0.78	0.154	-0.310	-0.844
$Au_4OH(O_2)^-$	C_1 (^3A)	-769.529684		0.03	-0.174	-0.606	-0.220
$Au_5OH(O_2)^-$(I)	C_1 (^2A)	-905.364643		0.88	0.114	-0.322	-0.835
$Au_5OH(O_2)^-$(II)	C_1 (^1A)	-905.351662	0.353				
$Au_5OH(O_2)^-$(III)	C_1 (^1A)	-905.350389	0.388				
$Au_5OH(O_2)^-$(IV)	C_1 (^1A)	-905.350389	0.388				

^{a}Energy difference with respect to the most stable structure. ^{b}Binding energy for the $Au_nOH(O_2)^-$ complexes is defined by E_b=E($Au_nOH(O_2)^-$)-E(Au_nOH^-)-E(O_2)

cannot take place under the experimental conditions relevant in this study. According to the calculations the affinity towards molecular oxygen is *reversed* compared to the reactivity of pure anionic gold clusters. The $Au_2OH(O_2)^-$ is not bound, in contrast to Au_2^- which strongly binds O_2 (compare Figure 4.5). The NBO analysis shows that there is almost no electron transfer from the Au_2 subunit to the O_2 molecule. In contrast, Au_3OH^- binds strongly O_2 and a significant charge amount of electron transfer from the Au_3 subunit takes place (cf. Table 4.2). The net charge which remains on the Au_3 subunit is +0.154e whereas OH group and O_2 groups carry -0.310e and -0.844e of charge, respectively. The O_2 molecule is bound as a superoxide subunit in the $Au_3OH(O_2)^-$ complex, as reflected in the NBO charge and in the O-O bond length of 1.308Å which is significantly longer than the one in molecular oxygen. The structure of the $Au_3OH(O_2)^-$ complex has a triangular Au_3 subunit which is actually the most stable structure of cationic Au_3 and the OH and O_2 are bound at the neighboring Au atoms. In contrast, the complex of $Au_4OH(O_2)^-$ is again only very weakly bound with a triplet ground electronic state indicating only very weak interaction with molecular oxygen. There is no significant electron transfer from the gold subunit to O_2 and correspondingly the O-O bond is shorter (cf. Table 4.2 and Figure 4.5). In the stable structure of $Au_5OH(O_2)^-$, the O_2 molecule is bound in a peroxo-like form, bridging the two gold atoms of the trapezoidal Au_5 subunit. The binding energy has the value of 0.88 eV and is slightly higher than for $Au_3OH(O_2)^-$(0.78 eV). Again, stronger interaction with the Au_5 subunit is reflected in the electron transfer which leaves the Au_5 subunit with a net charge of +0.114 eV while the O_2 group carries -0.835e of charge. Correspondingly, the O-O bond is elongated and has a length of 1.313Å In other higher isomers of $Au_5OH(O_2)^-$, O_2 is bound to a single Au atom, and therefore, the withdrawing of the electron from the gold subunit is lower than in the case of the lowest energy isomer.

The theoretical and experimental results presented in this section reveal that the Au_nOH^- species show a selective activity towards O_2 molecule which is exactly reversed compared to the activity of bare Au_n^- clusters. The easiest and perhaps most pleasing explanation for this finding which is based on the calculations performed may be formulated in terms of the frontier orbital model. Due to the high electron affinity of the OH group (1.8 eV) the electron transfer from the anionic clusters with even number of gold atoms (and therefore one unpaired electron) becomes highly favorable and causes the high stability of the Au_nOH^- complexes with n even. Moreover, due to the high electron affinity even the complexes with odd number of gold atoms also become stable. Due to this fact, the electronic structure of the cluster reverses from the situation seen for bare clusters, i. e., the bare odd-n Au_n^- clusters have no unpaired electrons, while the odd-n Au_nOH^- clusters now have an unpaired electron on the gold clusters. In the latter case,

Table 4.3: Experimental and theoretical values of ionization potentials (IP) for Au_n (n=2-6).

Reference	IP(eV) Au_2	Au_3	Au_4	Au_5	Au_6
[173][a]	9.50	7.50	8.60	8.00	8.80
[201][b]	9.16±0.10	7.27±0.15		7.61±0.20	
[202][c]	9.41	7.06	7.98	7.46	
[203][d]					7.60
this work and [165]	9.63	7.30	8.09	7.68	8.37

[a]Experimental, upper limits for IP. [b]Experimental; no value reported for Au_4 and Au_6. [c] Theoretical; no value reported for Au_6. [d]Theoretical; Au_6 is the smallest cluster reported.

in attempt to pair electrons again, the open shell complexes can adsorb molecular oxygen. The analysis of the experimental an theoretical results provides full support for this bonding mechanism and has been illustrated on the Au_3OH^- and Au_5OH^- clusters. First, the OH group binds to the closed shell $Au^-_{3(5)}$ cluster accompanied by a high electron transfer from the $Au_{3(5)}$ subunits resulting in an almost neutral $Au_{3(5)}$ subunit, which then, due to its open shell electronic structure, strongly binds O_2. In the resulting complexes the gold subunit has a positive charge while the negative charge is mainly localized at the O_2 superoxide subunit. With this mechanism in mind, a greater understanding of this system could be provided by further studies of the activity of the neutral gold clusters. In this case, the subsequent O_2 adsorption depends on the ionization potential (IP) of the neutral cluster species. Several experimental and theoretical values of Au_n ionization potentials are collected in Table 4.3.

An analysis of these values provides additional insight into the observed extents of reaction. While the absolute values of the cluster IPs are somewhat different, the overall trends are consistent. Beginning with Au_2 a strong even-odd oscillation in cluster IP is seen in agreement with the measured extents of reaction, with the even-n clusters having significantly higher IPs than the odd-n clusters. Within the odd-n clusters, the IP values for Au_5 is higher than that for Au_3 which is consistent with the lower extent of reaction for Au_5.

4.4.3 Cooperative activation of molecular oxygen by anionic silver clusters

The findings presented in Section 4.4.2 show that the binding of a strong electron acceptor group such as OH can induce the adsorption of molecular oxygen on unreactive anionic gold clusters with even number of electrons. Since anionic silver clusters have generally lower electron affinities (cf. Section 3.5) it can be foreseen that weaker electron acceptors such as O_2 may already induce electron transfer and activate the clusters with odd number of atoms (even number of electrons) (such as Ag^-, Ag_3^- , Ag_5^-). This can lead to an interesting new effect of the cooperative adsorption of two oxygen molecules in which the first adsorbed O_2 molecule serves as an activator.

The calculated energies for the binding of one and two O_2 molecules together with the structures of the corresponding complexes are shown in Figure 4.6 C. DFT calculations reveal that the binding energies for the first oxygen molecule exhibit even-odd oscillations (cf. blue curve in Figure 4.6 C). The first oxygen molecule is bound to the silver clusters with odd number of atoms by 0.36 eV, 0,36 eV and 0.53 eV for Ag^-, Ag_3^- and Ag_5^-, respectively. This is in contrast with the corresponding gold clusters which due to the higher electron affinities do not bind molecular oxygen at all. As expected, the clusters with even number of atoms (odd number of electrons) (Ag_2^- and Ag_4^-) bind strongly one oxygen molecule with the

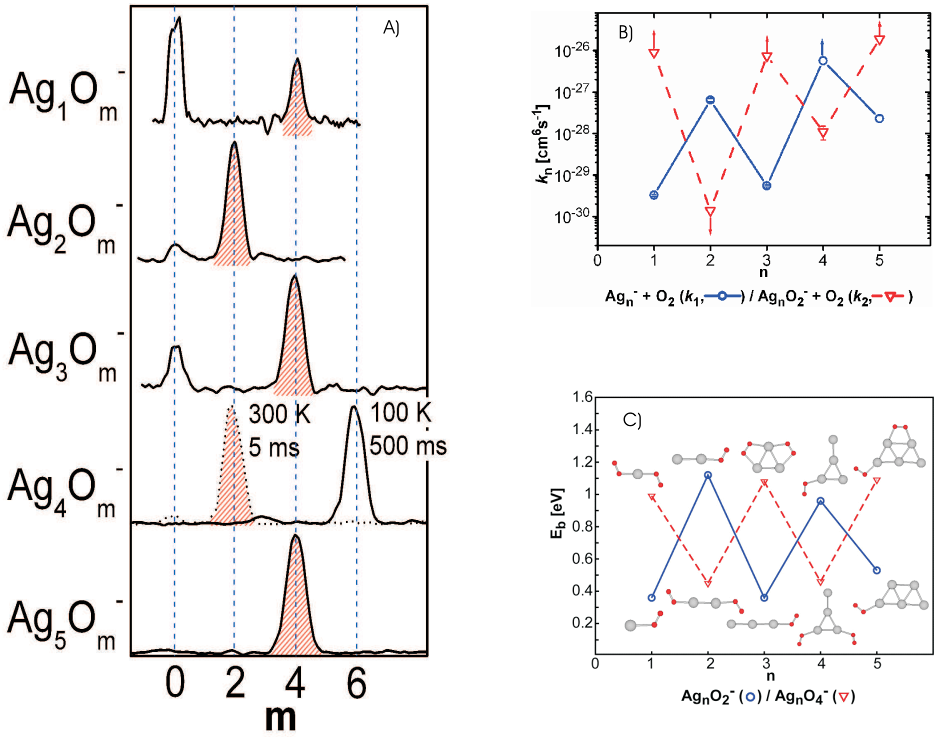

Figure 4.6: (A) Product ion mass spectra after reaction of Ag_n^- with O_2. Ion intensities are plotted as function of the number of adsorbed oxygen atoms m. (B) Experimental rate constants obtained for the adsorption of the first and second O_2 molecule onto Ag_n^- at $T_R = 300$K. (C) Theoretical binding energies E_b and lowest energy structures (grey spheres: silver atoms, red spheres: oxygen atoms).

binding energies of 1.12 eV and 0.96 eV. The mechanism of the bonding involves the electron transfer from the metal cluster into the π^* MO of O_2, as in the case of gold clusters.

The binding of the second oxygen molecule shows a reversed pattern (cf. red dashed curve in Figure 4.6 C) being stronger for clusters with odd number of atoms and weaker for the ones with even number of atoms. The latter ones with one unpaired electron bind strongly only one oxygen molecule since the electron transfer leaves them with a closed shell electronic structure. The cooperative binding of the second oxygen results in the case of Ag_3^- and Ag_5^- in new oxide species with doubly bound superoxo-like O_2 subunits as can be seen from Figure 4.6 C.

In early experiments [11] only the adsorption of one molecular oxygen on anionic silver clusters with even number of atoms has been detected. The theoretical study presented in this work stimulated the experiments performed by Wöste and coworkers. Our joint work [17] addresses the cooperative binding of two O_2 molecules which has been reported for the first time. Product ion mass spectra measured after reaction of mass selected silver clusters with oxygen are depicted in Figure 4.6 A. An oscillating size dependence in the reaction behavior is observed in agreement with our predictions of binding energies. This confirms that silver clusters with odd number of atoms adsorb two oxygen molecules, whereas the ones with even number of atoms adsorb only one O_2. The exception is Ag_4^- cluster which first forms $Ag_4O_2^-$ but then reacts with additional two O_2 molecules at long reaction times and low temperatures. The above mechanism can be extended to the adsorption of three oxygen molecules which should qualitatively exhibit similar behavior as the adsorption of one O_2. However, due to the sterical hindrance the adsorption of three oxygen molecules cannot occur on very small systems. The kinetics of the adsorption can be described by a sequential reaction mechanism:

$$Ag_n^- + 2O_2 \xrightarrow{k_1} Ag_nO_2^- + O_2 \xrightarrow{k_2} Ag_nO_4^- . \tag{4.5}$$

The measured rate constants k_1 and k_2 at 300 K are plotted in Figure 4.6 B as a function of cluster size. For Ag_n^- (n=1,3,5) the sequential adsorption of two oxygen molecules on the odd size clusters takes place without appearance of intermediate products $Ag_nO_2^-$ in the product ion mass spectra. This points towards the adsorption of the first O_2 being the rate determining step, whereas the addition of the secondary O_2 must proceed within the Langevin collision rate limit or at least on a much faster time scale than the resolution of the experiment (1 ms) [17]. The values of the measured rates constants compare very favorably with the experimentally obtained rate constants.

In summary, for Ag_n^- clusters with odd n a weakly bound first O_2 promotes the adsorption of a second O_2 which is then differently bound with the O-O bond elongated to 1.32 Å and thus activated for further oxidation reactions such as CO combustion.

4.4.4 Reactivity of atomic gold anions toward oxygen and oxidation of CO

In order to provide new insights into the reactive species of gold-oxygen anion complexes possessing one gold atom and to reveal the mechanism for the oxidation of CO on these species, the interaction of anionic gold species with O_2 and CO has been investigated. From the mass spectrum shown in Figure 4.7 A it can be seen that Au^- atom binds up to three oxygen atoms. The addition of CO results in a decrease in the intensity of the AuO^- peak, but does not influence that of AuO_2^-. Also a small decrease in the intensity of the AuO_3^- peak indicates that a slow reaction with CO takes place. Parallel to the decrease in intensity of AuO^- and AuO_3^- the Au^- peak increases. These experimental results indicate that the AuO^- is a very active species in the oxidation of CO.

The reaction of AuO^- with the CO molecule yields Au^- and CO_2 with a reaction energy of -3.604 eV. In order to follow the reaction mechanism, ab initio MD simulations have been performed starting from a bent arrangement of AuO^- and CO with a large O-C distance and zero initial kinetic energy. The examination of the potential energy surface for this reaction shows that a collinear approach of CO onto AuO^- is hindered by a barrier of 0.1 eV while, in the case of a nonlinear arrangement, there is no barrier for the formation of the complex. The snapshots of the reaction dynamics presented in Figure 4.7 B show that CO binds directly to the oxygen atom of AuO^- forming a complex which then quickly falls apart into Au^- and CO_2. In summary, the MD simulations together with the stationary DFT calculations show that the reaction of AuO^- with CO is a very fast and thermodynamically favorable reaction, leading to the oxidation of CO in agreement with the experimental findings presented here. Moreover, our results for the reactions of CO with AuO_3^- reveal the same mechanism for the oxidation of carbon monoxide. The reactions proceed via complex formation with CO bound to the oxygen atom, followed by either Au-O bond breaking or complex rearrangement to form a weakly bound CO_2 unit, leading to the elimination of CO_2.

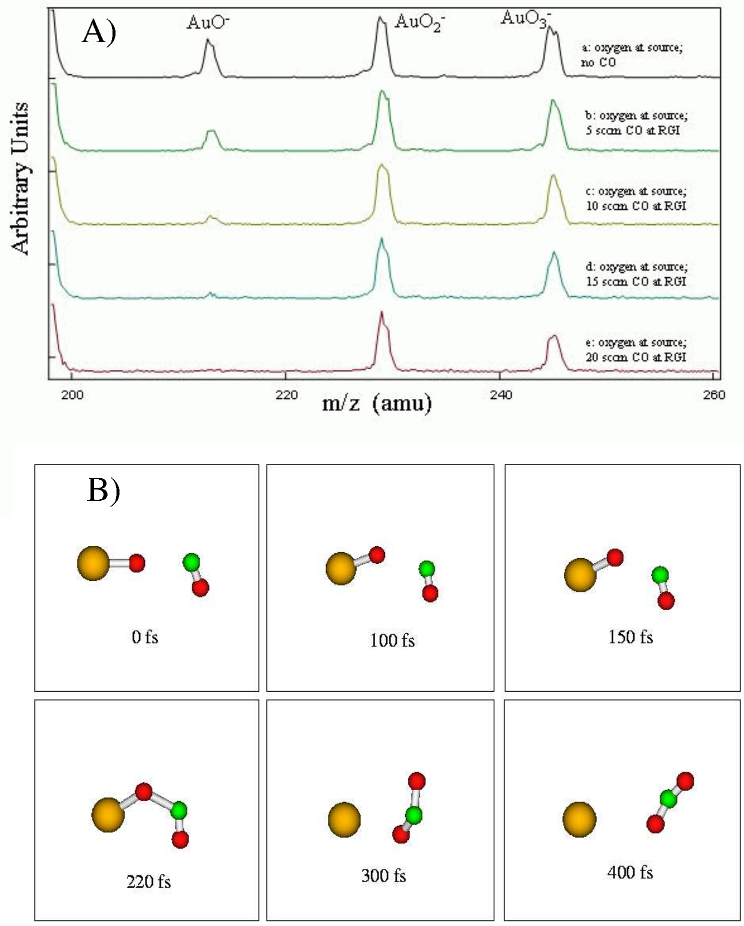

Figure 4.7: (A) Mass spectra showing the reactions of AuO_n^-(n=1,3) clusters with CO. (B) MD snapshots for the reaction of AuO^- and CO.

4.5 Conclusions

In summary, the theoretical and experimental results presented in this chapter show that binding of the strong electron withdrawing groups such as OH may significantly influence the activity of the anionic gold clusters towards molecular oxygen in the sense that the nonreactive bare clusters become active when in the form of Au_nOH^- while active bare clusters are inactive when OH is bound. The effects of the OH group on the activity of gold cluster anions provides insight into the mechanism and the possible role of water in the enhanced activity of supported gold cluster catalysts and shows a beautiful example how a study of cluster systems may contribute to gain a detailed understanding of the factors involved in catalytic activity. Furthermore, the same mechanism which was proposed in order to explain the effect of the OH group on the activation of anionic gold clusters has been extended to the anionic silver clusters. In this case, due to the generally lower electron affinities of the silver clusters a weaker electron acceptor such as O_2 can activate the cluster. In particular, it has been shown that one weakly bound O_2 provokes the reactivity of closed shell clusters Ag_n^- (odd n) towards a second O_2 molecule which is then strongly bound in an activated superoxo-like state. These findings of coadsorption properties of Ag_n^- clusters are conceptually important for understanding the role of silver clusters in oxidation processes.

While a separate understanding of the adsorption properties of O_2, CO, etc. is important to gain an understanding of the CO oxidation activity of free anionic gold clusters, it is their coadsorption properties that may play a major role. Recent experiments performed [186] have shown that in many cases CO and O_2 adsorb cooperatively on Au_n^- and that the presence of the preadsorbate (in this case O_2) increases the ability of the cluster to bind an incoming molecule. Very recent work by Wöste et al. also provided very exciting results on the reactions of $Au_{2,3}^-$ which show that only Au_2^- showed activity toward O_2 adsorption over the temperature range of 100-350 K [184]. However, when CO is preadsorbed, Au_3^- shows the adsorption of both one and two O_2 molecules leading to complexes of the form $Au_3(CO)(O_2)^-$ and $Au_3(CO)(O_2)_2^-$ [184]. Only under conditions in which CO is preadsorbed, and at low temperatures, O_2 adsorption was able to be seen on this odd-n cluster anions, reinforcing the concept of cooperative adsorption similar to the one found in this work.

Finally, results for the oxidation of CO in the presence of atomic Au^- have been presented which revealed that AuO^- and AuO_3^- can promote the oxidation of CO. DFT calculations and MD simulations allowed to propose the mechanism for the oxidation of CO. The mechanism proceeds via complex formation with CO bound to the oxygen atom, followed by the cleavage of the Au-O bond and the emanation of CO_2 [189].

Chapter 5

Theoretical consideration of the reactions between vanadium-oxide cluster cations and ethylene

5.1 Introduction and motivation

Among industrially important catalytic processes selective oxidation of hydrocarbons plays very important role [18] and design of effective catalysts which can serve for this purpose continues to be a highly desirable goal. Crucial for the intelligent design of catalysts is the identification of the active sites responsible for the catalytic activity and detailed understanding of the reaction mechanisms involved. However, currently available experimental surface science techniques have still difficulties to provide detailed information about the active sites. Therefore, alternative approaches have to be used. As pointed out in the literature [19, 20] a catalytically active metal surface may be considered as a collection of metal oxide clusters with varying compositions and sizes and therefore the study of mass selected gas phase clusters offers an opportunity to model the active sites of catalytic surfaces. In this way the influence of the composition, stoichiometry, charge, oxidation state, size and degree of coordinative saturation on reactivity can be systematically studied and can provide deeper insight into the nature of active sites. Experimental studies of this kind have been successfully performed using a guided ion beam mass spectrometer and have provided information about structure-reactivity properties of the clusters under investigation as convincingly demonstrated by Castleman and coworkers [204]. This approach is particularly successful when combined with theoretical studies of the chemical reactivity of clusters which can provide information about structure reactivity relation and reveal the reaction mechanisms involved.

This theoretical study [205, 206] has been motivated by the experiments on the reactivity of cationic vanadium oxide clusters with ethylene which have been performed by Castleman and coworkers [204, 21]. Vanadium oxides are of particular interest as an effective catalysts in the selective oxidation of hydrocarbons and have been of great interest to researchers [207, 208, 209]. Experiments have shown that when $(V_2O_5)_n^+$ was reacted with ethylene and ethane, $(V_2O_5)_{n-1}V_2O_4^+$ was identified as a very dominant reaction pathway. Additionally, this reaction channel was not observed to any appreciable extent with any other $V_xO_y^+$ cluster. The proposed product of the oxidation reaction as shown in Reaction 5.1

$$(V_2O_5)_n^+ + C_2H_4 \rightarrow (V_2O_5)_{n-1}V_2O_4^+ + (C_2H_4O) \tag{5.1}$$

cannot be detected experimentally using mass spectrometric techniques. The reaction shown above was proposed to be an oxygen transfer reaction from the metal oxide cluster to the hydrocarbon rather than oxygen loss because oxygen loss was not observed during collision induced dissociation (CID) experiments at thermal energies. The experimental studies of Castleman and coworkers are also in agreement with experiments performed by Rademann and Fielicke [210] which have shown also a distinct reactivity of $(V_2O_5)_n^+$ towards ethylene.

In this chapter the results of density functional calculations, which provide key information on the structure-reactivity relationship between the $V_xO_y^+$ clusters and ethylene are presented. These results include optimized structures of $V_2O_{2-6}^+$ and $V_4O_{8-10}^+$ clusters, of the $V_2O_{3-6}^+$-C_2H_4 and $V_4O_{10}^+$-C_4H_4 complexes, the transition states and the reaction energetics. In addition to the standard quantum chemical techniques, the reactions have been studied using ab initio molecular dynamics (MD). The theoretical results allow to propose a mechanism for the selective oxygen transfer due to the presence of the reactive centers for a given cluster size and stoichiometry, and they offer a clear explanation why different cluster sizes favor different processes.

5.2 Experimental studies

The experiments performed by the Castleman group which prompted present theoretical study were performed on a guided ion beam mass spectrometer coupled to a laser vaporization source described in detail elsewhere [211]. Briefly, the experimental setup consists of a metal rod ablated by a second harmonic of a Nd:YAG laser, and at a predetermined time oxygen seeded in helium (∼8 %) is pulsed over the source. The clusters were formed through plasma reactions and subsequently cooled using supersonic expansion. The ion of interest is then mass selected in the first quadrupole and focused into the octopole reaction cell through a set of electrostatic lenses. In the reaction chamber, ethylene is introduced and maintained at constant pressure while the energy of the octopole is increased incrementally ranging from 0 to 20 eV. The products of the reactions with ethylene were mass analyzed in the second quadrupole.

5.3 Computational methods

The calculations presented here were carried out at the density functional level of theory using the Becke's hybrid three parameter nonlocal exchange functional combined with the Lee-Yang-Parr gradient corrected correlation functional (B3LYP) [85, 86, 89] and employing the all-electron triple-ζ valence plus polarization basis set (TZVP) developed by Ahlrichs and co-workers [212]. In addition to the tests available in the literature the accuracy of the method for cationic vanadium oxide clusters was checked by calculating the dissociation energies for VO^+ and VO_2^+ clusters. The calculated dissociation energy for VO^+ is 3.80 eV which compares well with the experimental value of $D_e = 3.51 \pm 0.36$ eV obtained from CID studies [211] especially considering the large error bars. The dissociation energy for $VO_2^+ \rightarrow VO^+ + O$ is 5.52 eV which is somewhat lower than the experimental value of dissociation threshold which also includes the barrier $D_e = 6.09 \pm 0.28$ eV [211]. All structures reported here have been optimized employing gradient based minimization methods and the stationary points were characterized using vibrational frequency analysis. In order to study the mechanism of the oxygen transfer reaction transition state structures and the barriers corresponding to the involved reaction steps have been optimized using the synchronous transit guided quasi Newton method [213, 214]. The reaction pathways were also studied employing ab

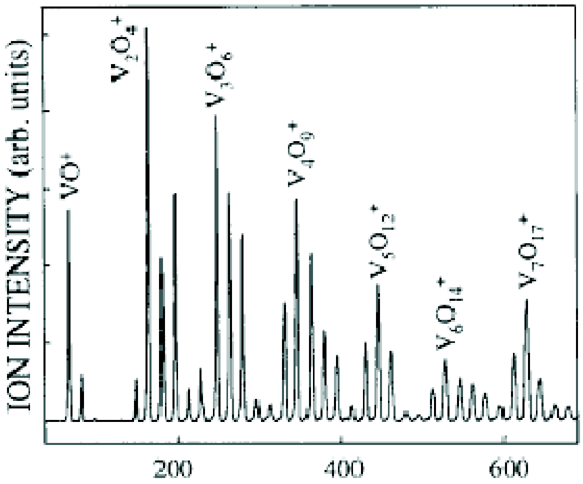

Figure 5.1: Mass distribution of vanadium oxide cluster cations taken from Reference [21].

initio molecular dynamics (MD) with forces calculated using the hybrid B3LYP functional or the RI-DFT procedure [215] with the non-hybrid BLYP functional. The MD simulations have been initiated from the activated complexes of $V_xO_y^+$ cluster with ethylene by randomly distributing the energy corresponding to the stability of the complex among all degrees of freedom. Such MD simulations allowed to follow the reaction mechanisms in detail and to verify the intermediates and reaction steps which have been deduced from the calculation of stationary points.

5.4 Results and discussion

5.4.1 Structures of $V_xO_y^+$ clusters

The optimized structures for the $V_2O_{2-6}^+$ and the $V_4O_{8-10}^+$ clusters are shown in Figures 5.2 and 5.3. As a measure of their thermodynamic stabilities binding energies per atom defined as

$$E_b/n = [E(V_xO_y^+) - E(V^+) - (x-1)E(V) - yE(O)]/(x+y). \tag{5.2}$$

are also included in Figures 5.2 and 5.3. The typical mass distribution of the vanadium oxide clusters obtained in experiments performed by Castleman and coworkers is shown in Figure 5.1. Each set of peaks corresponds to clusters having a particular number of vanadium atoms and the peaks within the given group differ by the number of oxygen atoms. The major peaks that are present in the $V_xO_y^+$ mass distribution are VO^+,$V_2O_{4-6}^+$, $V_3O_{6-8}^+$, $V_4O_{8-12}^+$, $V_5O_{11-13}^+$, $V_6O_{13-16}^+$ and $V_7O_{16-18}^+$.

Since all cationic vanadium oxide clusters studied in this work have an unpaired number of electrons calculations based on unrestricted (spin-polarized) DFT have been performed. The location of the unpaired electron is designated by an arrow. In general agreement with the literature, the double bridged structures for the $V_2O_{2-6}^+$ are calculated to be the most stable. For $V_2O_4^+$, two isomers with the terminal oxygen atoms occupying the trans and cis positions have been identified with an energy difference of 0.19 eV, the trans isomer being the more stable one. The $V_2O_5^+$ structure is found to be an oxygen centered radical and has one elongated V-O bond with the length of 1.89 Å compared to 1.56 Å for the other two terminal V-O bonds.

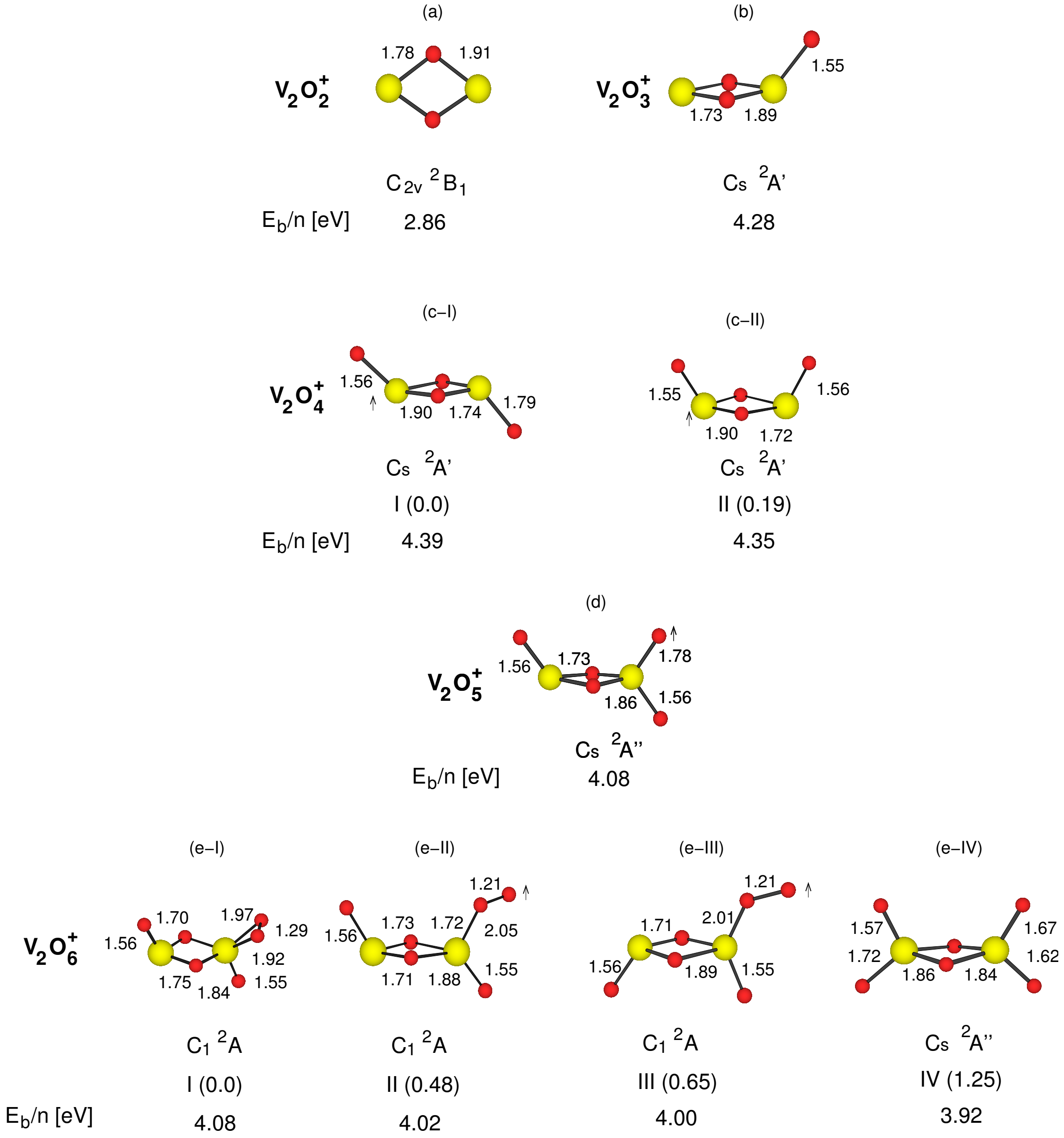

Figure 5.2: Structures for (a) $V_2O_2^+$ (b) $V_2O_3^+$ (c-I) trans $V_2O_4^+$, (c-II) cis $V_2O_4^+$, (d) $V_2O_5^+$, (e-I) peroxo $V_2O_6^+$, (e-II) trans $V_2O_6^+$, (e-III) $V_2O_6^+$ cis $V_2O_6^+$, (e-IV) $V_2O_6^+$, clusters. Energy difference in eV with respect to the most stable structures are given in round brackets. I-IV label the energy sequence of the isomers. Labels of the symmetry group and the ground electronic state are also given. Bond distances are given in Å Binding energies per atom (in eV) defined according to Equation 5.2 are also shown.

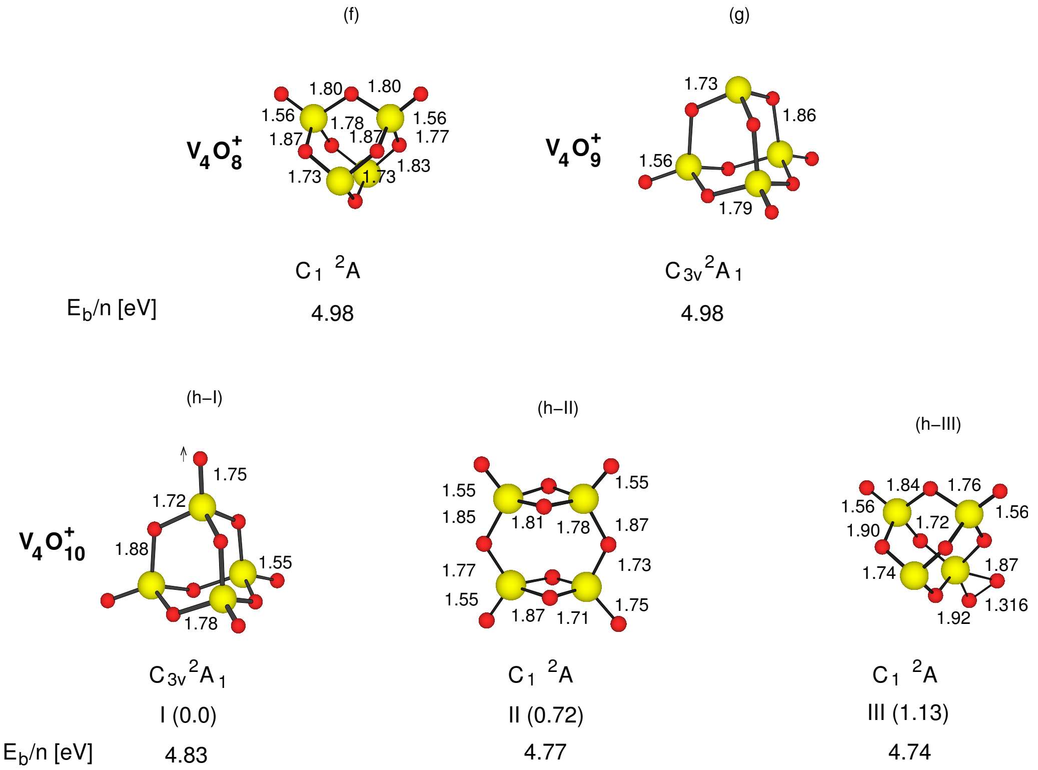

Figure 5.3: Structures for (f) $V_4O_8^+$, (g) $V_4O_9^+$,(h-I) $V_4O_{10}^+$, (h-II) $V_4O_{10}^+$ and (h-III) $V_4O_{10}^+$ clusters. Energy difference in eV with respect to the most stable structures are given in round brackets. I-IV label the energy sequence of the isomers. Labels of the symmetry group and the ground electronic state are also given. Bond distances are given in Å Binding energies per atom (in eV) defined according to Equation 5.2 are also shown.

For $V_2O_6^+$ four different isomers were found: the lowest energy structure has two terminal V-O bonds and the O_2 molecule is adsorbed to the cluster as a peroxide unit with the V-O bond lengths 1.92 and 1.97 Å and the O-O bond length 1.29 Å. Isomer III with the cis configuration of oxygen atom is higher in energy than the first isomer by 0.17 eV than the trans isomer. The fourth isomer, structure IV, shows four terminal V-O bonds and is higher in energy than the first isomer by 1.25 eV. The cationic structures of $V_2O_{2-6}^+$ are closely related to those obtained by Calatayud et al. [216, 217] with exception of $V_2O_4^+$ and $V_2O_6^+$ in which case we found the trans isomers to have lower energies than the cis configurations and the O_2 molecule forms two bonds toward vanadium instead of one.

The structures of $V_4O_{8-10}^+$ exhibit cage structures related to the familiar adamantane-like structure of P_4O_{10}. In the lowest energy structure of $V_4O_{10}^+$ as in the case of $V_2O_5^+$ an oxygen centered radical is present with a longer terminal V-O bond, and the unpaired electron is located on this oxygen atom.

5.4.2 Structures of $V_xO_y^+$-C_2H_4 complexes

Structures of the stable complexes with ethylene are shown in Figure 5.4. In the most stable complexes for $V_2O_3^+$-C_2H_4 and $V_2O_4^+$-C_2H_4, the ethylene is bound directly to a three coordinated vanadium atom with stabilities of $\Delta E = -0.26$ eV and -1.75 eV, respectively. The other structures in which ethylene is bound directly to the terminal oxygen atom have in both cases considerably higher energies as shown in Figure 5.4. For $V_2O_5^+$-C_2H_4 three isomers are shown. In the most stable structure the ethylene is bound directly to the cluster with two terminal V-O bonds with the stability of $\Delta E = -4.44$ eV. The second isomer has ethylene bound to only one oxygen atom with $\Delta E = -3.53$ eV. The third isomer is a weakly

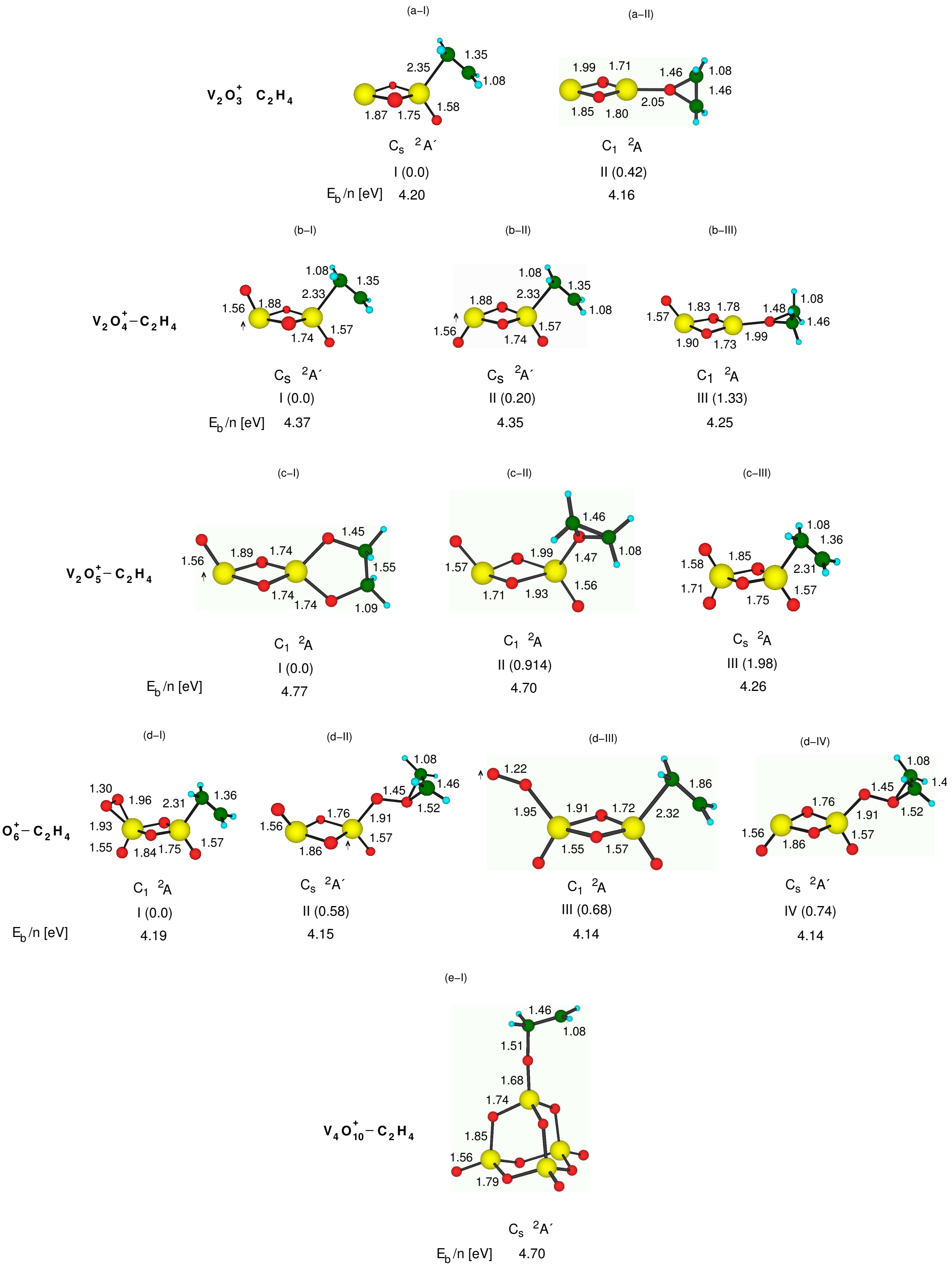

Figure 5.4: Structures for (a-I) $V_2O_3^+$-C_2H_4, (a-II) $V_2O_3^+$-C_2H_4 , (b-I) $V_2O_4^+$-C_2H_4, (b-II) $V_2O_4^+$-C_2H_4, (b-III) $V_2O_4^+$-C_2H_4, (c-I) $V_2O_5^+$-C_2H_4, (c-II) $V_2O_5^+$-C_2H_4, (c-III) $V_2O_5^+$-C_2H_4, (d-I) $V_2O_6^+$-C_2H_4, (d-II) $V_2O_6^+$-C_2H_4, (d-III) $V_2O_6^+$-C_2H_4, (d-IV) $V_2O_6^+$-C_2H_4 , (e-I) $V_4O_{10}^+$-C_2H_4 complexes. Binding energies per atom (in eV) are defined as $E_b/n = [E(\mathrm{V}_x\mathrm{O}_y^+\text{-}\mathrm{C}_2\mathrm{H}_4) - E(\mathrm{V}^+) - (x-1)E(\mathrm{V}) - yE(\mathrm{O}) - 2E(\mathrm{C}) - 4E(\mathrm{H})]/(x+y+6)$.

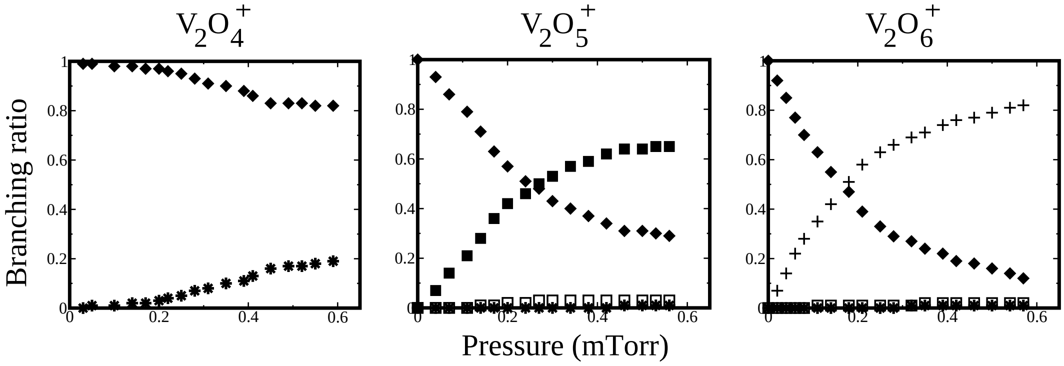

Figure 5.5: Relative product branching ratios of $V_2O^+_{4-6}$ with ethylene. (□) – $V_xO^+_{y-2}$, (■) – $V_xO^+_{y-1}$, (♦) – $V_xO^+_y$, (+) – $V_xO_{y-2}C_2H_4^+$, (∗) – $V_xO_yC_2H_4^+$

bound complex in which ethylene is bound directly to the positive vanadium center with the stability of $\Delta E = 2.46$ eV .

For $V_2O_6^+$-C_2H_4 four isomers have been found. In isomer I, the ethylene molecule is bound directly to the vanadium atom and the O_2 molecule is adsorbed as a peroxo group to the opposite vanadium atom with the stability of the complex of $\Delta E = -1.74$ eV. The second isomer (II) shows the ethylene bound to one oxygen atom of the adsorbed O_2, $\Delta E = -1.16$ eV. The third isomer differs from the isomer I by the O_2 molecule bound in the superoxo form and has the stability of $\Delta E = -1.06$ eV. Isomer IV is the trans configuration of isomer II. In the $V_4O_{10}^+$-C_2H_4 complex ethylene binds to the oxygen atom with the radical center as shown in Figure 5.4.

5.4.3 Reactions of $V_xO_y^+$ with ethylene

The reactions of $V_xO_y^+$ with ethylene have been experimentally studied by Castleman and coworkers and the experimental findings are summarized in Table 5.1. The experimental branching ratios for the reactions of $V_2O^+_{4-6}$ with ethylene are shown in Figure 5.5. Basically three different reaction channels have been observed: (i) association reaction for all studied clusters, (ii) single oxygen loss (or oxygen transfer) for $V_2O_5^+$ and $V_4O_{10}^+$, (iii) molecular oxygen loss for $V_2O_5^+$ and $V_2O_6^+$, (iv) replacement reaction in which ethylene is bound to the cluster and one O_2 molecule is released for $V_2O_6^+$.

5.4.3.1 $V_2O_4^+$+C_2H_4

No single atomic oxygen loss is observed experimentally in the case of $V_2O_4^+$. The calculated dissociation energy for a single oxygen atom in a collision process with a reactant gas shows that the reaction is highly thermodynamically unfavorable due to the breaking of a strong double V=O bond with the energy of +4.75 eV as shown in Reaction 5.3.

$$V_2O_4^+ + C_2H_4 \rightarrow V_2O_3^+ + O + C_2H_4 \quad \Delta E = +4.75 \text{ eV} \tag{5.3}$$

The loss of molecular oxygen is formally thermodynamically even more unfavorable and is as expected not seen experimentally. This channel is endothermic with a reaction energy of +9.64 eV

$$V_2O_4^+ + C_2H_4 \rightarrow V_2O_2^+ + O_2 + C_2H_4 \quad \Delta E = +9.64 \text{ eV}. \tag{5.4}$$

	$V_2O_4 + C_2H_4$	$V_2O_5 + C_2H_4$	$V_2O_6 + C_2H_4$	$V_4O_{10} + C_2H_4$
association:	$V_2O_4^+ + C_2H_4 \rightarrow V_2O_4C_2H_4^+$	$V_2O_5^+ + C_2H_4 \rightarrow V_2O_5C_2H_4^+$	$V_2O_6^+ + C_2H_4 \rightarrow V_2O_6C_2H_4^+$	$V_4O_{10}^+ + C_2H_4 \rightarrow V_4O_{10}C_2H_4^+$
calculated energy	$\Delta E = -1.75$ eV	$\Delta E = -4.44$ eV	$\Delta E = -1.74$ eV	$\Delta E = -2.18$ eV
experiment	only product observed	minor product observed; excess energy released through fragmentation	minor product observed; cleaving of V-O_2 bond, +0.92 eV likely	minor product observed
oxygen transfer:	$V_2O_4^+ + C_2H_4 \rightarrow V_2O_3^+ + C_2H_4O$	$V_2O_5^+ + C_2H_4 \rightarrow V_2O_4^+ + C_2H_4O$	$V_2O_6^+ + C_2H_4 \rightarrow V_2O_5^+ + C_2H_4O$	$V_4O_{10}^+ + C_2H_4 \rightarrow V_4O_9^+ + C_2H_4O$
calculated energy	$\Delta E = -0.02$ eV	$\Delta E = -2.53$ eV	$\Delta E = -0.71$ eV	$\Delta E = -1.36$ eV
experiment	not observed; not breaking O-O bond too costly, 4.75 eV	dominant product observed; mechanism discussed in energetic profile	not observed; breaking O-O bond too costly, 4.06 eV	dominant product observed; mechanism discussed in energetic profile
oxygen loss:	$V_2O_4^+ + C_2H_4 \rightarrow V_2O_3^+ + C_2H_4 + O$	$V_2O_5^+ + C_2H_4 \rightarrow V_2O_4^+ + C_2H_4 + O$	$V_2O_6^+ + C_2H_4 \rightarrow V_2O_5^+ + C_2H_4 + O$	$V_4O_{10}^+ + C_2H_4 \rightarrow V_4O_9^+ + C_2H_4 + O$
calculated energy	$\Delta E = +4.75$ eV	$\Delta E = +2.24$ eV	$\Delta E = +4.06$ eV	$\Delta E = +2.75$ eV
experiment	not observed; not energetically favourable	minor product observed; most likely oxygen transfer	not observed; not energetically favourable	not observed; not energetically favourable
molecular oxygen loss:	$V_2O_4^+ + C_2H_4 \rightarrow V_2O_2^+ + C_2H_4 + O_2$	$V_2O_5^+ + C_2H_4 \rightarrow V_2O_3^+ + C_2H_4 + O_2$	$V_2O_6^+ + C_2H_4 \rightarrow V_2O_4^+ + C_2H_4 + O_2$	
calculated energy	$\Delta E = +9.64$ eV	$\Delta E = +1.78$ eV	$\Delta E = +1.09$ eV	
experiment	not observed; not energetically favourable	minor product observed; most likely formaldehyde formation	minor product; collisional process, observed during CID	
replacement reaction:		$V_2O_5^+ + C_2H_4 \rightarrow V_2O_3^+ + 2CH_2CO$	$V_2O_6^+ + C_2H_4 \rightarrow V_2O_4C_2H_4^+ + O_2$	
calculated energy		$\Delta E = -0.65$ eV	$\Delta E = -0.66$ eV	
experiment			dominant product observed	

Table 5.1: Overview of the important theoretical and experimental reactions between $V_xO_y^+$ and C_2H_4.

The most favorable reaction channel and the one observed experimentally is the association

$$V_2O_4^+{+}C_2H_4 \rightarrow V_2O_4^+\text{-}C_2H_4 \quad \Delta E{=}{-}1.75 \text{ eV.} \tag{5.5}$$

Although this reaction product is already present under single collision conditions its intensity increases with increasing ethylene pressure in the collision cell. This is expected due to the stabilizing effect of the third-body collisions which occur under higher pressure and multiple-collision conditions providing a mechanism to remove the internal energy of the complex.

Formally the oxygen transfer reaction for $V_2O_4^+$ to yield acetaldehyde (CH_3CHO) is marginally thermodynamically favorable with a theoretical reaction energy of -0.02eV according to

$$V_2O_4^+{+}C_2H_4 \rightarrow V_2O_3^+{+}C_2H_4O \quad \Delta E{=}{-}0.02 \text{ eV.} \tag{5.6}$$

In spite of the exothermicity the above reaction channel has not been observed experimentally. This can be explained by mechanistic reasons. Namely, the oxygen transfer should occur first by forming the association product between the cluster and the ethylene molecule. Then, in order for oxygen transfer to occur a very strong V-O bond must be broken, requiring 4.75 eV of energy. Considering that the association only gains 1.75 eV of energy there is not enough energy to surmount the barrier for breaking of the V-O bond. Additionally, the reaction is also hindered by sterical reasons due to the fact that the ethylene molecule binds directly to the vanadium atom rather to an oxygen atom, making oxygen transfer mechanistically even more improbable. In summary, theoretical calculations performed provide an explanation why only one reaction pathway, namely association, is observed. Single and molecular oxygen losses are energetically highly unfavorable, and oxygen transfer has a large barrier which is difficult to overcome under the experimental conditions.

5.4.3.2 $V_2O_6^+{+}C_2H_4$

The single oxygen loss from $V_2O_6^+$ is an energetically highly unfavorable reaction with $\Delta E = +4.06$ eV

$$V_2O_6^+{+}C_2H_4 \rightarrow V_2O_5^+{+}O{+}C_2H_4 \quad \Delta E{=}4.06 \text{ eV} \tag{5.7}$$

and is as expected not observed experimentally. The energy calculated for the molecular oxygen loss for $V_2O_6^+$ was found to be $+1.09$ eV and is illustrated below:

$$V_2O_6^+{+}C_2H_4 \rightarrow V_2O_4^+{+}O_2{+}C_2H_4 \quad \Delta E{=}{+}1.09 \text{ eV.} \tag{5.8}$$

Even though the reaction is calculated to be endothermic, the loss of O_2 from $V_2O_6^+$ is observed experimentally and is most likely due to the ion-molecule impact. An alternative explanation is that the mass distribution contains also weakly bound complexes between $V_2O_4^+$ and O_2. This is supported by theoretical calculations which show that complexes with a quadruplet spin state have binding energies of ~ 0.4 eV and can be present in the molecular beam due to the fact that the doublet and quadruplet state have a degenerate dissociation limit. During collision-induced dissociation experiments for $V_2O_6^+$ interacting with xenon, molecular oxygen loss, forming $V_2O_4^+$ is observed near thermal energies implying that O_2 is bound to the cluster only weakly. A relatively weak bonding is also reflected in long bonds (1.97 and 1.92 Å) with which the O_2 molecule is bound to the cluster. The association reaction

$$V_2O_6^+ + C_2H_4 \rightarrow V_2O_6^+\text{-}C_2H_4 \quad \Delta E = -1.74 \text{ eV} \tag{5.9}$$

gains 1.74 eV of energy and is observed experimentally as a minor product since a three body mechanism is required for removing internal energy gained and stabilizing the complex.

The oxygen transfer reaction for the $V_2O_6^+$ cluster to yield acetaldehyde is thermodynamically favorable with an energy of -0.71 eV as shown in reaction 5.10

$$V_2O_6^+ + C_2H_4 \rightarrow V_2O_5^+ + CH_3CHO \quad \Delta E = -0.71 \text{ eV} \tag{5.10}$$

However, there is no experimental evidence for oxygen transfer to occur. For oxygen transfer to occur again a very strong double V=O bond has to be broken requiring 4.70 eV of energy. Since the association only gains 1.74 eV this is not enough to surmount the energy barrier for the reaction. The dominant channel found experimentally is the replacement reaction yielding $V_2O_4^+$-C_2H_4

$$V_2O_6^+ + C_2H_4 \rightarrow V_2O_4^+\text{-}C_2H_4 + O_2 \quad \Delta E = -0.66 \text{ eV.} \tag{5.11}$$

This reaction is slightly less energetically favorable than the oxygen transfer reaction although the energy difference may be within the limits of accuracy of the calculations. However, the important difference is that the replacement reaction does not require the cleavage of the strong O-O bond. Although the association product for $V_2O_6^+$ is energetically the most favorable channel it is observed experimentally much weaker than the replacement reaction. This is due to the need for a third-body collision to stabilize the association complex. Once the complex is formed the amount of energy released (1.74 eV) is sufficient to cleave the adsorbed O_2 after internal energy redistribution and to yield $V_2O_4^+$-C_2H_4 as indicated by MD simulations. Considering the amount of energy available to the complex and the ease with which $V_2O_6^+$ looses molecular oxygen during CID experiments this possibility is very likely to occur. In addition, at elevated reaction gas pressures, multiple collisions occur, increasing the likelihood of O_2 loss and favoring the replacement reaction. The single oxygen loss and oxygen transfer reactions are improbable due to energetic barriers involved in breaking the O-O bond. In conclusion, taking into account experimental conditions as well as structural and energetic properties of involved species, it can be concluded that the replacement reaction, the most dominant pathway observed experimentally, is energetically the most viable option for the $V_2O_6^+$ cluster.

5.4.3.3 $V_2O_5^+$+C_2H_4

In the case of $V_2O_5^+$-C_2H_4 the association reaction was determined to have three possible stable products, one formed through two terminal V-O bonds, the second with a single V-O terminal bond and a weakly bound complex in which ethylene is bound directly to the vanadium atom. The calculated association energies are 4.44 eV, 3.53 eV and 2.46 eV. Atomic and molecular oxygen loss pathways producing $V_2O_4^+$ and $V_2O_3^+$, respectively were calculated to be endothermic by +2.24 and +1.78 eV. Experimentally, $V_2O_4^+$ and $V_2O_3^+$ are observed during the reactions with ethylene at thermal energies, yet neither is observed during CID at thermal energies. Only after addition of 1-2 eV center of mass frame energy these products

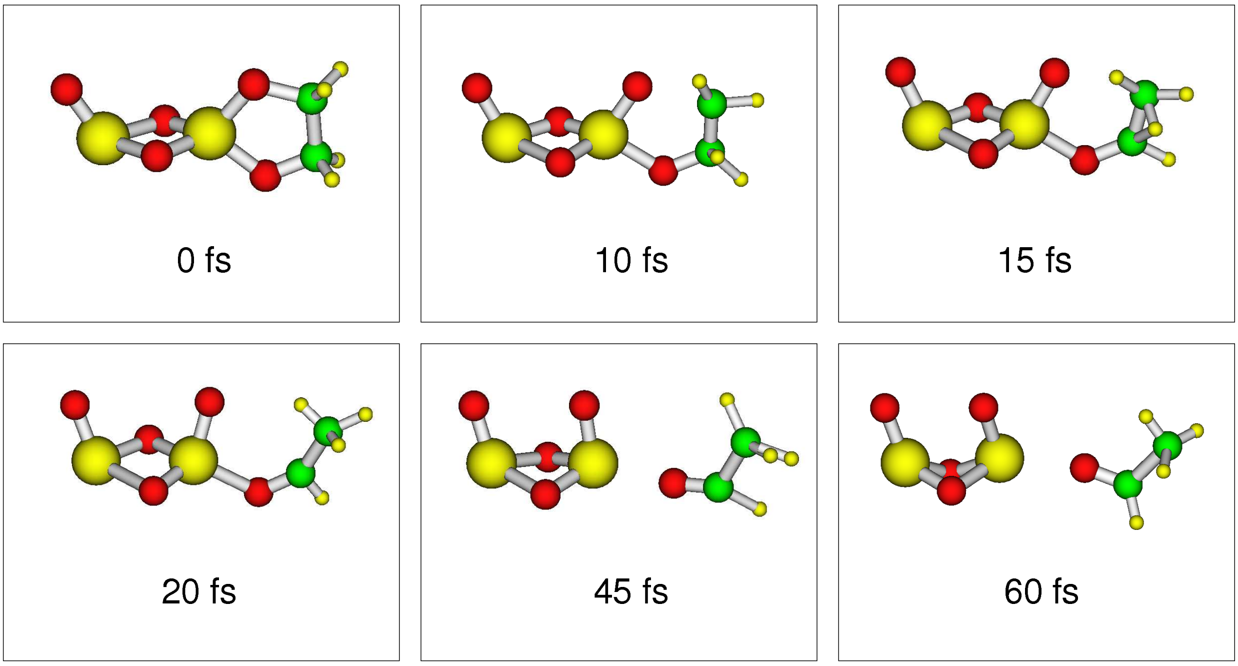

Figure 5.6: Snapshots of the ab initio MD trajectory calculated using RI-BP86 method for the reaction of $V_2O_5^+$ with C_2H_4 leading to formation of acetaldehyde.

appear during the CID studies. This lead to the assumption that another mechanism must be responsible for the observed oxygen loss in the reaction with ethylene at thermal conditions. Therefore, *oxygen transfer reaction* is proposed to be responsible for the atomic and molecular oxygen losses observed during the experiments. Single oxygen transfer is an exothermic reaction with $\Delta E = -2.53$ eV yielding $V_2O_4^+$ and acetaldehyde:

$$V_2O_5^+ + C_2H_4 \rightarrow V_2O_4^+ + CH_3CHO \quad \Delta E = -2.53 \text{ eV}. \tag{5.12}$$

Molecular oxygen loss was also a very minor reaction observed experimentally and was found to have two possible mechanisms forming either ethene-diol with $\Delta E = -1.05$ eV, or two formaldehyde molecules $\Delta E = -0.65$ eV. Despite the less favorable overall energy for producing two formaldehyde molecules, this reaction pathway is more likely to occur due to the high-energy barrier which makes the formation of ethene-diol difficult.

In order to gain further insight into the course of the oxygen transfer reaction and to obtain additional confirmation for the proposed mechanism ab initio simulations at constant energy corresponding to the microcanonical ensemble have been carried out. The snapshots of the MD trajectory are shown in Figure 5.6.

The results show that the association of ethylene to $V_2O_5^+$ is followed by a very rapid (20 fs) hydrogen transfer from the carbon atom bound to oxygen toward the terminal carbon atom. After the hydrogen transfer has taken place, the V-O bond is broken within the next 40 fs leading to acetaldehyde and $V_2O_4^+$ as final products. In addition the MD simulations at higher energies also confirmed the formation of two formaldehyde molecules leading to $V_2O_3^+$ which is a minor product in the experiment (cf. Figure 5.7). The calculated energetic profile for the reaction of $V_2O_5^+$ with ethylene is shown in Figure 5.8.

The reaction begins with the formation of the association product between $V_2O_5^+$ and ethylene which is an exothermic step with $\Delta E = -4.44$ eV. In this step, the radical center which was initially located on the oxygen atom of $V_2O_5^+$ is transferred to the second carbon atom of the ethylene molecule. In the next

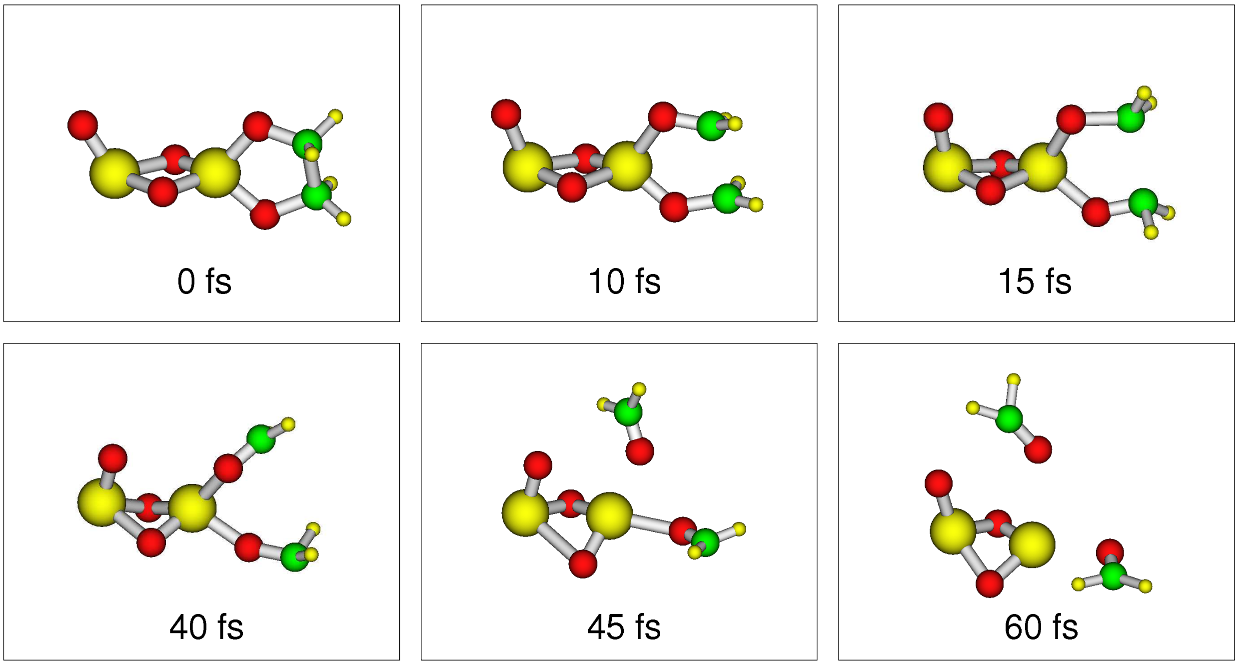

Figure 5.7: Snapshots of the ab initio MD trajectory calculated using RI-BP86 method for the reaction of $V_2O_5^+$ with C_2H_4 leading to the formation of two formaldehyde molecules.

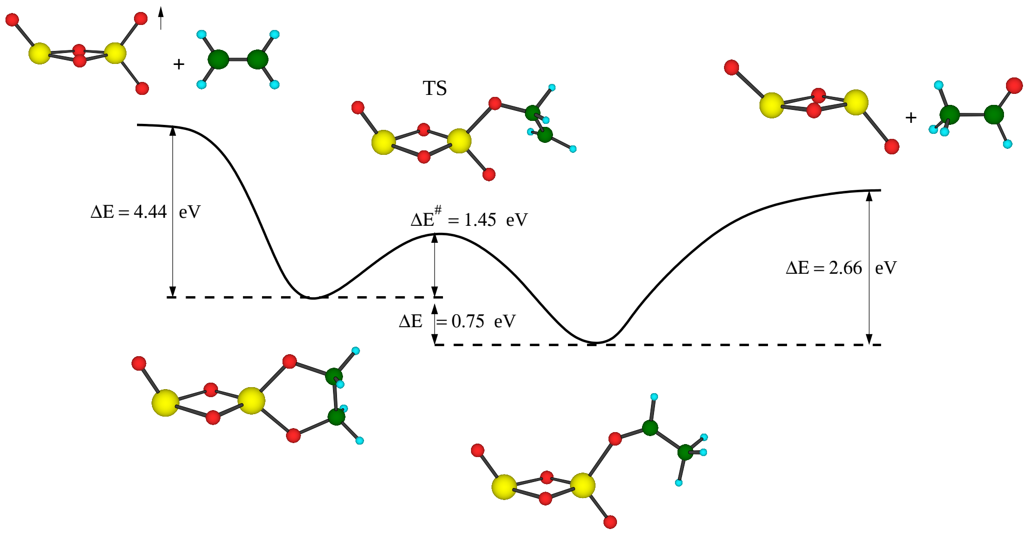

Figure 5.8: Energetic profile for the reaction between $V_2O_5^+$ and C_2H_4.

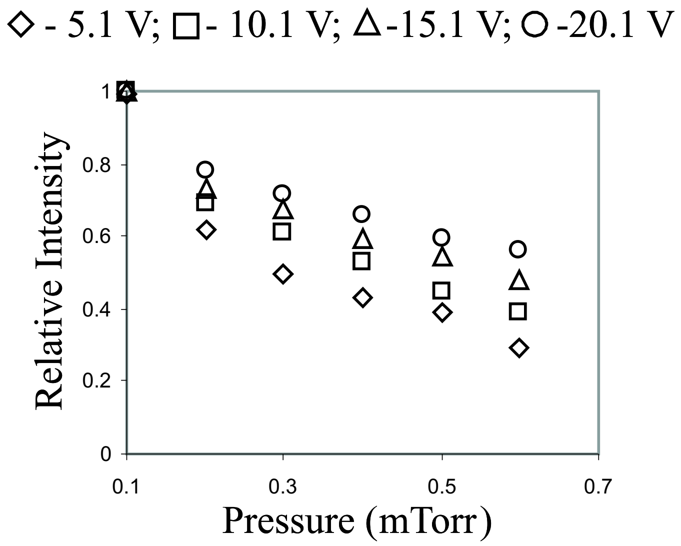

Figure 5.9: Relative intensity of $V_2O_5^+$ for the reaction between $V_2O_5^+$ and C_2H_4 as a function of pressure at four different energies. 5.1 eV, 10.1 eV, 15.1 eV and 20.1 eV represented by four different symbols.

step hydrogen transfer occurs leading to a shift of the radical center from the second carbon atom to the first carbon atom. In this step a terminal methyl group is formed. The barrier for the hydrogen transfer is 1.45 eV. However due to the 4.44 eV of energy gained which cannot be removed under single collision conditions, this barrier is facile to overcome as seen also in MD simulations. In the last step the V-O bond is cleaved leaving the vanadium atom which had been bound to the oxygen atom with a radical center.

Kinetic study of the oxygen transfer mechanism

As discussed above the observed oxygen loss in the case of $V_2O_5^+$ has been attributed to the exothermic oxygen transfer reaction and not to the collisionally induced oxygen loss. In order to get the confirmation for this and for the above proposed mechanism the energy dependent study of the reactivity has been proposed and performed experimentally. Namely, in the case of the collisionally induced oxygen loss which is an endothermic process it is expected that the reaction cross section increases with increasing collision energy leading to more $V_2O_4^+$ at higher collision energies. The relative intensities of $V_2O_5^+$ at varying energy are shown in Figure 5.9 as function of increasing pressure. A common observation at each pressure in the branching ratio is the relative increase of $V_2O_5^+$ and decrease of $V_2O_4^+$ as the energy is increased incrementally. This indicates that as the collision energy increases the efficiency of the reaction decreases, i. e., less oxygen is being transferred to the ethylene. This is opposite to the trend that would arise if the oxygen atom loss were merely due to an unreactive, energetic CID process. Taking into account the proposed mechanism for the oxygen transferred reaction a simple theoretical model has been devised which qualitatively shows how the decrease of the intensity of V_2O_5 can arise with increasing collision energy. Parameters which enter into the model are defined in Figure 5.10 where the schematic reaction profile corresponding to the proposed oxygen transfer mechanism is shown.

In following a shorthand notation will be used in which $V_2O_5^+$ is represented by A, C_2H_4 by B, the first association complex by C, the transition state for the hydrogen transfer by D, the second complex by E, and the products $V_2O_4^+$ and CH_3CHO by E and F, respectively . With this notation the reaction

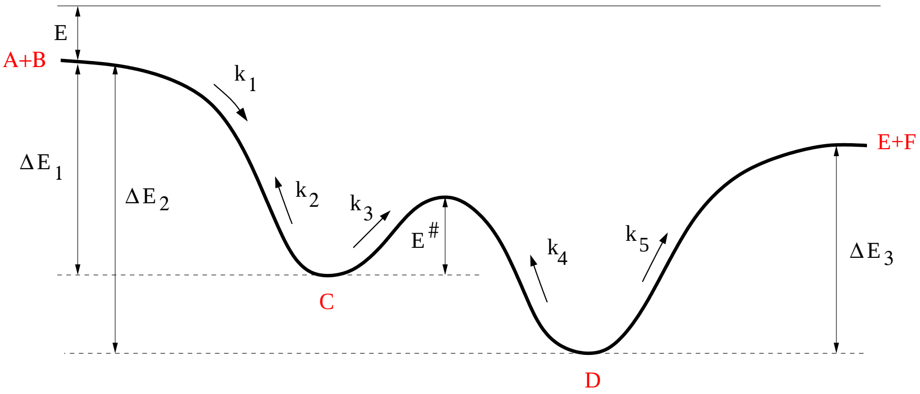

Figure 5.10: Schematic reaction profile representing the oxygen transfer reaction from $V_2O_5^+$ to C_2H_4. Parameters needed for calculation of the energy dependent reaction cross sections are shown. ΔE_{1-3} represent energy differences and k_{1-5} are kinetic constants for the elementary reaction steps, $E^\sharp$ is the barrier for the oxygen transfer reaction.

mechanism can be schematically written as

$$A + B \underset{k_2}{\overset{k_1}{\rightleftharpoons}} C \underset{k_4}{\overset{k_3}{\rightleftharpoons}} D \overset{k_5}{\rightarrow} E + F. \tag{5.13}$$

The rate equations for the complexes C and D are then

$$\frac{d[C]}{dt} = k_1[A][B] - k_2[C] - k_3[C] + k_4[D] \tag{5.14}$$

$$\frac{d[D]}{dt} = k_3[C] - k_4[D] - k_5[D]. \tag{5.15}$$

Since the association product between $V_2O_5^+$ and C_2H_4 is only very weakly observed in experiment the steady-state approximation can be applied for the concentrations of the intermediates C and D and leading to:

$$[C] = \frac{k_1[A][B]}{k_2 + k_3 - \frac{k_3k_4}{k_4+k_5}} \tag{5.16}$$

and

$$[D] = \frac{k_1k_3[A][B]}{(k_2 + k_3) \times (k_4 + k_5) - k_3k_4}. \tag{5.17}$$

The total reaction rate is determined by the rate the second complex D falls apart and is given by

$$\frac{d[E]}{dt} = k_5[D] = \frac{k_1k_3k_5}{(k_2 + k_3) \times (k_4 + k_5) - k_3k_4}[A][B] \tag{5.18}$$

and therefore the overall rate constant is

$$k = \frac{k_1k_3k_5}{(k_2 + k_3) \times (k_4 + k_5) - k_3k_4}. \tag{5.19}$$

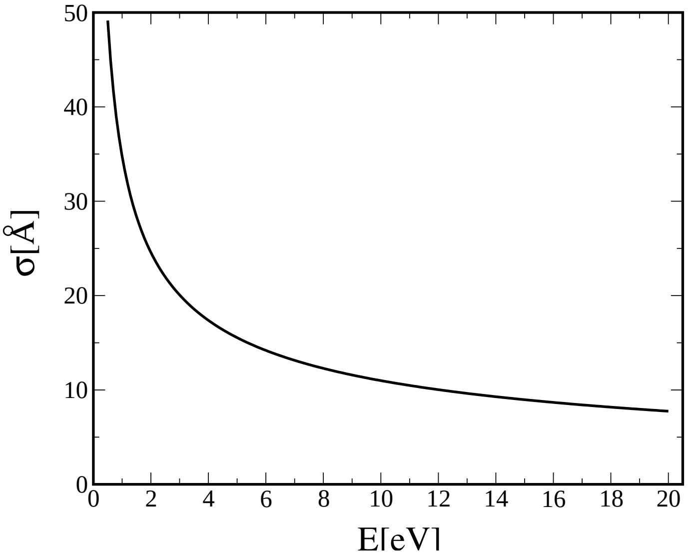

Figure 5.11: Energy dependent reaction cross section for the oxygen transfer from $V_2O_5^+$ to C_2H_4 calculated using Equation 5.21

Since the first step is an ion-molecule association reaction it can be assumed that k_1[1] is determined by the Langevin cross section σ_L

$$\sigma_L = \frac{e}{4\epsilon_0}\sqrt{\frac{2\alpha}{E}} \tag{5.20}$$

where E is the collision energy and α is the polarizability of the reactant gas and has for ethylene a value of 4.25 $\mathring{A}^3$. The total reaction cross section is then determined by the association cross section modified by the contribution from the internal rearrangement leading to the oxygen transfer and is given by,

$$\sigma = \sigma_L \times \frac{k_3 k_5}{(k_2 + k_3) \times (k_4 + k_5) - k_3 k_4}. \tag{5.21}$$

The calculated reaction cross section for the energy range 0-20 eV is shown in Figure 5.11 and it can be seen that the cross section decreases approximately inversely proportional to the energy. This is in sharp contrast to what would be expected for a collision induced dissociation and can be therefore used to distinguish the exothermic oxygen transfer reaction from an collisional oxygen loss. This negative energy dependence of the reaction cross section comes from the fact that for increasing energy according to the RRK expression the reaction steps in the reverse direction have higher reaction rates since the density of states is larger in the "deeper" (exothermic) side of the reaction profile.

The elementary rate constants which appear in this expression can be calculated using the RRK equation for unimolecular reactions

$$k_2 = A_2\Big(\frac{E}{E + \Delta E_1}\Big)^{N-1} \tag{5.22}$$

---

[1] The reaction rate constant can be generally obtained from the reaction cross section by averaging over the collision energies $k(T) = \langle v\sigma(E)\rangle$.

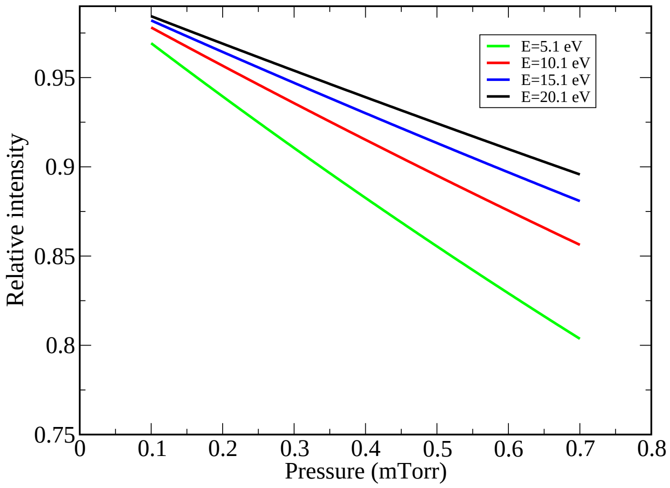

Figure 5.12: Calculated pressure dependence of the relative intensity of $V_2O_5^+$ for four different energies shown in the insert.

$$k_3 = A_3\Big(\frac{E + \Delta E_1 - E^\sharp}{E + \Delta E_1}\Big)^{N-1} \tag{5.23}$$

$$k_4 = A_4\Big(\frac{E + \Delta E_1 - E^\sharp}{E + \Delta E_2}\Big)^{N-1} \tag{5.24}$$

$$k_5 = A_5\Big(\frac{E + \Delta E_2 - \Delta E_3}{E + \Delta E_2}\Big)^{N-1} \tag{5.25}$$

where N is the number of internal degrees of freedom and the parameters ΔE_{1-3} and $E^\sharp$ are defined as in Figure 5.10. The frequency factor A_2 for the fragmentation of the initial complex back into the reactants can be approximated by the frequency of the normal mode leading into fragmentation with the calculated wavenumber of $\tilde{\nu} = 992$ cm^{-1}. The frequency factors A_3 and A_4 were calculated using theoretical normal mode frequencies for the complexes C and D and for the transition state (TS) according to

$$A_{3(4)} = \frac{\prod_i^N \nu_i}{\prod_i^{N-1} \nu_i^\sharp}. \tag{5.26}$$

Since in the last reaction step the V-O bond is broken the frequency factor A_5 has been approximated by the frequency of the V-O stretching vibration for which the calculated wavenumber has a value of $\tilde{\nu} = 484$ cm^{-1}.

The dependence of the relative intensity of the $V_2O_5^+$ ion signal which comes out of the reaction cell on the ethylene pressure and the collision energy is given by

$$I(\mathrm{V_2O_5^+})/I_0 = exp(-\frac{\sigma(E)p(\mathrm{C_2H_4})l}{k_BT}) \tag{5.27}$$

where p(C_2H_4) is the ethylene pressure and l is the length of the cell. The results for four different energies are presented in Figure 5.12. The curves corresponding to higher collision energies are shifted to higher energies in agreement with the experimental trend shown in Figure 5.9 providing a proof that an exothermic reaction and not collisional oxygen loss takes place and supporting the proposed mechanism for

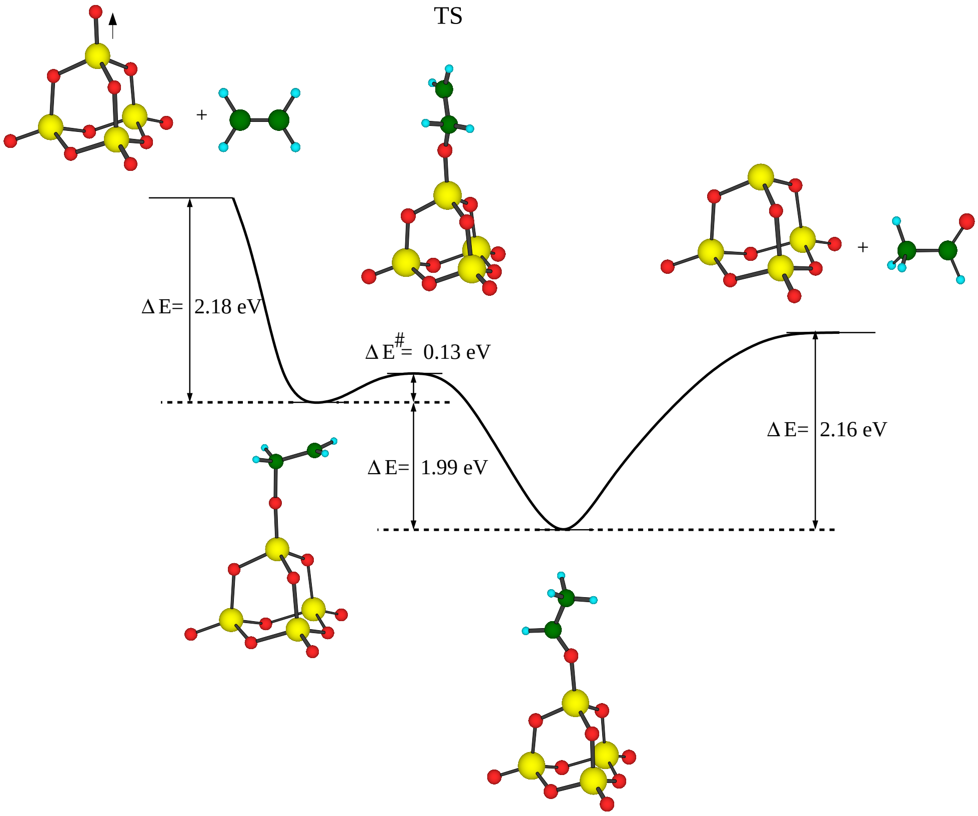

Figure 5.13: Energetic profile for the reaction between $V_4O_{10}^+$ and C_2H_4.

the oxygen transfer. It should be pointed out that while the above model reproduces fully the observed trends in reactivity it cannot reproduce the experimental data fully quantitatively due to very crude Langevin cross section used and to numerous approximations which were made.

5.4.3.4 $V_4O_{10}^+$+C_2H_4

Experimental studies have shown that the oxygen transfer reaction occurs only for clusters with the stoichiometry $(V_2O_5)_n^+$ with n=1,3 and the question arises if there is a common structural element present in each of the three clusters. According to the DFT calculations presented in this work $V_2O_5^+$ and $V_4O_{10}^+$ are oxygen centered radicals with an elongated and weakened terminal V-O bond. The oxygen transfer reaction between $V_4O_{10}^+$ and ethylene is energetically favorable with energy $\Delta E = -2.01$ eV as shown below

$$V_4O_{10}^+ + C_2H_4 \rightarrow V_4O_9^+ + CH_3CHO \quad \Delta E = -2.01 \text{ eV}$$

The energetic profile for the reaction is shown in Figure 5.13 and the reaction pathway found is very similar to the one found for $V_2O_5^+$. However, unlike the $V_2O_5^+$ cluster binding ethylene to two oxygen atoms, the $V_4O_{10}^+$ cluster initially binds the ethylene molecule through a single oxygen atom. This is due to the terminal oxygen atoms being too far apart in the $V_4O_{10}^+$ cluster for the ethylene to bind two terminal O atoms. Again after the complex formation the hydrogen transfer occurs in which the radical center is shifted from the terminal C-atom to the C-atom bound to the oxygen. The corresponding transition state has one C-H bond perpendicular to the carbon radical center in order to maximize the interaction with the p-orbital occupied by the unpaired electron. Hydrogen transfer leads to the formation of the

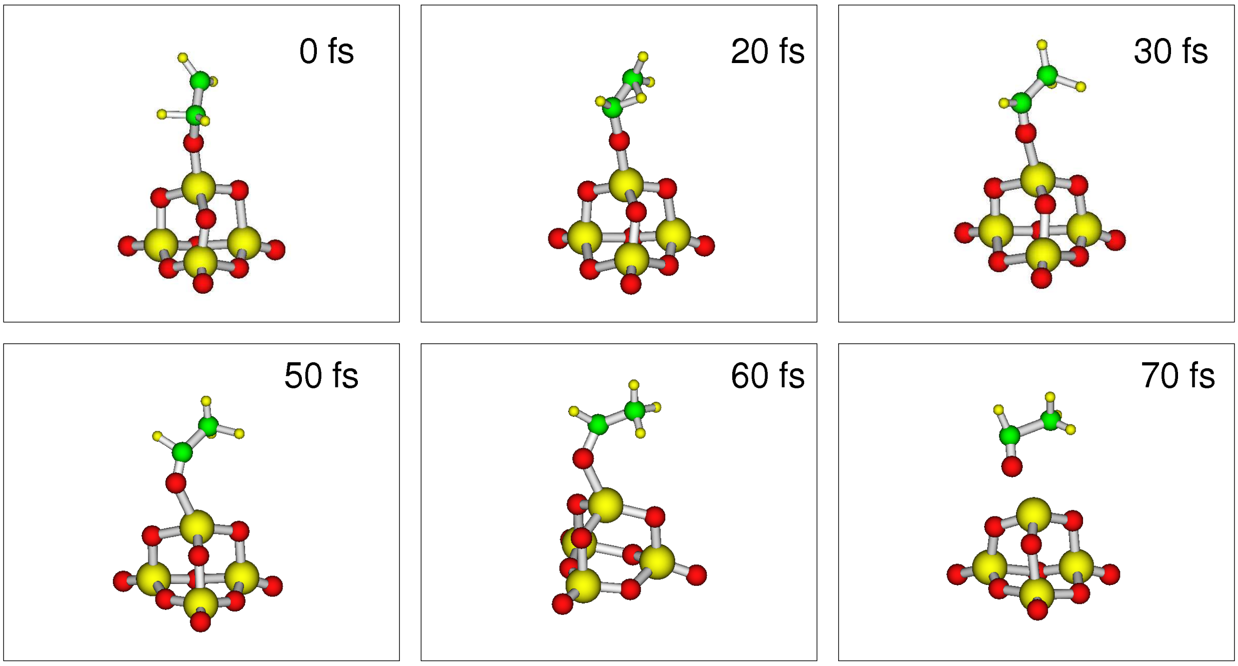

Figure 5.14: Snapshots of the ab initio MD trajectory calculated using B3LYP method for the reaction between $V_4O_{10}^+$ and C_2H_4 leading to the formation of acetaldehyde.

complex which may be considered as acetaldehyde adsorbed onto $V_4O_9^+$ cluster. In the last step a V-O bond is cleaved, separating acetaldehyde from $V_4O_9^+$. The reaction mechanism proposed was confirmed by ab initio MD simulations using forces calculated with the B3LYP method and starting with the initial structure corresponding to the first association complex. Initial velocities have been assigned randomly so that the total kinetic energy corresponds to the stability of the initial complex. The snapshots of one typical MD trajectory are shown in Figure 5.14 and they reveal that the association is followed by a very rapid hydrogen transfer (∼30 fs) and formation of acetaldehyde which is typically completed within 100 fs.

It should be also pointed out that a weak molecular oxygen transfer is also observed experimentally, giving $V_4O_8^+$ as product. This, however cannot be due to the most stable structure of $V_4O_{10}^+$ but to the higher isomer (cf. Figures 5.2 and 5.3). It is possible that in the cluster beam a small amount of $V_4O_8^+$ with adsorbed molecular oxygen, which can be easily released at thermal energies, is present. Experimentally, the production of $V_4O_8^+$ from $V_4O_{10}^+$ is most likely a collisional process since this reaction is observed during collision induced dissociation experiments conducted previously in our laboratory. In support of this, Asmis et. al observed the $V_4O_8^+$ when $V_4O_{10}^+$ was photodissociated, supporting the $V_4O_8^+$-O_2 as a higher energy structure of $V_4O_{10}^+$ [218].

5.4.4 IR-MPD spectroscopy of $V_xO_y^+$-C_2H_4 complexes

The direct information about the structures of the gas phase clusters can be obtained from vibrational spectroscopy. Recently IR multiple photon dissociation (IR-MPD) using a Free Electron Laser (FEL) as intense and widely tunable IR source has been used to obtain IR spectral information on oxide clusters of vanadium, niobium and tantalum as well as on some complexes of metal clusters [218, 219, 220, 221, 222]. Essentially, in these experiments the clusters and their complexes form a molecular beam that is overlapped with the intense infrared beam of the free electron laser. When the laser frequency is resonant with an IR active vibration of a cluster, the cluster can absorb several photons and subsequently undergo

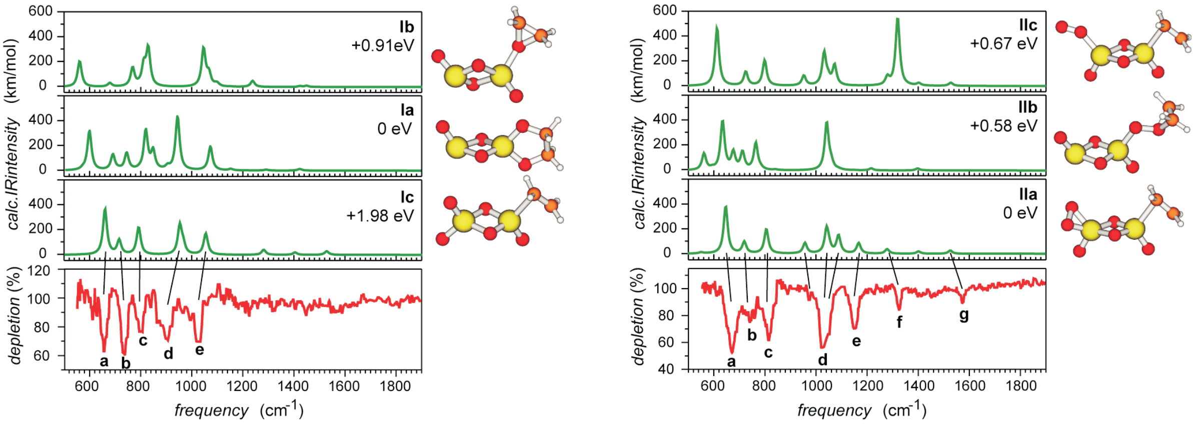

Figure 5.15: Infrared multiple photon dissociation (IR-MPD) spectra of $V_2O_5C_2H_4^+$ and $V_2O_6C_2H_4^+$ together with calculated spectra for several isomers.

fragmentation. The changes in the cationic mass distribution are monitored as a function of the wavelength. The detailed explanation of the mechanism of IR multiple photon absorption has recently been discussed in the context of IR resonance enhanced multiple photon ionization (IR-REMPI) spectroscopy of clusters [223] as well as of IR-MPD of gas phase molecular ions [224]. The use of the IR spectroscopy for structural identification depends on the ability of theoretical methods to predict accurately structural and dynamical properties as well as energetics. Therefore, the structural assignment is a joint experimental and theoretical effort. In this work [225] the interpretation of the IR-MPD spectra of the cationic vanadium oxide-ethylene complexes is given. For this purpose the vibrational frequencies and IR intensities have been calculated within the harmonic approximation and are compared with the experimental data.

IR-MPD spectra for the complexes of $V_2O_5^+$ and $V_2O_6^+$ with C_2H_4 are shown in Figure 5.15 together with the calculated spectra of several isomers. Due to the lack of reference data for similar gas-phase molecules, a rather arbitrary scaling factor of 0.95 has been used to scale the calculated frequencies. For $V_2O_6C_2H_4^+$ the best agreement between the measured and the calculated spectrum is obtained for the most stable isomer IIa (cf. right side of Figure 5.15), however in the case of $V_2O_5C_2H_4^+$ the measured pattern corresponds to the isomer Ic which is 1.98 eV higher in energy than the most stable isomer Ia. In addition to the IR spectral information, the fragmentation pathways can be identified in experiment by analyzing the frequency dependence of the intensity increase of the fragment ions. For $V_2O_5C_2H_4^+$ the observed fragmentation channel is C_2H_4 loss and for $V_2O_6C_2H_4^+$ the loss of [$C_2H_4O_2$] (presumably successive loss of C_2H_4 and O_2) is observed. In order to explain why in the case of $V_2O_5C_2H_4^+$ the spectrum corresponding to the higher lying isomer is measured a relative energetics of the $V_2O_5C_2H_4^+$ system is summarized in Figure 5.16 . During the complex formation a reaction between $V_2O_5^+$ and C_2H_4 could follow the lowest energy path leading to the formation of the acetaldehyde as oxidation product. So if the complex Ia is present in the cluster beam, pumping it with IR light is expected to induce the rearrangement to the complex of acetaldehyde with $V_2O_4^+$ and subsequent loss of acetaldehyde. Experimental neither the strong absorption at 1584 cm^{-1} characteristic for this complex nor loss of [C_2H_4O] have been observed. Although the IR spectra of Ia and Ic are similar, the observed loss of C_2H_4 makes the presence of Ic more probable since it contains a relatively weakly bound ethylene to the positive vanadium center, in contrast to Ia in which two very strong C-O bonds are present. From these findings the question arises why the vanadium oxide clusters behave differently during reactions with ethylene in the reactivity measurements of Castleman [204]. It is suggested here that this is due to the charge effect on the geometry of the

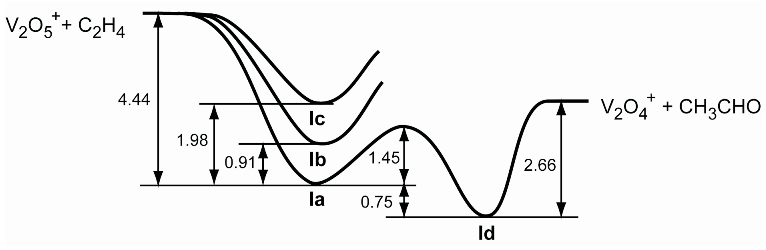

Figure 5.16: Schematic diagram showing the relative energies (in eV) of four different isomers of $V_2O_5C_2H_4^+$ (Ia-d) and the energetics of the ethylene oxidation on Ia leading to acetaldehyde (cf. Figure 5.8).

ion-molecule reaction. In the pure oxide clusters the positive charge is located at the lowest coordinated vanadium atom and can influence the orientation of the ethylene molecule. In this way an intermediate ion-molecule complex is formed which is not necessarily the lowest energy structure. Thus, the structure of $V_2O_5C_2H_4^+$ identified in the IR-MPD experiments resembles the primary collision complex that is formed at thermal collision energies. In mass selected reactivity measurements the collision energies are typically at least a few eV. Even if this energy is only partly transfered into internal energy, barriers can be overcome and more stable products can be formed. Moreover, the reactivity measurements are performed under single collision conditions under which all the reaction energy remains in the cluster providing additional driving force which can surmount the barriers. The comparison of the experimental and calculated spectra as well as experimental investigations of the laser power dependence gave no evidence for the presence of different structural isomers of $V_2O_5C_2H_4^+$ and $V_2O_6C_2H_4^+$. In particular, for $V_2O_6C_2H_4^+$ the calculated IR spectra of the higher isomers are very different, thus a very good agreement between experimental and calculated IR spectra supports the assignment to the most stable isomer I. For $V_2O_5C_2H_4^+$ the observed loss of C_2H_4 complements the ambiguous spectroscopic observations giving evidence for the presence of isomer Ic.

5.5 Conclusions

The structure-reactivity relationship for $V_xO_y^+$ clusters towards ethylene has been identified. The radical center located at one of the peripheral O atoms in $V_2O_5^+$ and $V_4O_{10}^+$ is responsible for the observed oxygen transfer in the framework of the radical-cation mechanism. The general scheme of the reaction mechanism is presented in Figure 5.17. The mechanism starts with the formation of the association complex followed by hydrogen transfer and subsequent release of acetaldehyde as a neutral product. In addition to the structural properties, the strength of the bond between the transition metal and the oxygen atom also plays an important role in the oxygen transfer. Theoretical results in combination with experimental findings provide evidence for the selectivity of $V_xO_y^+$ clusters due to the charge as well as to the capability of vanadium to assume different oxidation states for different cluster sizes. In the case of $(V_2O_5)_n^+$ n=1,2, the oxygen atom can be reversibly bound and released promoting catalytic oxidation of hydrocarbons, providing evidence that gas-phase clusters can serve as well suited prototypes for identification of reactive centers. Further support for the active sites identified in this work comes from the indirect experimental findings of active sites on vanadia/titania surface catalysts which were used to explain the formation of products such as acetaldehyde and formaldehyde [226].

This illustrates that the study of reactions involving gas-phase cationic vanadium oxide clusters and small hydrocarbons is suitable for the identification of reactive centers responsible for selectivity in heterogeneous

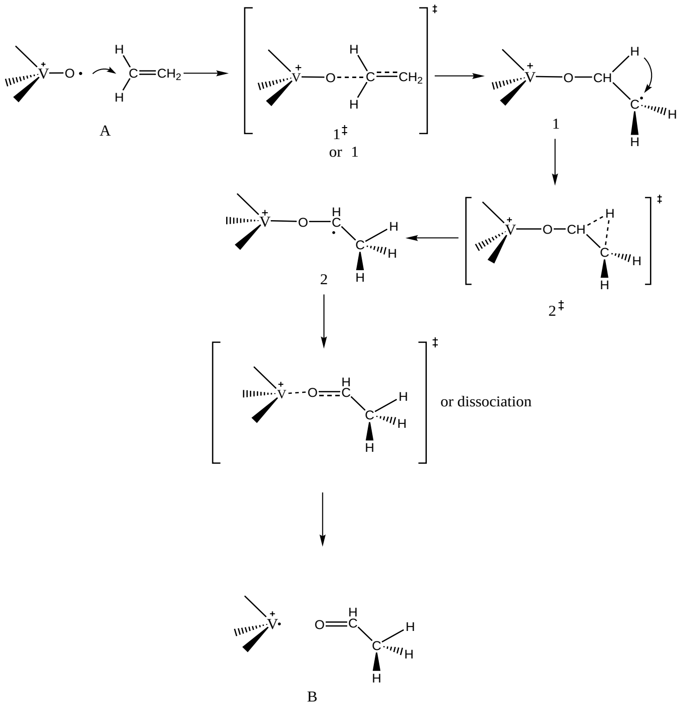

Figure 5.17: General reaction mechanism for the reaction between $(V_2O_5)^+_{n=1,2}$ and C_2H_4.

catalysis. Acetaldehyde which was identified to be the main product of the oxidation of ethylene on cationic vanadium oxide clusters is also an observed oxidation product of ethylene over vanadia/silica catalysts [227]. The infrared spectra of complexes of $V_2O_5^+$ and $V_2O_6^+$ with ethylene have been presented allowing for the first time to identify the structures of the intermediates involved in the reaction of the gas phase cluster with a hydrocarbon molecule. In summary, the findings presented in this chapter show that a greater understanding of the active sites which facilitate certain catalytic processes can serve as a guide to custom-designed catalysts for specific purposes. Moreover, the combination of the theoretical investigations with experimental reactivity studies involving mass selected clusters and with novel spectroscopic techniques for the structure identification can provide a deeper insight into the mechanistic aspects of the heterogeneous catalysis.

Chapter 6

Ab initio study of the absorption spectra of Ag_n (n=5-9) clusters

6.1 Introduction and motivation

Significance of the investigation of structural and electronic properties of small silver clusters on silver bromide surfaces has been recognized a long time ago in connection with their role in photography [228, 229, 230, 231]. Recent experimental findings on photoactivated fluorescence from individual silver nanoclusters produced upon visible illumination of silver oxide films further increased the importance of the study of optical properties of silver clusters because of the possible new applications as nanoscopic optical storage materials [22, 23]. Strong visible fluorescence has also been found from both neutral and charged small silver clusters with two to eight atoms in an argon matrix at cryogenic temperatures [232, 233, 234, 235, 236] supporting a discrete molecular nature of the excitations in small silver clusters. The finding of fluorescence for Ag_n (n>3) was rather unexpected due to the fact that electronic excitation of free gas phase clusters leads to fragmentation on a picosecond time scale which is much shorter than the typical fluorescence lifetime [237]. Moreover, in the case of the bulk metal the electronic excitation is quenched by a very fast nonradiative decay process which makes fluorescence impossible. However, reducing the dimensions of metal particles eventually leads to the discrete molecular-like excited states and can give rise to fluorescence as shown by recent work on silver clusters in argon matrix where the matrix prevents the fragmentation due to the caging effect [234]. An interesting open question in this regard is up to which cluster size fluorescence can still be observed. Namely, increasing the cluster size increases also the number of possible nonradiative relaxation channels which compete with fluorescence and eventually quench it.

Absorption spectroscopy on small metal clusters represents also a very powerful technique which can, in combination with theory, provide information about structural properties of clusters since for small clusters the transition energies as well as intensities of the absorption peaks are strongly dependent on the structural properties [1]. Essential for the structure determination is that experimental spectra are recorded at low temperatures where thermal broadening is low so that the fine structure of the spectra which is structure specific can be resolved. On the other hand, successful structure identification also requires theoretical spectra of high accuracy.

From a theoretical point of view the accurate description of ground and excited states of silver clusters is feasible since their complexity lies between the alkali metals in which the structural and electronic properties are determined by the s-electrons only, and the transition metals in which the d-electrons also participate in the bonding [157, 158]. In the previous work structural and other ground state properties such as ionization potential, electron affinities and vertical detachment energies have been determined as a function of cluster size [157, 158] and compared with the available experimental data [172, 238, 239, 240, 241]. Furthermore, ab initio calculations of electronic excited states have been carried out for the photodetachment spectra of Ag_{2-9}^- [157] and for the absorption spectra of Ag_{2-4} and Ag_{2-4}^+ [159]. In general, comparison of accurate quantum chemical results with experimental findings, in particular in the gas phase and at low temperatures, allows to identify the structures responsible for the measured features. The assignment of structural properties to the recorded spectra was particularly successful for Na_n^+(n=2-9,11,21) clusters, due to an excellent agreement between depletion spectra obtained at low temperature [242] and calculated absorption spectra for the most stable structure [243, 244].

Structural properties of silver and alkali metal clusters are often very similar due to strongly localized d-electrons at Ag-atoms which are therefore not involved in the bonding. In contrast, the role of d-electrons in the optical response of pure and doped (e.g. by oxygen) silver clusters as a function of their size remains still an important issue which is addressed in this work. In early experimental work, the optical absorption spectra of small silver clusters embedded in solid argon [245, 246] were characterized by relatively broad bands which did not allow unequivocal for structural identification. Depletion spectra of Ag_nKr complexes [247] exhibited better resolution but the bands remained relatively broad for clusters larger than tetramers. Recent experiments using new techniques such as laser-induced fluorescence in an argon matrix [236] and resonance two-photon ionization in helium droplet [248, 249] allowed to record narrow bands for the Au_{5-9} clusters which might serve as suitable fingerprints of structural properties when compared with theoretical results.

The aspects mentioned above motivated to study the optical response of silver clusters larger than tetramers presented in this chapter. For this purpose an accurate theoretical treatment based on the equation-of-motion coupled cluster (EOM-CC) method has been carried out. This approach allows an accurate treatment of correlation effects in combination with 11-electron relativistic effective core potential (11e-RECP) taking into account both s- and d-electrons on silver atoms. Computational aspects are briefly described in Section 6.2 . The absorption spectra calculated for the most stable structures as well as for energetically close lying isomers are presented in Section 6.3. They are compared with the available experimental data in Section 6.4 and structural assignment has been discussed. Also, in Section 6.4 the relaxation in excited states and the fluorescence observed in the rare gas matrices is discussed on the example of Ag_8 and Ag_9. Conclusions are presented in Section 6.5.

6.2 Computational

For the calculation of the optical response of silver clusters Ag_n (n=2-9) an 11-electron relativistic effective core potential (11e-RECP) together with AO basis set developed in the Bonačić-Koutecký group and designed for accurate description of the excited states of the silver atom has been employed [159]. In the previous work it has also been demonstrated that 11e-RECP provides accurate description of the excited states of small silver clusters [159]. In this work a slightly larger (6s5p5d) AO basis set with contraction scheme (21111/311/311) is used, since the excited states in a larger energy interval are needed requiring the use of more diffuse basis functions. Such relatively small AO basis set providing adequate accuracy is requested, since 11 electrons per atom have to be correlated in the framework of linear response methods based on coupled cluster approach. This is computationally very demanding for the cluster sizes considered in this work because the calculation of many excited states is necessary in order to obtain the full information about absorption spectra. The spectra are calculated using the EOM-CCSD method [250] and the related similarity transformed equation of motion coupled cluster technique (STEOM-CCSD) [251] described in section 2.4.5.2. The STEOM-CCSD theory has been derived from a similarity transform of the second quantized Hamiltonian which reduces the coupling between singly excited configurations and more highly excited ones 2.4.5.2. On all tested systems the STEOM yields comparable accuracy as the EOM-CCSD method at lower computational requirements. As well known EOM-CCSD method gives reliable transition energies and oscillator strengths for states dominated by singly excited configurations. For the excited states in which doubly excited configurations have a leading role, less accurate results are expected. In order to determine if the latter is the case, approximate excitation levels (AEL) (cf. section 2.4.5.2) can be used as a measure of the number of electrons which are excited from the CCSD ground state described by the single and double excitations with respect to the single reference configuration. However, the transitions with large oscillator strengths are dominantly determined by single excitations, because double excitations are dipole forbidden. Therefore the EOM-CCSD method is suitable for determining patterns of absorption spectra. It is to expect that the errors of transition energies due to the approximate treatment of correlation effects are not larger than 0.1 eV. For transitions to very high excited states above 6 eV the accuracy can strongly be influenced by the AO basis set which is in the present work of very moderate size. The calculations of absorption spectra for Ag_9 cluster have been carried out using the less expensive RPA method described in section 2.4.5.1. Also the structural relaxation in the excited states with dominant intensities which is responsible for the observed fluorescence has been studied using the RPA method. For the systems with close shell electronic structures the analytic gradients formulated in the framework of the RPA approach have been employed for the geometry optimizations while in the open shell case the energy gradients have been calculated numerically using the finite difference method.

6.3 Structures and absorption spectra for Ag_{5-9} clusters

6.3.1 Structural properties

In order to provide a consistent theoretical description of the ground and excited states, the structures have been optimized in the framework of the analytical gradient CCSD procedure correlating 11 electrons per Ag-atom. The exception is the Ag_9 cluster for which the structure has been optimized at the DFT level of theory due to the high computational demand. The geometries of global and local minima for which the harmonic frequency analysis has been carried out are shown in Figure 6.1.

The ground state properties are summarized in Table 6.1 in which also the results obtained from the DFT calculations employing BLYP functional are listed for comparison. Both approaches yield equivalent energy ordering of the isomeric forms for the given cluster size and comparable stabilities (binding energies per atom). Generally, an accurate determination of the energy ordering of the isomeric forms is still a difficult task. The geometry optimization at the CCSD level of theory taking into account also correlation of d-electrons presented here yields for the planar structure of Ag_5 lower energy than for the trigonal bipyramid which is in agreement with earlier findings [157]. Similarly according to present and previous results [157] for Ag_7, the pentagonal bipyramid is considerably lower in energy than the bicapped trigonal bipyramid with C_{3v} symmetry. The situation is different for Ag_6 and Ag_8. As shown in Figure 6.1 the planar trapezoidal D_{3h} structure of Ag_6 corresponds to the global minimum while the flat pentagonal pyramid C_{5v} and the threedimensional C_{2v} structure are higher lying isomeric forms with well separated

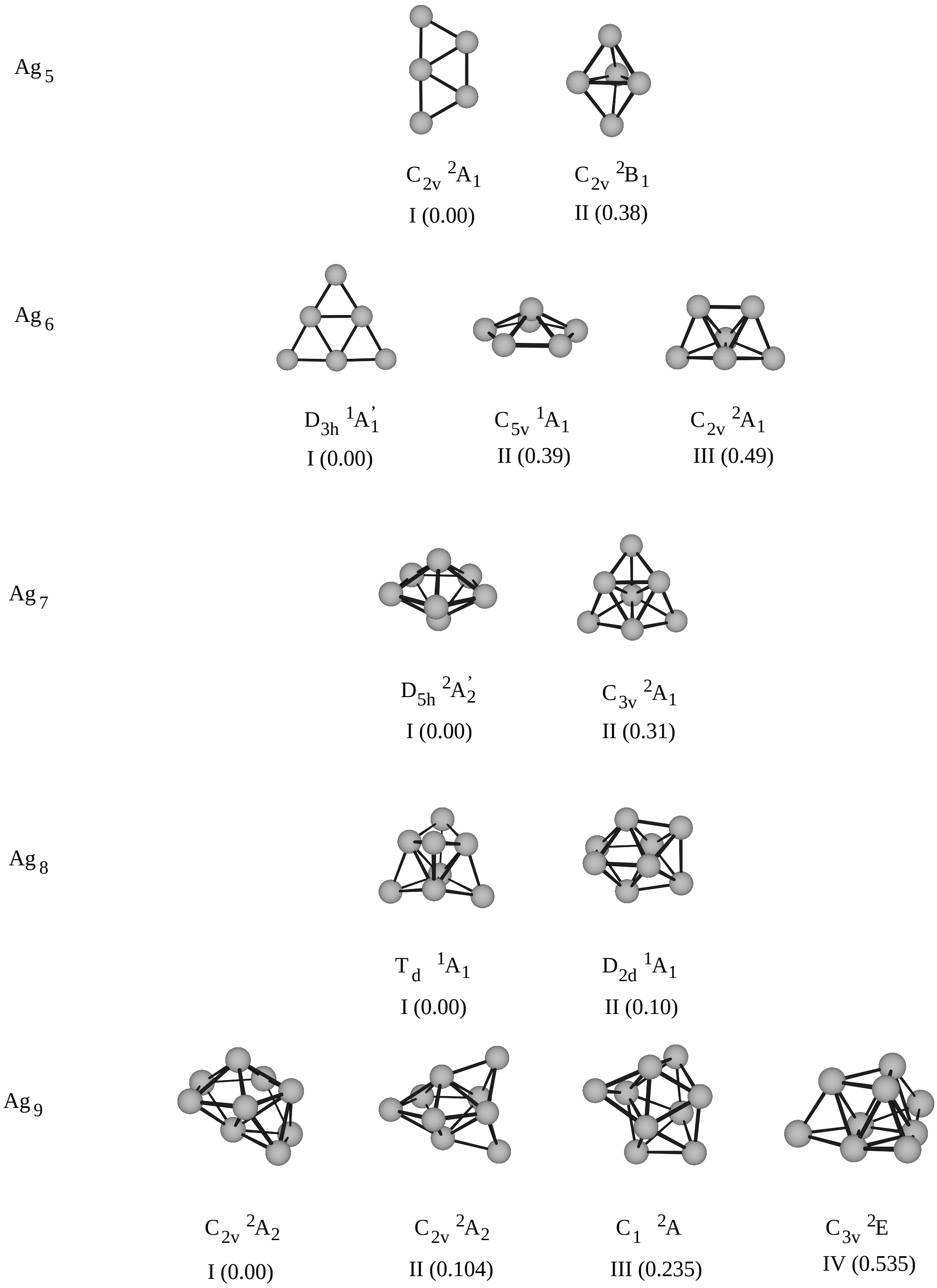

Figure 6.1: CCSD optimized geometries of the Ag_{5-8} clusters and BP86 optimized structures of Ag_9 using 11e-RECP with associated AO basis set. Labels of the point group and the ground state are given below structures together with relative energies in eV with respect to the most stable structure. The isomeric forms for the same cluster size are numbered as I-IV.

Table 6.1: Ground state energies of the DFT- and CCSD-optimized Ag_n (n=5-8) clusters.

Cluster[a]	Sym	State	E_{DFT} (au)	ΔE[b] (eV)	E_b/n (eV)	E_{CCSD} (au)	ΔE[c] (eV)	E_b/n (eV)
Ag_5(I)	C_{2v}	${}^2A_1$	-194.943839		1.49	-187.409370		1.49
Ag_5(II)	C_{2v}	${}^2B_1$	-194.917626	0.71	1.35	-187.395445	0.38	1.41
Ag_6(I)	D_{3h}	${}^1A_1'$	-233.976683		1.69	-224.943828		1.72
Ag_6(II)	C_{5v}	${}^1A_1$	-233.962674	0.38	1.62	-224.929496	0.39	1.66
Ag_6(III)	C_{2v}	${}^1A_1$	-233.940361	0.99	1.53	-224.925687	0.49	1.64
Ag_7(I)	D_{5h}	${}^2A_2''$	-272.881915		1.34	-261.564692		1.65
Ag_7(II)	C_{3v}	${}^2A_1$	-272.870330	0.31	1.29	-261.55146	0.36	1.70
Ag_8(I)	T_d	${}^1A_1$	-312.004988		1.81	-300.005562		2.00
Ag_8(II)	D_{2d}	${}^1A_1$	-312.001480	0.09	1.80	-300.001887	0.10	1.99
Ag_9(I)	C_{2v}	${}^2A_2$	-349.234367		1.52			
Ag_9(II)	C_{2v}	${}^2A_2$	-349.230531	0.104	1.51			
Ag_9(III)	C_1	${}^2A$	-349.225705	0.235	1.49			
Ag_9(IV)	C_{3v}	${}^2E$	-349.214686	0.535	1.46			

[a] For geometries of clusters, (I), (II) and (III) label isomers according to the energy ordering.

[b] The DFT (BLYP) energy difference between isomers.

[c] The CCSD energy difference between isomers.

energies. These three structures are almost degenerate at the lower level of theory [157] with the energy ordering: $C_{5v} \leq D_{3h} \leq C_{2v}$. The energy ordering of the isomeric forms of the Ag_8 cluster seems to be even more sensitive on the details of the theoretical treatment. The highly symmetric T_d structure corresponds to the global minimum and the related D_{2d} structure to the local minimum in the framework of the CCSD or DFT approach with 11e-RECP (cf. Figure 6.1). In the earlier work, the HF geometry optimization yielded also $T_d < D_{2d}$ but the post HF correlation treatment inverted the energy ordering [157].

In order to determine whether the optimization of geometries at the correlated level of theory or/and the inclusion of d-electrons in correlation effects can change the energy ordering of isomers the DFT-BLYP geometry optimization with the 1e-RECP have been carried out. The results are independent from the inclusion of d-electrons in the correlation treatment for Ag_5, Ag_6 and Ag_7 clusters. In the case of Ag_8, the T_d structure is the global minimum only with the 11e-RECP in the framework of the CCSD or DFT methods. The results above indicate that d-electrons which are strongly localized at Ag atoms usually do not influence considerably structural properties. But in the case that isomeric forms assume closely related structures, like for Ag_8, an accurate determination of the energy ordering of isomers is more difficult and the inclusion of d-electrons in correlation treatments might be necessary. Notice that at the higher level of theory the global minima are well separated from the local ones (cf. for energy differences of isomeric forms Figure 6.1 and Table 6.1).

Due to the high computational demand the structures of the Ag_9 cluster have been optimized using RI-DFT procedure with BLYP functional. In the ground state four isomers close in energy have been obtained. The lowest energy structure with C_{2v} symmetry assumes a pentagonal bipyramid structure with two atoms capping two neighboring faces of one pyramid as shown in Figure 6.1. The second isomer is 0.104 eV higher in energy and has also a pentagonal bipyramid with two atoms capping two neighboring faces belonging to the different pyramids. The third isomer is a C_1 structure which can be obtained by capping one face of the D_{2d} structure in Ag_8 and is 0.235 eV higher in energy than isomer I. The fourth isomer has trigonal structure with C_{3v} symmetry (a section of the fcc lattice) and lies 0.535 eV higher in energy.

It should be emphasized that the most stable structures of Ag_{5-9} presented in this work have the same topologies as the ones corresponding to the global minima of sodium Na_n (n=5-9) clusters. This is also the case for trimers and tetramers as it has previously been pointed out [159].

6.3.2 Absorption spectra

The absorption spectra calculated with the EOM-CCSD and STEOM-CCSD methods for the most stable structures of Ag_{5-8} and with the RPA method for the most stable structure of Ag_9 are given in Figure 6.2 allowing to illustrate the changes in the leading features of the absorption patterns as a function of the cluster size. The absorption spectra calculated for the second isomers of Ag_5 and Ag_6 assuming three-dimensional (3D) structures are shown in Figure 6.3 in order to compare them with those obtained for the planar (2D) structures. From Figure 6.2 the influence of the addition of the single Ag atom i) within the planar cluster growth and ii) within the three-dimensional structural frame on the locations of transition energies with pronounced intensities and relative magnitudes of oscillator strengths for $Ag_{5,6}$ and Ag_{7-9} clusters, respectively, can be studied.

i) The significant change in spectroscopic patterns occurs between Ag_5 and Ag_6. For the planar structure of Ag_5 the single dominantly intense transition to the 5 $^2B_2$ state with $f_e \approx 1.6$ is located at 3.55 eV and five transitions with oscillator strengths ranging from 0.1 to 0.5 are distributed in a relatively narrow energy interval between 3.8 eV and 4.7 eV. The intense transitions (e.g. to the 8 $^2B_2$ state) in the Ag_5 (C_{2v}) spectrum are characterized by the leading configurations with excitations of the s- and not the d-electrons. For the planar structure of Ag_6, the transition to the 2 $^1E'$ state located at 3.7 eV with $f_e = 2.4$ gives rise to an even more pronounced single dominant peak due to the high symmetry. Only two transitions with low intensities, which are red and blue shifted with respect to the dominant one, are present in the energy interval up to 5 eV. The three configurations with excitations from doubly degenerate HOMO occupied by four s-electrons to LUMO and to LUMO + k contribute with weights up to ∼70% to the expansion of the wavefunction of the 2 $^1E'$ state with a dominant intensity.

ii) In the case of the three-dimensional D_{5h} structure of Ag_7, the transition to the 7 $^2E_1''$ with dominant intensity located at 3.9 eV is blue shifted by 0.2 eV with respect to the 2 $^1E'$ transition calculated for the planar D_{3h} form of Ag_6. Again the wavefunction of the 7 $^2E_1''$ state contains largest contributions from configurations with excitations involving singly occupied HOMO and doubly degenerate HOMO-1 orbitals (in other words s-electrons). Consequently, the leading features of spectroscopic patterns of the planar Ag_6 (D_{3h}) and the three-dimensional Ag_7 (D_{5h}) have common characteristics while the locations and intensities of weak resonances are different. The analogous situation has been found for the T_d structure of Ag_8. The excitations of s-electrons from the triple degenerate HOMO to LUMO + k are mainly responsible for the transition to the 5 $^1T_2$ state with the dominant intensity (f_e=3.8 eV) located at 4.16 eV. In addition to this dominant peak, the low energy transition to the 3 $^2T_2$ state exhibits considerable intensity ($f_e \sim 1$ eV). The transitions with weaker intensity at 4.58 eV and others above 5 eV are also valuable for the characterization of different structures. They are usually easier to obtain for the closed shell than for the open shell systems due to technical aspects. Notice that in Figure 6.2 the results for Ag_5 and Ag_7 clusters are available for transitions only until 5 eV.

For Ag_9 the absorption spectra for the lowest energy isomer shows one dominant transition at 3.92 eV and the lower intensity transitions are distributed in the blue and red region with respect to the dominant

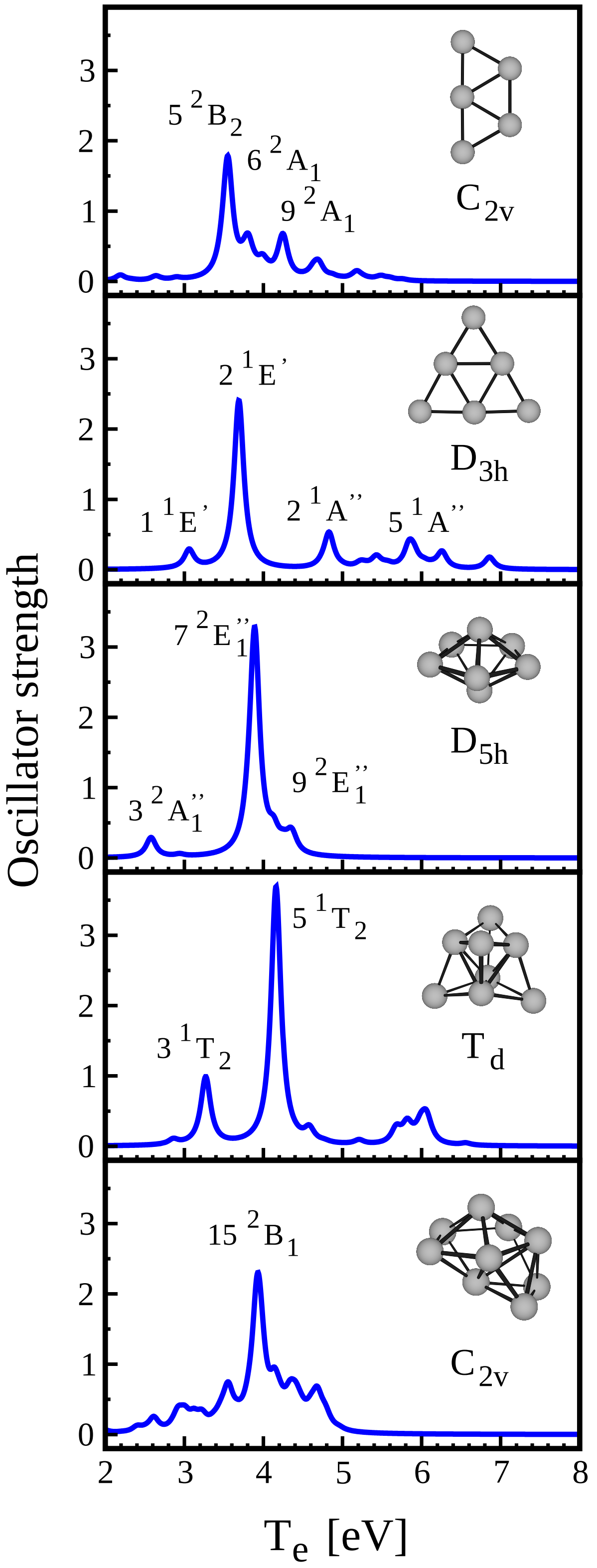

Figure 6.2: Absorption spectra of the most stable isomers of Ag_{2-8} obtained from EOM-CCSD and STEOM-CCSD methods using 11e-RECP and of the most stable structure of Ag_9 cluster obtained from the RPA method. The lines have been broadened using Lorentzian function with the width of 0.15 eV.

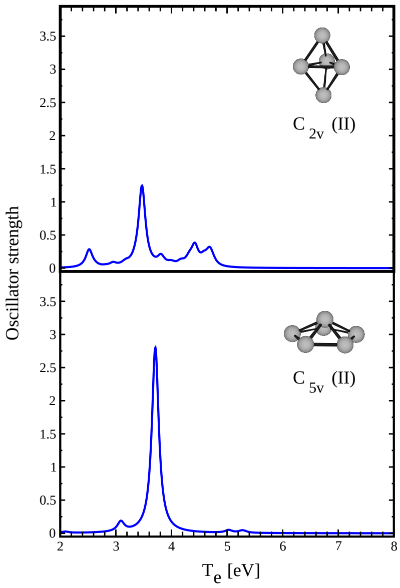

Figure 6.3: Absorption spectra for the second isomers of Ag_5 and Ag_6 calculated with the EOM-CCSD method. The transition energies are given in eV.

transition. In the blue region there are three main groups of transitions at 4.14 eV, ∼4.35 eV and 4.68 eV.

It should be emphasized that for the single dominant peak in all four cases of $Ag_6(D_{3h})$, $Ag_7(D_{5h})$, Ag_8 (T_d) and Ag_9 (C_{2v}) (cf. Figure 6.2), only three leading configurations with single excitations involving s- and not d-electrons contribute with the weights up to 70% in the expansion of the wavefunctions. Moreover in each case the same linear combination of configurations with different sign and magnitudes of coefficients can be found in the expansion of wavefunctions of the states to which transitions with considerably weaker intensities have been calculated. This confirms that the spectroscopic patterns of Ag_n (n=5-9) clusters are due to interference phenomena known for molecules [1]. Due to the common structural and related electronic properties the absorption spectra of Na_n (n=5-9) and Ag_n (n=5-9) exhibit striking similarities in leading features which will be addressed later. However, although the d-electrons of Ag atoms are not directly involved in excitations of the leading configurations contributing to states for which intense transitions have been calculated, their inclusion in the correlation effects is mandatory for the accurate determination of the transition energies and can be attributed to the polarization of the d-electrons. The calculations correlating only s-electrons yield too large transition energies. Consequently, any 1e-RECP is not suitable for predicting the absorption spectra of silver clusters independently from the choice of the correlation treatment.

The calculated absorption spectra for the second isomers of Ag_5 and Ag_6 clusters which assume three-dimensional structures are presented in Figure 6.3. From the comparison of their patterns with those obtained for the planar structures of Ag_5 and Ag_6 (cf. Figure 6.2), the conclusion can be drawn that the main difference between spectra of two isomers for the given cluster size is reflected in the locations and intensities of weaker resonances. This is particularly the case for Ag_6 since the flat pentagonal bipyramid with C_{5v} symmetry is closely related to the planar D_{3h} form, and therefore dominant resonances for both structures are located at ∼3.7 eV. In contrast, the spectra obtained for both C_{2v} isomers of Ag_5

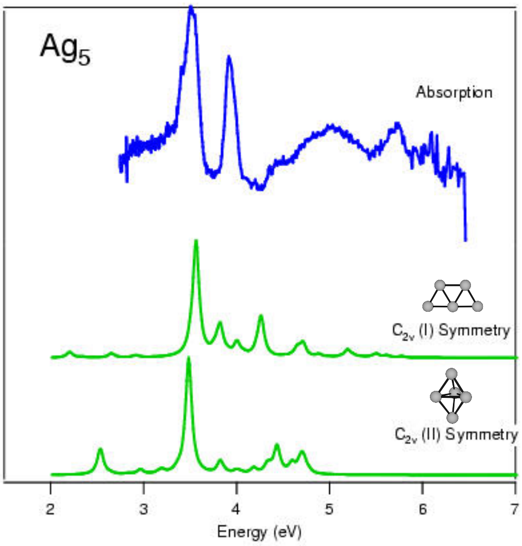

Figure 6.4: Comparison between the calculated spectra for the two lowest isomers of Ag_5 and the experimental absorption spectrum measured in Argon matrix. Experimental results have been taken from Reference [252]. In order to take into account the shift of the lines due to the Argon matrix the experimental spectrum has been shifted for 0.20 eV to the blue.

having planar (2D) and three-dimensional (3D) structures differ from each other mainly in the locations of transitions with moderate intensities. The findings above show clearly that the identification of the structure, which is responsible for the recorded spectrum, is possible, if the measurements have been carried out in a sufficiently large energy interval so that in addition to the dominant resonances other features of spectroscopic patterns can also be revealed. This is particularly important in the case that the isomers assume related structures.

6.4 Comparison of absorption spectra with experimental findings

6.4.1 Ag_5 and Ag_7

In summary, the spectroscopic patterns of Ag_n (n=5-9) obtained for the most stable structures (cf. Figure 6.2) exhibit a single dominant peak located in the region between 3.5 and 4.2 eV and a number of transitions with low intensities at very different locations for each cluster size which can be used as a fingerprint in the identification of the structures. The absorption spectra of small mass selected Ag_n (n=2-21) clusters embedded in solid argon have been measured in the range of 2.5-6.2 eV [253, 252]. The trend concerning dominant peaks calculated here is in a very good agreement with these early experimental findings, however the resolution of the fine structure is generally not sufficiently high to allow unambiguous structural identification in all studied cases when compared with calculated spectra. Moreover, during the deposition process a cluster fragmentation can occur and the fragments can also contribute to the absorption features. As an illustration the theoretical absorption spectra of Ag_5 and Ag_7 are compared with experimental data in Figures 6.4 and 6.5. The experimental spectra have been shifted for 0.25 eV to the blue in order to take into account the matrix shift and allow comparison with the spectra calculated for the gas phase clusters. In the case of the Ag_5 cluster both lowest energy isomers with the planar trapezoidal and three-dimensional trigonal bipyramid structure show spectral features which are in very

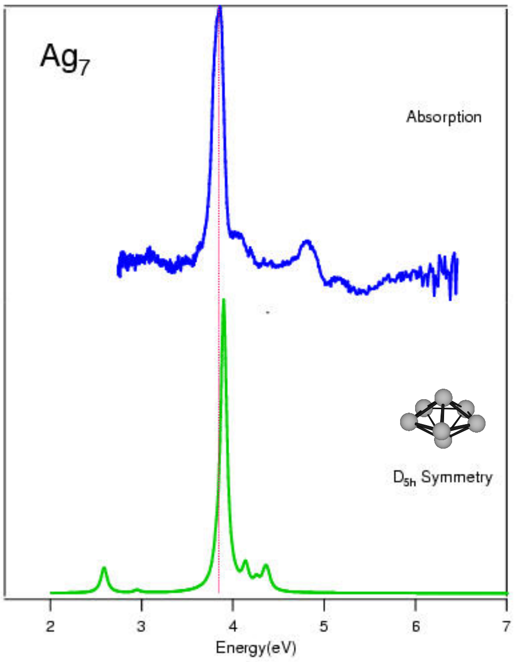

Figure 6.5: Comparison between the calculated spectra for the two lowest isomers of Ag_7 and the experimental absorption spectrum measured in Argon matrix. Experimental results have been taken from Reference [252]. In order to take into account the shift of the lines due to the Argon matrix the experimental spectrum has been shifted for 0.20 eV to the blue.

good agreement with the experimental spectra (compare Figure 6.4). However, due to the fact that both structures are energetically well separated (0.38 eV) the measured features can be assigned to the most stable isomer.

In Figure 6.5 the experimental and calculated spectra for the lowest isomer of Ag_7 with the pentagonal bipyramid structure are compared. Both experimental and theoretical spectra show one dominant peak at ∼3.9 eV and additional weaker transitions located at ∼4.15 eV which allow to assign the measured features to the most stable isomer of Ag_7 which is energetically well separated from other higher energy isomers.

6.4.2 Ag_8

A very important issue concerning the absorption spectroscopy on metal clusters is isomer selectivity. The molecular beams of size selected clusters are in general not formed from a single isomer. This is in particular true if the clusters are formed by a sputtering source which leads to the clusters with very high temperatures. Even in the case when the clusters are cooled by adiabatic expansion or collisions with a low temperature gas such as helium, they can be trapped in a geometry which does not correspond to the true minimum energy configuration. One main difficulty is that usually the measurements of the optical absorption of size selected clusters in a beam or trapped in a matrix reflects the sum of different isomers present. This is illustrated for the Ag_8 cluster in Figure 6.6. The absorption spectra for the T_d and D_{2d} isomers are shown in green and yellow lines respectively. The two isomers are very closely related since the isomerization from the T_d structure to the D_{2d} structure involves only the formation of one bond between the atoms of the outer tetrahedron and breaking of one bond of the inner tetrahedron. However,

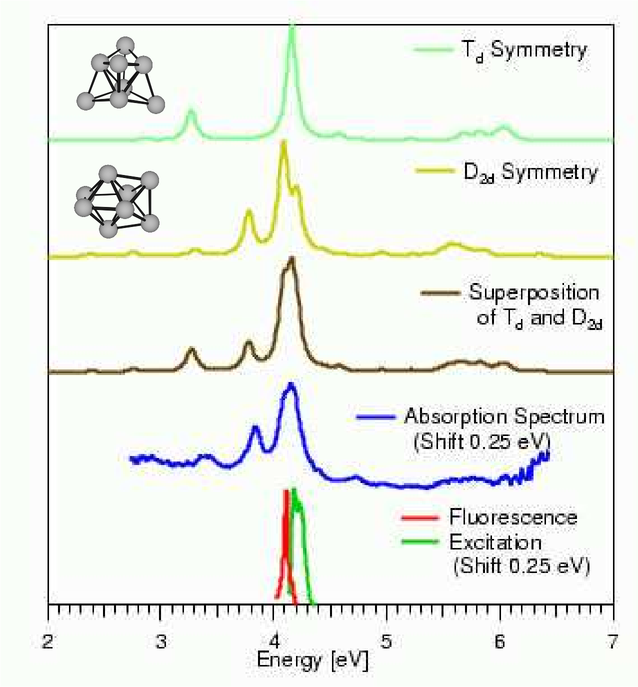

Figure 6.6: Comparison of the calculated absorption spectra for T_d (green) and D_{2d} structures (yellow) of Ag_8, their superposition (brown) with experimental absorption spectrum (blue) [252]. Excitation spectrum and the observed fluorescence band are shown in the bottom panel. Experimental spectra have been shifted to the blue for 0.25 eV in order to account for the matrix effect

the spectroscopic patterns of the two isomers differ considerably. The measured absorption spectrum can be fully explained by assuming that during the deposition process both isomers are present in the matrix and that the measured spectrum is a superposition of spectra corresponding to both isomers. The amounts of the isomers present can be determined by fitting the recorded absorption profile (blue line) to the weighted sum of the absorption spectra of both isomers. The result of fitting is shown in brown line and reproduces perfectly the measured absorption profile with 60% contribution of the T_d isomer and 40 % contribution of the D_{2d} isomer. Recently, a very narrow fluorescence line for Ag_8 clusters trapped in argon matrix have been observed [234] and the excitation spectrum has been measured by changing the excitation wavelength while recording the fluorescence intensity at the position of a fluorescence line (compare lowest panel of Figure 6.6). Due to the narrowness of the fluorescence line it is assumed that fluorescence comes from a single isomer and therefore the corresponding excitation spectrum should also belong to a single isomer. As can be seen from the lowest panel of Figure 6.6 the excitation line is slightly splitted presumably due to the deformation of the T_d structure caused by the Argon matrix. In order to explain these experimental findings the relaxation in the 5^1T_2 state with dominant intensity in the isomer I has been studied by performing geometry optimization at the RPA level of theory. The geometric relaxation in excited state lowers the energy by 0.2 eV which is in a good agreement with the observed Stokes shift between the fluorescence and excitation lines. The additional support for these findings came from recent measurements using resonant two-photon ionization technique [249] in helium droplets shown in Figure 6.7 and which is discussed below.

In the case of the T_d structure the calculated resonance with the dominant intensity involving transition to the 3 $^1T_2$ state located at 4.16 eV is blue shifted with respect to the measured peak located at 4.0 eV. The low energy transition to the 2 $^1T_2$ state calculated at 3.27 eV with considerable intensity has not been recorded. The lifetime of the low energy resonance is not expected to be shorter than the

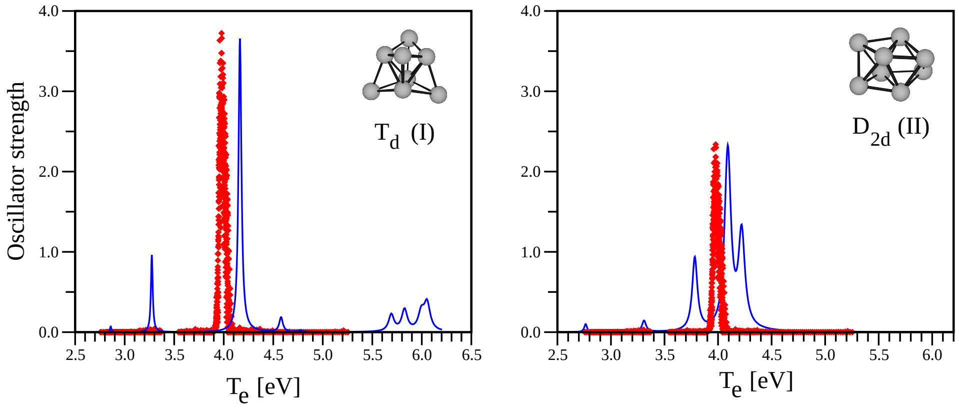

Figure 6.7: Comparison of the optical spectrum of Ag_8 obtained in helium droplet using resonant two-photon ionization (Ref. [249]) and calculated absorption spectra for T_d (left) and D_{2d} (right) structures of Ag_8.

lifetime of the dominant one because of similar nature of excitations found for both resonances. Since the R2PI-technique uses the nanosecond pulses to populate the excited levels both resonances should be detected. It seems that the low energy transitions might not be accessible in this experiment because the He-environment increases the ionization potential of the silver clusters above the threshold which allows the detection.

In contrast, the calculated spectrum for the D_{2d} structure (cf. Figure 6.7) is characterized by two almost degenerate transitions to the 3 $^1B_2$ and 6 ^1E states located at 4.08 and 4.09 eV with $f_e = 0.78$ and 1.59, respectively, by the one moderately blue shifted transition to the 6 ^1E state at 4.21 eV with $f_e = 1.18$ and by the red shifted transition to the 2 $^1B_2$ state at 3.78 eV with $f_e = 0.91$, all of them lying in a relatively narrow energy interval. In addition two weak resonances at the lower energies (2.76 and 3.31 eV) have been obtained. The right hand side of the measured peak is broader than the left one which is very steep and actually excludes the presence of an additional red shifted resonance. This means that in the case that the resonance related to the transitions to the 2 $^1B_2$ state at 3.78 eV were present, it should have been recorded in this energy interval. Since the nature of excitations of the 2 $^1B_2$ state is very similar to the one of the 3 $^1B_2$ state, similar lifetimes are also expected which means that the nanosecond pulses used in the experiment should have allowed to detect both resonances. The broadening of the measured intense peak towards the higher energies does not exclude the presence of an additional resonance which might arise due to the geometric distortion caused by the surrounding, which will be discussed below.

In order to clarify the blue shifts for calculated locations of the intense transitions with respect to experimental findings in different environment, either in a matrix or in a helium droplet, as well as to interprete the shape of the dominant peaks obtained in different experiments, several model calculations at the RPA level of theory have been carried out. The purpose was to gain a better understanding of the influence of the environment on the spectral features and not to perform quantitative simulation of the environment. i) For this purpose the T_d structure has been distorted in order to lower the symmetry and ii) the geometric changes were introduced involving formation and breaking of the bonds which transform the T_d into the D_{2d} structure. The following results have been obtained: i) Distortion of the T_d structure elongating one of the bond distances from the outer and one from the inner tetrahedron by 0.2 Å gives rise to the red shift of all peaks, the dominant one and less intense ones by 0.3 eV. This is due to destabilization of the equilibrium T_d structure which is reflected in the decrease of HOMO-LUMO and HOMO-LUMO + k energy gaps leading to the lowering of transition energies. Moreover a distortion of the T_d structure

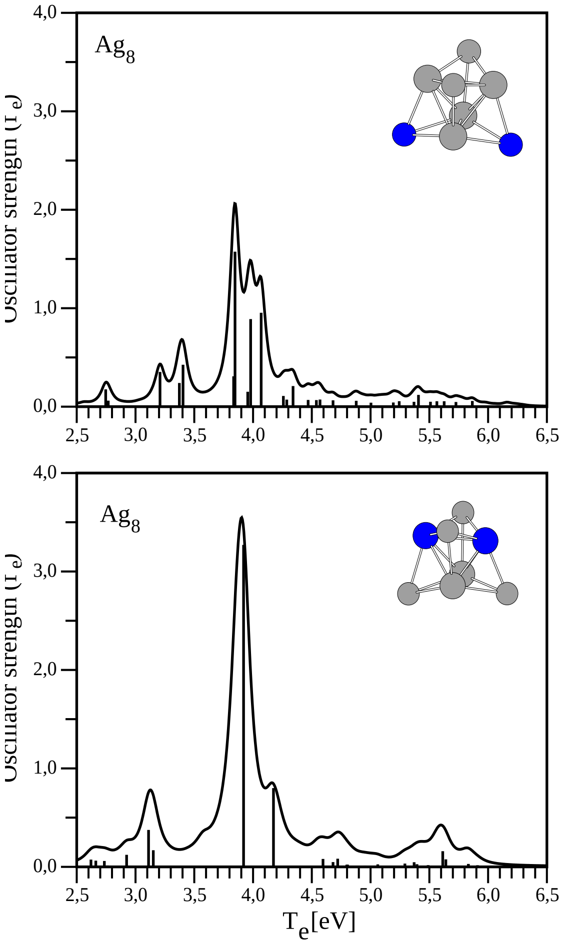

Figure 6.8: Absorption spectra for distorted T_d structures obtained from RPA calculations by shortening one distance between two atoms (blue circles) of the outer tetrahedron relating T_d and D_{2d} structures (upper panel) and by elongating one distance between two atoms (blue circles) of the inner tetrahedron.

causes also the splitting of the T-states into transitions very close lying in energy within 0.01 eV. In other words, any interaction with the environment which elongates the bond distances and destabilizes equilibrium structures can cause the red shift of transitions. ii) Geometric changes relating the T_d and the D_{2d} structures illustrate the conditions under which spectroscopic pattern for the D_{2d} structure arises, characterized by the resonance at ∼3.8 eV and by the dominant peaks located in the energy interval of 4 - 4.3 eV (cf. Figure 6.7). Deformation of the T_d structure achieved by shortening the distance between two atoms of the outside tetrahedron gives rise to the spectroscopic pattern shown on the upper panel of Figure 6.8. It is characterized by the resonances with moderate intensities located at ∼ 3.2 and ∼ 3.4 eV, by the dominant peak located at 3.84 eV and by two transitions with considerable oscillator strengths at 4.0 and 4.07 eV. Of course additional rich fine structure due to the lowering of the symmetry is also present. In other words, the distortion described above of the T_d structure gives rise to the spectroscopic pattern which is qualitatively similar to the one obtained for the D_{2d} structure. Therefore, the influence of the environment has to be considered carefully in order to assign structural properties to the measured features.

The second type of distortion of the T_d structure involving elongation of the bond between two atoms of the inner tetrahedron gives rise to the red shift of the dominant peak. Moreover the energy difference between the dominant peak and the higher energy transition with lower oscillator strength decreases in comparison with the one obtained for the stable T_d structure. In fact the absorption spectrum obtained

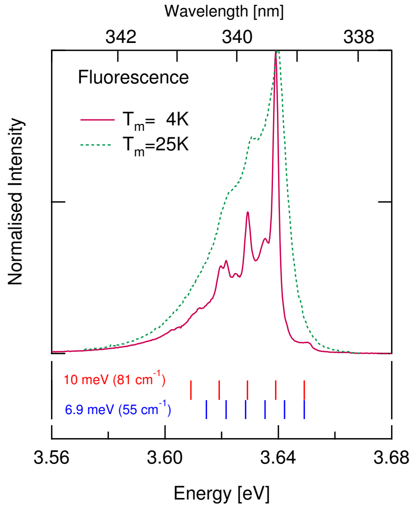

Figure 6.9: Fluorescence spectra of Ag_9 at 25 K and 4 K (laser excitation 4.03 eV). Cooling the sample down unravels the details of vibrational progression of the ground state of Ag_9. Two vibrations have been identified and are indicated in the lower part of the figure. Accordingly, the fluorescence peak origin is at 3.649±0.001 eV.

by elongating one bond of the inner tetrahedron of the T_d structure presented in Figure 6.8 indicates that related distortions might be responsible for the double-peak features in the energy interval of 3.95 - 4.05 eV measured by the R2PI in a He-droplet [249] and in the recent laser-induced fluorescence experiments on Ag_8 in Ar-matrix [234].

6.4.3 Ag_9

An isomer selective spectroscopy has recently been accomplished on the Ag_9 cluster where a narrow fluorescence line and a well defined ground state vibrational structure have been observed giving a strong indication that the fluorescence is associated to a single isomer [254]. This allowed to measure the excitation spectrum by changing the excitation wavelength while recording the fluorescence intensity at the position of the fluorescence line. The comparison between the absorption spectrum measured in an argon matrix and the excitation spectrum is shown in Figure 6.10. Although the absorption spectrum shows broad features due to a contribution of different isomers, the excitation spectrum has a well defined four peaks structure and is isomer selective. The dominant excitation peak is located at 3.69 eV and is very close to the fluorescence peak. Three different narrow peaks of lower intensities are located at 4.02, 4.20 and 4.34 eV. The small Stokes shift (0.04 eV) between the excitation and fluorescence lines indicates that for both the same electronic states is responsible. In order to clarify these experimental findings absorption spectra for the four low lying isomers of Ag_9 have been calculated and the geometry optimization in the excited state has been performed by using numerically calculated gradients combined with the conjugated gradient method. The calculated absorption spectra for different isomers are shown in Figure 6.11. They exhibit very distinct spectral features and allow for the interpretation of the measured data. In particular, the absorption spectrum of isomer I shows one dominant transition at 3.92 eV corresponding to the measured dominant band in the excitation spectrum shifted by 0.25 eV to account for the influence of the argon matrix. Lower intensity transitions are distributed in the blue and red region with respect to the dominant transition. In the blue region the calculated intense transition at 4.14 eV, few close lying transitions at ∼4.35 eV and the one located at 4.68 eV could correspond to the weaker features measured in the excitation spectrum. While the position of the most dominant peak is very well

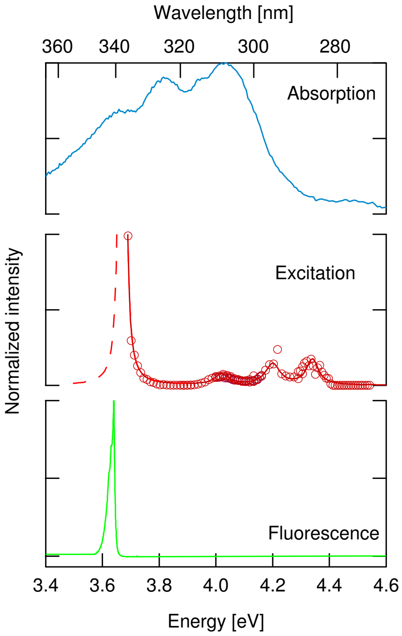

Figure 6.10: Absorption, excitation and fluorescence spectra of Ag_9 in an argon matrix.

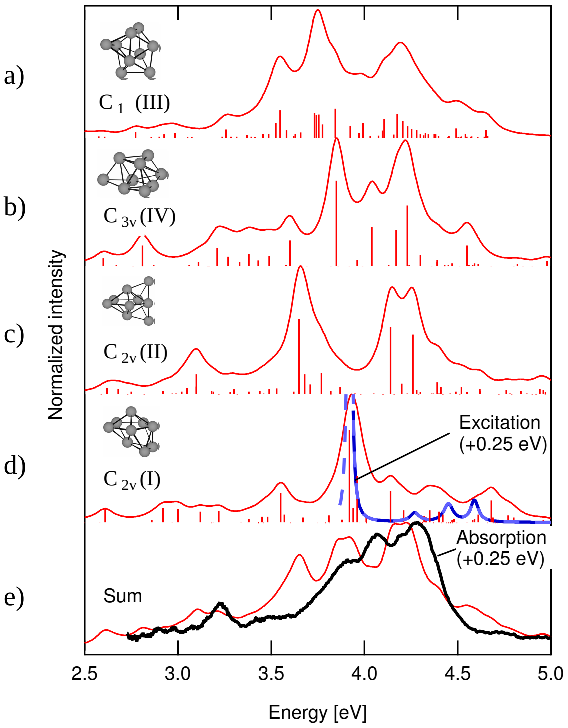

Figure 6.11: (a-d) Calculated absorption spectra for the four lowest isomer of Ag_9, (e) Measured excitation spectrum shifted by 0.25 eV to account for the matrix shift. (f) Measured absorption spectrum of Ag_9 shifted by 0.25 eV compared to the sum of the different spectra with the following weights: C_{2v}(I) 26 %, C_{2v} (II) 37 %, C_{3v} (IV) 37 %.

reproduced in the framework of the RPA method the positions of the secondary peaks are less accurate. This is due to the fact that the RPA method cannot describe accurately those transitions in which doubly excited configurations have significant contributions. The calculated spectra for other isomers do not match the most intense transition, which supports the conclusion that the isomer I is responsible for the measured fluorescence and excitation spectra. In the lowest part of Figure 6.11 the absorption spectrum in an argon matrix is compared with the weighted sum of the absorption spectra of isomers I, II and IV showing a fairly good agreement. This supports the assumption that a sample of Ag_9 clusters deposited in an argon matrix is indeed composed of several isomers.

In order to determine the position of the fluorescence band, a geometry optimization of the excited state with the largest oscillator strength, corresponding to the vertical transition at 3.92 eV of isomer I, has been carried out. It has been found that the ground state and the 16 $^2B_1$ excited states have related structures with the same symmetry. The calculated lowering of energy with respect to the vertical transition is equal to 0.19 eV which is quantitatively larger than the experimental finding of 0.04 eV . This difference lies within the accuracy of the method used. In addition, since the ground and excited state structures have the same symmetry, the structural relaxation in the ground state after the fluorescent deexcitation of the first excited state should take place along totally symmetric normal modes in the ground state. Harmonic vibrational frequencies for the ground state structures of Ag_9 have been calculated. Altogether seven totally symmetric vibrational modes have been obtained with frequencies of 50.7, 61.3, 79.9, 92.1, 101.3, 142.3 and 159.2 cm^{-1}. The low lying vibrational modes with 50.7 and 79.3 cm^{-1} are in perfect agreement with experimentally observed progressions in the fluorescence spectrum with spacing of 55 and 81 cm^{-1}(compare Figure 6.9). In summary, it has been shown that the narrow fluorescence line of Ag_9 cluster in an argon matrix, and the corresponding excitation spectrum can be assigned to a single lowest energy isomer with C_{2v} symmetry. In principle, the laser induced fluorescence spectroscopy in combination with accurate theoretical methods can provide a way to perform isomer selective spectroscopy on clusters.

6.5 Conclusions

The absorption spectra of Ag_{5-9} clusters calculated for the most stable structures assuming 2D- (Ag_5 and Ag_6) and 3D-(Ag_7, Ag_8 and Ag_9) forms are most suitable for comparison with measurements in the gas phase and at low temperature, allowing to assign the structures to the measured features. The spectroscopic patterns are characterized by a dominant peak located in the energy interval between 3.5 and 4.1 eV, dependent on the cluster size. Addition of the single atom causes blue shift of this resonance by 0.2 eV. The weaker resonances are distributed in a larger energy interval and their location and intensities are strongly dependent on the individual structural features. The excitations of d-electrons are not actively contributing to the intense transitions, but their contribution is of basic importance for the accurate locations of transitions. The spectra can be interpreted in terms of interference phenomena typical for molecules. Due to common structural properties of Ag_{5-8} and Na_{5-8} clusters as well as due to the leading role of the s-electron excitations in both cases, the spectroscopic patterns exhibit similar features with exception of pentamers (cf. Reference [1]). Of course the transition energies for silver cluster are blue shifted by more than 1 eV with respect to those of Na_n and quantitative differences are present.

The experimental findings of the optical response in the gas phase are not yet available for the cluster sizes considered in this work. The measurements in a solid matrix [245, 246] or a helium droplet [248, 249] give rise to the red shifts of resonances in comparison with the calculated ones for the most stable cluster structures. This is an important finding, in particular concerning the experiments in a He-droplet which is assumed to be an ultracold and weakly interacting medium for metallic clusters. The environment clearly destabilizes structures due to the interaction with the silver atoms and therefore causes a decrease of HOMO-LUMO and HOMO-LUMO + k gaps and consequently a decrease of transition energies as illustrated in this work. Interaction with the rare gas atoms or He-atoms can also deform the structures with higher symmetry which might additionally influence features of the spectroscopic pattern. In fact it has been found that although a large part of helium is in a superfluid state [248], the friction within a droplet can lead to large deformations forming chains from molecules with large dipole moments [255]. The absorption spectra calculated for the models of geometric distortions of the T_d structure of the Ag_8 cluster presented in this contribution allow the interpretation of the available experimental findings. According to our results, a distorted T_d structure of Ag_8 is responsible for the measured intense resonance in the He-droplet and in the Ar-matrix.

An important aspect of optical properties of silver clusters is their ability to fluoresce, which indicates that the lifetime of the dominant resonance is not extremely short and proves that the excitations have a discrete molecular character. Calculations of geometry relaxation in the excited states of Ag_8 and Ag_9 clusters confirm these findings. Moreover, isomer selective spectroscopy based on laser induced fluorescence together with ab initio calculations allows to identify the structures of the isomers responsible for the measured excitation patterns and fluorescence.

Chapter 7

Theoretical investigation of the ultrafast NeNePo spectroscopy of coinage metal clusters

7.1 Motivation and introduction

Clusters as a finite aggregates of atoms represent ideal systems in which the evolution of the dynamic features can be studied as a function of the size. One of the important objectives of cluster science is the study of structural and dynamical properties of mass selected neutral clusters. A very convenient experimental technique which allows to achieve this goal is femtosecond negative ion-to neutral-to positive ion (NeNePo) spectroscopy developed by Wöste, Berry and coworkers [24, 256, 257, 258] which can be also called charge reversal spectroscopy. The basic idea of this method consists in preparing and mass selecting anionic clusters which are then subjected to the photodetachment by an ultrashort laser pulse. In this process a nonstationary state in the neutral electronic ground state is reached which subsequently evolves on the neutral potential energy surface. The time evolution is probed by a time delayed ultrashort laser pulse which ionizes the system. The signal which is experimentally detected is the cationic ion current. This process is schematically shown in Figure 7.1. The first experimental application of this technique was made by Wöste and Berry [24] in the study of the $Ag_3^-/Ag_3/Ag_3^+$ system. Parallel to the experimental studies a general theoretical approach for simulation of NeNePo spectra based on the combination of ab initio quantum chemical methods with Wigner-Moyal representation of the vibronic density matrix has been developed in the Bonačić-Koutecký group [126, 131, 132, 163, 259, 260, 261, 262] as described in Section 2.5.3. In the study of the $Ag_3^-/Ag_3/Ag_3^+$ system three potential energy surfaces corresponding to the anionic, neutral and cationic state have been precomputed and used to carry out classical molecular dynamics simulations [126, 259]. This approach allowed accurate simulations of pump-probe signals with temperature dependent initial conditions and it has revealed the processes which are involved in the ground state dynamics induced by the photodetachment. Furthermore, the time scale for geometric relaxation has been determined and the IVR process has been understood in detail. In addition, it has been found that experimental results can be reproduced only if continuum for the ionization in anionic and cationic state was introduced. In this case the geometric relaxation processes and the IVR were smeared out in the signals. Therefore it was suggested that experiments under zero electron kinetic energy (ZEKE) should be developed which allows to determine the time scales of different processes. The results of the semiclassical simulations have been fully confirmed by the quantum dynamics simulations [263] which stimulated us to apply the semiclassical approach on other systems.

The main goal of the work presented here was to extend this approach to larger systems in which the precalculation of the potential energy surfaces is not possible and to establish general conditions under which different processes can be identified in the NeNePo spectroscopy [163, 260]. Since standard quantum dynamical simulations based on the numerical solution of the time dependent Schrödinger equation are not feasible in systems with more than three degrees of freedom and semiclassical approach in the case of Ag_3 provided almost identical NeNePo signals as full quantum dynamics [263], in which the separation of modes into active ones and the bath is not possible, which is particularly the case in metal clusters, here semiclassical simulations have been performed.

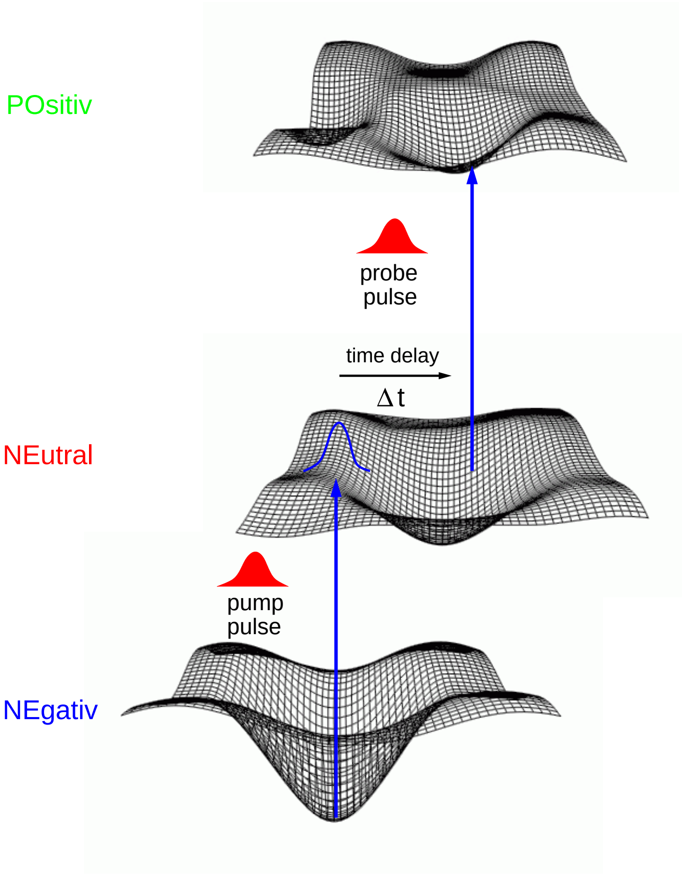

Figure 7.1: General scheme of the NeNePo pump probe spectroscopy. The system is prepared in the anionic state. Then the pump pulse detaches the electron leaving the neutral clusters in a non-equilibrium state (blue curve) which subsequently evolves on the neutral potential energy surface. The dynamics is probed by time delayed ionization and cationic clusters are detected by mass spectrometry.

For this purpose a combination of the ab initio MD carried out "on the fly" with semiclassical Wigner distribution approach has been employed. In this chapter simulation and analysis of NeNePo signals for the mixed Ag_2Au trimer and for Au_4 and Ag_4 tetramers will be presented. The choice of these systems has been made from three different points of view:

- The study of dynamics of mixed coinage metal trimer starting from the nonequilibrium state after one-electron photodetachment of linear nonsymmetrical Ag_2Au involves an isomerization process from the linear geometry which is a transition state in the neutral electronic ground state to the triangular structure in which a hetero Ag-Au bond is formed. This process offers an opportunity to study the effect of a heavy gold atom on the dynamics in the hetero-trimer involving large amplitude motion.

- Up to date structural properties of mass selected neutral gas phase coinage metal clusters have not been directly experimentally accessible. In the case of the $Ag_4^-/Ag_4/Ag_4^+$ system ab initio calculations show that the most stable structures in the anionic state and in the neutral state assume related rhombic forms. Therefore, it can be expected that the information about vibrational frequencies of the neutral Ag_4 cluster can be resolved in the NeNePo-ZEKE-like experiments since the non-equilibrium state reached after photodetachment is close to the global minimum in the neutral state and therefore the photodetachment process excites the vibrational modes of the neutral global minimum structure. In this case the NeNePo-ZEKE-like technique can directly provide structural information which can then serve as a fingerprint for identification of the structure of neutral clusters which in an important task. The corresponding vibrational spectra can be obtained from the time resolved spectrum by performing Fourier transform.
- In contrast to the silver tetramer anionic and neutral Au_4 clusters assume different geometries. In the case of anionic Au_4^- the most stable structure is either the linear chain or the related almost linear zig-zag structure, dependent on the theoretical treatment, while the neutral Au_4 assumes rhombic or T-form structure. Therefore, the simulation of NeNePo signals should enable to study the cluster isomerization process and to determine time scales for the involved processes which can provide valuable insight into the intracluster relaxation processes which is particularly important in the context of cluster reactivity.

Based on the semiclassical Wigner distribution method presented in Section 2.5.3 the method used for the simulation of NeNePo signals will be outlined. In the Section 7.2.1 the simulated NeNePo spectra for Ag_2Au will be analyzed and compared with the experimental data. The scope of the NeNePo method will be illustrated on the pure gold and silver tetramers which present, due to their different structural properties, ideal model systems to show the ability of the NeNePo spectroscopy to provide both structural and dynamical information about neutral clusters.

7.2 Wigner distribution approach for the simulation of NeNePo spectra

The most general theoretical approach for simulation of pump-probe spectra would require the solution of the time dependent Schrödinger equation (or Liouville-von Neumann equation for the density operator evolution) equation for the molecular system along with the interaction with the laser electromagnetic fields. However, the applicability of this approach is limited to systems with a small number of degrees of freedom (typically three or less) in which the global potential energy surfaces are known.

In order to treat moderately complex systems in which no separation of degrees of freedom into the active ones and the bath is possible an alternative semiclassical approach based on the Wigner representation of the density operator has been developed in the Bonačić-Koutecký group [126, 259, 163, 261, 260, 131, 132] and is described in Section 2.5.3. In his lower order this approach ultimately requires the propagation of the ensemble of classical trajectories which can be carried out "on the fly" (without precalculation of the potential energy surface) and using efficient and accurate quantum chemical methods such as DFT methods. The electronic structure calculations and classical trajectory simulations on $Ag_2Au^-/Ag_2Au/Ag_2Au^+$

system have been performed using 19e-RECP from the Stuttgart group [174] together with the BP86 density functional [85, 175] . As shown in Chapter 3, the 1e-RECP [163] gives reliable description of the structural properties and the energetics of the gold and silver tetramers at a much lower computational demand than the 19e-RECP. Therefore the 1e-RECP together with the BLYP functional [85, 86] have been employed for the classical MD simulations in the $Au_4^-/Au_4/Au_4^+$and $Ag_4^-/Ag_4/Ag_4^+$ systems.

Assuming gaussian pulse envelopes for the pump and probe pulses an analytic expression for time resolved NeNePo-ZEKE signals which is given by the total occupation of the cationic state can be derived (cf. Section 2.5.3):

$$\begin{aligned} S[t_d] \sim \int d\mathbf{q}_0 d\mathbf{p}_0 \int_0^\infty d\tau_1 exp\left\{-\frac{(\tau_1 - t_d)^2}{\sigma_{pu}^2 + \sigma_{pr}^2}\right\} \times \\ exp\left\{-\frac{\sigma_{pr}^2}{\hbar^2}[E_{pr} - V_{IP}(\mathbf{q}_1(\tau_1; \mathbf{q}_0, \mathbf{p}_0))]^2\right\} \times \\ exp\left\{-\frac{\sigma_{pu}^2}{\hbar^2}[E_{pu} - V_{VDE}(\mathbf{q}_0)]^2\right\} P_0(\mathbf{q}_0, \mathbf{p}_0) \end{aligned} \tag{7.1}$$

In the expression above, $E_{pu}(E_{pr})$ and $\sigma_{pu}(\sigma_{pr})$ are the excitation energies and durations of the pump (probe) pulses, t_d is the time delay between the pulses and $V_{IP}(\mathbf{q}_1(\tau_1; \mathbf{q}_0, \mathbf{p}_0))$ is the time dependent energy gap between cationic and the neutral electronic states calculated at the time τ_1 with corresponding coordinates $\mathbf{q}_1(\tau_1)$ on the neutral ground state with the initial coordinates and momenta $\mathbf{q}_0$ and $\mathbf{p}_0$ given by the anionic Wigner distribution $P_0(\mathbf{q}_0, \mathbf{p}_0)$ and $V_{VDE}(\mathbf{q}_0)$ are the vertical detachment energies of the initial anionic ensemble. The above expression suggests the following procedure for simulation of the NeNePo-ZEKE signals:

- First an ensemble of initial phase space points $(\mathbf{q}_0, \mathbf{p}_0)$ is generated by sampling the Wigner distribution function corresponding to the initial state. This can be done either for the single vibronic state or for the thermal ensemble invoking harmonic approximation in which the Wigner distribution functions can be calculated analytically. In this work initial conditions have been generated by sampling the canonical initial ensemble for which the Wigner distribution function of each independent normal mode has the form:

$$P(q,p) = \frac{\alpha}{\pi\hbar} exp\Big[-\frac{2\alpha}{\hbar\omega}(p^2 + \omega^2 q^2)\Big] \tag{7.2}$$

  where $\alpha = tanh(\hbar\omega/2k_BT)$ and ω is the normal mode frequency. This expression corresponds fully to the quantum mechanical density distribution and is suitable for low or moderate initial temperatures where anharmonic effects can be neglected. For higher temperatures where quantum effects of the initial distribution are not important but anharmonicities are, the initial phase space distribution can be obtained by sampling a long classical trajectory which is for long simulations expected to sample the canonical ensemble if the classical MD is carried out under constant temperature conditions. Since the momentum and coordinate distributions in Equation (7.2) are independent a gaussian random number generator has been used to generate the values of normal coordinates and momenta. These are subsequently transformed into the cartesian form since the propagation is performed by using classical equations of motion in cartesian coordinates. For the integration of the Newton's equations of motion the Verlet algorithm has been employed. The procedure described above generates a discrete ensemble of phase space points which are necessary for the MD simulations in the neutral state after the photodetachment process. The transition probabilities for the photodetachment process are given by the last exponential in Equation (7.1).

- In the second step the phase space ensemble is propagated on the neutral electronic state by solving the classical Hamilton equations of motion using forces calculated "on the fly". In parallel to the propagation of the initial ensemble, time dependent energy gaps between the neutral and the cationic state $V_{IP}(\mathbf{q}_1(\tau_1; \mathbf{q}_0, \mathbf{p}_0))$ are calculated for each trajectory. The probe step involves the transition to the cationic state whose probability is determined by the second exponential in Equation (7.1).
- The pump probe signal is calculated for each trajectory according to Equation (7.1) and the signals are averaged over the whole ensemble. The time resolution of the signal is determined by the pump-probe correlation function with the probe window located around the time delay t_d (first exponential in Equation (7.1)).

7.2.1 Nuclear dynamics and NeNePo-ZEKE signals of Ag_2Au

The $Ag_2Au^-/Ag_2Au/Ag_2Au^+$ system offers an opportunity to study the dynamics of a system in which after photodetachment a transition state in the neutral state is reached and subsequently an isomerization process is induced. In the framework of the 19e-RECP the most stable isomer in the ground state is the linear one with peripheral position of the gold atom (cf. Figure 7.2). The other linear symmetric isomer is 0.38 eV higher in energy. In the neutral Ag_2Au assumes a triangular structure. Both linear isomers found for the anionic states have in the neutral ground state two imaginary frequencies along the degenerate bending mode and represent transition states for the isomerization between equivalent triangular structures.

For the simulations the temperature of 20 K has been selected. Due to the low temperature and the large energy difference between the two isomers only the most stable isomer is populated and additionally it can be safely assumed that a harmonic approximation is valid under these conditions. Therefore the initial conditions for the MD simulations have been generated by sampling the canonical Wigner distribution in harmonic approximation according to Equation (7.2). The histogram of the vertical detachment energies (VDE) is shown in Figure 7.3 and exhibits almost a gaussian shape centered around 2.78 eV. [1] In the neutral state totally 420 trajectories have been propagated and the time-dependent energy gaps to the cationic state which are required for the simulation of the NeNePo-ZEKE spectra according to Equation 7.1 have been calculated. The snapshots of the neutral state dynamics up to 3.5 ps are shown in Figure 7.5. At t=0 a localized ensemble is prepared with a very narrow spread in the coordinate space corresponding to the low temperature of 20 K. After the photodetachment system reaches the transition state region in the neutral ground electronic state and starts to evolve "downhill". The dynamics up to 1 ps is mainly characterized by the broadening of the initial ensemble which is also reflected by divergent energy gaps to the cationic state shown in Figure 7.4. As seen from Figures 7.4 and 7.5 the isomerization process towards the triangular global minimum is completed in the interval between 1.5 and 2 ps. The onset of the isomerization is particularly well reflected in the time dependent energy gaps in Figure 7.4 in which the swarm of energy gaps changes from 7.5 eV to 6.5 eV within the first 2 ps and then all energy gaps oscillate in the interval between 6.1 and 6.5 eV corresponding to the vibrational dynamics within the triangular isomer I. Therefore, by adjusting the probe pulse energy essentially two different kinds of processes can be probed in the NeNePo-ZEKE signals. The probe-pulse energy between 6.5 eV and 7.5 eV probes the onset

---

[1] It should be pointed out that all 19e-RECP which have been tested in this work show a tendency to overestimate the vertical detachment energies and ionization potential. The VDE's have therefore been scaled with factor 0.927.

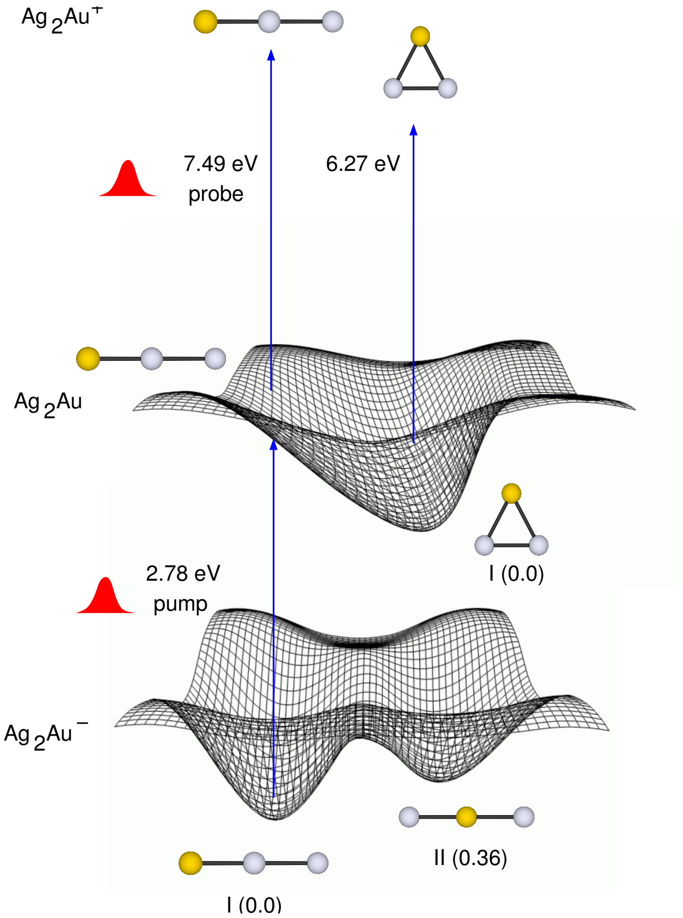

Figure 7.2: Scheme of the multistate femtosecond dynamics of Ag$_2$Au in the framework of the NeNePo pump-probe spectroscopy involving anionic, neutral and cationic states. Vertical excitation energies are given by arrows. All corresponding geometries of isomers are drawn. Numbers in parentheses are energies with respect to the ground electronic state of the most stable isomer.

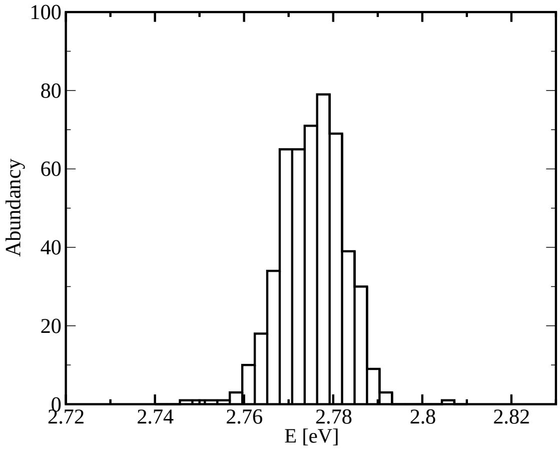

Figure 7.3: Histogram of the vertical detachment energies between the anionic and neutral Ag$_2$Au at 20 K initial temperature obtained from 500 initial phase space points.

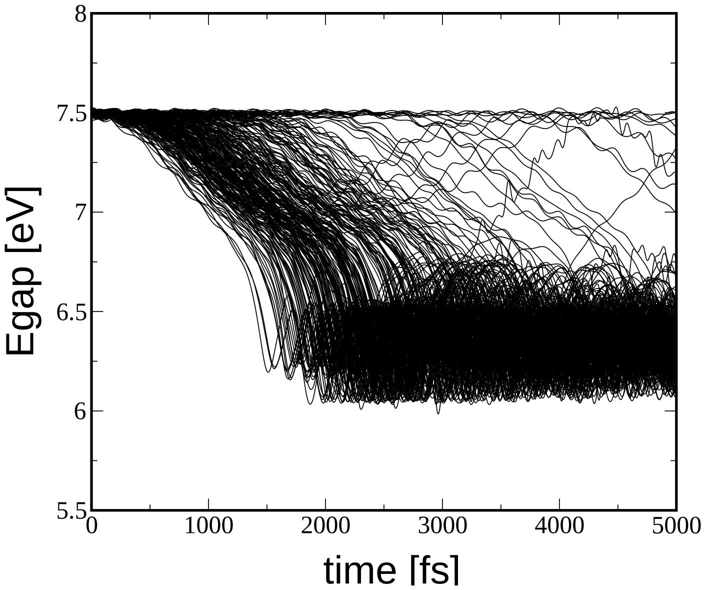

Figure 7.4: Bunch of the energy gaps between the neutral and cationic state of Ag_2Au for 420 trajectories during the dynamics on the neutral electronic ground state obtained for the initial temperature of 20 K.

of the isomerization process and it is expected that the signals in this energetic region show a maximum at the time delay when the probe pulse energy is resonant with the energy gaps and then should decrease to zero at later times. Selecting the probe pulse energy below 6.5 eV serves as a probe for the arrival and subsequent dynamics within the triangular isomer and it is expected that this signal rises after 2 ps and remains constant at later times. As an illustration of these two possibilities two different probe pulse energies of 7.09 and 6.10 eV have been selected and pump-probe signals shown in Figure 7.6 have been simulated and compared to the experimental results obtained by Wöste and coworkers [262]. The signal at 7.09 eV rises after ~750 fs and has a maximum at ~1.3 ps after which it decreases to zero and it corresponds to the passage through a bent intermediate structure on the way from the linear one towards the triangular one. On the other hand, the 6.10 eV signal rises after 2.0 ps and shows a maximum at ~2.3 ps corresponding to the intracluster collision between the gold and silver atoms after arriving to the triangular structure. After passing a maximum this signal remains constant on average and shows irregular oscillation pattern which is characteristic of the IVR process within the triangular structure. The irregularity is a consequence of a large excess of energy 0.31 eV gained during the isomerization process. The experimental results reveal for the first time geometric relaxation as well as an IVR process which means that they close to ZEKE conditions which is a necessary condition for the separation of time scales of these processes. As can be seen from Figure 7.6 the agreement between the experimental and simulated signals is excellent, proving on the one hand the ability of the NeNePo technique to provide very detailed information on the relaxation dynamics of neutral metal clusters and on the other hand serving as a convincing demonstration that the Wigner distribution approach represents a general and powerful theoretical framework able to predict and interpret experimental results with a great accuracy.

Finally, recent advances in the experimental technique [264] have enabled to measure the time and energy resolved photoelectron spectra (TRPES) by measuring the distribution of kinetic energies of photoelectrons at various time delays. These spectra can be simulated in the framework of the Wigner distribution approach by a slight modification of the Equation (7.1) for the ZEKE pump-probe signals which takes into account that a part of the pump-pulse energy E_{pr} changes into the kinetic energy of the electrons E

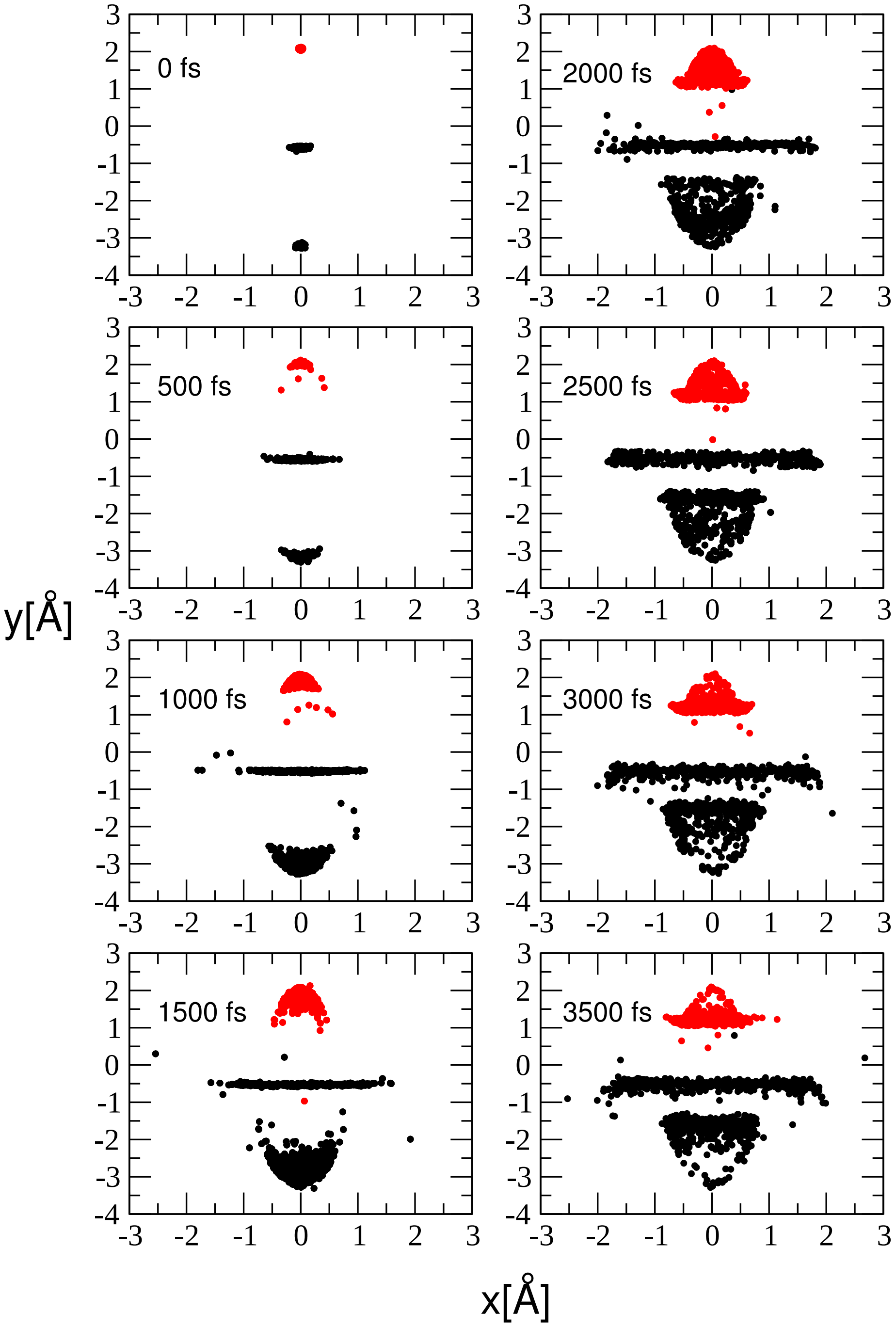

Figure 7.5: Snapshots of the dynamics in the neutral ground state of Ag_2Au after the photodetachment. The projection of 420 phase space points onto the xy plane is shown. Red circles represent Au atoms and black circles Ag atoms.

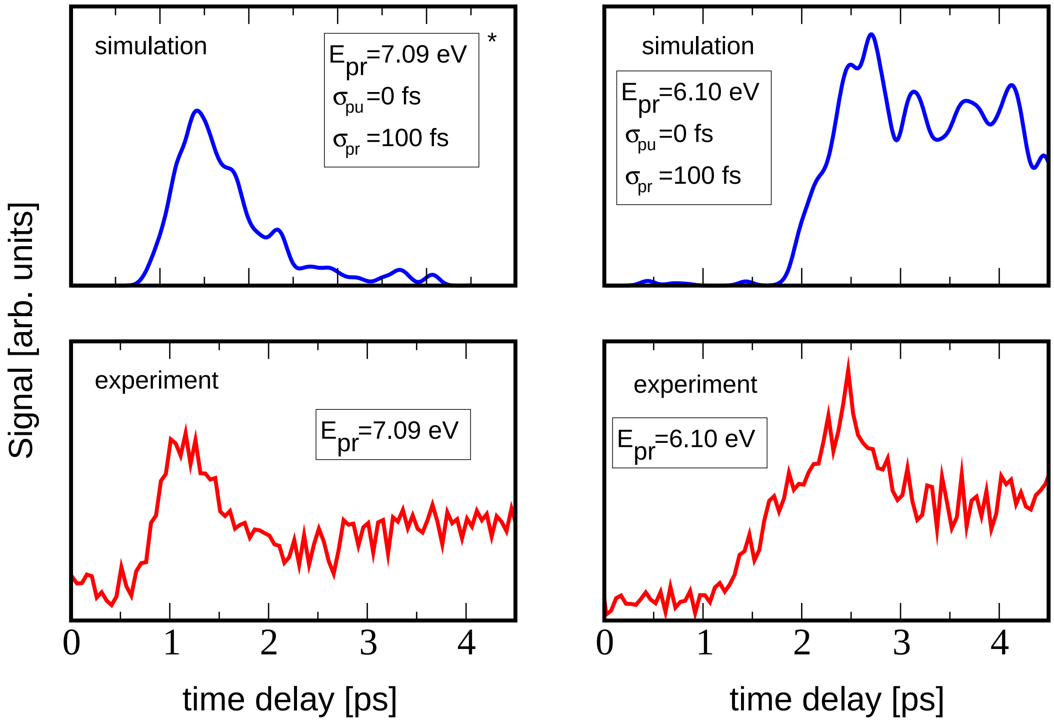

Figure 7.6: Comparison between the simulated NeNePo-ZEKE signals and experimental NeNePo signals for 20 K initial ensemble of Ag_2Au at different energies of the probe pulse.

$$S(t_d, E) \sim \int\int d\mathbf{q}_0 d\mathbf{p}_0 \int_0^\infty d\tau_1 exp - \frac{(\tau_1 - t_d)^2}{\sigma_{pu}^2 + \sigma_{pr}^2} \times$$

$$exp\left\{ -\frac{\sigma_{pr}^2}{\hbar^2}[E_{pr} - V_{21}(\mathbf{q}_1(\tau_1; \mathbf{q}_0)) - E]^2 \right\} \times \quad exp\left\{ -\frac{\sigma_{pu}^2}{\hbar^2}[E_{pu} - V_{10}(\mathbf{q}_0)]^2 \right\} P_{00}(\mathbf{q}_0, \mathbf{p}_0).$$

The time resolved photoelectron spectrum simulated with the probe-pulse energy of 7.09 eV and the pump-pulse duration of 100 fs is shown in Figure 7.7. At lower time delays where the energy gap between the neutral and the cationic state is around 7 eV photoelectrons with low kinetic energies are mainly detected. As the energy gaps decrease the contribution of electrons with higher kinetic energies starts to increase leading to the disappearance of the maximum in the kinetic energy distribution which is present up to 2 ps. After that the form of the signal changes reflecting again dynamics in the triangular structure. The gradual change of the qualitative form of the kinetic energy distribution is an indicator of the isomerization process. Another, perhaps useful way to look at the time resolved photoelectron spectra is to understand it as a collection of the ZEKE spectra corresponding to the probe pulse energy which is a difference between the fixed energy of the probe pulse in TRPES and the kinetic energy of the photoelectrons. In this respect the NeNePo signals presented in Figure 7.6 and all other possible NeNePo-ZEKE signals are contained in the energy resolved photoelectron spectrum.

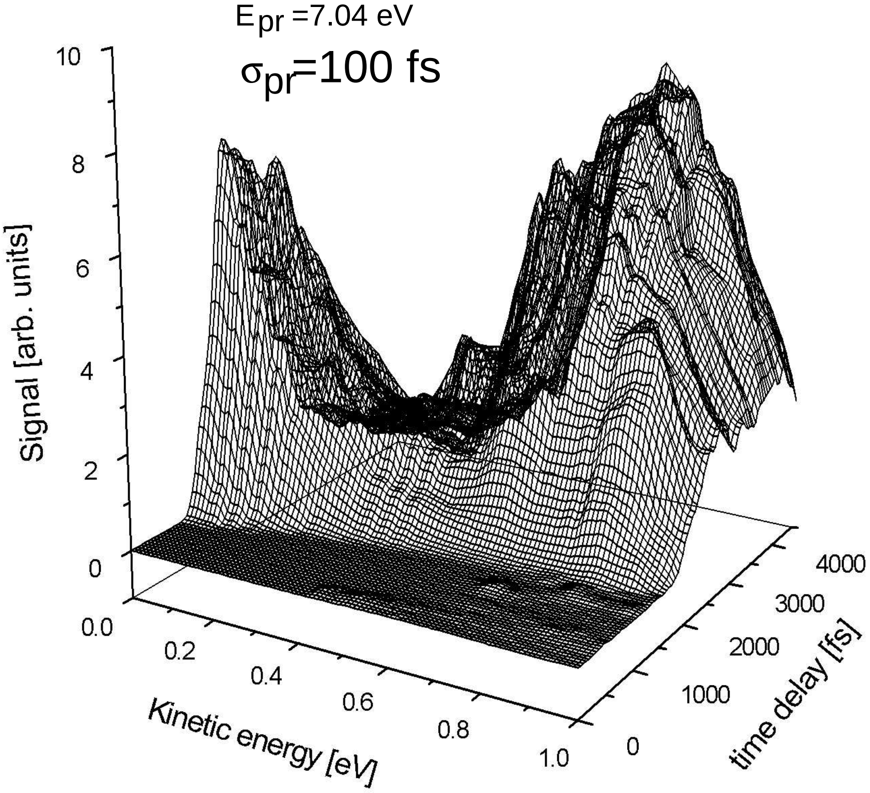

Figure 7.7: Simulated time resolved photoelectron spectrum (TRPES) of Ag_2Au using the probe pulse energy E_{pr} = 7.04 eV and the pulse duration σ_{pr}=100 fs.

7.2.2 Nuclear dynamics and NeNePo-ZEKE signals of Ag_4

As already mentioned in the introductory section of this chapter NeNePo spectroscopy can offer a unique opportunity to obtain information about the vibrational spectrum of neutral mass selected clusters and is therefore a useful technique for the identification of structures of these species. Since in the $Ag_4^-/Ag_4/Ag_4^+$ system the anionic and neutral species have related structures this system offers an ideal opportunity to study the capability of the NeNePo spectroscopy to provide detailed information about vibrational frequencies. The aim of this section is to explore characteristic features of the NeNePo signals in connection with the underlying normal mode dynamics providing the structural signatures of the global minimum in the ground state.

The NeNePo scheme including energies and structures for the $Ag_4^-/Ag_4/Ag_4^+$ are shown in Figure 7.8. In the anionic ground state three isomers have been found. The most stable one is the rhombic isomer with D_{2h} symmetry. The linear structure is almost degenerate with the rhombic structure but is well separated from it by a large barrier. The third T-shape isomer is higher in energy by 0.12 eV and therefore, for the initial ensemble in NeNePO spectroscopy at low temperature only the rhombic structure can be assumed to contribute. This is confirmed by the temperature dependent long MD simulations in the ground anionic state which do not show isomerization to the linear structure or T-shape structure at 50 K. The results of these simulations are shown in Figure 7.9. The classical MD simulations have been performed at constant total energy and the temperature has been calculated from the average kinetic energy according to

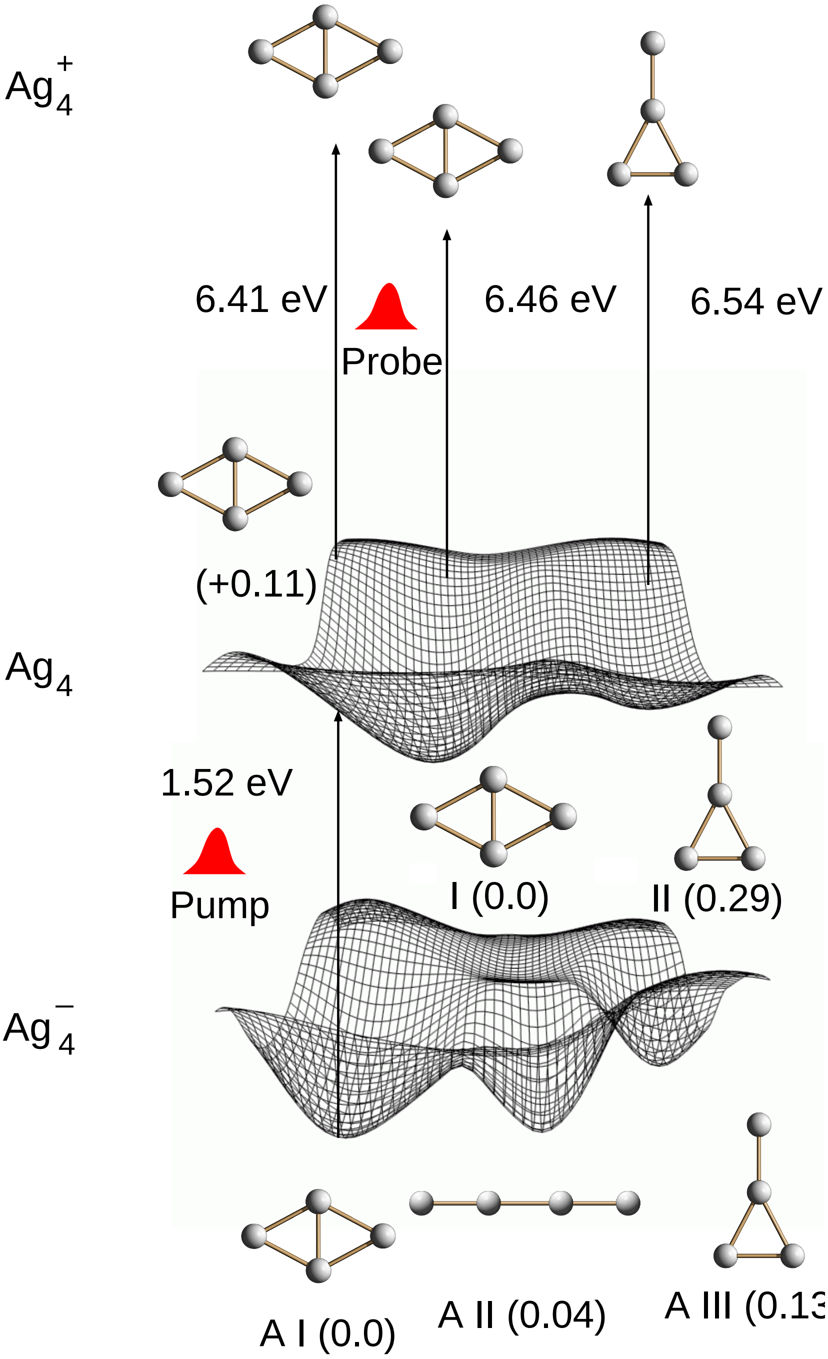

Figure 7.8: Scheme of the multistate femtosecond dynamics of Ag_4 in the framework of the NeNePo pump-probe spectroscopy. Vertical transition energies are given by arrows. All corresponding structures of isomers are drawn. Numbers in parentheses refer to energies with respect to the ground electronic state of the corresponding most stable isomer.

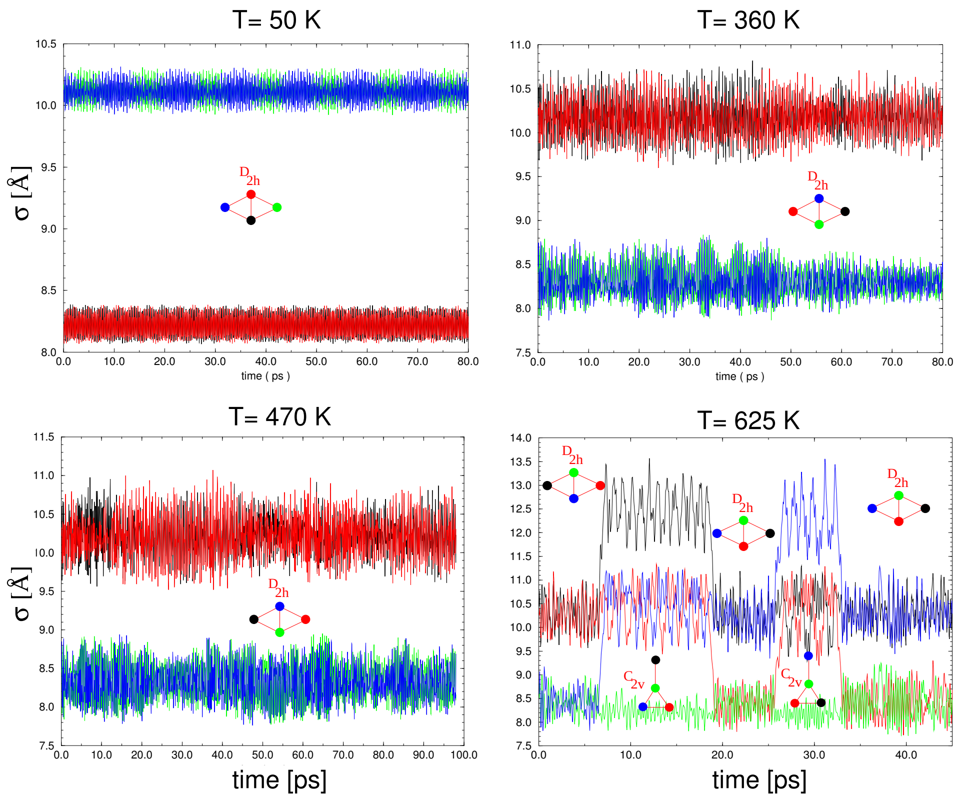

Figure 7.9: Temperature dependence of the isomerization process in the anionic Ag_4 obtained from classical molecular dynamics simulations performed at constant energies. The graphs show dependence of the σ indices defined in Equation (7.4) on time. σ indices are assigned to the atoms by colors.

$$T = \frac{2\langle E_k \rangle}{k_B(3N-6)} \tag{7.3}$$

where E_k is the time average of the kinetic energy over the whole length of the trajectory, k_B is the Boltzmann constant and N is the number of atoms. The simulations have been carried out for 90 ps at four different energies. An isomerization process has been analyzed in terms of bond indices (σ indices) which are defined for each particular atom as the sum of the distances from all other atoms:

$$\sigma_i = \sum_j r_{ij} \quad i = 1, N \tag{7.4}$$

The time dependence of the σ indices is shown in Figure 7.9. At 50 K the system remains localized within the basin corresponding to the rhombic structure and performs very regular oscillations which are also an indication for resonant IVR. Increasing the temperature up to almost 500 K leads to the increase of the amplitudes of vibrations and the dynamics becomes irregular but no isomerization occurs. Finally, at 625 K the system has gained sufficient vibrational energy to cross the barrier between the rhombic and T-shape structure and both isomers are interchangeably populated. The population of higher T-shape isomer is also reflected in the temperature dependent Franck-Condon factors shown in Figure 7.10. They have been obtained by sampling the long trajectory at time intervals corresponding to 100 time steps and calculating the vertical detachment energy to the neutral ground states. At 50 K the distribution of the VDE's is very narrow and symmetric around the energy of 1.52 eV reflecting the localization in the D_{2h} rhombic isomer. Increasing the temperature to 360 K leads to the thermal broadening of the

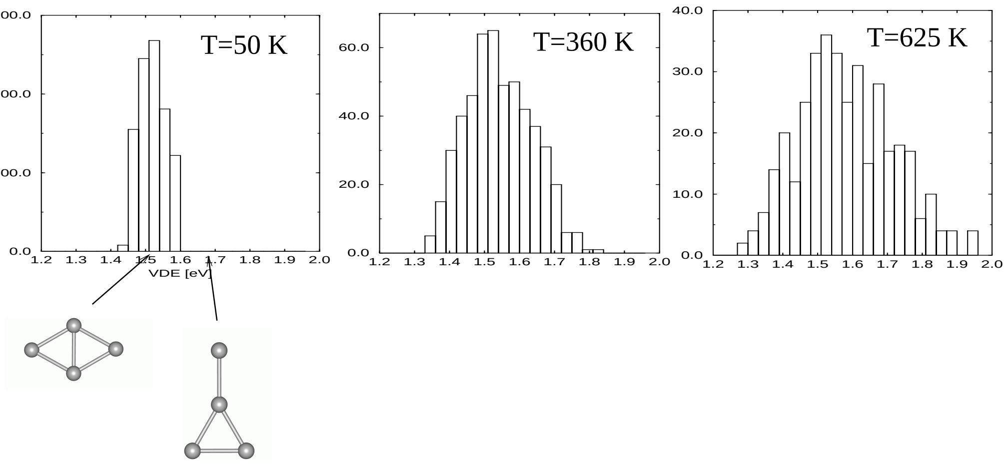

Figure 7.10: Histogram of the vertical detachment energies (Franck-Condon profile) between the anion and neutral Ag_4 for 50 K, 360 K and 625 K initial temperature ensemble obtained by sampling 1000 phase space points

Franck-Condon profile and to the asymmetry due to the anharmonic effects. At 625 K the Franck-Condon profile becomes bimodal due to the occupation of both rhombic and T-shape isomers which have different VDE values.

For the simulations of NeNePo spectra the initial temperature of 50 K has been chosen. Since under these conditions the harmonic approximation is sufficiently accurate the initial conditions for the simulations have been calculated by sampling the harmonic canonical Wigner distribution function from Equation (7.2) using harmonic frequencies given in Table 7.1. MD simulations have been carried out on the neutral electronic ground state up to 5 ps using 50 representative initial conditions of the ensemble. The relaxation of the rhombic structure toward the minimum of Ag_4 excites mainly the ω_3 and ω_4 normal modes which correspond to the relaxation along the short and long diagonal of the rhombic structure, respectively. Other normal modes are only weakly excited according to their thermal occupation. Only the lowest ω_1 mode corresponding to a “butterfly” out-of-plane vibration contributes at the given low temperature of 50 K. The role of the particular modes for the femtosecond dynamics can be illustrated by studying the time dependent energy gaps between cationic and neutral ground electronic states, which are also essential for the simulation of the NeNePo signals. In Figure 7.11 a bunch of 30 energy gaps up to 5 ps are shown. They exhibit oscillations with periodicity of $T_6 = 170$ fs which corresponds to the relaxation process along the short diagonal as expected from the difference between the structural parameters in the anionic and neutral state. The energy gaps show also dephasing which takes place after ~ 2 ps due to the anharmonicities and coupling with other modes.

The NeNePo-ZEKE signals have been calculated using zero pump-pulse duration ($\sigma_{pr} = 0$). Thus, the dynamics of the total initial phase space without selection of particular parts of the phase space by the pump-pulse has been considered. Two probe-pulse energies have been used: $E_{pr} = 6.41$ eV corresponding to the initial rhombic configuration after photodetachment and $E_{pr} = 6.46$ eV giving information about the dynamics in the vicinity of the relaxed neutral rhombic structure corresponding to the global minimum. The simulated NeNePo-ZEKE signal at 6.41 eV for probe pulse duration of 50 fs is shown in Figure 7.12. The pronounced oscillations have a vibrational period of ~ 170 fs corresponding to the ω_6 mode, as already mentioned, and reflect the relaxation along the long diagonal. The Fourier analysis of the signal reveals also a modulation due to the ω_4 mode (long diagonal stretching) and the ω_1 (“butterfly”) modes. Dephasing can be identified by studying the signal at $E_{pr} = 6.46$ eV. Since the probe window

Table 7.1: Energies, geometries, harmonic frequencies and vibrational periods for the isomeric forms of neutral and charged Ag_4 clusters.

		Ag_4^-	
isomer	I(D_{2h})	II($D_{\infty h}$)	III(C_{2v})
E(a.u.)	-1.33641	-1.33491	-1.33187
ΔE(eV)	0.0	0.04	0.12
$r_1/r_2/r_3$(Å)	2.716/2.773	2.648/2.702	2.734/2.749/2.628
		$\nu/cm^{-1}(T/fs)$	
ω_1	34.5 (967)	15.2 (2191)^b	22.3 (1494)
ω_2	80.5 (414)	37.8 (883)	33.6 (991)
ω_3	92.8 (360)	79.4 (420)	87.3 (382)
ω_4	110.9 (301)	151.0 (221)	87.7 (380)
ω_5	148.4 (225)	182.4 (183)	131.5 (254)
ω_6	151.4 (220)		181.0 (184)

		Ag_4	
isomer	I(D_{2h})	II(C_{2v})	III($D_{\infty h}$)
E(a.u.)	-1.28479	-1.27404	-1.26147
ΔE(eV)	0.0	0.29	0.63
$r_1/r_2/r_3$ (Å)	2.723/2.569	2.555/2.817/2.572	2.570/2.766
		$\nu/cm^{-1}(T/fs)$	
ω_1	36.4 (916)	1.0 (32511)	6.6 (5075)^b
ω_2	80.7 (413)	24.8 (1343)	15.7 (2121) ^{b}
ω_3	90.2 (370)	77.7 (429)	72.3 (462)
ω_4	114.3 (292)	83.6 (399)	185.1 (180)
ω_5	165.1 (202)	188.3 (177)	197.6 (169)
ω_6	196.1 (170)	201.1 (166)	

		Ag_4^+	
isomer	I(D_{2h})	II(C_{2v})	
E(a.u.)	-1.04774	-1.03778	
ΔE(eV)	0.0	0.27	
$r_1/r_2/r_3$ (Å)	2.716/2.773	2.633/2.708/2.748	
		$\nu/cm^{-1}(T/fs)$	
ω_1	18.0 (1852)	6.9 (4389)	
ω_2	80.7 (413)	18.2 (1831)	
ω_3	94.2 (354)	84.4 (395)	
ω_4	101.3 (329)	116.3 (287)	
ω_5	134.1 (249)	148.0 (225)	
ω_6	178.9 (187)	182.1 (183)	

[a] Isomers (I, II, III) are labeled according to increasing energies; the point group of the corresponding geometry is given in brackets. [b] degenerate bending mode.

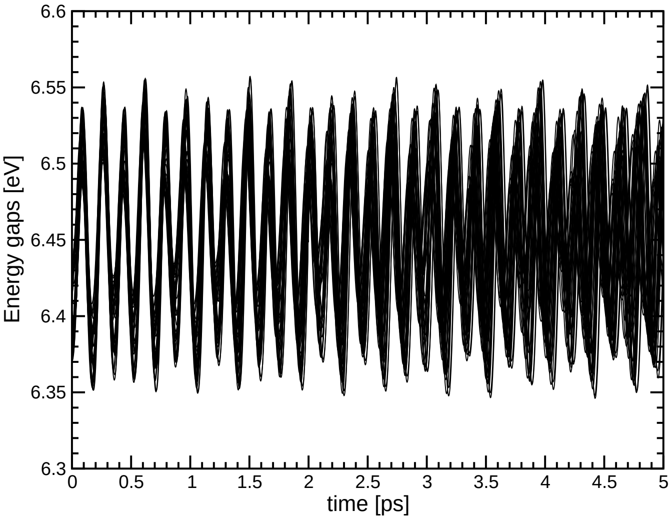

Figure 7.11: Bunch of the energy gaps between the neutral and cationic state of Ag_4 for 30 trajectories during the dynamics on the neutral electronic ground state obtained for initial temperature of 50 K.

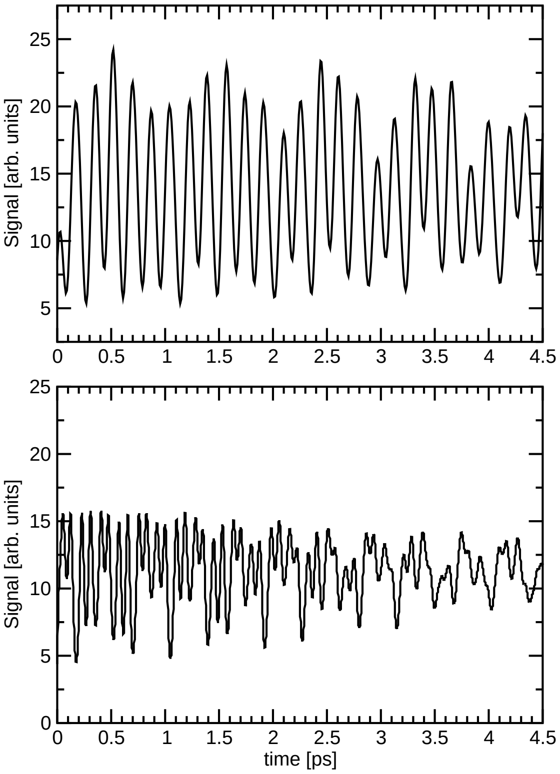

Figure 7.12: Simulated NeNePo-ZEKE pump-probe signals for 50 K initial ensemble of Ag_4 at different excitation energies E_{pr} and pulse duration σ_{pr} of the probe pulse.

is passed twice by the energy gaps during one vibrational period, the probe pulse duration σ_{pr} has to be much shorter for an appropriate temporal resolution. In the lower part of Figure 7.12, the simulated NeNePo-ZEKE signal for $\sigma_{pr} = 10$ fs is shown. From the analysis of the signal it can be seen that up to 2 ps the signal is dominated by vibrations of 85 fs, which is as expected half the period of the short diagonal vibration. However, after 2 ps the signal becomes aperiodic providing the time scale of dephasing of the system due to the superposition with other modes.

In summary, the oscillatory features that are characteristic of the minimum rhombic structure allow to obtain the information about the vibrational frequencies of the neutral gas phase cluster and open the possibility to identify the structure of a gas phase Ag_4 using NeNePo spectroscopy.

7.2.3 Nuclear dynamics and NeNePo-ZEKE signals of Au_4

The stable isomers of Au_4^- and Au_4 are linear and rhombic, respectively. Due to this fact it is expected that after photodetachment a structural relaxation from the linear towards rhombic isomer is induced. However, in the neutral ground state there is also a local linear minimum present. As a consequence, trapping effects of the local minimum influence the character and the time scale of the isomerization

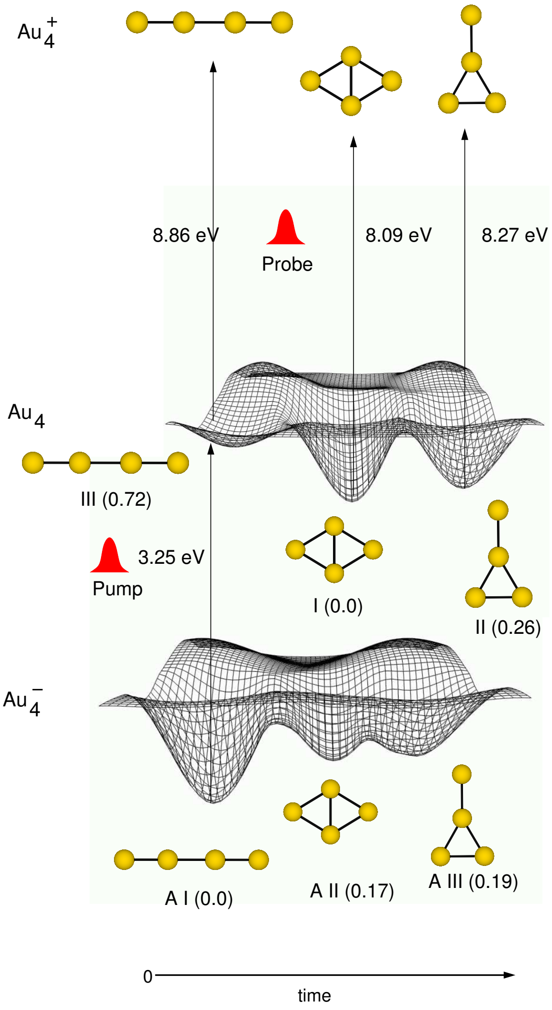

Figure 7.13: Scheme of the multistate femtosecond dynamics of Au_4 in the framework of the NeNePo pump-probe spectroscopy. Vertical transition energies are given by arrows. All corresponding geometries of isomers (AI, AII, AIII of the anion; I, II, III of the neutral) are drawn. Numbers in parentheses are energies with respect to the ground electronic state of the corresponding most stable isomer.

dynamics. It should be pointed out that dependent on theoretical treatment either linear or zig-zag forms are the most stable in the anionic ground state but this is not expected to change the main features of the processes involving the long amplitude motion under investigation. The NeNePo scheme with the structural and energetic information of the $Au_4^-/Au_4/Au_4^+$ is shown in Figure 7.13.

Table 7.2: Energies, geometries, harmonic frequencies and vibrational periods for isomeric forms of neutral and charged Au_4 clusters.

		Au_4	
isomer	I($D_{\infty h}$)	II(D_{2h})	III(C_{2v})
E(a.u.)	-1.68481	-1.67857	-1.67784
ΔE(eV)	0.0	0.17	0.19
$r_1/r_2/r_3$(Å)	2.557/2.590	2.649/2.767	2.681/2.676/2.533
		$\nu/cm^{-1}(T/fs)$	
ω_1	14.9 (2225)^b	27.6 (1207)	18.3 (1821)
ω_2	31.8 (1049)^b	66.8 (499)	32.5 (1025)
ω_3	76.5 (436)	75.1 (444)	73.6 (453)
ω_4	141.0 (236)	91.9 (363)	78.1 (427)
ω_5	176.1	127.1 (262)	115.7 (288)
ω_6		129.4 (257)	167.7 (199)

		Au_4	
isomer	I(D_{2h})	II(C_{2v})	III($D_{\infty h}$)
E(a.u.)	-1.59433	-1.58468	-1.56797
ΔE(eV)	0.0	0.26	0.72
$r_1/r_2/r_3$ (Å)	2.637/2.527	2.492/2.744/2.438	2.491/2.722
		$\nu/cm^{-1}(T/fs)$	
ω_1	29.6 (1128)	9.5 (3502)	8.6 (3602)^b
ω_2	70.0 (476)	27.2 (1225)	19.0 (1751)^b
ω_3	79.8 (418)	71.9 (463)	65.3 (510)
ω_4	102.8 (324)	73.9 (451)	171.8 (194)
ω_5	149.9 (222)	171.0 (195)	179.0 (186)
ω_6	171.3 (195)	184.4 (181)	

		Au_4^+	
isomer	I(D_{2h})	II(C_{2v})	III($D_{\infty h}$)
E(a.u.)	-1.29865	-1.28672	-1.24039
ΔE(eV)	0.0	0.32	1.58
$r_1/r_2/r_3$ (Å)	2.670/2.657	2.569/2.634/2.626	2.582/2.653
		$\nu/cm^{-1}(T/fs)$	
ω_1	10.6 (3135)	5.2 (6376)	2.2 (14908)
ω_2	72.4 (460)	23.1 (1445)	6.4 (5194)
ω_3	84.7 (393)	80.3 (415)	70.2 (474)
ω_4	91.9 (363)	107.7 (309)	133.4 (250)
ω_5	125.2 (266)	136.4 (244)	180.6 (185)
ω_6	157.9 (211)	168.1 (198)	

$^{a)}$Isomers (I, II, III) are labeled according to increasing energies; the point group of the corresponding geometry is given in brackets. $^{b)}$degenerate bending mode.

For the preparation of the uniquely defined initial ensemble in which only one isomer contributes low temperature conditions have to be assumed in order to exclude contributions from the rhombic and T-shape isomers which lie 0.17 and 0.19 eV higher in energy in the anionic state, respectively. The photodetachment energy corresponding to the linear isomer is 3.25 eV and the relaxation dynamics can

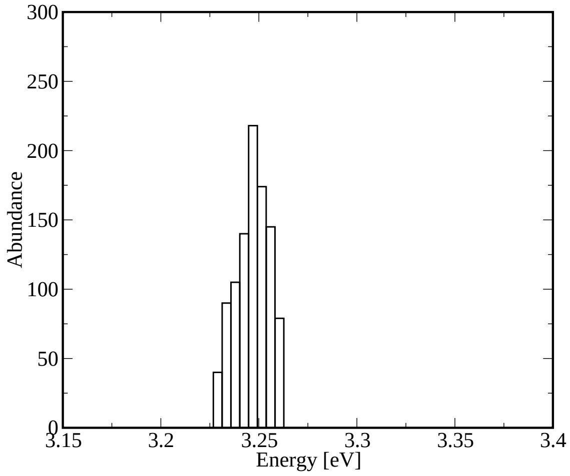

Figure 7.14: Histogram of the vertical detachment energies between the anion and neutral Au_4 for 50 K initial temperature ensemble obtained from 1000 phase space points.

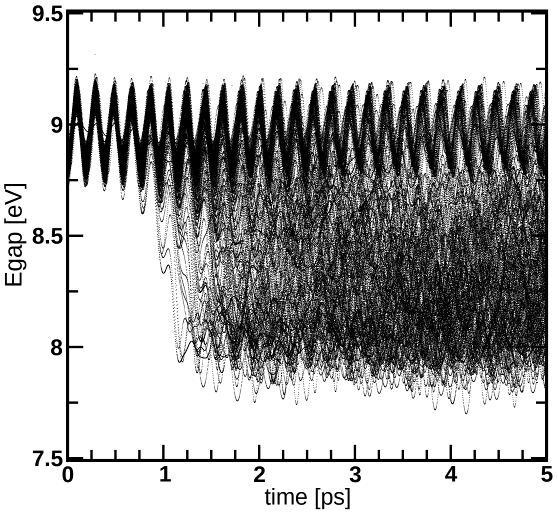

Figure 7.15: Bunch of the energy gaps between the neutral and cationic state of Au_4 for 250 trajectories during the dynamics on the neutral electronic ground state obtained for the initial temperature of 50 K.

be monitored by the two-photon ionization with the probe pulse energies between 8.86 eV and 8.09 eV as can be seen from the bunch of the energy gaps shown in Figure 7.15.

The MD simulations have been performed with initial anionic ensemble obtained by sampling the canonical Wigner distribution in the harmonic approximation at 50 K temperature and using normal mode frequencies from Table 7.2. With these initial conditions the Franck-Condon profile for the photodetachment process has been calculated classically and is shown in Figure 7.14. The maximum in the Franck-Condon profile corresponds to the VDE of the linear structure and shows the localization around the linear structure. Totally, 250 classical trajectories have been propagated on the neutral state for 5 ps. The dynamics is strongly influenced by the linear local minimum and a geometric relaxation after the photodetachment. The geometric relaxation changing the bond lengths within the linear isomer is contained in the ω_3 , ω_4 and ω_5 normal modes, respectively (cf. bond lengths of the $D_{\infty h}$ isomers given in Table 7.2 and visualization of the normal modes given in geometries of Figure 7.16). Each of the 2-fold degenerate bending modes ω_1 and ω_2 are only thermally activated according to the occupation probability of the initial ensemble. Since the temperature is low, they do not influence the relaxation in the vicinity

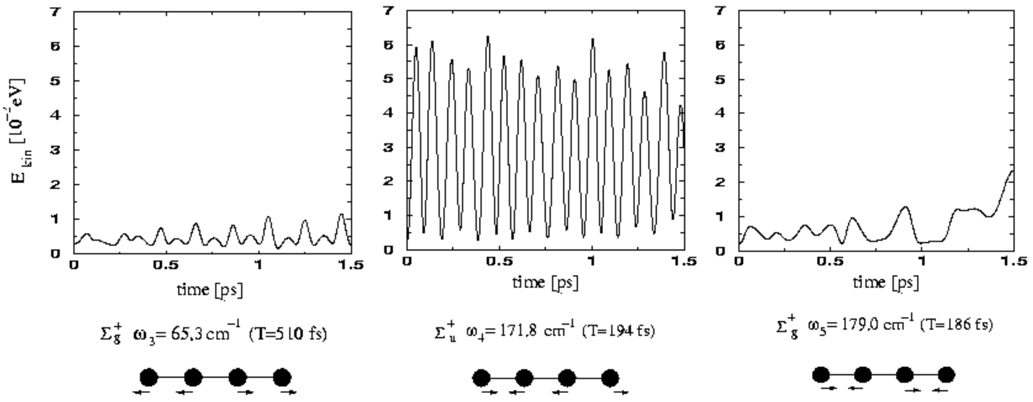

Σ_g^+ ω_3= 65.3 cm^{-1} (T=510 fs)

Σ_u^+ ω_4= 171.8 cm^{-1} (T=194 fs)

Σ_g^+ ω_5= 179.0 cm^{-1} (T=186 fs)

Figure 7.16: Ensemble averaged kinetic energy decomposed into the ω_3, ω_4 and ω_5 normal modes of the neutral linear structure (cf. table 7.2) during the first 1.5 ps of propagation on the neutral ground state of Au_4.

of the local minimum. To determine the contribution and significance of the particular modes in the relaxation process, the ensemble averaged kinetic energy is decomposed in normal modes and the result is shown in Figure 7.16. It can be seen that the ω_4 mode is mostly activated. This can be understood from the change of steepness between the potential surfaces of the anionic and neutral state along each normal mode. For example, the ω_4 modes of the anion and the neutral are 141 and 171.8 cm^{-1} and the curvature of the potential energy surfaces are given by the squares of these values. Thus, the steepness of the neutral state in the vicinity of the linear geometry is by $\sim$10000 cm^{-2} larger along the ω_4 mode compared with the anionic state, leading to the higher forces and consequently to a strong activation of this mode.

The isomerization process from the linear toward rhombic and T-shape isomers is explored by studying time dependent energy gaps between the neutral and the cationic state. Up to 1 ps, only regular oscillations are visible due to the strong activation of the ω_4 mode. Beyond 1 ps, onset of isomerization can be seen from the decrease of the energy gap values. The isomerization process spans a long time interval and is not yet accomplished after 5 ps. Because of high internal vibrational energy that the system gains during the isomerization process the phase space density covers a wide range of the potential energy surface and the contributions of the rhombic and T-shape isomers cannot be separated.

The NeNePo signals have been calculated on the basis of the calculated energy gaps. The probe-pulse duration was selected to be 100 fs and three different energies have been used: E_{pr} =8.86 eV corresponding to the initial Franck-Condon transition and allowing to probe the dynamics in the vicinity of the linear structure; E_{pr} = 8.09 eV and E_{pr}=8.27 eV allowing to probe the dynamics close to the rhombic and T-shape isomers. In all calculations pump-pulse duration is assumed to be 0 fs allowing to get the most comprehensive information on the dynamics without selection of parts of the phase space by the pump-pulse. The signal at E_{pr} = 8.86 eV characterizing the dynamics within the local linear isomer reached immediately after the photodetachment is shown in Figure 7.17. It is dominated by the regular oscillation belonging to the ω_4 mode whivh can be attributed to the nondephased relaxation process of the initial nonequilibrium ensemble. The signal intensity starts to decrease after 1 ps indicating the isomerization process which depopulates the linear isomer and leads to the rhombic structure. Correspondingly, the signal intensities at E_{pr} = 8.09 eV and E_{pr} =8.27 eV increase. Additionally the signal at 8.09 eV shows a weak maximum at 1.9 ps indicating a temporally higher yield of the rhombic isomer. Otherwise, relatively structureless signal shapes of both signals are a signature of the wide spread phase space occupation due to the large excess of vibrational energy. Thus, particular isomerization involving rhombic or T-shape

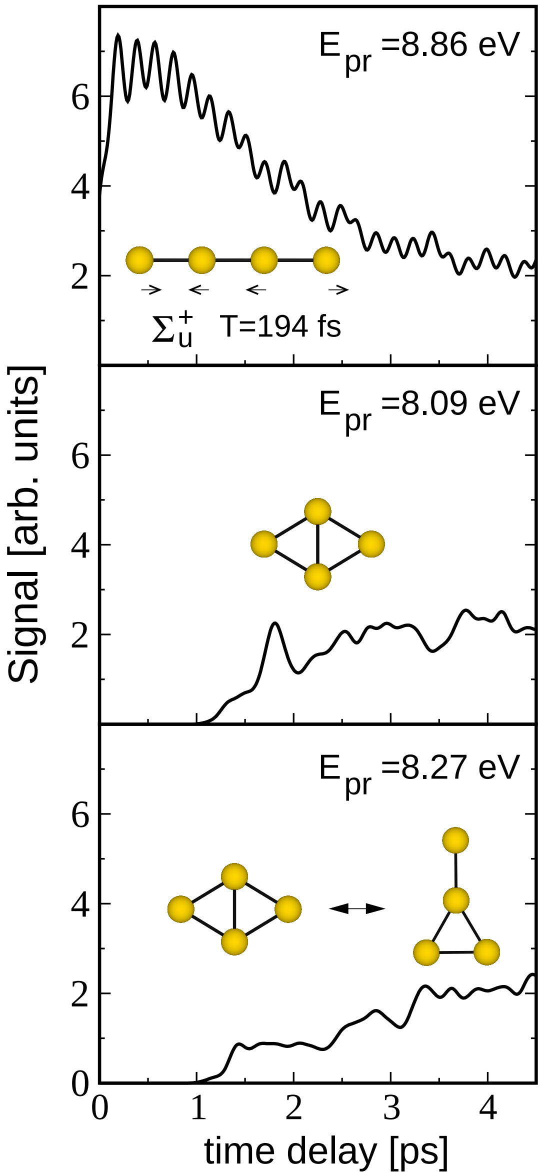

Figure 7.17: Simulated NeNePo-ZEKE pump-probe signals for 50 K initial ensemble of Au_4 at different excitation energies of the probe pulse E_{pr} corresponding to different geometries are shown with a probe pulse duration of 100 fs.

isomers cannot be identified.

7.3 Conclusions

In this chapter the ultrafast ground state dynamics of Ag_2Au, Ag_4 and Au_4 have been investigated in the framework of the NeNePo-ZEKE pump-probe spectroscopy involving the initial anionic state, the ground electronic state in which the dynamics takes place after the photodetachment process and the cationic state which is reached by the probe-pulse. The aim of the work was to determine the scope and perspectives of the NeNePo spectroscopy, particularly as a tool for studying structural and dynamical properties of neutral metal clusters. The theoretical approach used is based on the semiclassical Wigner distribution approach combined with the ab-initio molecular dynamics carried out “on the fly”. The main conclusions are summarized below.

The investigations have revealed the connection between three objectives: The structural relation of anionic and neutral species, the nature of the nonequilibrium state reached after photodetachment by the pump-pulse and the subsequent character of ultrafast neutral ground state dynamics. Generally the following situations can occur in which (i) the transition state, (ii) the global minimum, and (iii) the local minimum influence essentially the dynamics after the photodetachment.

(i) In cases where the anionic structure is close to a transition state of the neutral electronic ground state (e.g. $Ag_3^-/Ag_3/Ag_3^+$ and $Ag_2Au^-/Ag_2Au/Ag_2Au^+$) large amplitude motion towards the most stable isomer dominates the dynamics and different types of IVR can be initiated. The dynamics is in this case incoherent but localized in phase space. The joint theoretical and experimental results for Ag_2Au reveal that the ZEKE conditions are necessary in order to identify the geometry relaxation and subsequent IVR in the NeNePo pump-probe signals and to determine their timescales.

(ii) In cases where the anionic structure is close to the global minimum of the neutral electronic ground state, vibrational relaxation dynamics reflecting the structural properties of the neutral stable isomer (e.g. Ag_4) takes place. The dynamics is dominated by one or few modes along which the structural relaxation between anionic and neutral structures occurs. Other modes and anharmonicities contribute weakly leading to dephasing on a time scale up to several picoseconds (longer than 2 ps for Ag_4). This offers an opportunity to use the NeNePo spectroscopy for structural identification of neutral clusters based on the information about their vibrational frequencies which can be extracted from the NeNePo pump-probe spectra measured under ZEKE conditions.

(iii) In cases where the anionic structure is close to the local minimum (energetically high-lying isomer) of the neutral electronic ground state (e.g. Au_4) the character of the nonequilibrium state reached after the photodetachment is governed by the local minimum, and the vibrational relaxation within the local minimum is likely to dominate the ultrashort dynamics (in the case of Au_4 this happens on a time scale less than 1 ps). Furthermore, a highly symmetric homonuclear systems such as Au_4 can exhibit nondephased regular vibrational dynamics where pronounced activation of only few modes takes place since the normal modes of the anionic and neutral species are almost identical. The local minimum can also act as a strong capture area for nuclear motions with time scales up to several picoseconds as demonstrated on the example of Au_4. As a consequence the isomerization process towards the global minimum can be widely spread in time leading to highly delocalized phase space ensembles.

In summary, characterization of the signals with respect to different dynamical processes including their time scales is of particular interest for proposing experimental conditions under which these processes can be revealed as successfully demonstrated in recent experiments on $Ag_2Au^-/Ag_2Au/Ag_2Au^+$.

Chapter 8

Kinetics and equilibrium of small metallic clusters: Ab initio confinement molecular dynamics study of Au$_4$

8.1 Introduction an motivation

The molecular dynamics simulations offer general framework in which the equilibrium properties and kinetics of finite many-body systems such as clusters can be studied. The simplest approach which allows a comprehensive study of many-body systems has been introduced by Stillinger and Weber [265]. They proposed to supplement the classical MD (or equivalently Monte-Carlo) simulations by a diagnostic quenching of the system at regular time intervals. In this way each quench leads to a certain minimum on the PES, and the whole PES can be therefore partitioned into separate catchment basins that surround a given minimum. In the course of the simulation the system repeatedly visits different catchment basins and as a result equilibrium properties such as residence times and transition rates between different catchment basins can be calculated. Although general, this approach meats some computational difficulties which makes it inefficient for larger systems. The first one is that larger systems, in particular clusters, possess a large number of isomers and if we are interested in the properties of the system as a whole, an unreasonably long time may be required to visit during the simulation all structures whose contribution can be essential. On the contrary, if we are interested in specific structures and channels of transitions, since every particular structure is visited rarely, it is difficult to gain satisfactory statistics necessary for the calculation of the quantities of interest. The other problem is that the PES can have a very complicated structure with minima with large energy differences or separated by high barriers. Furthermore, minima may group together forming superbasins or funnels, which are separated by even higher barriers. Since the PES is sampled in accordance with the Boltzmann statistics, the system largely resides in lower parts of the PES and may therefore remain trapped in the superbasins. Recently, a more efficient heuristic approach based on the confinement MD has been proposed [266, 267, 25, 268]. The idea of the method is to confine the MD trajectory of the system to the catchment basins of the PES. As in the Stillinger-Weber approach, the system is quenched at regular time intervals in order to check if it is still in a given basin or has left it for another, neighboring basin. If left, the system can then either be allowed to pass into the basin in which it was found or it is returned into the previous basin to allow for further exploration. To return the system into the basin a procedure for reversing the trajectory is essential. It is important to note that in this approach, in contrast to the conventional dynamics, the system can now be kept in a current

Table 8.1: Characteristics of the isomers: Energies, U^0(a.u), harmonic frequencies, ν^0(cm^{-1}), and vibrational periods (ps)

Isomer	1 (D_{2h})	2 (C_{2v})	3 ($D_{\infty h}$)
U^0	-1.594328	-1.584677	-1.567974
ν_1	29.6 (1.128)	9.5 (3.502)	8.6 (3.602)[a]
ν_2	70.0 (0.476)	27.2 (1.225)	19.0 (1.751)[a]
ν_3	79.8 (0.418)	71.9 (0.463)	65.3 (0.510)
ν_4	102.8 (0.324)	73.9 (0.451)	171.8 (0.194)
ν_5	149.9 (0.222)	171.0 (0.195)	179.0 (0.186)
ν_6	171.3 (0.195)	184.4 (0.181)	

[a] Degenerate bending mode

Table 8.2: Characteristics of the transition states: Energies, U^*(a.u), and harmonic frequencies ν^* (cm^{-1}).

TS	$1 \leftrightarrow 2(C_1)$	$2 \leftrightarrow 3(C_1)$
U^*	-1.583489	-1.567629
ν_1^*	20.1	7.6
ν_2^*	60.8	13.6
ν_3^*	102.2	79.9
ν_4^*	167.7	160.5
ν_5^*	177.4	174.1

basin for an arbitrary long time. In this way, all characteristics of the structure corresponding to this basin can be calculated with desired accuracy. Moreover, by counting the number of attempts to leave a given basin the rates of transitions can also be obtained. In this work the confinement MD simulations have been implemented in the framework of the ab initio molecular dynamics based on density functional theory [269, 270, 271] giving a general approach for accurate simulations of the thermodynamic and kinetic properties of metal clusters. It should be emphasized, that up to date no reliable semiempirical potentials are available which accurately describe potential energy surfaces of metal clusters. Therefore, the availability of efficient simulation methods based on the DFT are essential for accurate simulations of metal clusters. The scope of the approach has been illustrated in this work on the Au_4 whose PES consists of very shallow and deep basins which make a homogeneous sampling of the PES very problematic.

8.2 The problem

As already described in Section 7.2.3 the Au_4 cluster exists in the form of 3 isomers, which assume rhombic, T-shape and linear structures (labeled below as 1, 2 and 3) and their characteristics are summarized in Table 8.1. The transition states (TSs) presented in Table 8.2 connect linear and T-shape isomers and T-shape and rhombic isomers, respectively. A schematic picture of the PES, based on these data, is shown in Figure 8.1. The simulations in this work have been performed by introducing the internal energy of the linear isomer corresponding to the temperature of about 100 K which is comparable to the TS barrier from the linear to the T-shape isomer (108.6 K in temperature units). Under these conditions, it can be expected that the system lives in the basin of the linear isomer very short time, and when leaving this basin once, hardly returns to it. This also corresponds to the conditions under which the simulations of the NeNePo pump-probe spectra presented in Section 7.2.3 have been carried out.

In this situation, a straightforward way to obtain statistically representative data on the behavior of the system would be to run a set of the MD trajectories started in the linear isomer basin at various atomic distortions and velocities taken from a thermal ensemble. However, since the TS barrier is very low, the thermalization of the system in this basin is difficult to achieve in a conventional way, i.e. by allowing the system to live in the basin for a sufficient time before leaving it. Therefore an alternative approach, which not only solves this particular problem but is applicable to a variety of other problems, is a heuristic, successive confinement approach proposed in [266]. It offers essentially unlimited flexibility in the distribution of the residence times of the systems in different regions of the PES, and thus a possibility to sample these regions as carefully as desirable.

8.3 Computational

The essential idea behind the confinement molecular dynamics approach is to confine the MD trajectory of the system successively to various basins on the PES in a way that the choice of the basin for detailed examination and the time to be spent in the basin can be controlled [266]. To control the basin that is currently sampled, the MD trajectory is mapped on the PES by regular identification of the atomic structures (at time intervals τ_q). For implementation of this approach, a method to generate phase trajectory of the system, a routine to identify a structure and a procedure to confine the MD trajectory to a basin are needed.

Ab initio molecular dynamics. To generate a phase trajectory of the system, ab initio MD "on the fly" (i.e. without precalculation of the PES) based on the gradient corrected density functional approach with Gaussian atomic basis has been employed. The 1-electron relativistic effective core potential (1e-RECP) for Au has been employed [163]. The energy gradients were calculated analytically. Classical (Newtonian) equations of motion for nuclei were solved using the Verlet algorithm, with the time step of numerical integration equal to 1 fs.

Identification of structures. In order to determine to which isomer a current atomic structure should be related, a combination of the quenching of the system with bond length analysis has been employed. For the former, a standard steepest descent method was used, and for the latter a bond length matrix $\mathbf{B} = \{b_{ij}\}$, where b_{ij} is the length of the bond between the i-th and j-th atoms has been considered. Beforehand, each isomer (Table 8.1) was characterized by its potential energy $U^{0,l}$ and bond length matrix $\mathbf{B}^{0,l} = \{b_{ij}^{0,l}\}$, where l (=1,2,3) labels the isomers. With this, the procedure of identification of a current structure includes a repeated set of three operations: 1) quenching the system, 2) calculating the bond length matrix of the quenched system and 3) comparing this matrix with $\mathbf{B}^{0,l}$ ($l = 1, 2, 3$) by calculating the distance in bond space $\sum_{ij} \mid b_{ij} - b_{ij}^{0,l} \mid$. All possible permutations of the atoms for each isomer, dependent on the symmetry of the structure, were taken into account. The initial quench was taken to be deep, until the norm of the gradients was as low as $3 \cdot 10^{-9}$ (all values, here and below, are in atomic units), and the subsequent quenches were restricted to 5 successful steps, i.e. the steps leading to a decrease of the energy. The structure was considered to be in the basin for a certain isomer if two successive sets of the operations satisfied the conditions: the potential energy of the structure at the output of the later set was lower than that for the preceding one, and this structure was closer in the bond space to an isomer, to which it was closest in the preceding set. This approach allowed to reduce the total number of evaluations of potential energy and gradients, which were required to identify a structure, approximately to one hundred, in average.

Confinement of the MD trajectory. When the system is supposed to be confined to a certain basin but is found outside this basin, it has to be returned into the basin. One way to do this, that was used in this work, is to place the system (i.e. its representative point) at the point where it was found in the given basin last time, but to use random velocities obeying a Maxwell distribution instead of the atomic velocities that the system had at this point. Specifically, this procedure includes the following steps [25]: velocities are randomly chosen from a normalized gaussian distribution, then overall translation and rotation of the cluster are excluded and finally, the velocities are rescaled so that the kinetic energy of the cluster would be the same as it was at the point to which the system has been returned.

8.4 Kinetics

A usual way to describe the kinetics is to use the master equation which describes the time evolution of the probability P_i(t) for finding the system in a state i by

$$\frac{dP_i(t)}{dt} = \sum_{j=1}^{N} (W_{ij}P_j(t) - W_{ji}P_i(t)) \tag{8.1}$$

where N is the total number of states, and W_{ij} is the probability of the transition from state j to state i per time unit. In the case of basin-to-basin kinetics $P_i(t)$ represents the probability to find the system in the basin i and W_{ij} is the rate of transition from basin j to i. The transition rates can in principle be obtained by using the transition state theory. The rate constants for a particular channel l of transition from basin i to the basin j can be obtained using the Rice-Ramsperger-Kassel-Marcus (RRKM) theory [272] expression

$$k_{ji}^{(l)}(E) = \frac{\prod_{m=1}^{N} \nu_{i,m}}{\prod_{m=1}^{N-1} \nu_{l,m}^{*}} \left(\frac{E - U_l^{*}}{E}\right)^{N-1} \tag{8.2}$$

where N is the number of vibrational degrees of freedom, $\nu_{i,m}$ and $\nu_{l,m}^{*}$ are the frequencies of the m-th normal mode in the minimum of the basin i and at $l-$th transition state between basins i and j and U_l^{*} is the height of the barrier corresponding to the transition state l. The transition rate W_{ji} which enters into the master equation (8.1) is then calculated as the sum of k_{ji}^{l} over all channels of transitions from basin i to j. However, confinement molecular dynamics simulations [266] allows direct calculations of the transition rates which is expected to be accurate also in those cases when the transition state theory in its simplest harmonic approximation is expected to fail. This is particularly expected to be the case when the basins are shallow or highly anharmonic or when the temperature of the system is high. By confining the system to a current basin (i), we can calculate the probability, q_{ji}, that the system will be found in basin j (including the original one, i) at the subsequent checking after a time interval τ_{q}. These quantities constitute the transition probability matrix $\mathbf{Q}(\tau_{\mathrm{q}}) = \{q_{ij}(\tau_{\mathrm{q}})\}$, which is related to the rate constant matrix, $\mathbf{W} = \{w_{ij}\}$, as

$$\mathbf{Q}(\tau_{\mathrm{q}}) = \exp(\mathbf{W}\tau_{\mathrm{q}}). \tag{8.3}$$

Having $\mathbf{Q}(\tau_{\mathrm{q}})$ and treating the transitions between isomers as a Markov process in the discrete time domain of checking intervals τ_{q}, we can calculate how the populations of the isomers $\mathbf{P} = \{p_i\}$ ($\sum_i p_i = 1$) change with time. They obey the equation

$$\mathbf{P}(t = k\tau_{\mathrm{q}}) = \mathbf{Q}^{k}(\tau_{\mathrm{q}})\mathbf{P}(t = 0) \tag{8.4}$$

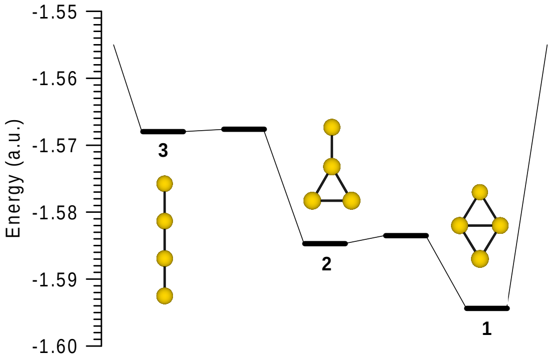

Figure 8.1: Schematic picture of the potential energy surface of Au_4.

Table 8.3: Transition probabilities, q_{ij}, for the time interval of 0.1 ps. In brackets, there are given the corresponding values of q_{ij} obtained in direct simulations.

Isomer from/to	1	2	3
1	0.937(0.932)	0.058(0.059)	0.0(-)
2	0.063(0.068)	0.942(0.941)	0.151(-)
3	0.0(0.0)	0.0(0.0)	0.849(-)

where $\mathbf{P}(t=0)$ is the vector of initial populations. Each multiplier in the product $\mathbf{Q}^k$ moves the system on time step τ_q. The equilibrium populations, $\mathbf{P}^\mathrm{eq}$, are obtained at $t \to \infty$ or can be found from the equation $\mathbf{P}^\mathrm{eq} = \mathbf{Q}\mathbf{P}^\mathrm{eq}$.

The diagonal elements of the transition probability matrix, q_{ii}, characterize lifetimes of the isomers. Assuming a Poisson distribution of the lifetimes, for the mean lifetime of the system in basin i we have

$$\tau_{\mathrm{life},i} = -\tau_\mathrm{q}/\ln q_{ii}. \tag{8.5}$$

A current lifetime can also be estimated directly, calculating the period of time (the number of checking intervals of the known length τ_q) during which the system did not leave the basin cf. also time dependent populations of isomers (Figure 8.3). Correspondingly, a manifold of the lifetimes for a given basin makes possible to build the lifetime distributions for this basin.

8.5 Results and discussion

During the simulations the MD trajectory was successively confined to basins for linear, T-shape and rhombic isomers, until it made at least 100 attempts to leave the current basin. The cluster did not execute the overall translation and rotation, and its total energy E was equal to -1.566067 a.u., which corresponds to the heating of the linear isomer approximately to 110K. The checking interval τ_q was equal to 0.1 ps. Note, that in general case, when the variety of isomers is unknown, first one should find and characterize the isomers. This can be done by surveying the PES with the help of the successive confinement method [266, 25, 268]. In the course of the simulation, transitions were observed from the linear isomer to the T-shape one, and also between T-shape and rhombic isomers. No transition from T-shape and rhombic isomers to the linear isomer has been detected. The corresponding transition

Table 8.4: Transition probabilities, q_{ij}, for the time interval of 0.1 ps, predicted by RRKM theory. The RRKM rate constants w_{ij} were calculated using data of Tables 8.1 and 8.2.

Isomer from/to	1	2	3
1	0.875	$0.501{\cdot}10^{-1}$	-
2	0.125	0.949	$0.119{\cdot}10^{-2}$
3	-	$0.469{\cdot}10^{-5}$	0.998

Table 8.5: Mean lifetimes, calculated from the transition probabilities of Table 8.3 via Eq. 8.5, 'temperatures' of the isomers, calculated from the kinetic energies of the system in the corresponding basins, and the equilibrium populations of the isomers from Figure 8.1. In brackets there are given the corresponding values found in the direct simulations.

Isomer	τ_{life}[ps]	T [K]	p^{eq}
1	1.540 (1.532)	1221 (1225)	0.480 (0.464)
2	1.672 (1.721)	814 (901)	0.520 (0.526)
3	0.608 (-)	110 (-)	0.0 (-)

probabilities are presented in Table 8.3. For comparison, Table 8.4 shows the values of q_{ij} that are predicted by the Rice-Ramsperger-Kassel-Markus (RRKM) theory [272]. It is seen that if the barrier is not so small as that for the linear-to-T-shape transition, the RRKM theory is reasonably accurate. We can thus suppose that the prediction for the probability of the transition from the T-shape isomer to the linear one is also correct, at least by the order of magnitude. Correspondingly, the time required to observe this transition in the simulations is 10^4 times larger than it is taken, in average, for a single act of the transition from the T-shape isomer to the rhombic one. Figure 8.2 shows lifetime distributions for the isomers and their comparison with the theoretical (Poisson) distributions based on the mean lifetimes τ_{life} of Table 8.5. As seen, the lifetimes follow the Poisson law and are consistent with the values of mean lifetimes obtained from the transition probabilities. Having the transition probabilities, we can use Equation (8.4) to calculate time-dependent populations of the isomers for initial conditions of interest. Figure 8.3 shows such populations for a scenario characteristic of the NeNePo experiments. It is remarkable that though the T-shape isomer is higher in energy than the rhombic one, which presents the ground state atomic

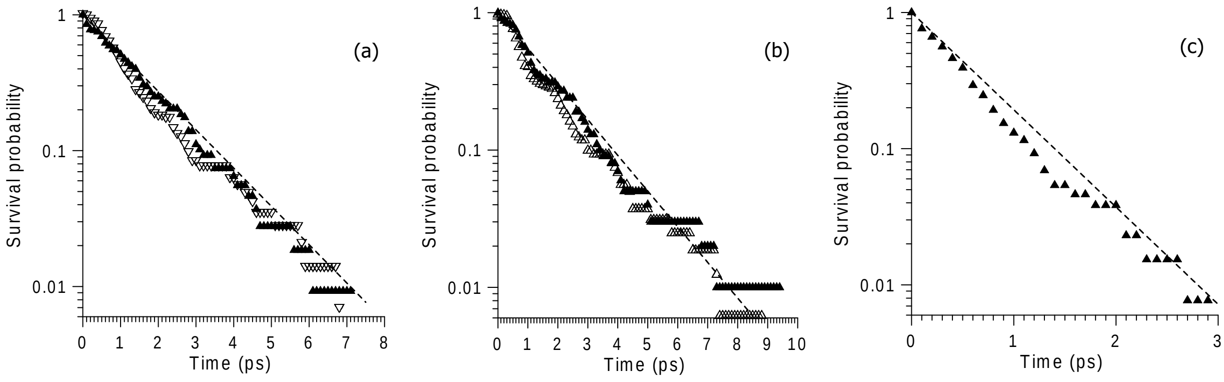

Figure 8.2: Lifetime distributions for (a) rhombic, (b) T-shape, and (c) linear isomers. Solid and empty triangles label the confinement and direct simulations, respectively. Dashed lines show the Poisson distributions based on the mean lifetimes of Table 8.5.

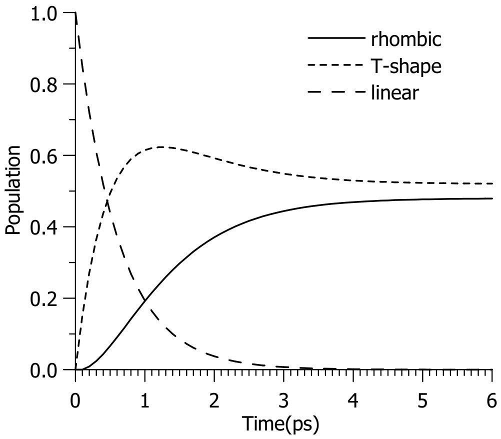

Figure 8.3: Time-dependent populations of the isomers.

configuration of the cluster, its equilibrium population is higher. A reason is that the T-shape isomer, looser in constitution, samples larger conformation space than the compact rhombic isomer, and thus should have a larger conformation entropy.

Along with the confinement simulations we also performed a direct simulation, allowing the system to pass between the basins freely. The total energy of the system was as before, and the system started the exploration of the PES in the basin for linear isomer. The total length of the run was 0.5 ns (5 $\cdot 10^5$ time steps). The system left the basin for linear isomer in a short time (0.3 ps), and then kept making the transitions between T-shape and rhombic isomers (in total, approximately 150 transitions were made in each direction). In accord with the previously discussed RRKM estimates, the system never returned in the linear isomer basin for the given length of time. The results of the direct simulation are presented in Tables 8.3 and 8.4, and Figure 8.2, and they are in good correspondence with the confinement simulation results. In conclusion this work shows that in addition to the energy ordering of the isomers their thermodynamic properties such as conformational entropy are very important [25] for determining the residence times. This issue is relevant not only in clusters but also in conformational studies of biological systems.

Chapter 9

New strategy for optimal control of femtosecond pump-dump processes; Illustration on the isomerization in Na_3F_2 cluster

9.1 Introduction

The recent experimental development of techniques for ultrafast pulse-shaping [26, 27, 28, 29, 273, 274, 275, 276] made it possible to generate tailored light fields with very complex forms which may be used to control molecular processes by suppressing the undesired products and favoring the desired ones. Parallel to the experimental developments optimal control theory [138, 139, 277, 278, 279, 280] and methods based on quantum interference phenomena [140, 141] have been developed and used to compute the light fields which are able to drive a material system to a desired goal or objective. However, most of the theoretical applications have been so far considering either the model systems or diatomic or three-atomic systems where the full quantum mechanical solution of the problem is feasible. The first strategy for control of chemical reactions was the Tannor-Rice pump-dump scheme [138] involving two electronic states. This approach exploits the fact that the ground and excited state may have very different potential energy surfaces and an ultrashort laser field can therefore be used to excite the system to the excited state and another ultrashort pulse dumps the system back to the ground state at appropriate time delay when it reaches the region of the potential energy surface corresponding to the desired products. Is is still an open question weather the optimal control involving more than one electronic state can be achieved for systems of moderate complexity. In contrast to simple one-dimensional systems, here, at least two problems arise which have to be solved. The first problem concerns the existence of the connective pathway between the initial state and the objective when the latter is reached via a different electronic state and the second problem is, even if the connective pathway exists, how the optimal path can be found at a reasonable computational demand. In this work a new optimal control strategy applicable for systems of moderate complexity is presented. This method combines the Wigner-Moyal representation of the vibronic density matrix with ab initio molecular dynamics (MD) in the ground and excited electronic states without precalculation of the potential energy surfaces which makes it applicable for systems with considerable number of degrees of freedom. The pump-dump control employing two phase unlocked ultrafast fields in the weak field regime is considered. The analysis of the classical trajectories obtained from the ab initio MD "on the fly" allows to introduce the new strategy for optimal control through the concept of an intermediate target in the excited state [281, 282]. The intermediate target is defined as a localized ensemble in the excited state corresponding to the maximum overlap between the forward propagated phase space density on the excited electronic state (starting from the initial state) and the backward propagated phase space density from the objective, at the optimal time delay between the pulses. In this way the intermediate target guarantees the existence of a connective pathway between the initial state and the objective and selects the appropriate Franck-Condon window for the dump-process. The advantage of this optimal control strategy is that it provides an easy access to underlying ultrashort processes reflected in the shape of the pulses because of the available analysis of the molecular dynamics. The developed strategy is illustrated by optimizing the pump- and dump-pulses for driving the isomerization process in Na_3F_2 which is one of the nonstoichiometric Na_nF_{n-1} clusters.

9.2 Optimal control strategy

In this section the optimal pump-dump control is considered in the weak field limit which suggests the use of perturbation theory. Starting from the initial ensemble in the lowest energy ground state isomer, the aim is to occupy maximally the second isomer (the objective) at a given time t_f by using a phase-unlocked pump-dump control strategy involving dynamics on the first excited state (pumping) and the ground state (dumping). We assume that the pump- and dump-pulses have the form

$$\epsilon_{P(D)}(t) = E_{P(D)}(t) exp(-i\omega_{eg}t) + E^*_{P(D)}(t) exp(i\omega_{eg}t) \tag{9.1}$$

where $E_{P(D)}(t)$ is the slowly varying envelope of the pump (dump) field, respectively, and ω_{eg} is the difference between the energies of the minima of the excited and ground state. The parameters to be optimized are therefore the temporal shapes of both pulses and implicitly the time delay between them. In the case of the isomerization process leading to the second ground state isomer, the objective in the ground state can be described in the Wigner representation by an operator

$$\hat{A} = A(\Gamma)|g\rangle\langle g| \tag{9.2}$$

where $A(\Gamma)$ is the Wigner representation of the objective in the multidimensional phase space $\Gamma = (q_i, p_i)$ of coordinates and momenta and $|g\rangle\langle g|$ is the ground state projection operator. In principle the target operator may be chosen to represent any desired objective but since the focus of this work is to occupy maximally the second isomer, only the spatial localization of the phase space density is of relevance, and an arbitrary distribution of momenta in the objective is assumed. Thus, the target operator can be written as

$$A(p, q) = \prod_{i=1}^{N} \frac{1}{\sqrt{2\pi}\Delta q_i} exp\left\{-\frac{(q_i - \bar{q}_i)^2}{2(\Delta q_i)^2}\right\} \Theta\left(E_{min} - \sum_{i=1}^{N} \frac{p_i^2}{2m_i}\right) \tag{9.3}$$

where $\bar{q}_i$ denotes the cartesian coordinates of the second isomer and Δq_i are the deviations. The theta function ensures that the kinetic energy of the phase space ensemble is kept below the lowest isomerization barrier E_m which separates the basin of the desired isomer from the other basins. The yield of the control process is generally given by the expectation value of the target operator at the time t_f,

$$A(t_f) = Tr[A\rho] = \int d\Gamma A(\Gamma)\rho(\Gamma, t_f). \tag{9.4}$$

The time evolution of the density operator is generally determined by the Liouville-von Neumann equation

$$i\hbar\frac{\partial\hat{\rho}}{\partial t} = [\hat{H}, \hat{\rho}], \tag{9.5}$$

where in the special case involving two electronic states coupled by the pump- and dump- fields the Hamilton operator has the form

$$\hat{H} = \hat{H}_0 + \hat{H}_1 \tag{9.6}$$

where H_0 is the molecular Hamiltonian

$$\hat{H} = \hat{H}_g|g\rangle\langle g| + \hat{H}_e|e\rangle\langle e| \tag{9.7}$$

with H_g and H_e being nuclear Hamiltonians in the ground and excited electronic states, respectively, and $\hat{H}_1$ is the operator representing the interaction with the pump (dump) field:

$$\hat{H}_1 = -\hat{\mu}E_{P(D)}(t)(|g\rangle\langle e| + |e\rangle\langle g|) \tag{9.8}$$

In the weak field limit the density operator can be expanded in a perturbation series $\hat{\rho} = \hat{\rho}^{(0)} + \hat{\rho}^{(1)} + \hat{\rho}^{(2)} + \cdots$ leading to the following set of coupled equations for the different orders in the perturbation strength:

$$i\hbar\frac{\partial\hat{\rho}^{(0)}}{\partial t} = [\hat{H}_0, \hat{\rho}^{(0)}] \tag{9.9}$$

$$i\hbar\frac{\partial\hat{\rho}^{(j)}}{\partial t} = [\hat{H}_0, \hat{\rho}^{(j)}] + [\hat{H}_1, \hat{\rho}^{(j-1)}]. \quad j = 1, 2, \cdots \tag{9.10}$$

In the case when the perturbation is absent time evolution is determined by the zeroth-order Green's function

$$G^{(0)}(t) = \Theta(t)e^{-\frac{i}{\hbar}\hat{H}t}\rho(0)e^{-\frac{i}{\hbar}\hat{H}t} \tag{9.11}$$

which allows to write the formal solution of the system 9.10 as

$$\hat{\rho}^{(j)}(t) = -\frac{i}{\hbar}\int_0^t G^{(0)}(t-\tau)[\hat{H}_1, \hat{\rho}^{(j-1)}(\tau)]d\tau. \tag{9.12}$$

Due to the fact that the population transfer between the ground and excited electronic states in the perturbation theory treatment appears first at the second order in the field the second order density operator is needed to calculate the yield of the optimization. Furthermore, for the field free Green's function the classical approximation derived in Section 2.5.3 has been used allowing to derive the following expression for the yield in the Wigner representation

$$\begin{aligned} A(t_f) &= \int\int d^2\Gamma \int_0^{t_f} d\tau \int_0^{\tau} d\tau' \int_0^{\tau'} d\tau'' \int_0^{\tau''} d\tau''' A(\Gamma_g(t_f-\tau;\Gamma_e(\tau'-\tau'';\Gamma_0))) && (9.13) \\ & \quad e^{i(\omega_{eg}-U_{ge}(\Gamma_e(\tau'-\tau'';\Gamma_0)))(\tau-\tau')} \times e^{i(\omega_{eg}-U_{ge}(\Gamma_0))(\tau''-\tau''')} && (9.14) \\ & \quad \rho_{gg}(\Gamma_0) E_P(\tau''') E_P^*(\tau'') E_D(\tau') E_D^*(\tau). && (9.15) \end{aligned}$$

This expression involves the propagated excited and ground state ensemble Γ_e and Γ_g induced by the pump- and the dump-pulses, respectively. U_{ge} is the time dependent energy gap between the states, and $\rho_{gg}(\Gamma_0)$ denotes the initial phase space distribution in the Wigner representation. In order to maximize the yield at time t_f and determine the optimal pump- and dump-fields the following functional has been considered

$$J(t_f) = A(t_f) - \lambda_P \int_0^{t_f} |E_P(t)|^2 dt - \lambda_D \int_0^{t_f} |E_D(t)|^2 dt. \tag{9.16}$$

The last two terms are introduced due to the general constraint of the finite total energy of the pump and dump pulses, respectively. Optimal pump- and dump-fields have been obtained by calculating the extrema of the control functional from Equation (9.16) from the variational procedure. This leads after invoking the rotating wave approximation (RWA) to the following pair of coupled integral equations of the Fredholm type for the field envelopes:

$$\int_0^{t_f} d\tau' M_P(\tau,\tau';E_D) E_P(\tau') = \lambda_P E_P(\tau) \tag{9.17}$$

$$\int_0^{t_f} d\tau' M_D(\tau,\tau';E_P) E_D(\tau') = \lambda_D E_D(\tau) \tag{9.18}$$

where the integral kernels usually denoted as material response functions are given by

$$\begin{aligned} M_P(\tau,\tau';E_D) &= \int\int d^2\Gamma_0 \int_0^{t_f} d\tau'' \int_0^{\tau''} d\tau''' A(\Gamma_g(t_f-\tau'';\Gamma_e(\tau'''-\tau;\Gamma_0))) \times \\ & \quad e^{i(\omega_{eg}-U_{eg}(\Gamma_e(\tau'''-\tau;\Gamma_0)))(\tau''-\tau''')} e^{i(\omega_{eg}-U_{eg}(\Gamma_0))(\tau-\tau')\times} \\ & \quad \rho_{gg}(\Gamma_0) E_D(\tau''') E_D^*(\tau'') \qquad \tau \geq \tau' && (9.19) \end{aligned}$$

$$\begin{aligned} M_D(\tau,\tau';E_P) &= \int\int d^2\Gamma_0 \int_0^{\tau'} d\tau'' \int_0^{\tau''} d\tau''' A(\Gamma_g(t_f-\tau;\Gamma_e(\tau'-\tau'';\Gamma_0))) \times \\ & \quad e^{i(\omega_{eg}-U_{eg}(\Gamma_e(\tau'-\tau'';\Gamma_0)))(\tau-\tau')} e^{i(\omega_{eg}-U_{eg}(\Gamma_0))(\tau''-\tau''')\times} \\ & \quad \rho_{gg}(\Gamma_0) E_P(\tau''') E_P^*(\tau^{''}) \qquad \tau \geq \tau' && (9.20) \end{aligned}$$

These coupled nonlinear integral equations can be solved iteratively giving a solution for optimal pump- and dump-fields. However, this is computationally a very demanding task even for systems of moderate complexity because coupled classical trajectory simulations on the ground and excited states have to be performed. As can be seen from Equations (9.19) and (9.20) this requires the propagation of the ensemble of classical trajectories onto the ground state Γ_g starting at different initial conditions which are obtained from the propagated ensemble Γ_e of the excited state at every time step. However, a new strategy can be proposed which reduces the problem to solving single Fredholm-type integral equations for the optimal pump- and dump-fields at acceptable computational demand by restricting the optimization problem to field envelopes in the ultrashort fs-regime. The strategy involves the following steps:

(i) In the zeroth order of an iterative procedure for solving the system of Equations (9.18) it is justified to calculate the kernel functions M_P and M_D with strongly localized pulse envelopes $E_P \propto \delta(t)$ and $E_D \propto \delta(t - t_d)$ where t_d is the time delay between the pulses to be determined. This yields for the zeroth order material response functions (9.19) and (9.20):

$$\begin{aligned} M_P^{(0)}(\tau,\tau') &= \int\!\!\int d^2\Gamma_0 A(\Gamma_g(t_f - t_d; \Gamma_e(t_d - \tau; \Gamma_0))) \times \qquad (9.21) \\ &\quad e^{i(\omega_{eg} - U_{eg}(\Gamma_0))(\tau - \tau')} \rho_{gg}(\Gamma_0) \qquad \tau \geq \tau' \qquad (9.22) \end{aligned}$$

$$\begin{aligned} M_D^{(0)}(\tau,\tau') &= \int\!\!\int d^2\Gamma_0 A(\Gamma_g(t_f - \tau; \Gamma_e(\tau'; \Gamma_0))) \\ &\quad \times e^{i(\omega_{eg} - U_{eg}(\Gamma_e(\tau^{'}; \Gamma_0)))(\tau - \tau')} \rho_{gg}(\Gamma_0) \qquad \tau \geq \tau' \qquad (9.23) \end{aligned}$$

In this approximation the equation for the pump-and dump-fields are obviously decoupled. According to Equation (9.22) the pump pulse optimization involves the propagation on the excited state $\Gamma_e(t_d - \tau)$ from $\tau = 0$ until $\tau = t_d$ starting from the initial ensemble Γ_0 whereas for the dump-pulse optimization according to Equation (9.23) the dynamics on the ground state $\Gamma_g(t_f - \tau; \Gamma_e(t_d))$ for $\tau' = t_d$ until $\tau' = t_f$ has to be performed with initial conditions given by the ensemble of the excited state $\Gamma_e(t_d)$ at t_d. We call the ensemble $\Gamma_e(t_d)$ at t_d the *intermediate target* which can be determined from the maximal overlap between the forward propagated ensemble from the first isomer on the excited state and a backward propagated ensemble from the second isomer on the ground state.

(ii) Once the material response functions in the zeroth order are calculated the optimal pump-pulse in the first order of the iterative procedure can be calculated from Equation (9.18). The role of the pump pulse is to localize the phase space density at the intermediate target at the optimal dump time t_D.

(iii) In the third step the optimal dump-pulse is calculated by solving the Equation (9.18) which projects the intermediate target to the ground state and localizes optimally the phase space density in the the objective at the specified final time t_f.

The problem of the connective pathway between the initial state and the objective mentioned above is related to the existence of the intermediate target at a time t_d. The necessary condition for this is that the yield functional in the limit of δ-like pump and dump pulses reduces simply to $A(\Gamma_g(t_f - t_d; \Gamma_e(t_d))$ has nonvanishing contributions as it follows from Equations (9.19) and (9.20). The optimal time delay t_d for which this occurs can be determined from classical trajectory simulations by dumping the system at variable time delays t_d followed by propagation from t_d to t_f and subsequent calculation of the target functional. Thus the optimal time delay t_d is given by the time for which maximal overlap is achieved. The procedure described above can in principle be continued iteratively leading to fully optimized pump- and dump-pulses. However, in many practical cases, as will be shown on the example of Na_3F_2 in the next section, it can be expected that the zeroth and first order iteration lead to sufficient accuracy. The proposed strategy allows to reach the objective with maximal yield by independent optimization of the pump- and dump-pulses and is applicable therefore for systems of moderate complexity. At the same time, the analysis of the ensemble of classical trajectories corresponding to the dynamics in the excited state and in the ground state allows a relatively easy interpretation of the shaped pulses and of the underlying dynamical processes.

9.3 Nonstoichiometric Na_nF_{n-1} clusters

The structural and electronic properties of nonstoichiometric Na_nF_{n-1} clusters have been in the past investigated theoretically [130, 283] since they allow to study optical properties of the finite systems with some bulk characteristics such as F-color centers. In these systems a single excess electron is either localized at one of the Na atoms or at the site of the halide vacancy and is not involved in the strong ionic bonding. Due to the excitations of the excess electrons placed in a large energy gap between occupied and unoccupied one-electron levels, the Na_nF_{n-1} clusters show a strong absorption in the visible-infrared energy interval. This kind of the situation allows for a simple and accurate description of the excited electronic based on the "frozen ionic bond" approximation presented in Section 2.5.4. Furthermore, this method allows to calculate the forces in excited states and nonadiabatic coupling matrix elements which are necessary to carry out MD "on the fly".

In order to illustrate the new strategy for the pump-dump optimal control Na_3F_2 cluster has been selected. The system has totally nine degrees of freedom and is particularly suitable for the pump-dump control because in the ground state two isomers with different structures and a relatively low isomerization barrier of 0.12 eV are present. The lowest energy isomer I (cf. lower part of Figure 9.2) has C_s symmetry and is characterized by an ionic Na_2F_2 subunit to which the Na atom is attached. The second isomer with C_{2v} symmetry has a metallic Na_3 subunit bicapped by the F atoms [283]. The stationary absorption spectra for both ground state isomers are shown in Figure 9.1. The lowest excited state of isomer I is a 2^2A' state with the vertical excitation energy of 1.33 eV. Isomer II has a vertical excitation energy of 1.77 eV corresponding to the 1^2B_2 electronic state. The first excited state exhibits a shallow local minimum related to the transition state of the ground state and the global minimum with a linear geometry corresponding to a conical intersection between the ground and the first excited state [132]. The nonadiabatic dynamics of this system has been studied in the Bonačić-Koutecký group and the pump-probe spectra have been simulated [132]. From the analysis of the nonadiabatic dynamics , the time scales for the Na-Na bond breaking of $\sim$90 fs, for the ionic Na-F bond breaking of $\sim$220 fs and for the passage trough the conical intersection after 400 fs have been determined. The isomerization through conical intersection is characterized by a large excess of energy ($\approx$ 0.65 eV) and therefore leads to highly vibrationally excited ground state products which excludes the possibility to occupy only the single isomer II. Thus, another pathway due to the optimal control is preferable for selective occupation of the isomer II. This finding stimulated us to apply our new strategy for optimal control in order to populate only one of the isomers.

9.4 Optimal control of the isomerization of Na_3F_2

In this section the new strategy for optimal control of pump-dump processes and the concept of the intermediate target are applied to the pump-dump induced isomerization of the Na_3F_2 cluster. While

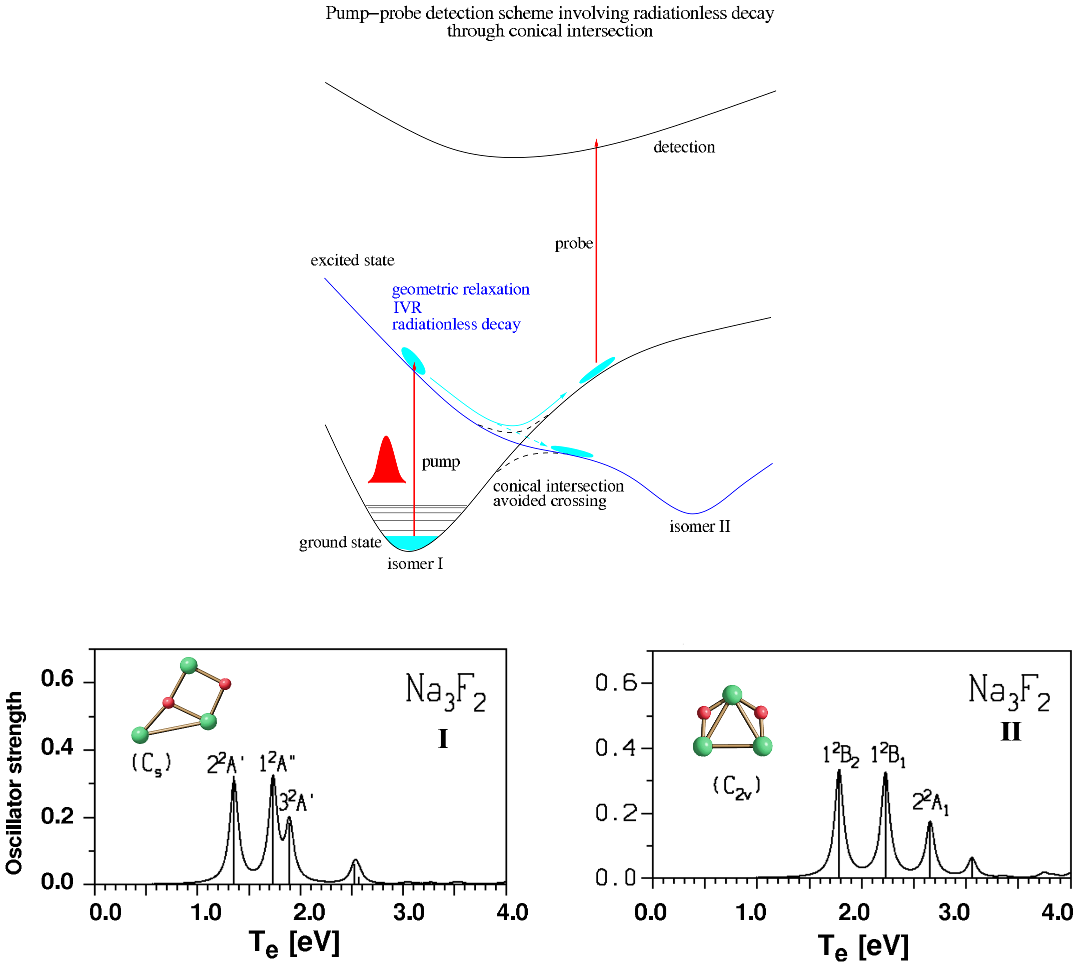

Figure 9.1: (Upper part) Pump probe scheme involving radiationless decay through conical intersection in Na_3F_2. The system is prepared in the ground state isomer I and subsequently excited by the pump-pulse to the first excited state where geometric relaxation followed by a radiationless decay to the ground state occurs. This process can be probed by ionizing the system to the cationic state. (Lower part) Stationary absorption spectra for two isomers of Na_3F_2.

the experimental pulse shaping techniques very often produce fields which achieve the desired goals very efficiently the pulses obtained have very often complicated structure. Therefore, the aim of this work is also to gain understanding of the mechanisms behind the pump-dump control.

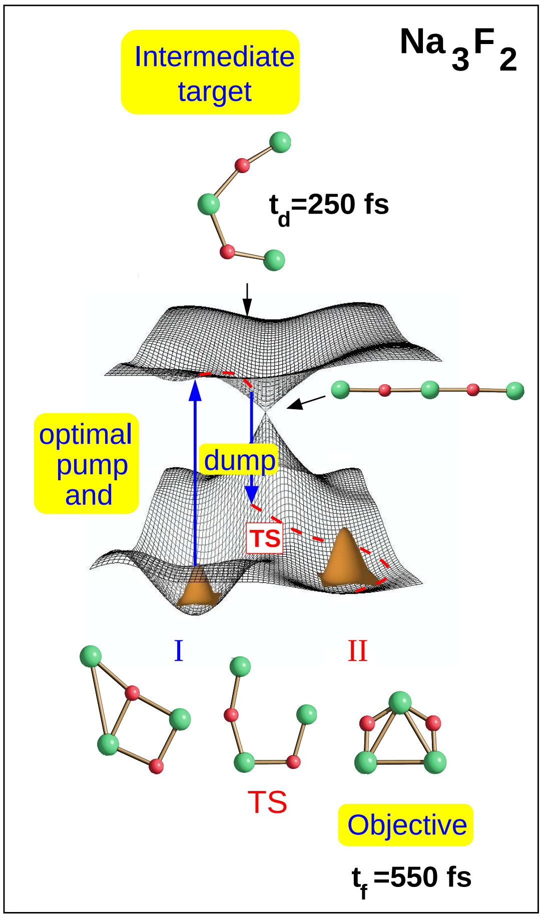

Figure 9.2: Scheme for the pump-dump optimal control in Na_3F_2 cluster with geometries of the two ground state isomers and the transition state (TS) separating them, the conical intersection and the intermediate target.

For this purpose, according to the optimal control strategy described in Section 9.2 first the initial ensemble corresponding to the C_s isomer is generated and then the intermediate target is determined which allow to optimize pump and dump pulses designed to populate selectively only isomer II in the ground state.

The scheme for the optimal pump-dump control in Na_3F_2 is shown in Figure 9.2. The initial conditions were generated by sampling 50 K canonical distribution in the ground state of the C_s Na_3F_2 isomer in the Wigner representation (cf. Equation (7.2)). Totally 800 initial conditions were generated and propagated classically for 300 fs on the first excited state with a vertical excitation energy of 1.33 eV. To define the intermediate target and the optimal dump time t_d the ensemble was dumped back to the ground state every 25 fs and subsequently propagated for 1 ps. The propagation in the ground state has shown that the objective can be reached by using the excited state ensemble at $t_d = 250$ fs as a starting ensemble and that the residence time in the isomer II in the ground state is at least 500 fs. It should be noted that also for times larger than 250 fs the objective can be reached but the residence time and the occupation are much smaller because of the larger excess of energy gained by the propagation on the excited state.

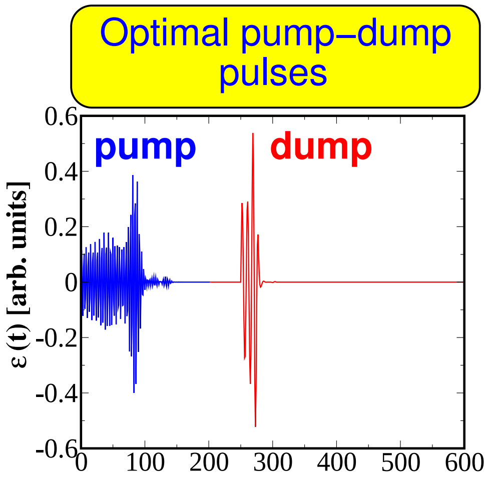

Figure 9.3: The optimal electric fields corresponding to the optimal pump- (blue line) and dump- (red line) fields.

For the intermediate target in the Wigner representation a minimum uncertainty wave packet of the form

$$A(q_i, p_i) = \prod_{i=1}^{3N=15} \frac{1}{2\pi\Delta q_i \Delta p_i} e^{-(q_i-\bar{q}_i)^2/2(\Delta q_i)^2} e^{-(p_i-\bar{p}_i)^2/2(\Delta p_i)^2} \tag{9.24}$$

has been assumed. The ensemble averaged geometry at $t_d = 250$ fs defines the coordinates $\bar{q}_i$ of the intermediate target as shown in Figure 9.2 and the momenta $\bar{p}_i$ were obtained by averaging the corresponding components over the ensemble. The analysis of the averaged momenta at t_d=250 fs has shown that they are directed in the phase space in the way which leads to the isomer II and the averaged kinetic energy of the intermediate target corresponds to about 75 % of the isomerization barrier in the ground state guaranteeing therefore that after the dump-process the isomerization back to the isomer I does not take place. The uncertainties in the coordinates Δq_i were defined such that they correspond to the spreading of the initial ensemble which is about 0.053 Å and the uncertainties in the momenta are given by $\Delta p_i = 1/\Delta q_i$. The material response function $M(\tau, \tau')$ for the pump-pulse was calculated on a time grid with spacing of 1 fs, then symmetrized, and finally according to Equation (9.17) diagonalized using the standard Jacobi procedure. The largest eigenvalue which corresponds to the globally optimal pump-pulse was obtained to be 0.82 which corresponds to a 82 % efficiency of localizing the ensemble in the intermediate target. The optimized pump-pulse is shown in Figure 9.3 and has a complex temporal shape consisting of two portions with durations of ≈70 fs and ≈20 fs, respectively. Physical insight into the mechanism of the pump-dump control can be obtained by considering the Fourier transform and Wigner transform of the pump-pulse (cf. Figure 9.4 and 9.5). The envelope of the Franck-Condon profile has been calculated by sampling the initial Wigner distribution corresponding to the isomer I and calculating vertical excitation energies for an ensemble of 1000 initial phase space points. Comparing the Fourier transform of the pump-pulse with the initial Franck-Condon profile of the isomer I shows that the excitation of the low lying Franck-Condon transition around 1.2 eV of the initial ensemble is mainly responsible for reaching the intermediate target. This spectral region corresponds to lower lying vibrational modes which open the C_s structure by breaking the Na-Na bond and one Na-F bond. The Wigner transform defined as

$$W(t, \omega) = 2Re \int_0^{+\infty} d\tau e^{-i\omega\tau} E^*(t + \frac{\tau}{2}) E(t - \frac{\tau}{2}) \tag{9.25}$$

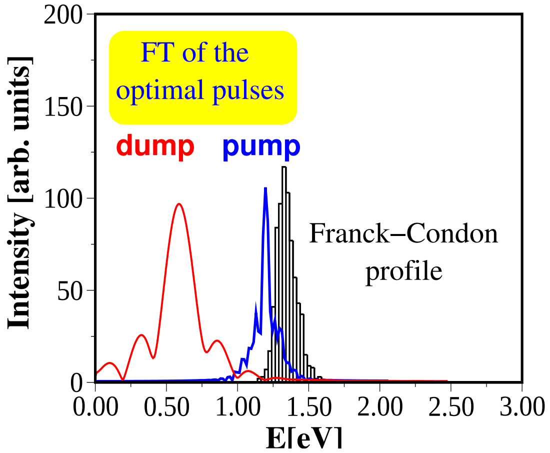

Figure 9.4: Fourier transform of the optimal pump-pulse (blue line) and the optimal dump-pulse (red line) compared with the Franck-Condon profile for the first excited state corresponding to the excitation energy $T_e =$ 1.33eV.

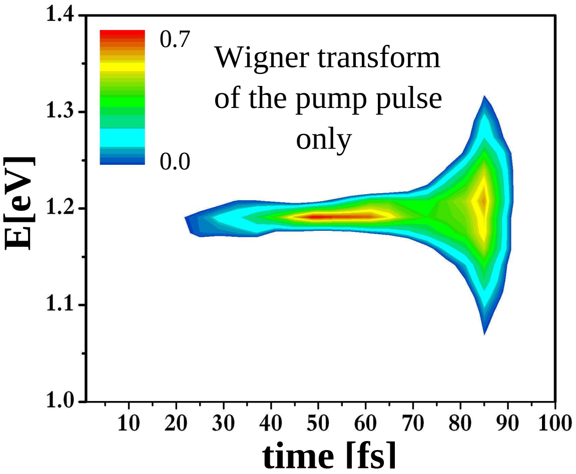

Figure 9.5: Wigner transform of the optimal pump-pulse showing the time resolved energy profile of the pump-pulse.

provides an additional insight into the pulse structure by providing both time and energy resolution of the pulse[1]. The first energetically sharp portion of the Wigner transform (cf. Figure 9.5) corresponds to the first temporal portion ($\approx$ 70fs) of the pulse, whereas the very short second portion after 80-90 fs with the duration of $\approx$ 10 fs is energetically much wider. The latter region is related to the lower and higher lying tails of the Fourier transform (cf. Figure 9.4) which are symmetric with respect to the 1.2 eV.

For the dump-pulse optimization leading to spatial localization of the phase space density in the objective,

---

[1] Wigner transform presents a convenient way to represent electric fields graphically and to extract important features such as the way in which frequency of the field varies with time. The integration in the frequency domain gives directly the field strength

$$\int_{-\infty}^{+\infty} d\omega W(t,\omega) = |E(t)|^2$$

and the integration over the time domain gives the power spectrum of the field,

$$\int_{\infty}^{+\infty} dt W(t,\omega) = |E(\omega)|^2$$

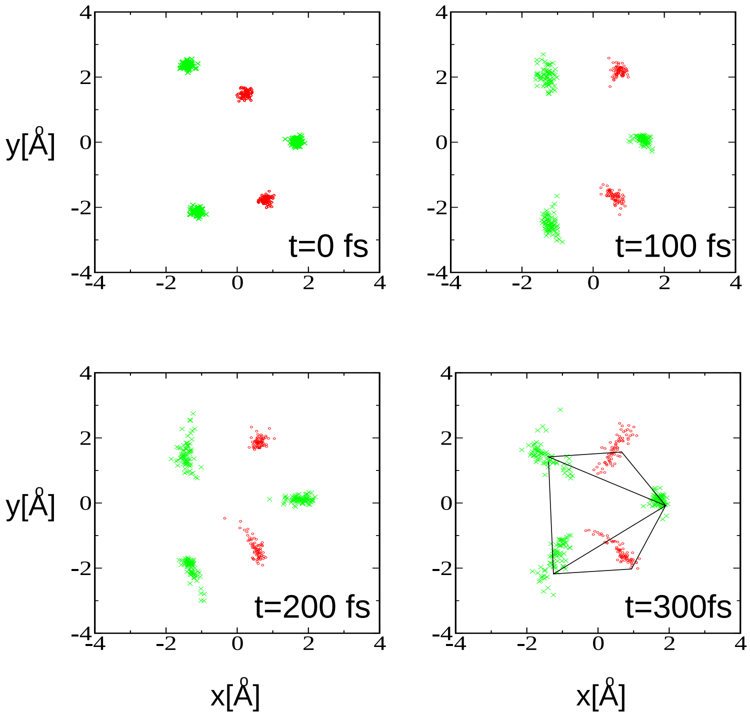

Figure 9.6: Snapshots of the dynamics obtained by propagating the ensemble corresponding to the intermediate target after the optimized pump-dump at 250 fs on the ground state showing the localization of the phase space density in the basin corresponding to the isomer II.

the intermediate target Equation (9.24) was propagated on the ground state and the dump-pulse was determined from the solution of Equation (9.18). The largest eigenvalue obtained was 0.78 corresponding to 78 % efficiency of the localization in the second isomer. The obtained dump-pulse with a duration of only ≈20 fs (cf. Figure 9.3) gives the evidence that the time window around t_d for the depopulation of the excited state induced by the dump-pulse is very short in accordance with the fact that the system gains rapidly a large amount of excess energy on the excited state. Fourier transform of the dump-pulse is centered around 0.6 eV corresponding to the Franck-Condon transition at t_d.

The snapshots of the dynamics propagated onto the ground state after the dump-process are shown in Figure 9.6. It can be seen that the ground phase space density is confined within the basin of the isomer II after about 450 fs and that it remains localized there due to the fact that the average kinetic energy is lower than the isomerization barrier. In contrast to the nonselective isomerization through conical intersection which leads to equal population in both isomers the controlled pump-dump process therefore allows to populate selectively only one desired isomer which is an ultimate goal of femtochemistry.

9.5 Summary and conclusion

A new strategy for optimal pump-dump control of photochemical reactions in multidimensional systems has been developed by introducing the concept of the intermediate target in the excited state. Its role is to select the appropriate Franck-Condon window at a given time delay between the pump- and dump-pulses and to ensure the connective pathway between the initial state and the objective. This is a necessary condition for carrying out the decoupled iterative optimization procedure for the pump and dump pulses separated by the optimal dump time, which allows to decrease the computational demand and permits the application to larger systems. The strategy is illustrated on the example of Na_3F_2. It has been shown that optimal pulses can be found which drive the isomerization process in the desired objective via an excited electronic state. Also, the analysis of the underlying dynamics and of tailored pulses allows to gain insight into the mechanism based on selection of appropriate vibrational modes responsible for reaching the objective. This opens the possibility for an optimal control of complex systems provided that the intermediate target can be found. The knowledge gained from the analysis of the pulse shapes can be used to introduce a guidance towards a better understanding of experimentally shaped pulses.

Chapter 10

Conclusions

The theoretical studies of

(A) Structural, electronic properties and reactivity of metal clusters,

(B) Stationary optical properties of silver clusters and

(C) Real time investigation and control of ultrafast processes in noble metal clusters and in nonstoichiometric sodium fluoride clusters presented in this work let to the following findings:

(A) Structural, electronic properties and reactivity of metal clusters

- The structural and electronic properties of the pure gold and mixed silver-gold clusters have been systematically investigated in the framework of the density functional theory [164, 165]. It has been established that the neutral gold clusters in the range Au_n (n=2-10) assume planar 2D structures in contrast to the pure silver clusters which become three-dimensional at the size of seven atoms. This new finding has been explained by the relativistic effects which lower the energy of the 6s orbital of gold and promote the s-d hybridization which favors the 2D structures. The structural and electronic properties of charged and neutral Ag_mAu_n (m+n=2-5) clusters as well as of neutral Ag_mAu_m (m=2-5), $Ag_{12}Au_8$ and Au_8Ag_2 have been determined. Due to the difference in the electronegativity of silver and gold atoms mixed clusters show a significant charge transfer from silver to gold. Additionally, it has been shown that the electronic properties of these clusters such as IP and VDE can be varied systematically by doping the pure clusters with the other component allowing therefore to tune their reactivity towards for example O_2 or CO. These results stimulated recent experimental ion-mobility studies by Kappes and coworkers [166] performed on cationic mixed clusters up to the size of pentamers which fully confirmed structural predictions made in this work and provided experimental evidence for the predicted role of the charge transfer.

- The study of the reactivity of anionic silver and gold clusters towards O_2 revealed that the reactivity of clusters can be specifically influenced by binding of the electron acceptor groups such as OH or O_2. Specifically, the bare anionic gold clusters with odd number of electrons (e.g. Au_2^-, Au_4^- etc.) bind strongly molecular oxygen while the bare clusters with even number of electrons (e.g. Au_3^-, Au_5^- etc) do not bind molecular oxygen. This situation can, however, be inverted by binding of the OH group to the cluster. This has been explained in the framework of the frontier orbital model and confirmed by density functional calculations in the following way: Binding of the OH group to the cluster with odd number of electrons (e.g. Au_2^-, Au_4^- etc.) leads to the electron transfer from the cluster to the OH group. This leaves the cluster effectively neutral and with a closed shell electronic structure which is unfavorable for the binding of O_2. On the other hand, if the OH group is bound to the cluster with an even number of electrons (e.g. Au_3^-, Au_5^- etc.) due to the strong electron withdrawing effect of the OH group an electron transfer occurs leaving the cluster with an unpaired electron which leads to the strong binding of O_2. These findings provided a valuable insight into the mechanism by which water may influence the activation of O_2 on anionic gold clusters and have been fully confirmed experimentally [16]. The same mechanism proposed for the activation of anionic gold clusters by the OH group has been extended to the anionic silver clusters. Due to the fact that silver clusters exhibit lower electron affinities than gold clusters it has been shown that a cooperative adsorption of molecular oxygen can occur on anionic silver clusters with even number of electrons. In this case the first adsorbed oxygen molecule serves as an activator inducing a strong binding of a second oxygen molecule. This stimulated experiments in which the new oxidized species with activated molecular oxygen like $Ag_3(O_2)_2^-$ and $Ag_5(O_2)_2^-$ have been detected for the first time [17]. Finally, on the example of the reactions between AuO_n^- (n=1,3) with CO it has been demonstrated that oxidized anionic gold species with atomic oxygen bound can play an active role in the oxidation of CO and a mechanism for the oxidation has been revealed based on the ab initio MD simulations supporting recent experimental findings [189].

- The structure-reactivity relationship for $V_xO_y^+$ clusters towards ethylene has been established and a radical center located on one of the peripheral O atoms in $V_2O_5^+$ and $V_4O_{10}^+$ has been identified as an active center for the observed oxygen transfer reaction [205, 206]. Based on the DFT calculations and the ab initio MD simulations a radical cation mechanism leading to the acetaldehyde has been proposed for the observed oxygen transfer in $V_2O_5^+$ and $V_4O_{10}^+$. Based on the comparison between the theoretical IR spectra and experimental infrared multiple-photon dissociation (IR-MPD) spectra, for the first time the structures of the complexes between gas phase clusters and organic molecules have been determined in the case of $V_2O_5C_2H_4^+$ and $V_2O_6C_2H_4^+$ [225]. This study illustrated that the investigation of reactions involving gas-phase cationic vanadium oxide clusters and small hydrocarbons can be suitable for the identification of reactive centers responsible for the selectivity in heterogeneous catalysis.

(B) Stationary optical properties of silver clusters

- The evolution of the structural and optical properties of the small silver clusters in the range Ag_n (n=5-9) have been systematically studied using the equation-of-motion coupled cluster (EOM-CCSD) and the random phase approximation (RPA) methods [160, 254]. This provided the basis for structural assignment based on the comparison between theoretical and experimental absorption spectra. Additionally, the structural relaxation in the excited states of Ag_8 and Ag_9 which leads to the observed fluorescence has been determined.

(C) Real time investigation and control of ultrafast processes in noble metal clusters and in nonstoichiometric sodium fluoride clusters

- The study of the ultrafast dynamics of small coinage metal clusters based on the semiclassical Wigner distribution approach allowed to determine the scope of the NeNePo spectroscopy and to characterize the specific situations in which it can provide the information about the structural properties of the neutral clusters on the one hand, and the isomerization dynamics and structural relaxation on the other hand [163, 260]. Specifically, in the case of the Ag_2Au system the simulated NeNePo spectra revealed that the isomerization process and accompanying IVR in the final isomer can be monitored by selecting the appropriate probe-pulse energies and by performing the experiment under ZEKE-like conditions [262]. For the Ag_4 cluster which assumes related structure in the anionic and neutral ground state the NeNePo spectra show coherent oscillations due to the simultaneous excitation of several normal modes in the neutral global minimum. This allows to extract the vibrational frequencies of the neutral cluster from the pump-probe spectrum and provides a powerful method for structural identification of neutral clusters which is not accessible by other experimental techniques. In the case of Au_4 it has been shown that the local minimum reached after the photodetachment process can act as the "trapping area" for the nuclear dynamics leading to the statistical isomerization process which is spread over a large time scale. Moreover, in addition to the isomerization time scale for the geometric relaxation a structural fingerprint of the local minimum can be obtained from the pump-probe spectra. The theoretical results presented in this work stimulated the NeNePo experiments on Ag_2Au and Ag_4 clusters performed by Wöste and coworkers which fully confirmed the theoretical prediction. The theoretical approach based on the semiclassical Wigner distribution approach in combination with the ab initio MD "on the fly" based on the DFT methods provides a general framework for the accurate simulations of the ultrafast processes in the ground states of complex systems in which all degrees of freedom need to be treated explicitly.

- The confinement molecular dynamics simulations implemented in the framework of the ab initio MD based on the DFT methods [271] allow to study the thermodynamic properties and kinetics in the systems with complex potential energy surfaces in which conventional MD simulations are inefficient. This has been illustrated on the isomerization of the Au_4 cluster in which the equilibrium populations of three different isomer have been calculated together with the rate constants for the isomer interconversion. The results show that in addition to the energy ordering, the conformational entropy may play a significant role for the equilibrium population of different isomers. This issue is very important not only in cluster science but also in conformational studies of biological systems.

- A new strategy for the optimal control with tailored pump-dump pulses has been proposed and formulated in the framework of the semiclassical Wigner distribution approach [281, 282]. It is based on the concept of the intermediate target in the excited state which represents a localized phase distribution whose role is to ensure the connective pathway leading from the ground state via an electronically excited state towards a desired isomer in the ground state and which selects the appropriate Franck-Condon window at a given time delay between the two pulses mandatory for reaching optimally the desired objective. The existence of the intermediate target is necessary for the controllability of multidimensional systems involving two electronic states. The scope of this concept has been shown by optimizing the pump- and dump-pulse which drive the isomerization process in Na_3F_2 cluster to the second ground state isomer via an electronically excited state. It has been shown that the selectivity of this reaction can be dramatically increased by optimizing the pulse which allow to avoid the unselective radiationless transition through the conical intersection between the first excited and the ground electronic state.

In summary, small clusters in the nonscalable regime in which each atom counts exhibit large variety of novel properties.

Kapitel 11

Zusammenfassung

Die Untersuchungen der nichtskalierbaren Eigenschaften von Clustern in dem Größenregime, in dem jedes Atom zählt, zeigten, dass hier neuartige Phänomene und Funktionalität entstehen können. Dadurch motiviert wurden im Rahmen dieser Arbeit:

(A) Strukturelle und elektronische Eigenschaften sowie die Reaktivität von Metall-Clustern,

(B) Stationäre optische Eigenschaften und

(C) Zeitabhängige Eigenschaften und optimale Kontrolle von ultraschnellen Prozessen

theoretisch untersucht und folgende Erkenntnisse gewonnen:

(A) Strukturelle und elektronische Eigenschaften sowie die Reaktivität von Metall Clustern

- Ein Bereich, in dem die Nichtskalierbarkeit von physikalischen Eigenschaften eine wichtige Rolle spielt, ist die chemische Reaktivität von Clustern. Strukturelle und elektronische Aspekte von reinen Gold- und gemischten Silber-Gold Clustern wurden aus diesem Grund systematisch im Rahmen der Dichtefunktionaltheorie untersucht. Eine neue Erkenntnis war, dass neutrale Goldcluster Au_n bis zu einer Größe von zehn Atomen planare 2D Strukturen bilden, wohingegen reine Silber-Cluster bereits ab sieben Atomen dreidimensional vorliegen. Ursache dafür sind relativistische Effekte, die die Energie des 6s Orbitals von Gold in der Art absenken, dass eine s-d Hybridisierung induziert wird und somit 2D Strukturen bevorzugt werden. Darüber hinaus wurden Eigenschaften reiner Gold- und Silber-Cluster mit denen von sowohl neutralen als auch geladenen gemischten Silber-Gold Clustern verglichen, da in diesen zu erwarten war, dass der große Elektronegativitätsunterschied zu einem beträchtlichen Ladungstransfer von Silber zu Gold führt. Ferner können die elektronischen Eigenschaften (z.B. IP und VDE) und dadurch die Reaktivität gemischter Silber-Gold Cluster durch Dotierung der reinen Cluster mit der jeweils anderen Komponente über einen weiten Bereich gezielt eingestellt werden. Dies kann gerade im Zusammenhang mit der Oxidation von CO mit O_2 eine wichtige Rolle spielen.
- Die Untersuchung der Reaktivität von anionischen Gold- und Silber-Clustern hat gezeigt, dass man deren Reaktivität spezifisch beeinflussen kann, indem man Elektronakzeptor-Gruppen (z. B. OH oder O_2) bindet, was schließlich zu kooperativen Effekten, die eine wichtige Rolle für die katalytische Aktivität von Clustern spielen können, führt. So binden z.B. anionische Gold-Cluster mit

ungerader Zahl von Elektronen (z.B. Au_2^-, Au_4^- usw.) ein O_2 Molekül, während die reinen mit gerader Zahl von Elektronen (z.B. Au_3^-, Au_5^- usw.) O_2 nicht binden. Dieses Verhalten kann jedoch vollständig durch die Bindung einer OH Gruppe umgekehrt werden. Im Falle von reinen anionischen Silber-Clustern erreicht man eine Aktivierung schon durch schwächere Elektronenakzeptor-Gruppen. Speziell konnte gezeigt werden, dass die Bindung eines ersten Moleküls Sauerstoff zur kooperativen Bindung eines weiteren Moleküls führen kann, wodurch neuartige aktivierte $Ag_n(O_2)_4^-$ (n=1,3,5) Spezies entstehen, die eine wichtige Rolle für die Oxidationsreaktionen gegenüber CO spielen sollen. In der Tat konnte man zeigen, dass oxidierte Gold-Systeme wie z.B. $AuO_{n=1,3}^-$ gegenüber CO reaktiv sind. Diese Erkenntnisse wurden durch fruchtbare Zusammenarbeit mit experimentellen Gruppen erzielt.

- Die Struktur-Reaktivitäts-Beziehung zwischen $V_xO_y^+$ Clustern und Ethylen konnte basierend auf DFT Untersuchungen und ab initio MD Simulationen aufgeklärt werden. Ein Radikal-Zentrum, das für den beobachteten selektiven Sauerstoff-Transfer in $(V_2O_5^+)_{n=1,2}$ verantwortlich ist, konnte identifiziert, und ein radikal-kationischer Mechanismus für die Oxidation von C_2H_4 an $(V_2O_5^+)_{n=1,2}$ konnte vorgeschlagen werden. Dadurch konnte bestätigt werden, daß Gasphasen-Cluster als Prototypen für die Identifizierung von reaktiven Zentren geeignet sind. Darüber hinaus wurden die berechneten Strukturen von Vanadiumoxid-Komplexen mit Ethylen durch Vergleich mit experimentellen Infrarotspektren bestätigt.

(B) Stationäre optische Eigenschaften

- Optische Eigenschaften von Clustern, die durch Dimensionsreduzierung entstehen, bieten potentiell viele Anwendungsmöglichkeiten. Die kürzlich gefundene photoaktivierte Fluoreszenz von Silber-Clustern an Silber-Oxid Oberflächen kann in der Datenspeicherung angewandt werden. In dieser Arbeit wurden optische Eigenschaften von Silber-Clustern systematisch im Rahmen der EOM-CCSD und RPA Methoden untersucht. Die gewonnenen Ergebnisse ermöglichten im Vergleich mit experimentellen Absorpions- und Fluoreszenz-Anregungs Spektren die Identifizierung struktureller Eigenschaften von kleinen Silber-Clustern. Darüber hinaus wurde die für die Fluoreszenz verantwortliche geometrische Relaxation ermittelt.

(C) Zeitabhängige Eigenschaften und optimale Kontrolle von ultraschnellen Prozessen

- Durch geeignete Wahl von Systemen ist es uns gelungen, Erkentnisse über die Tragweite der NeNePo Technik zu gewinnen. Die Simulationen der NeNePo-ZEKE pump-probe Spektren wurden im Rahmen einer Kombination von der semiklassischer Methode der Wignerverteilungen und ab initio MD "on the fly" basierend auf Dichtefunktionaltheorie durchgeführt. Betreffend der Anwendungen im Rahmen des NeNePo Schemas sind drei Situationen nach dem Photodetachment vorstellbar, die zur Identifikation unterschiedlicher Prozesse in den Signalen dienen können: (i) Ein Übergangszustand des neutralen Systems wird erreicht, und anschließend ist die Dynamik durch die Geometrierelaxation zum globalen oder lokalen Minimum geprägt. Am Beispiel des $Ag_2Au^-/Ag_2Au/Ag_2Au^+$ Systems konnte zwischen struktureller Relaxation und Inter-Cluster-Schwingungsrelaxation (IVR) in simulierten NeNePo-ZEKE und experimentellen NeNePo Spektren unter ZEKE-ähnlichen Bedingungen unterschieden werden. Die außerordentlich gute Übereinstimmung zwischen Theorie und Experiment zeigt, dass eine Auflösung zwischen unterschiedlichen Prozessen in gemessenen zeitaufgelösten

NeNePo Spektren unter ZEKE-ähnlichen Bedingungen vorhanden ist. (ii) In dem Fall, dass das globale Minimum des neutralen Clusters in der Nähe des erreichten Nichtgleichgewichtszustandes liegt, sollte dessen Grundzustandgeometrie aus den Schwingungsmustern identifizierbar sein. Am Beispiel des Systems $Ag_4^-/Ag_4/Ag_4^+$ konnte gezeigt werden, dass die NeNePo Spektroskopie in der Lage ist, strukturelle Infomation über neutrale Cluster in der Gasphase mittels aufgelöster Schwingungsmuster des globalen Minimums zu liefern. (iii) Der erreichte Nichtgleichgewichtszustand liegt in der Nähe eines lokalen Minimums des neutralen Systems und infolgedessen sollten nicht nur zugehörige strukturelle Merkmale durch Schwingungsmuster erkennbar sein, sondern vielmehr ist zu erwarten, dass die Isomerisierungsprozesse dadurch stark beeinflusst werden, wie es am Beispiel von $Au_4^-/Au_4/Au^+$ gezeigt wurde.

- Um eine effiziente Simulation von thermodynamischen und kinetischen Eigenschaften von Clustern und Biomolekülen durchzuführen, wurde die "confinement molecular dynamics" methode im Rahmen der Dichtefunktionaltheorie implementiert. Die Tragweite der Methode wurde am Beispiel der Isomerisierung von Au_4 gezeigt, wo es uns gelungen ist, Gleichgewichtspopulationen von Isomeren sowie die kinetischen Konstanten für die Isomerisierung zu bestimmen.
- Eine neue Strategie für die optimale Kontrolle mit maßgeschneiderten pump-dump Pulsen wurde vorgeschlagen und im Rahmen der semiklassischen Wignerverteilung ausgearbeitet. Sie basiert auf dem Konzept des sogenannten "intermediate target" im angeregten Zustand. Dies entspricht einem lokalisierten Ensemble (Wellenpaket) im angeregten Zustand bei optimaler Zeitverzögerung, für die eine maximale Überlappung mit dem Zielprodukt im Grundzustand sichergestellt wird. Der Erfolg dieser Strategie wurde am Beispiel einer optimalen pump-dump Kontrolle der Isomerisierungsprozesse im Na_3F_2 Cluster illustriert. In diesem Fall sollte der optimierte pump-dump Puls den Weg bevorzugen, der die konische Durchschneidung vermeidet und das Zielprodukt mit einer maximalen Ausbeute besetzt.

Abbildungsverzeichnis

3.1 Structures of neutral gold clusters Au_n (n=2-6) optimized at the 19e-RECP/BP86 level of theory with labels of the symmetry group and of the ground electronic states. The energy difference (in eV) with respect to the lowest energy structure are given in brackets. 62

3.2 Structures of neutral gold clusters Au_n (n=7-10) optimized at the 19e-RECP/BP86 level of theory with labels of the symmetry group and of the ground electronic state. The energy difference (in eV) with respect to the lowest energy structure are given in brackets. 63

3.3 Binding energies per atom for neutral gold clusters $E_b/n = [E(Au_n) - nE(Au)]/n$ as function of the cluster size n calculated for the most stable structures on Figures 3.1 and 3.2. For isomers with energy difference smaller than 0.1 eV both structures are shown. 64

3.4 Calculated (full line) and experimental (dashed line, Ref. [173]) vertical ionization potentials and the most stable structures for Au_n(2-10). 65

3.5 Structures of charged and neutral bimetallic trimers $Ag_mAu_n{}^{0,+,-}$(m+n=3) optimized at the 1e-RECP and 19e-RECP level of theory. The energy difference (in eV) with respect to the most stable structure obtained from the former and latter approach are given in the round and square brackets, respectively. I-III denote energy sequence of the isomers according to 1e-RECP results. Labels of the symmetry group and of the ground electronic state are also given. 66

3.6 Structures of charged and neutral bimetallic tetramers $Ag_mAu_n{}^{0,+,-}$(m+n=4) optimized at the 1e-RECP and 19e-RECP level of theory. The energy difference with respect to the most stable structure obtained from the former and the latter approach are given in the round and square brackets, respectively. I-IV denote energy sequence of the isomers according to 1e-RECP BLYP results. Labels of the symmetry group and of the ground electronic states are also given. 68

3.7 The most stable structures of charged and neutral bimetallic pentamers $Ag_mAu_n^{0,+,-}$ obtained from 1e-RECP BLYP method. 69

3.8 Structures of neutral bimetallic Ag_3Au_3, Ag_4Au_4 and Ag_5Au_5 clusters optimized at 1e-RECP and 19e-RECP level of theory. The energy differences with respect to the most stable structure (in eV) obtained from the the former and latter approach are given in round and square brackets, respectively. I-IV denote the energy sequence of isomers according to 1e-RECP BLYP results. Labels of the symmetry group and the ground electronic states are also given. 70

3.9 Optimized structures of $Ag_{10}Au_{10}$ and $Ag_{12}Au_8$ clusters at 1e-RECP level of theory with relative energy differences in brackets. 72

3.10 Calculated VDE and IP values for Au_nAu_m(n+m=3,4,5) varying the number of Ag atoms m. . . 73

3.11 (Left side) Calculated (full line) and experimental (dashed line, Ref. [173]) vertical ionization potentials and the most stable structures for Au_n(2-10). (Right side) Vertical ionization potentials and structures for Ag_mAu_m(m=1-5). 73

3.12 Catalytic cycle for the oxidation of CO on $AgAu^-$ dimer. 74

4.1 (Bottom) Mass spectrum of negatively charged gold clusters, Au_n^- and various hydrates of the form $Au_n(OH)_{0,1,2}(H_2O)_{0,1,2}^-$ generated by adding H_2O into the buffer gas of the cluster source and the secondary gas pulse is temporally offset from the main cluster pulse corresponding to the situation where no reactant gas (O_2) has been added. (Top) Mass spectrum obtained when the secondary gas pulse containing ∼20% O_2:He is temporally overlapped with the main pulse. In addition to the depletion of the Au_4^- peak and Au_3OH^-, peaks appear at 32 amu higher mass, corresponding to the O_2 adsorption. 79

4.2 Optimized structures of the Au_nOH^- complexes (n=2-5). For the Au_5 system, ΔE values (in eV) for different isomers are given in parentheses. Oxygen and hydrogen atoms are labeled by large red and small blue circles, respectively. Isomers corresponding to the local minima whose relative energies are less than 1 eV with respect to the most stable structure are shown. 80

4.3 (Top) Binding energies of O_2 (triangles) and OH (circles) on Au_n^- clusters (n=2-5). (Bottom) O_2 adsorption energies on Au_nOH^- clusters. 82

4.4 Cluster size dependence of the extent of reaction as a function of the partial pressure of O_2 in the reactor. 83

4.5 Optimized structures of $Au_nOH(O_2)^-$ complexes (n=2-5). For the Au_5 system, ΔE values (in eV) for different isomers are given in parentheses. Oxygen and hydrogen atoms are labeled by large red and small blue circles, respectively. Isomers corresponding to the local minima whose relative energies are less than 1 eV with respect to the most stable structure are shown. 84

4.6 (A) Product ion mass spectra after reaction of Ag_n^- with O_2. Ion intensities are plotted as function of the number of adsorbed oxygen atoms m. (B) Experimental rate constants obtained for the adsorption of the first and second O_2 molecule onto Ag_n^- at $T_R = 300$K. (C) Theoretical binding energies E_b and lowest energy structures (grey spheres: silver atoms, red spheres: oxygen atoms). 87

4.7 (A) Mass spectra showing the reactions of AuO_n^-(n=1,3) clusters with CO. (B) MD snapshots for the reaction of AuO^- and CO. 89

5.1 Mass distribution of vanadium oxide cluster cations taken from Reference [21]. 93

5.2 Structures for (a) $V_2O_2^+$ (b) $V_2O_3^+$ (c-I) trans $V_2O_4^+$, (c-II) cis $V_2O_4^+$, (d) $V_2O_5^+$, (e-I) peroxo $V_2O_6^+$, (e-II) trans $V_2O_6^+$, (e-III) $V_2O_6^+$ cis $V_2O_6^+$, (e-IV) $V_2O_6^+$, clusters. Energy difference in eV with respect to the most stable structures are given in round brackets. I-IV label the energy sequence of the isomers. Labels of the symmetry group and the ground electronic state are also given. Bond distances are given in Å Binding energies per atom (in eV) defined according to Equation 5.2 are also shown. 94

5.3 Structures for (f) $V_4O_8^+$, (g) $V_4O_9^+$,(h-I) $V_4O_{10}^+$, (h-II) $V_4O_{10}^+$ and (h-III) $V_4O_{10}^+$ clusters. Energy difference in eV with respect to the most stable structures are given in round brackets. I-IV label the energy sequence of the isomers. Labels of the symmetry group and the ground electronic state are also given. Bond distances are given in Å Binding energies per atom (in eV) defined according to Equation 5.2 are also shown. 95

5.4 Structures for (a-I) $V_2O_3^+$-C_2H_4, (a-II) $V_2O_3^+$-C_2H_4 , (b-I) $V_2O_4^+$-C_2H_4, (b-II) $V_2O_4^+$-C_2H_4, (b-III) $V_2O_4^+$-C_2H_4, (c-I) $V_2O_5^+$-C_2H_4, (c-II) $V_2O_5^+$-C_2H_4, (c-III) $V_2O_5^+$-C_2H_4, (d-I) $V_2O_6^+$-C_2H_4, (d-II) $V_2O_6^+$-C_2H_4, (d-III) $V_2O_6^+$-C_2H_4, (d-IV) $V_2O_6^+$-C_2H_4 , (e-I) $V_4O_{10}^+$-C_2H_4 complexes. Binding energies per atom (in eV) are defined as $E_b/n = [E(V_xO_y^+\text{-}C_2H_4) - E(V^+) - (x-1)E(V) - yE(O) - 2E(C) - 4E(H)]/(x+y+6)$. 96

5.5 Relative product branching ratios of $V_2O_{4-6}^+$ with ethylene. (□) – $V_xO_{y-2}^+$, (■) – $V_xO_{y-1}^+$, (◆) – $V_xO_y^+$, (+) – $V_xO_{y-2}C_2H_4^+$, (∗) – $V_xO_yC_2H_4^+$ 97

5.6 Snapshots of the ab initio MD trajectory calculated using RI-BP86 method for the reaction of $V_2O_5^+$ with C_2H_4 leading to formation of acetaldehyde. 101

5.7 Snapshots of the ab initio MD trajectory calculated using RI-BP86 method for the reaction of $V_2O_5^+$ with C_2H_4 leading to the formation of two formaldehyde molecules. 102

5.8 Energetic profile for the reaction between $V_2O_5^+$ and C_2H_4. 102

5.9 Relative intensity of $V_2O_5^+$ for the reaction between $V_2O_5^+$ and C_2H_4 as a function of pressure at four different energies. 5.1 eV, 10.1 eV, 15.1 eV and 20.1 eV represented by four different symbols. 103

5.10 Schematic reaction profile representing the oxygen transfer reaction from $V_2O_5^+$ to C_2H_4. Parameters needed for calculation of the energy dependent reaction cross sections are shown. ΔE_{1-3} represent energy differences and k_{1-5} are kinetic constants for the elementary reaction steps, $E^\sharp$ is the barrier for the oxygen transfer reaction. 104

5.11 Energy dependent reaction cross section for the oxygen transfer from $V_2O_5^+$ to C_2H_4 calculated using Equation 5.21 105

5.12 Calculated pressure dependence of the relative intensity of $V_2O_5^+$for four different energies shown in the insert. 106

5.13 Energetic profile for the reaction between $V_4O_{10}^+$ and C_2H_4. 107

5.14 Snapshots of the ab initio MD trajectory calculated using B3LYP method for the reaction between $V_4O_{10}^+$ and C_2H_4 leading to the formation of acetaldehyde. 108

5.15 Infrared multiple photon dissociation (IR-MPD) spectra of $V_2O_5C_2H_4^+$ and $V_2O_6C_2H_4^+$ together with calculated spectra for several isomers. 109

5.16 Schematic diagram showing the relative energies (in eV) of four different isomers of $V_2O_5C_2H_4^+$ (Ia-d) and the energetics of the ethylene oxidation on Ia leading to acetaldehyde (cf. Figure 5.8). . 110

5.17 General reaction mechanism for the reaction between $(V_2O_5)_{n=1,2}^+$ and C_2H_4. 111

6.1 CCSD optimized geometries of the Ag_{5-8} clusters and BP86 optimized structures of Ag_9 using 11e-RECP with associated AO basis set. Labels of the point group and the ground state are given below structures together with relative energies in eV with respect to the most stable structure. The isomeric forms for the same cluster size are numbered as I-IV. 115

6.2 Absorption spectra of the most stable isomers of Ag_{2-8} obtained from EOM-CCSD and STEOM-CCSD methods using 11e-RECP and of the most stable structure of Ag_9 cluster obtained from the RPA method. The lines have been broadened using Lorentzian function with the width of 0.15 eV. 118

6.3 Absorption spectra for the second isomers of Ag_5 and Ag_6 calculated with the EOM-CCSD method. The transition energies are given in eV. 119

6.4 Comparison between the calculated spectra for the two lowest isomers of Ag_5 and the experimental absorption spectrum measured in Argon matrix. Experimental results have been taken from Reference [252]. In order to take into account the shift of the lines due to the Argon matrix the experimental spectrum has been shifted for 0.20 eV to the blue. 120

6.5 Comparison between the calculated spectra for the two lowest isomers of Ag_7 and the experimental absorption spectrum measured in Argon matrix. Experimental results have been taken from Reference [252]. In order to take into account the shift of the lines due to the Argon matrix the experimental spectrum has been shifted for 0.20 eV to the blue. 121

6.6 Comparison of the calculated absorption spectra for T_d (green) and D_{2d} structures (yellow) of Ag_8, their superposition (brown) with experimental absorption spectrum (blue) [252]. Excitation spectrum and the observed fluorescence band are shown in the bottom panel. Experimental spectra have been shifted to the blue for 0.25 eV in order to account for the matrix effect 122

6.7 Comparison of the optical spectrum of Ag_8 obtained in helium droplet using resonant two-photon ionization (Ref. [249]) and calculated absorption spectra for T_d (left) and D_{2d} (right) structures of Ag_8. 123

6.8 Absorption spectra for distorted T_d structures obtained from RPA calculations by shortening one distance between two atoms (blue circles) of the outer tetrahedron relating T_d and D_{2d} structures (upper panel) and by elongating one distance between two atoms (blue circles) of the inner tetrahedron. 124

6.9 Fluorescence spectra of Ag_9 at 25 K and 4 K (laser excitation 4.03 eV). Cooling the sample down unravels the details of vibrational progression of the ground state of Ag_9. Two vibrations have been identified and are indicated in the lower part of the figure. Accordingly, the fluorescence peak origin is at 3.649±0.001 eV. 125

6.10 Absorption, excitation and fluorescence spectra of Ag_9 in an argon matrix. 126

6.11 (a-d) Calculated absorption spectra for the four lowest isomer of Ag_9, (e) Measured excitation spectrum shifted by 0.25 eV to account for the matrix shift. (f) Measured absorption spectrum of Ag_9 shifted by 0.25 eV compared to the sum of the different spectra with the following weights: C_{2v}(I) 26 %, C_{2v} (II) 37 %, C_{3v} (IV) 37 %. 126

7.1 General scheme of the NeNePo pump probe spectroscopy. The system is prepared in the anionic state. Then the pump pulse detaches the electron leaving the neutral clusters in a non-equilibrium state (blue curve) which subsequently evolves on the neutral potential energy surface. The dynamics is probed by time delayed ionization and cationic clusters are detected by mass spectrometry. . . 130

7.2 Scheme of the multistate femtosecond dynamics of Ag_2Au in the framework of the NeNePo pump-probe spectroscopy involving anionic, neutral and cationic states. Vertical excitation energies are given by arrows. All corresponding geometries of isomers are drawn. Numbers in parentheses are energies with respect to the ground electronic state of the most stable isomer. 134

7.3 Histogram of the vertical detachment energies between the anionic and neutral Ag_2Au at 20 K initial temperature obtained from 500 initial phase space points. 134

7.4 Bunch of the energy gaps between the neutral and cationic state of Ag_2Au for 420 trajectories during the dynamics on the neutral electronic ground state obtained for the initial temperature of 20 K. 135

7.5 Snapshots of the dynamics in the neutral ground state of Ag_2Au after the photodetachment. The projection of 420 phase space points onto the xy plane is shown. Red circles represent Au atoms and black circles Ag atoms. 136

7.6 Comparison between the simulated NeNePo-ZEKE signals and experimental NeNePo signals for 20 K initial ensemble of Ag_2Au at different energies of the probe pulse. 137

7.7 Simulated time resolved photoelectron spectrum (TRPES) of Ag_2Au using the probe pulse energy $E_{pr} = 7.04$ eV and the pulse duration σ_{pr}=100 fs. 138

7.8 Scheme of the multistate femtosecond dynamics of Ag_4 in the framework of the NeNePo pump-probe spectroscopy. Vertical transition energies are given by arrows. All corresponding structures of isomers are drawn. Numbers in parentheses refer to energies with respect to the ground electronic state of the corresponding most stable isomer. 139

7.9 Temperature dependence of the isomerization process in the anionic Ag_4 obtained from classical molecular dynamics simulations performed at constant energies. The graphs show dependence of the σ indices defined in Equation (7.4) on time. σ indices are assigned to the atoms by colors. . . 140

7.10 Histogram of the vertical detachment energies (Franck-Condon profile) between the anion and neutral Ag_4 for 50 K, 360 K and 625 K initial temperature ensemble obtained by sampling 1000 phase space points 141

7.11 Bunch of the energy gaps between the neutral and cationic state of Ag_4 for 30 trajectories during the dynamics on the neutral electronic ground state obtained for initial temperature of 50 K. . . 143

7.12 Simulated NeNePo-ZEKE pump-probe signals for 50 K initial ensemble of Ag_4 at different excitation energies E_{pr} and pulse duration σ_{pr} of the probe pulse. 143

7.13 Scheme of the multistate femtosecond dynamics of Au_4 in the framework of the NeNePo pump-probe spectroscopy. Vertical transition energies are given by arrows. All corresponding geometries of isomers (AI, AII, AIII of the anion; I, II, III of the neutral) are drawn. Numbers in parentheses are energies with respect to the ground electronic state of the corresponding most stable isomer. 144

7.14 Histogram of the vertical detachment energies between the anion and neutral Au_4 for 50 K initial temperature ensemble obtained from 1000 phase space points. 146

7.15 Bunch of the energy gaps between the neutral and cationic state of Au_4 for 250 trajectories during the dynamics on the neutral electronic ground state obtained for the initial temperature of 50 K. . 146

7.16 Ensemble averaged kinetic energy decomposed into the ω_3, ω_4 and ω_5 normal modes of the neutral linear structure (cf. table 7.2) during the first 1.5 ps of propagation on the neutral ground state of Au_4. 147

7.17 Simulated NeNePo-ZEKE pump-probe signals for 50 K initial ensemble of Au_4 at different excitation energies of the probe pulse E_{pr} corresponding to different geometries are shown with a probe pulse duration of 100 fs. 148

8.1 Schematic picture of the potential energy surface of Au_4. 155

8.2 Lifetime distributions for (a) rhombic, (b) T-shape, and (c) linear isomers. Solid and empty triangles label the confinement and direct simulations, respectively. Dashed lines show the Poisson distributions based on the mean lifetimes of Table 8.5. 156

8.3 Time-dependent populations of the isomers. 157

9.1 (Upper part) Pump probe scheme involving radiationless decay through conical intersection in Na_3F_2. The system is prepared in the ground state isomer I and subsequently excited by the pump-pulse to the first excited state where geometric relaxation followed by a radiationless decay to the ground state occurs. This process can be probed by ionizing the system to the cationic state. (Lower part) Stationary absorption spectra for two isomers of Na_3F_2. 164

9.2 Scheme for the pump-dump optimal control in Na_3F_2 cluster with geometries of the two ground state isomers and the transition state (TS) separating them, the conical intersection and the intermediate target. 165

9.3 The optimal electric fields corresponding to the optimal pump- (blue line) and dump- (red line) fields. 166

9.4 Fourier transform of the optimal pump-pulse (blue line) and the optimal dump-pulse (red line) compared with the Franck-Condon profile for the first excited state corresponding to the excitation energy $T_e = 1.33$eV. 167

9.5 Wigner transform of the optimal pump-pulse showing the time resolved energy profile of the pump-pulse. 167

9.6 Snapshots of the dynamics obtained by propagating the ensemble corresponding to the intermediate target after the optimized pump-dump at 250 fs on the ground state showing the localization of the phase space density in the basin corresponding to the isomer II. 168

Tabellenverzeichnis

3.1 Ground state properties of the atoms and dimers obtained with the 1e-RECP BLYP and the 19e-RECP BP96(in square brackets) methods. 60

3.2 Vertical ionization potentials (IP_v) and vertical detachment energies (VDE) for Ag_mAu_n (m+n=2,3,4,5), Ag_nAu_n (n=3,4,5,10) and $Ag_{12}Au_8$ clusters obtained with 1e-RECP BLYP and 19e-RECP BP86 (in square brackets) methods. 66

4.1 Ground state energies and properties of optimized Au_nOH^-(n=2-5) clusters obtained with the B3LYP method. 81

4.2 Ground state energies and properties of optimized $Au_nOH(O_2)^-$(n=2-5) clusters obtained from the B3LYP method. 85

4.3 Experimental and theoretical values of ionization potentials (IP) for Au_n (n=2-6). 86

5.1 Overview of the important theoretical and experimental reactions between $V_xO_y^+$and C_2H_4. . . . 98

6.1 Ground state energies of the DFT- and CCSD-optimized Ag_n (n=5-8) clusters. 116

7.1 Energies, geometries, harmonic frequencies and vibrational periods for the isomeric forms of neutral and charged Ag_4 clusters. 142

7.2 Energies, geometries, harmonic frequencies and vibrational periods for isomeric forms of neutral and charged Au_4 clusters. 145

8.1 Characteristics of the isomers: Energies, U^0(a.u), harmonic frequencies, ν^0(cm^{-1}), and vibrational periods (ps) 152

8.2 Characteristics of the transition states: Energies, U^*(a.u), and harmonic frequencies ν^* (cm^{-1}). . 152

8.3 Transition probabilities, q_{ij}, for the time interval of 0.1 ps. In brackets, there are given the corresponding values of q_{ij} obtained in direct simulations. 155

8.4 Transition probabilities, q_{ij}, for the time interval of 0.1 ps, predicted by RRKM theory. The RRKM rate constants w_{ij} were calculated using data of Tables 8.1 and 8.2. 156

8.5 Mean lifetimes, calculated from the transition probabilities of Table 8.3 via Eq. 8.5, 'temperatures' of the isomers, calculated from the kinetic energies of the system in the corresponding basins, and the equilibrium populations of the isomers from Figure 8.1. In brackets there are given the corresponding values found in the direct simulations. 156

Literaturverzeichnis

[1] V. Bonačić-Koutecký, P. Fantucci, J. Koutecký, Chem. Rev., **91**, 1035 (1991).

[2] J. Jortner, Z. Phys. D **24**, 247 (1992).

[3] U. Landman, Int. J. Mod. Phys. B **6**, 3623 (1992).

[4] A. W. Castleman Jr., K. H. Bowen, J. Phys. Chem., **100**, 12911 (1996).

[5] W. Ekardt (ed.), “Metal Clusters”, John Wiley & Sons, New York, 1999.

[6] A. H. Zewail, in “Femtosecond Chemistry”, Eds.: J. Manz, L. Wöste, VCH, Weinheim, 1995.

[7] A. H. Zewail, J. Phys. Chem. A, **104**, 5660 (2000).

[8] A. H. Zewail, in “Femtochemistry”, Eds.: F. C. de Schryver, S. de Feyter and G. Schweitzer, John Wiley-VCH, 1 2001.

[9] M. Haruta, Catal. Today, **36**, 153 (1997).

[10] A. Sanchez, S. Abbet, U. Heiz, W. D. Schneider, H. Häkkinen, R. N. Barnett, U. Landman, J. Phys. Chem. A, **103,** 9753 (1999).

[11] T. H. Lee, K. M. Ervin, J. Phys. Chem. **98**, 10023 (1994).

[12] B. E. Salisbury, W. T. Wallace, R. L. Whetten, Chem. Phys. **262**, 131 (2000).

[13] M. Haruta, N. Yamada, T. Kobayashi, J. Catal., **115**, 301 (1989).

[14] M. Haruta, S. Tsubota, T. Kobayashi, et. al., J. Catal., **144**, 175 (1993).

[15] F. Boccuzzi, A. Chiorino, J. Phys. Chem. B, **104**, 5414 (2000).

[16] W. T. Wallace, R. B. Wyrwas, R. L. Whetten, R. Mitrić, V. Bonačić-Koutecký, J. Am. Chem. Soc., **125**, 8408 (2003).

[17] J. Hagen, L. D. Socaciu, J. Le Roux, D. Popolan, T. M. Bernhardt, L. Wöste, R. Mitrić, H. Noack, V. Bonačić-Koutecký, J. Am. Chem. Soc., submitted.

[18] B. K. Warren, S. T. Oyama, “Heterogeneous Hydrocarbon Oxidation”, American Chemical Society, Washington DC, 1993.

[19] E. L. Mutterties, Science, **196**, 839 (1977).

[20] X. Lai, D. W. Goodman, J. Mol. Catal. A, **162**, 33 (2000).

[21] K. A. Zemski, D. R. Justes, A. W. Castleman Jr., J. Phys. Chem. B, **106**, 6136 (2002).

[22] L. A. Peyser, A. E. Vinson, A. P. Bartko, R. M. Dickson, Science, **291**, 103 (2001).

[23] L. A. Peyser, T. H. Lee, R. M. Dickson, J. Phys. Chem. B, **106**, 7725 (2002).

[24] S. Wolf, G. Sommerer, S. Rutz, E. Schreiber, T. Leisner, L. Wöste, R. S. Berry, Phys. Rev. Lett., **74**, 4177 (1995).

[25] S. F. Chekmarev: In *"Atomic Clusters and Nanoparticles", Lectures at the Les Houches Summer School, Session No. LXXIII*, ed. by C. Guet, P. Hobza, F. Spiegelman and F. David, Springer-Verlag and EDP Sciences, Les Ulis 2001, pp. 509-563.

[26] T. Brixner, G. Gerber, ChemPhysChem, **4**, 418 (2003).

[27] A. Assion, T. Baumert, M. Bergt, T. Brixner, B. Kiefer, V. Seyfried, M. Strehle, G. Gerber, Science, **282**, 919 (1998).

[28] S. Vajda, A. Bartelt, E. C. Kaposta, T. Leisner, C. Lupulescu, S. Minemoto, P. Rosendo-Francisco, L. Wöste, Chem. Phys., **267**, 231 (2001).

[29] C. Daniel, J. Full, L. Gonzalez, C. Kaposta, M. Krenz, C. Lupulescu, J. Manz, S. Minemoto, M. Oppel, P. Rosendo-Francisco, S. Vajda, L. Wöste, Chem. Phys., **267**, 247 (2001).

[30] R. S. Judson, H. Rabitz, Phys. Rev. Lett., **68**, 1500 (1992).

[31] P. A. M. Dirac, "Quantum mechanics", 4th ed., Oxford Univ. Press, London, 1958; J. J. Sakurai, "Modern quantum mechanics", Addison-Wesley Publ., Reading, Massachusetts, 1994.; E. Merzbacher, "Quantum mechanics", 2nd ed., Wiley, New York, 1970.

[32] H. Goldstein, "Classical mechanics", 2nd ed. Addison-Wesley Publ., Reading, Massachusetts, 1980.

[33] E. P. Wigner, Phys. Rev., **40**, 749 (1932).

[34] W. P. Schleich, "Quantum Optics in Phase Space", Wiley-VCH, Berlin, (2001).

[35] J. von Neumann, "Mathematische Grundlagen der Quantenmechanik", Springer Verlag, Berlin, 1932.

[36] B. T. Sutcliffe, Adv. Quantum. Chem., **28**, 65 (1997).

[37] M. V. Berry, Proc. Roy. Soc. London, **A392**, 45 (1984).

[38] G. Herzberg, H. C. Longuet-Higgins, Disc. Faraday Soc. **35**, 77 (1963).

[39] G. Delacrétaz, E. R. Grant, R. L. Whetten, L. Wöste, J. W. Zwanziger, Phys. Rev. Lett., **56**, 2958 (1986).

[40] R. Fletcher, "Practical methods of optimization", Vol. 1 and Vol. 2, Wiley, New York, 1980.

[41] H. B. Schlegel, in "Modern electronic structure theory", Part I, ed. D. Yarkony, World Scientific, 1995.

[42] F. Jensen, "Introduction to Computational Chemistry", John Wiley & Sons, New York, 1999.

[43] P. Pulay, in "Modern electronic structure theory", Part I, ed. D. Yarkony, World Scientific, 1995.

[44] R. Fletcher, M. J. D. Powell, Comput. J., **6**, 76 (1970); W. Davidson, Argonne National Lab. Report ANL-5900.

[45] C. G. Broyden, J. Inst. Math. Appl., **6**, 76 (1970); R. Fletcher, Comput. J., **13**, 317 (1970).; D. Goldfarb, Math. Comput., **24**, 23 (1970); D. F. Shanno, Math. Comput., **24**, 647 (1970).

[46] P. Pulay, G. Fogarasi, G. Pongor, J. E. Boggs, A. Vargha, J. Am. Chem. Soc., **105,** 7037 (1982).

[47] S. Kirkpatrick, C. D. Gelatt Jr., M. P. Vecchi, Science, **220**, 671 (1983); P. J. M. van Laarhoven, E. H. L. Aarts, Simulated Annealing: Theory and Applications, D. Reidel, Dordrecht, 1988.

[48] G. Chang, W. C. Guida, W. C. Still, J. Am. Chem. Soc., **111**, 4379 (1989).

[49] R. S. Judson, Rev. Comput. Chem., **10**, 1 (1997).

[50] J. Kostrowicki, H. A. Scheraga, J. Phys. Chem., **96**, 7442 (1992).

[51] E. B. Wilson, J. C. Decius, P. C. Cross, “Molecular Vibrations”, McGraw-Hill, New York, (1955).

[52] T. A. Halgren, W. N. Lipscomb, Chem. Phys. Lett., **49**, 225 (1977).

[53] S. Bell, J. S. Crighton, J. Chem. Phys., **80**, 2464 (1984).

[54] C. Peng, H. B. Schlegel, Isr. J. Chem., **33**, 449 (1993).

[55] R. Czerminski, R. Elber, Int. J. Quantum. Chem. Symp., **24**, 167 (1990).

[56] M. J. S. Dewar, E. F. Healy, J. P. Stewart, J. Chem. Soc. Faraday Trans., **80**, 227 (1984).

[57] D. A. Liotard, Int. J. Quantum. Chem., **44**, 723 (1992).

[58] K. Fukui, Acc. Chem. Res., **14**, 363 (1981).

[59] C. Gonzales, H. B. Schlegel, J. Chem. Phys., **95**, 5853 (1991).

[60] A. Szabo, N. S. Ostlund, “Modern Quantum Chemistry”, McGraw-Hill, New York, 1982.

[61] R. McWeeny, “Methods of Molecular Quantum Mechanics”, Academic Press, London, 1992.

[62] V. R. Saunders, I. H. Hillier, Mol. Phys., **28**, 819 (1974).

[63] P. Pulay, J. Comput. Chem., **3**, 556 (1982).

[64] R. Seeger, J. A. Pople, J. Chem. Phys., **65**, 265 (1976).

[65] E. R. Davidson, J. Comput. Phys. **17**, 87 (1975).

[66] J. Čížek, J. Chem. Phys., **45**, 4256 (1966).

[67] J. Čížek, Adv. Chem. Phys., **14**, 35 (1968).

[68] R. J. Bartlett, J. Phys. Chem., **93**, 1697 (1989).

[69] E. A. Salter, G. W. Trucks, R. J. Bartlett, J. Chem. Phys., **90**, 1752 (1989).

[70] J. Gauss, J. F. Stanton, R. J. Bartlett, J. Chem. Phys., **95**, 2639 (1991).

[71] R. G. Parr, W. Yang, “Density Functional Theory”, Oxford Univ. Press, London, 1989.

[72] L. H. Thomas, Proc. Cambridge Philos. Soc., **23**, 542 (1927).; E. Fermi, Z. Phys., **48**, 73 (1928).

[73] P. A. M. Dirac, Proc. Cambridge Philos. Soc., **26**, 376 (1930).

[74] J. C. Slater, Phys. Rev., **81**, 385 (1951).

[75] C. F. von Weizsäcker, Z. Phys., **96**, 431 (1935).

[76] P. Hohenberg, W. Kohn, Phys. Rev., **136**, 864 (1964).

[77] W. Kohn, L. J. Sham, Phys. Rev., **140**, 1133 (1965).

[78] E. Teller, Rev. Mod. Phys., **34**, 627 (1962).

[79] J. A. Pople, R. K. Nesbet, J. Chem. Phys., **22**, 571 (1954).

[80] D. M. Ceperley, B. J. Alder, Phys. Rev. Lett., **45**, 566 (1980).

[81] S. J. Vosko, L. Wilk, M. Nusair, Can. J. Phys., **58**, 1200 (1980).

[82] A. D. Becke, in “Modern Electronic Structure Theory”, Part I, ed. D. R. Yarkony, World Scientific, (1995).

[83] J. P. Perdew, Phys. Rev. Lett., **55**, 1665 (1985).

[84] J. P. Perdew, Y. Wang, Phys. Rev. B, **33**, 8800 (1986).

[85] A. D. Becke, Phys. Rev. A, **98**, 3098 (1988).

[86] C. Lee, W. Yang, R. G. Parr, Phys. Rev. B, **37**, 785 (1988).

[87] R. Colle, D. Salvetti, Theor. Chim. Acta, **37**, 329 (1975).

[88] J. Harris, Phys. Rev. A, **29**, 1648 (1984).

[89] A. D. Becke, J. Chem. Phys., **98**, 5648 (1993).

[90] J. P. Perdew, Y. Wang, Phys. Rev. B, **45**, 13244 (1992).

[91] R. T. Sharp, G. K. Horton, Phys. Rev., **90**, 317 (1953).

[92] J. D. Talman, W. F. Shadwick, Phys. Rev. A, **14**, 36 (1976).

[93] T. Grabo, T. Kreibich, S. Kurth, E. K. U. Gross, in “Strong Coulomb Correlations in Electronic Structure: Beyond the Local Density Approximation”, ed. V. I. Anisimov, Gordon & Breach, Tokyo, 1998.

[94] J. M. Perez-Jorda, A. D. Becke, E. San-Fabian, J. Chem. Phys., **100**, 6520 (1994).

[95] P. M. W. Gill, B. G. Johnson, Chem. Phys. Lett., **209**, 506 (1993).

[96] B. I. Dunlap, J. W. D. Connolly, J. R. Sabin, J. Chem. Phys., **71**, 3396 (1979).

[97] K. Eichkorn, O. Treutler, H. Öhm, M. Häser, R. Ahlrichs, Chem. Phys. Lett., **109**, 40 (1995).

[98] R. E. Stratmann, G. E. Scuseria, M. J. Frisch, Chem. Phys. Lett., **257**, 213 (1996).

[99] J. A. Pople, P. M. W. Gill, B. G. Johnson, Chem. Phys. Lett., **199**, 577 (1992).

[100] B. G. Johnson, P. M. W. Gill, J. A. Pople, J. Chem. Phys., **98**, 5612 (1993).

[101] B. G. Johnson, M. J. Frisch, J. Chem. Phys., **100**, 7429 (1994).

[102] N. Oliphant, R. J. Bartlett, J. Chem. Phys., **100**, 6550 (1994).

[103] L. A. Curtiss, K. Raghavachari, P. C. Redfern, J. A. Pople, J. Chem. Phys., **106**, 1063 (1997).

[104] E. J. Meijer, M. Spirik, J. Chem. Phys., **105**, 8684 (1996).

[105] J. Oddershede, Adv. Chem. Phys., **69**, 201 (1987).

[106] C. Fuchs, V. Bonačić-Koutecký, J. Koutecký, J. Chem. Phys., **98**, 3121 (1993).

[107] J. F. Stanton, R. J. Bartlett, J. Chem. Phys., **98**, 7029 (1993).

[108] R. J. Bartlett, J. F. Stanton, Rev. Comp. Chem., **5**, 65 (1994).

[109] J. F. Stanton, R. J. Bartlett, J. Chem. Phys., **98**, 7029 (1993).

[110] M. Nooijen, R. Bartlett, J. Chem. Phys., **106**, 6441 (1997).

[111] S. F. Boys, Proc. R. Soc. (London), **A200**, 542 (1950).

[112] T. Helgaker, P. R. Taylor, in "Modern Electronic Structure Theory", Part I, ed. D. R. Yarkony, World Scientific, 1995.

[113] H. Taketa, S. Huzinaga, K. Ohata, J. Phys. Soc. Japan, **21**, 2313 (1996).

[114] M. Dupuis, J. Rys, H. F. King, J. Chem. Phys., **65**, 111 (1976).

[115] W. J. Heher, R. F. Steward, J. A. Pople, J. Chem. Phys., **51**, 2657 (1969).

[116] J. S. Binkley, J. A. Pople, J. Am. Chem. Soc., **102**, 939 (1999).

[117] M. J. Frisch, J. A. Pople, J. S. Binkley, J. Chem. Phys., **80**, 3265 (1984).

[118] L. Szasz, "Pseudopotential Theory of Atoms and Molecules", Wiley, New York, 1985.

[119] J. Almlöf, O. Gropen, Rev. in Computational Chemistry, Vol. 8, VCH Publishers, Inc. New York, 1996.

[120] T. R. Cundari, M. T. Benson, M. L. Lutz, S. O. Sommerer, Rev. in Computational Chemistry, Vol. 8, VCH Publishers, Inc. New York, 1996, and the references therein.

[121] P. A. Christiansen, Y. S. Lee, K. S. Pitzer, J. Chem. Phys., **71**, 4445 (1979).

[122] M. Born, Science, **122**, 675 (1955).

[123] M. Hillery, R. F. O'Connell, M. O. Scully, E. P. Wigner, Phys. Rep., **106**, 121 (1984).

[124] Z. Li, J. Y. Fang, C. C. Martens, J. Chem. Phys., **104**, 6919 (1996).

[125] A. Donoso, C. C. Martens, Phys. Rev. Lett., 87, 223202 (2001).

[126] M. Hartmann, J. Pittner, V. Bonačić-Koutecký, A. Heidenreich, J. Jortner, J. Chem. Phys. **108**, 3096 (1998).

[127] L. Verlet, Phys. Rev., **159**, 98 (1967).

[128] H. J. C. Berendsen, J. P. M. Postma, W. F. van Gunsteren, A. DiNola, J. R. Haak, J. Chem. Phys., **81**, 3684 (1984).

[129] R. Car, M. Parrinello, Phys. Rev. Lett., **55**, 2471 (1985).

[130] J. Pittner, "Ab initio Study of Optical Properties of Neutral and Charged Pure and Mixed Alkali Metal Clusters", VWF Verlag für Wissenschaft und Forschung GmbH, Berlin, 1997.

[131] M. Hartmann, J. Pittner, V. Bonačić-Koutecký, J. Chem. Phys., **114**,, 2106 (2001).

[132] M. Hartmann, J. Pittner, V. Bonačić-Koutecký, J. Chem. Phys., **114**, 2123 (2001).

[133] Y. Yamaguchi, J. Osamura, J. D. Goddard, H. F. Schaefer III, "A new Dimension to Quantum Chemistry: Analytic Derivative Methods in Ab initio Molecular Electronic Structure Theory", Oxford University Press, New York, 1994, p. 72.

[134] J. E. Rice, R. D. Amos, N. C. Handy, T. J. Lee, H. F. Schaefer III, J. Chem. Phys., **85**, 963 (1986).

[135] T. J. Lee, N. C. Handy, J. E. Rice, A. C. Scheiner, H. F. Schäfer III, J. Chem. Phys., **85**, 3930 (1986).

[136] J. C. Tully, J. Chem. Phys., **93**, 1061 (1990).

[137] S. A. Rice, M. Zhao, "Optical Control of Molecular Dynamics", John Wiley & Sons, New York, 2000.

[138] D. J. Tannor, S. A. Rice, J. Chem. Phys., **83**, 5013 (1985).

[139] D. J. Tannor, R. Kosloff, S. A. Rice, J. Chem. Phys., **85**, 5805 (1986).

[140] M. Shapiro, P. Brumer, J. Chem. Phys., **84**, 4103 (1986).

[141] M. Shapiro, P. Brumer, Int. Rev. Phys. Chem., **13**, 187 (1994).

[142] R. Kosloff, S. A. Rice, P. Gaspard, S. Tersigni, D. D. Tannor, Chem. Phys., **139**, 201 (1989).

[143] A. P. Pierce, M. A. Dahleh, H. Rabitz, Phys. Rev. A, **42**, 1065 (1990).

[144] Y. J. Yan, Z. W. Shen, Y. Zhao, Chem. Phys., **233**, 191 (1998).

[145] J. X. Cheng, Z. W. Shen, Y. J. Yan, J. Chem. Phys., **109**, 1654 (1998).

[146] K. J. Taylor, C. L. Pettiette-Hall, O. Cheshnovsky, R. E. Smalley, J. Chem. Phys., **96**, 3319 (1992).

[147] J. Ho, K. M. Ervin, W. C. Lineberger, J. Chem. Phys., **93**, 6987 (1990).

[148] H. Handschuh, G. Ganteför, P. S. Bechthold, W. Eberhardt, J. Chem. Phys., **100**, 7093 (1994).

[149] K. Balasubramanian, M. Z. Liao, J. Chem. Phys., **86**, 5587 (1987).

[150] G. Bravo-Pérez, I. L. Garzón, O. Novaro, Chem. Phys. Lett., **313**, 655 (1999).

[151] H. Häkkinen, U. Landman, Phys. Rev. B, **62**, R2287 (2000).

[152] H. Grönbeck, W. Andreoni, Chem. Phys., **262**, 1 (2000).

[153] H. Häkkinen, M. Moseler, U. Landman, Phys. Rev. Lett., **89**, 033401 (2002).

[154] S. Gilb, P. Weis, F. Furche, R. Ahlrichs, M. Kappes, J. Chem. Phys., **116**, 4094 (2002).

[155] F. Furche, R. Ahlrichs, P. Weiss, C. Jacob, S. Gilb, T. Bierweiler, M. M. Kappes, J. Chem. Phys., **117**, 6982 (2002).

[156] P. Weis, T. Bierweiler, S. Gilb, M. Kappes, Chem. Phys. Lett., **355**, 355 (2002).

[157] V. Bonačić-Koutecký, L. Češpiva, J. Koutecký, J. Chem. Phys., **98**, 7981 (1993).

[158] V. Bonačić-Koutecký, L. Češpiva, P. Fantucci, J. Pittner, J. Koutecký, J. Chem. Phys., **100**, 490 (1994).

[159] V. Bonačić-Koutecký, J. Pittner, M. Boiron, P. Fantucci, J. Chem. Phys., **110**, 3876 (1999).

[160] V. Bonačić-Koutecký, V. Veyret, R. Mitrić, J. Chem. Phys., **115**, 10450 (2001) .

[161] Y. Negishi, Y. Nakajima, K. Kaya, J. Chem. Phys., **115**, 3657 (2001).

[162] C. W. Bauschlicher, Jr., S. R. Langhoff, H. Partridge, J. Chem. Phys., **91**, 2412 (1989), and references therein.

[163] R. Mitrić, M. Hartmann, B. Stanca, V. Bonačić-Koutecký, P. Fantucci, J. Phys. Chem. A, **105**, 8892 (2001).

[164] V. Bonačić-Koutecký, J. Burda, R. Mitrić, M. Ge, G. Zampella, P. Fantucci, J. Chem. Phys., **117**, 3120 (2002).

[165] R. Mitrić, C. Bürgel, J. Burda, V. Bonačić-Koutecký, Eur. Phys. J. D, **24**, 41 (2003).

[166] P. Weis, O. Welz, E. Vollmer, M. M. Kappes, J. Chem. Phys., submitted.

[167] C. E. Moore, "Atomic energy levels", Circ. No. 467; Nat. Bureau of Standards, Washington, DC, 1958; Vol. III.

[168] V. Beutel, H. G. Krämer, G. L. Bhale, M. Kuhn, K. Weyers, W. Demtröder, J. Chem. Phys., **98**, 2669 (1993).

[169] J. Ho, K. M. Ervin, W. C. Lineberger, J. Chem. Phys., **93**, 6987 (1990).

[170] B. Simard, P. A. Hackett, J. Mol. Spectrosc., **142**, 310 (1990).

[171] L. L. Ames. R. F. Barrow, Trans. Faraday Soc., **63**, 39 (1967).

[172] C. Jackschath, I. Rabin, W. Schulze, Z. Phys. D: At. Mol. Clusters, **22**, 517 (1992).

[173] C. Jackslath, I. Rabin, W. Schulze, Ber. Bunsen-Ges. Phys. Chem., **96**, 1200 (1992).

[174] D. Andrae, U. Haeussermann, M. Dolg, H. Stoll, H. Preuss, Theor. Chim. Acta, **77**, 123 (1990).

[175] J. Perdew, Phys. Rev. B, **33**, 8822 (1986).

[176] P. J. Hay, W. R. Wadt, J. Chem. Phys., **82**, 270 (1985).; W. R. Wadt, P. J. Hay, J. Chem. Phys., **82**, 284 (1985).; P. J. Hay, W. R. Wadt, J. Chem. Phys., **82**, 299 (1985).

[177] R. Fournier, J. Chem. Phys., **115**, 2165 (2001).

[178] V. Beutel, H. G. Krämer, G. L. Bhale, M. Kuhn, K. Weyers, W. Demtröder, J. Chem. Phys., **98**, 2699 (1993).

[179] J. C. Fabbi, J. D. Langenberg, Q. D. Costello, M. D. Morse, L. Karlsson, J Chem. Phys., **115**, 7543 (2001).

[180] R. Wesendrup, T. Hunt, P. Schwerdtfeger, J. Chem. Phys., **112**, 9356 (2000).

[181] B. C. Gates, "Catalytic Chemistry", John Wiley & Sons, New York, 1992.

[182] D. M. Cox, R. Brickman, K. Creegan, et al., Z. Phys. D, **19**, 353 (1991).

[183] D. M. Cox, R. Brickman, K. Creegan, Mater. Res. Soc. Symp. Proc., **206**, 34 (1991).

[184] J. Hagen, L. D. Socaciu, M. Elijazyfer, et al., Phys. Chem. Chem. Phys., **4**, 1707 (2002).

[185] K. J. Taylor, C. L. Pettiette-Hall, O. Cheshnovsky, et al., J. Chem. Phys., **96**, 3319 (1992).

[186] W. T. Wallace, R. L. Whetten, J. Am. Chem. Soc., **124**, 7499 (2002).

[187] T. Engel, G. Ertl, Adv. Catal., **28**, 1 (1979).

[188] D. Stolcic, M. Fischer, G. Ganteför, Y. D. Kim, Q. Sun, P. Jena, J. Am. Chem. Soc., **125**, 2848 (2003).

[189] M. L. Kimble, A. W. Castleman Jr., R. Mitrić, C. Bürgel, V. Bonačić-Koutecký, J. Am. Chem. Soc., in press.

[190] L. D. Socaciu, J. Hagen, U. Heiz, T. M. Bernhardt, T. Leisner, L. Wöste, Chem. Phys. Lett., **340**, 282 (2001).

[191] A. W. Castleman Jr., K. G. Weil, R. E. Sigsworth, R. E. Leuchtner, R. G. Keese, J. Chem. Phys., **86**, 3829 (1987).

[192] R. E. Leuchtner, A. C. Harms, A. W. Castleman Jr., J. Chem. Phys., **92**, 6527 (1990).

[193] H. Häkkinen, U. Landman, J. Am. Chem. Soc., **123**, 9704 (2001).

[194] G. Mills, M. S. Gordon, H. Metiu, Chem. Phys. Lett., **359**, 493 (2002).

[195] G. Mills, M. S. Gordon, H. Metiu, J. Chem. Phys., **118**, 4198 (2003).

[196] D. H. Wells Jr., W. N. Delgass, K. T. Thompson, J. Chem. Phys., **117**, 10597 (2002).

[197] A. D. McLean, G. S. Chandler, J. Chem. Phys., **72**, 5639 (1980).

[198] R. Krishnan, J. S. Binkley, R. Seeger, J. Chem. Phys., **72**, 650 (1980).

[199] W. T. Wallace, A. J. Leavitt, R. L. Whetten, Chem. Phys. Lett., **368**, 774 (2003).

[200] A. E. Reed, L. A. Curtiss, F. Weinholt, Chem. Rev., **88**, 899 (1988).

[201] M. A. Cheeseman, J. R. Eyler, J. Phys. Chem., **96**, 1082 (1992).

[202] C. W. Bauschlicher, S. R. Langhoff, H. Partridge, J. Chem. Phys., **93**, 8133 (1990).

[203] O. D. Häberlen, S. C. Chung, M. Stener, et al., J. Chem. Phys., **106**,, 5189 (1997).

[204] K. A. Zemski, D. R. Justes, A. W. Castleman Jr., J. Phys. Chem. A, **105**, 10237 (2001).

[205] D. R. Justes, R. Mitrić, N. Moore, V. Bonačić-Koutecký, A. W. Castleman Jr., J. Am. Chem. Soc., **125**, 6289 (2003).

[206] D. R. Justes, A. W. Castleman Jr., R. Mitrić, V. Bonačić-Koutecký, Eur. Phys. J. D, **24**, 331 (2003).

[207] K. Ruth, R. Burch, R. Kieffer, J. Catal., **175**, 27 (1998).

[208] V. S. Escribano, G. Busca, V. Lorenzelli, J. Phys. Chem., **94**, 8945 (1990).

[209] S. T. Oyama, G. A. Somorjai, J. Phys. Chem. **94**, 5022 (1990).

[210] A. Fielicke, K. Rademann, Phys. Chem. Chem. Phys. **4**, 2621 (2002).

[211] R. C. Bell, K. A. Zemski, D. R. Justes, A. W. Castleman Jr., J. Chem. Phys., **114**, 798 (2001).

[212] A. Schäfer, H. Horn, R. Ahlrichs, J. Chem. Phys. **100**, 5829 (1994).

[213] C. Peng, H. B. Schlegel, Isr. J. Chem., **33**, 449 (1993).

[214] C. Peng, P. Y. Ayala, H. B. Schlegel, M. J. Frisch, Comput. Chem., **16**, 49 (1995).

[215] K. Eichkorn, O. Treutler, H. Öhm, M. Häser, R. Ahlrichs, Chem. Phys. Lett., **109**, 42 (1995).

[216] S. F. Vyboishchikov, J. Sauer, J. Phys. Chem. A, **104**, 10913 (2000).

[217] M. Calatayud, J. Andres, A. Beltran, J. Phys. Chem. A, **105**, 9760 (2001).

[218] K. R. Asmis, M. Brümmer, C. Kaposta, G. Santambrogio, G. von Helden, G. Meijer, K. Rademann, L. Wöste, Phys. Chem. Chem. Phys., **4**, 1101 (2002).

[219] A. Fielicke, G. Meijer, G. von Helden, Eur. Phys. J. D, **24**, 69 (2003).

[220] A. Fielicke, G. Meijer, G. von Helden, J. Am. Chem. Soc., **125**, 3659 (2003).

[221] B. Simard, S. Denommee, D. M. Rayner, D. van Heijnsbergen, G. Meijer, G. von Helden, Chem. Phys. Lett., **357**, 195 (2002).

[222] A. Fielicke, G. von Helden, G. Meijer, B. Simard, S. Denommee, D. M. Rayner, J. Am. Chem. Soc., **125**, 11184 (2003).

[223] G. von Helden, D. van Heijnsbergen, G. Meijer, J. Phys. Chem. A, **107**, 1671 (2003).

[224] J. Oomens, A. G. G. M. Tielens, B. Saratkov, G. von Helden, G. Meijer, Astrophys. J., **591**, 968 (2003).

[225] A. Fielicke, R. Mitrić, G. Meijer, V. Bonačić-Koutecký, G. von Helden, J. Am. Chem. Soc., in press.

[226] Z. Luan, P. A. Meloni, R. S. Czernuszewicz, L. Kevan, J. Phys. Chem. B, **101**, 9046 (1997).

[227] S. T. Oyama, A. M. Middlebrook, G. A. Somorjai, J. Phys. Chem. **94**, 5029 (1990).

[228] P. Fayet, F. Granzer, G. Hegenbart, E. Moisar, B. Pishel, L. Wöste, Phys. Rev. Lett., **55**, 3002 (1985).

[229] M. Mostafavi, J. L. Marignier, J. Amblard, J. Belloni, Z. Phys. D: At. Mol. Clusters, **12**, 31 (1989).

[230] R. S. Eachus, A. P. Marchetti, A. A. Muenter, Annu. Rev. Phys. Chem., **50**, 117 (1999).

[231] A. P. Marchetti, A. A. Muenter, R. C. Baetzold, R. T. McCleary, J. Phys. Chem. B, **102**, 5287 (1998).

[232] L. König, I. Rabin, W. Schulze, G. Ertl, Science, **274**, 1353 (1996).

[233] I. Rabin, W. Schulze, G. Ertl, J. Chem. Phys., **108**, 5137 (1998).

[234] C. Felix, C. Sieber, W. Harbich, J. Buttet, I. Rabin, W. Schulze, G. Ertl, Chem. Phys. Lett., **313**, 105 (1999).

[235] I. Rabin, W. Schluze, G. Ertl, C. Felix, C. Siebach, W. Harbich, J. Buttet, Chem. Phys. Lett., **320**, 59 (2000).

[236] C. Felix, C. Sieber, W. Harbich, J. Buttet, I Rabin, W. Schulze, G. Ertl, Phys. Rev. Lett., **86**, 2992 (2001).

[237] J. Blanc, M. Broyer, J. Chavaleyre, P. Dugourd, H. Kuhling, P. Labastie, M. Ulbricht, J. P. Wolf, L. Wöste, Z. Phys. D, **19**, 7 (1991).

[238] G. Alameddin, J. Hunter, C. Cameron, M. M. Kappes, Chem. Phys. Lett., **192**, 122 (1992).

[239] J. Ho, K. M. Ervin, W. C. Lineberger, J. Chem. Phys., **93**, 6987 (1990).

[240] K. J. Taylor, C. L. Pettiete-Hall, O. Chesnovsky, R. E. Smalley, J. Chem. Phys., **96**, 3319 (1992).

[241] H. Handschuh, C. Y. Cha, P. S. Bechtold, G. Ganteför, W. Eberhardt, J. Chem. Phys., **102**, 6406 (1995).

[242] C. Ellert, M. Schmitt, G. Schmidt, T. Reiner, H. Haberland, Phys. Rev. Lett., **75**, 1731 (1995).

[243] V. Bonačić-Koutecký, J. Pittner, C. Fuchs, P. Fantucci, M. F. Guest, J. Koutecký, J. Chem. Phys., **104**, 1427 (1996).

[244] V. Bonačić-Koutecký, J. Pittner, D. Reichardt, P. Fantucci, J. Koutecký, in "Metal Clusters", Wiley series in Theoretical Chemistry, edited by W. Ekardt, Wiley, Chichester, 1999, p. 26-68.

[245] W. Harbich, S. Fedrigo, J. Buttet, Chem. Phys. Lett., **195**, 613 (1992).

[246] S. Fedrigo, W. Harbich, J. Buttet, Phys. Rev. B, **47**, 10706 (1993).

[247] B. A. Collings, K. Athanassenas, D. M. Lacombe, D. M. Rayner, P. A. Hackett, Chem. Phys. Lett., **227**, 490 (1994).

[248] F. Federmann, K. Hoffmann, N. Quaas, J. P. Toennies, Eur. Phys. J. D, **9**, 11 (1999).

[249] T. Diederich, J. Tiggesbäumker, K. H. Meiwes-Broer, J. Chem. Phys., **116**, 3263 (2002).

[250] J. F. Stanton, R. J. Bartlett, J. Chem. Phys., **98**, 7029 (1993).

[251] M. Nooijen, R. J. Bartlett, J. Chem. Phys., **106**, 6441 (1997).

[252] S. Fedrigo, W. Harbich, J. Buttet, Phys. Rev. B, **47**, 10706 (1993).

[253] W. Harbich, S. Fedrigo, J. Buttet, Chem. Phys. Lett., **195**, 613 (1992).

[254] C. Sieber, J. Buttet, W. Harbich, C. Felix, R. Mitrić, V. Bonačić-Koutecký, Phys. Rev. Lett., submitted.

[255] S. Grebenev, J. P. Toennies, A. F. Vilesov, Science, **279**, 2083 (1998).

[256] S. Wolf., Ph. D. Thesis, Department of Physics of the Freie Universität Berlin, Berlin, 1997.

[257] H. Hess, S. Kwiat, L. Socaciu, S. Wolf, T. Leisner, L. Wöste, Appl. Phys. B, **71**, 337 (2000).

[258] T. Leisner, S. Vajda, S. Wolf, L. Wöste, R. S. Berry, J. Chem. Phys., **111**, 1017 (1999).

[259] M. Hartmann, A. Heidenreich, J. Pittner, V. Bonačić-Koutecký, J. Jortner, J. Phys. Chem. A, **108**, 4069 (1998).

[260] M. Hartmann, R. Mitrić, B. Stanca, V. Bonačić-Koutecký, Eur. Phys. J. D, **16**, 151 (2001).

[261] M. Hartmann, J. Pittner, H. van Dam, V. Bonačić-Koutecký, Eur. Phys. J. D, **9**, 393 (1999).

[262] J. Hagen, L. Socaciu, T. M. Bernhardt, L. Wöste, R. Mitrić, V. Bonačić-Koutecký, in preparation.

[263] I. Andrianov, V. Bonačić-Koutecký, M. Hartmann, J. Manz, J. Pittner, K. Sundermann, Chem. Phys. Lett., **318**, 256 (2000).

[264] D. M. Neumark, Annu. Rev. Phys. Chem., **52**, 255 (2001).

[265] F. H. Stillinger, T. A. Weber, Phys. Rev. A, **25**, 978 (1982).

[266] S. V. Krivov, S. F. Chekmarev, M. Karplus, Phys. Rev. Lett. **88**, 038101 (2002).

[267] S. F. Chekmarev, S. V. Krivov, Chem. Phys. Lett., **287**, 719 (1998).

[268] S. F. Chekmarev, Phys. Rev. E, **64**, 036703 (2001).

[269] D. Reichardt, V. Bonačić-Koutecký, P. Fantucci, J. Jellinek, Z. Phys. D, **40**, 486 (1997).

[270] V. Bonačić-Koutecký, L. Češpiva, P. Fantucci, J. Pittner, J. Koutecký, J. Chem. Phys., **98**, 7981 (1993).

[271] S. F. Chekmarev, R. Mitrić, V. Bonačić-Koutecký, Eur. J. Phys. D, **24**, 45 (2003).

[272] W. Forst, ”Theory of unimolecular reactions”, Academic Press, London 1973.

[273] B. Kohler, V. V. Yakovlev, J. Che, J. L. Krause, M. Messina, K. R. Wilson, N. Schwentner, R. M. Whitnell, Y. J. Yan, Phys. Rev. Lett., **74**, 3360 (1995).

[274] N. F. Scherer, A. J. Ruggiero, M. Du, G. R. Fleming, J. Chem. Phys., **93**, 856 (1990).

[275] A. M. Weiner, D. E. Leaird, G. P. Wiederrecht, K. A. Nelson, Science, **247**, 1317 (1990).

[276] S. Rice, S. P. Shah, Phys. Chem. Chem. Phys. **4**, 1683 (2002).

[277] R. Kosloff, S. A. Rice, P. Gaspard, S. Tersigni, D. J. Tannor, J. Chem. Phys., **139**, 201 (1989).

[278] S. A. Rice, Science, **258**, 412 (1992).

[279] W. S. Warren, H. Rabitz, M. Dahleh, Science, **259**, 1581 (1993).

[280] Y. Yan, J. Che, J. Krause, J. Chem. Phys., **217**, 297 (1997).

[281] R. Mitrić, M. Hartmann, J. Pittner, V. Bonačić-Koutecký, J. Phys. Chem., A, **106**, 10477 (2002).

[282] R. Mitrić, M. Hartmann, J. Pittner, V. Bonačić-Koutecký, Eur. Phys. J. D, **24**, 17 (2003).

[283] V. Bonačić-Koutecký, J. Pittner, J. Koutecký, Chem. Phys., **210**, 313 (1996).

Erklärung

Ich erkläre hiermit, daß

- ich die vorliegende Dissertationsschrift „Structure-Reactivity Relation, Optical Properties and Real-Time Study of Ultrafast Processes in Atomic Clusters“ selbstständig und ohne unerlaubte Hilfe angefertigt habe;
- ich mich nicht bereits anderwärts um einen Doktorgrad beworben habe oder einen solchen besitze;
- mir die Promotionsordnung der Mathematisch-Naturwissenschaftlichen Fakultät II der Humboldt-Universität zu Berlin bekannt ist.

Berlin, 15.11.2003 Roland Mitric